eman ta zabal zazu

Universidad del País Vasco

Euskal Herriko Unibertsitatea

PhD THESIS
February 2019

TESIS DOCTORAL
Febrero 2019

Selective catalytic reduction with internal NH_3 generation in previous NO_x storage and reduction catalyst for NO_x removal in light-duty diesel vehicles

Reducción catalítica selectiva con producción previa de NH_3 en catalizador de almacenamiento y reducción de NO_x para eliminación de NO_x en vehículos ligeros diésel

Maitane Urrutxua Andia

DEPARTAMENTO DE INGENIERÍA QUÍMICA
INGENIARITZA KIMIKOA SAILA

Selective catalytic reduction with internal NH_3 generation in previous NO_x storage and reduction catalyst for NO_x removal in light-duty diesel vehicles

Reducción catalítica selectiva con producción previa de NH_3 en catalizador de almacenamiento y reducción de NO_x para eliminación de NO_x en vehículos ligeros diésel

MEMORIA

para optar al Grado de
Doctor Internacional en Ingeniería Química
presentada por

Maitane Urrutxua Andia

Leioa, febrero de 2019

Lehen da bizi gustatuko litzaidakeen urte guzti hauetan ondoan izan ditudan pertsona guztiei eskerrak eman. Zuek gabe hau ez zen posible izango.

A mis directores Dr. Juan Ramón González Velasco y Dr. Beñat Pereda Ayo por todo el tiempo dedicado y la confianza depositada en mí para que esta tesis fuera posible. Eskerrik asko!

A mi grupo de investigación, TQSA, a los Doctores Miguel Ángel, José Ignacio, Rubén, José Antonio, María Pilar, José Luis, Beatriz, Asier, Zouhair, Jon Iñaki y José María y a mis compañeros de laboratorio Itxaso, Karina, Carmen, Edwin, Cristina, Unai, Ainara, Andoni Salbi, Miren, Jonatan, Miryam, Jon Ander, Adriana, Alberto, Andoni, Adrian, Alejandro, Juani y Asier, eskerrik asko por las risas en la hora de la comida. También a aquellos que han realizado el trabajo fin de grado conmigo: Adrian, Dulce, Jon y Ander. A todas las personas que he tenido el placer de conocer durante la realización de la tesis. Baina batez ere gustatuko litzaidakeen eskerrak eman karrera hasi eta gaur egun lagun handi ditudan Arregi eta Miryameri hainbeste momentu on alkarregaz igarotzeagatik. Bereziki mila esker Miry momentu on eta txarretan ondoan izatearren eta amaigabeak izan diren eta gaur egun diren elkarrizketa guzti horiegatik. Dudarik gabe urte guzti hauek zu gabe ez ziren berdinak izango.

Thanks to Professor Louise Olsson for giving me the opportunity to join the Chemical Engineering Division and KCK during my stay at Chalmers Tekniska Högskola and for making me feel part of the group from the first day. Special thanks also to Lidija, Kurnia, Kunpeng and Jesus for their continuous help and good moments shared. Also, to all the rest of the group for a nice time at fika and also, the great times off-campus. Tack så mycket!

A todos los investigadores y técnicos del Servicio General de Análisis (SGIKER) de la UPV/EHU por su colaboración en la caracterización de tan variadas muestras. Especialmente al Dr. Luis Lezama por la realización de las medidas de las muestras y el análisis de los resultados mediante EPR.

Al Ministerio de Economía y Competitividad por la Beca predoctoral concedida (BES-2013-065349) y la financiación de la estancia en la Universidad Tecnológica de Chalmers (EEBB-I-17-12428).

Lagun guztiei.

Azkenik, nire bizitzan pertsonarik garrantzitsuenak diren nire guraso eta Joneri. Zuek zarete nire euskarri sendoak eta zuek barik etapa honi amaiera ematea ez zen posible izango. Gora zuek!!!

Beti nire ondoan dagoen familia horri

Eskerrik asko bihotz bihotzez

ÍNDICES

ÍNDICE DE CONTENIDOS

ÍNDICE DE FIGURAS

ÍNDICE DE TABLAS

Capítulo 1

PLANTEAMIENTO DEL PROBLEMA Y ALCANCE DE LA TESIS

Capítulo 1

PLANTEAMIENTO DEL PROBLEMA Y ALCANCE DE LA TESIS

RESUMEN

El uso de motores diésel y de motores de mezcla pobre está aumentando debido a su mayor eficiencia de combustible y menores emisiones de CO_2 en comparación con los motores de gasolina. Sin embargo, el exceso de oxígeno en los gases de combustión imposibilita la reducción de los NO_x mediante catalizadores de tres vías (TWC). Estos catalizadores son ineficientes en ambientes oxidantes. Para la eliminación de los NO_x en los motores diésel y de mezcla pobre se han desarrollado dos tecnologías: almacenamiento y reducción de NO_x (NSR) —también conocida como LNT (lean NO_x trap)— y reducción catalítica selectiva (SCR). Con el fin de presentar al lector el tema de esta tesis en este capítulo, se realiza una revisión de las tecnologías más prometedoras, como son la tecnología NSR, NH_3-SCR y sistemas combinados NSR-SCR. Se analizan los conceptos básicos de estas tecnologías, las formulaciones de los catalizadores y los mecanismos de reacción; NSR y NH_3-SCR. Finalmente, se explica el objetivo y diseño de la tesis así como el alcance de la investigación.

Chapter 1

PROBLEM STATEMENT AND SCOPE OF THE THESIS

ABSTRACT

The use of diesel engines and lean burn gasoline engines in vehicles application is increasing due to their higher fuel efficiency and lower CO_2 emissions compared to stoichiometric gasoline engines. However, the introduction of excess oxygen for fuel combustion produces an oxygen rich exhaust and makes NO_x reduction a challenging endeavor, because well-established three-way catalysts (TWC) are inefficient in such oxygen rich environment. Two different approaches have been developed in order to mitigate NO_x emissions from diesel and lean burn engines, NO_x storage and reduction (NSR) —also denominated lean NO_x trap (LNT)— and selective catalytic reduction (SCR). In order to introduce the reader to the subject of this thesis, a review of most promising technologies, namely NSR, NH_3-SCR and combined NSR-SCR systems is presented in this chapter. The basic concepts of those technologies, the catalysts formulations, the NSR and NH_3-SCR reactions network, as well as kinetic mechanisms already reported in the scientific and technical literature are reviewed. Thus, motivation of the thesis is explained and then the scope of the research and the layout of the thesis are described.

1. PLANTEAMIENTO DEL PROBLEMA Y ALCANCE DE LA TESIS

La contaminación del aire durante los últimos años se ha incrementado prácticamente en todas las ciudades de Europa [1]. En las últimas décadas se han logrado reducciones de las emisiones de los principales focos contaminantes tales como la industria, la producción de energía, hogares, transporte y agricultura. A pesar de ello, para la Directiva de la Calidad del Aire de la Unión Europea [1], la limpieza del aire sigue siendo un reto.

El sector del transporte por carretera es una de las principales causas de la producción del dióxido de carbono (CO_2), óxidos de nitrógeno (NO_x) y materia particulada ($MP_{2.5}$ y MP_{10}). La repercusión de este sector en las ciudades es muy grave, ya que los contaminantes están en contacto directo con las personas. Durante las últimas dos décadas, la Comisión Europea (CE) se ha centrado especialmente en la reducción de emisiones de CO_2 en los automóviles privados, para así reducir su impacto en el notable cambio climático [2], ya que las emisiones de CO_2 del transporte por carretera han aumentado en un 17% entre 1990 y 2014. Este aumento se debe tanto al crecimiento del número de vehículos de pasajeros como al transporte de mercancías, que ha conllevado un incremento importante del consumo de combustible [1].

El catalizador de tres vías (TWC) para motores que operan en condiciones estequiométricas reduce exitosamente los NO_x, el CO y los hidrocarburos inquemados (HCs) [3]. Sin embargo, la necesidad de motores de combustión con mayor eficiencia ha hecho que aumente el número de motores diésel, que proporcionan una combustión más completa que los motores gasolina. Debido al exceso de oxígeno en la combustión en los motores diésel, los catalizadores de tres vías no son capaces de reducir los contaminantes, por lo que son necesarios otros sistemas catalíticos para la reducción de las emisiones, especialmente de NO_x, en los motores de mezcla pobre.

Los avances realizados en la tecnología de los motores diésel son exitosos para la reducción de los NO_x, aunque insuficientes para poder cumplir la actual legislación. Hoy en día, la legislación vigente para las emisiones de los motores diésel es la norma Euro 6 y el límite de emisiones de NO_x en los motores diésel está en 0,08 g km^{-1}. Por ello, es fundamental la aplicación de un tratamiento catalítico en los gases de escape para mitigar las emisiones.

La Tabla 1.1 resume los valores de emisiones estándar de vehículos de pasajeros con motores diésel en Europa. Como se observa en la Tabla 1.1, las restricciones han ido aumentando desde la norma Euro 1 (1992) a la norma Euro 6 (2014). El catalizador de oxidación (DOC) es parte de la tecnología catalítica implementada en los motores diésel para cumplir los límites de emisiones desde que entraron en vigor las regulaciones [4]. Normalmente, el primer dispositivo después del motor suele ser el DOC, que oxida el CO y los HCs a CO_2 y H_2O. Hasta la implementación de la norma Euro 3 era suficiente utilizar el DOC para reducir las emisiones; fue la primera vez que se limitaron las emisiones de los NO_x. El control de las emisiones de NO_x y PM es un reto tecnológico, ya que muchas veces cuando se reduce la emisión de uno de los componentes aumenta la emisión del otro [4]. En general, a temperaturas bajas de operación del motor se reducen las emisiones de NO_x, pero al mismo tiempo se incrementan las emisiones de PM. A altas temperaturas ocurre lo contrario [5]. Para poder desligar las emisiones de NO_x y PM, a comienzos del año 2000 se implementó un filtro para las partículas diésel (DPF) [6]. En Europa, la introducción de la norma Euro 5 hizo que se incluyera obligatoriamente el filtro de partículas (DPF) [7].

Implementando DOC y DPF en los motores diésel se consigue disminuir las emisiones de CO, HC y PM. Sin embargo, la conversión de NO_x con dicha configuración catalítica (DOC+DPF) es algo menor del 10% [8], lo que se sitúa muy lejos del objetivo fijado por la norma Euro 6.

Tabla 1.1. Límites de emisión de vehículos diésel de pasajeros en la Unión Europea [9].

Norma	Fecha	Límite, g km^{-1}				
		CO	HC+NO_x	NO_x	PM	PN, # per g
Euro 1	1992.07	2,73 (3,16)	0,97 (0,13)	-	0,14 (0,18)	
Euro 2, IDI	1996.01	1,0	0,7	-	0,08	
Euro 2, DI	1996.01[c]	1,0	0,9	-	0,10	
Euro 3	2000.01	0,64	0,56	0,50	0,05	
Euro 4	2005.01	0,50	0,30	0,25	0,025	
Euro 5a	2009.09[d]	0,50	0,23	0,18	0,005	
Euro 5b	2011.09[e]	0,50	0,23	0,18	0,005	$6{,}0x10^{11}$
Euro 6	2014.09	0,50	0,17	0,08	0,005	$6{,}0x10^{11}$

[a] En las etapas Euro 1 a 4, los vehículos de pasajeros> 2500 kg fueron homologados como vehículos de la categoría N_1. [b] Los valores entre paréntesis son los límites de conformidad de producción (COP) [c] Hasta 30-09-1999 (posteriormente los motores DI deben cumplir con los límites IDI). [d] 2011.01 para todos los modelos. [e] 0,0045 g km^{-1} utilizando el método PMP para la medición.
PN: número de partículas; DI: inyección directa; IDI: inyección indirecta; PMP: programa de medición de partículas.

En las dos últimas décadas se han desarrollado e implementado dos estrategias catalíticas para la eliminación de NO_x: reducción catalítica selectiva (SCR) y almacenamiento y reducción de NO_x (NSR), también conocido como lean NO_x trap (LNT). El catalizador NSR necesita mayores cantidades de metales preciosos que el catalizador TWC, porque requiere compuestos capaces de almacenar los NO_x y para así poder trabajar bajo ciclos pobres y ricos [7, 8, 10]. La tecnología SCR necesita NH_3 como agente reductor de NO_x. El NH_3 es generado por la descomposición de la urea que es almacenada en el vehículo [10-12]. Las tecnologías NSR y SCR tienen una ventana de operación limitada. De hecho, estas dos tecnologías deben ser mejoradas para aumentar

el rendimiento, tanto a bajas temperaturas como a altas temperaturas, y también mejorar la estabilidad de los catalizadores.

El catalizador NSR normalmente produce NH_3 como subproducto, que puede ser utilizado como reductor en el catalizador SCR. Por este motivo, hay estudios recientes combinando ambos catalizadores, NSR y SCR.

1.1. CONCEPTO Y ESTADO ACTUAL DE LA TECNOLOGÍA DE ALMACENAMIENTO Y REDUCCIÓN DE NO_x, NSR

1.1.1. Concepto NSR

El concepto NSR fue introducido por Toyota a mediados del año 1990 [13, 14]. El catalizador NSR trabaja en condiciones cíclicas con periodos pobres (oxidantes) y ricos (reductores), que están definidos por la relación aire-combustible (A/C). Cuando el automóvil está en marcha las condiciones pobres y ricas se alternan [15, 16]. Durante el periodo pobre, con exceso de O_2 (alto A/C), los NO_x se adsorben en el catalizador. Después, bajo condiciones ricas (A/C< 13,63/1 w/w) los NO_x almacenados en la etapa pobre son liberados y reducidos. Por ello, el catalizador NSR necesita centros para el almacenamiento de los NO_x (compuestos de metales alcalinos o alcalino-térreos) y centros para la oxidación/reducción de los NO_x (metales nobles, similares a los contenidos en los TWCs). En la literatura, se observa que la mayoría de los estudios utilizan Ba como material de almacenamiento variando la carga entre el 8 y 20 % en peso [17, 18]. También se han estudiado otros metales para el almacenamiento como el Na, K, Mg, Sr y Ca [19]. Estudios termodinámicos y cinéticos han demostrado que la basicidad de los componentes alcalinos y alcalino-térreos está relacionada directamente con la capacidad de almacenamiento de los NO_x; por ejemplo a 350 °C, la capacidad de almacenamiento de NO_x decrece según: K>Ba>Sr>Na>Ca>Li>Mg [17, 19]. Normalmente, los metales nobles se incorporan con bajo contenido, 1-2% en peso. Al igual que en la tecnología TWC, el platino, el paladio y el rodio son los

más utilizados [18-21]. El metal participa en dos etapas fundamentales en el mecanismo del catalizador NSR: la oxidación de NO a NO_2 durante el periodo pobre y la reducción de NO_x durante el periodo rico. En la literatura, se indica que el platino es un buen metal para la oxidación del NO y que el Rh es activo para la reducción de NO_x. Obviamente, los compuestos de almacenamiento y los metales preciosos deben de estar dispersos sobre materiales porosos con gran área superficial (Al_2O_3, ZrO_2, CeO_2, MgO o mezcla de óxidos), que a su vez están depositados sobre una estructura monolítica, normalmente de cordierita [18, 22].

En la actualidad, está establecido que el mecanismo NSR se ajusta, en general, a las cinco etapas siguientes, contenidas en la representación esquemática en la Figura 1.1.

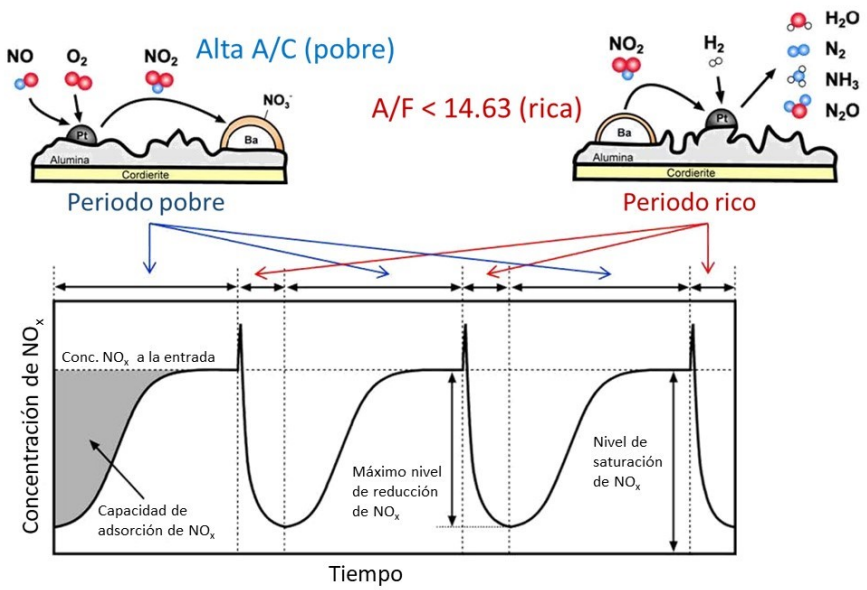

Figura 1.1. Almacenamiento y reducción de NO_x a) representación esquemática del mecanismo; b) representación de la concentración de NO_x durante los periodos de mezcla pobre y rico [23].

1. Oxidación del NO a NO_2 (condiciones pobres, atmósfera oxidante).
2. Adsorción de NO_x como nitritos o nitratos sobre los centros de almacenamiento (periodo pobre, atmósfera oxidante).
3. Inyección y evolución de los agentes reductores utilizados: H_2, CO o hidrocarburos (HCs).
4. Liberación de los NO_x almacenados desde la superficie del catalizador hasta la corriente gaseosa (periodo rico, atmósfera reductora).
5. Reducción de NO_x a N_2 (periodo rico, atmósfera reductora).

Al comienzo del periodo pobre, gran parte de los NO_x ($NO+NO_2$) de la corriente de escape son almacenados en el catalizador, posteriormente los centros de almacenamiento del catalizador comienzan a saturarse y los NO_x empiezan a detectarse en la corriente de salida. Cuando la saturación es completa, la concentración de salida de los NO_x se iguala a la concentración de la entrada. Durante el posterior periodo rico, se inyecta el agente reductor y los NO_x adsorbidos en la superficie del catalizador reaccionan con el agente reductor formando N_2O, NH_3, CO y N_2. En este periodo, los sitios de almacenamiento son regenerados quedando activos para el siguiente periodo pobre.

1.1.2. Química del proceso NSR

En la literatura hay muchos estudios sobre el mecanismo de almacenamiento de los NO_x en el catalizador NSR. Los estudios realizados por el grupo de investigación de Fridell [24-26] y de Forzatti [27-32] son los más relevantes. Fridell y cols. [24-26] propusieron tres pasos para el mecanismo de almacenamiento de los NO_x donde el NO_2 se adsorbe en el BaO como especies $BaO\text{-}NO_2$; después estas especies se descomponen a BaO_2 y NO (que es liberado a la fase gas) y finalmente el peróxido de bario reacciona con el NO_2 en fase gas para formar nitrato de bario. Esta reacción es conocida como desproporcionación de NO_2 (Reacción 1.1) y ha sido ampliamente estudiada para la tecnología NSR.

$$3NO_2 + BaO \rightarrow Ba(NO_3)_2 + NO \quad (1.1)$$

Hoy en día, de acuerdo con la propuesta de Forzatti y cols. [32] las vías de reacción más aceptadas para la adsorción de NO_x son las indicadas en la Tabla 1.2. La "ruta nitrato", consiste en la oxidación del NO a NO_2 en los centros de Pt, seguido de la reacción de desproporcionación del NO_2 en BaO para formar nitratos con la formación de una molécula de NO en fase gaseosa. Esta ruta implica la liberación de una molécula de NO con el consumo de tres moléculas de NO_2.

En la segunda ruta, denominada "ruta nitrito", el NO se oxida en los sitios de Pt y se almacena directamente en los sitios de Ba vecinos en forma de nitrito (Reacción 1.2). La proximidad del BaO a los sitios de Pt promueve el derramamiento "spillover" del oxígeno desde los átomos de Pt a BaO, catalizando el Pt la formación del nitrato de bario a partir de especies nitrito (Reacción 1.3) a temperaturas superiores a 200 °C (con limitaciones cinéticas a temperaturas inferiores) e inferiores a 350 °C (con limitaciones termodinámicas a altas temperaturas).

$$BaO_2 + 2NO \rightarrow Ba(NO_2)_2 \quad (1.2)$$

$$Ba(NO_2)_2 + 2O\text{-}Pt^* \rightarrow Ba(NO_3)_2 + 2Pt^* \quad (1.3)$$

El siguiente paso consiste en la regeneración y conlleva la reducción de los nitratos y nitritos metálicos a una mezcla de carbonatos, óxidos y hidróxidos de bario, generando como producto fundamentalmente nitrógeno. La duración del periodo de regeneración es mucho más corta que el periodo de almacenamiento, normalmente de minutos y segundos, respectivamente. La descomposición de los nitritos y nitratos puede llevarse a cabo por el calor generado por la reducción [33, 34] al disminuir la concentración de oxígeno porque disminuye la estabilidad de los nitratos [17, 35]. Sin embargo, bajo condiciones isotérmicas, se ha comprobado que el proceso de reducción no comienza con la descomposición térmica de los nitratos y nitritos almacenados, sino por una vía catalítica que implica la participación del Pt

Tabla 1.2. Rutas de almacenamiento de NO_x durante la fase pobre en las reacciones NSR [23].

Ruta nitrato	Ruta nitrito
$O_2 + 2Pt^* \rightarrow 2O\text{-}Pt^*$	$O_2 + 2Pt^* \rightarrow 2O\text{-}Pt^*$
$NO + Pt^* \rightarrow NO\text{-}Pt^*$	$NO + Pt^* \rightarrow NO\text{-}Pt^*$
$NO + O\text{-}Pt^* \rightarrow NO_2\text{-}Pt^*$	$NO + O\text{-}Pt^* \rightarrow NO_2\text{-}Pt^*$
$NO\text{-}Pt^* + O\text{-}Pt^* \rightarrow NO_2\text{-}Pt^* + Pt^*$	$NO\text{-}Pt^* + O\text{-}Pt^* \rightarrow NO_2\text{-}Pt^* + Pt^*$
$NO_2\text{-}Pt^* \rightarrow NO_2 + Pt^*$	$NO_2\text{-}Pt^* \rightarrow NO_2 + Pt^*$
Oxidación de NO: $2NO + O_2 \rightarrow NO_2$	Oxidación de NO: $2NO + O_2 \rightarrow NO_2$
Formación del peróxido de bario:	Formación del peróxido de bario (I):
$O\text{-}Pt^* + (s)BaO \rightarrow (s)BaO_2 + Pt^*$	$O\text{-}Pt^* + (s)BaO \rightarrow (s)BaO_2 + Pt^*$
$NO_2 + (s)BaO \rightarrow (s)BaO\text{-}NO_2$	$NO_2 + (s)BaO \rightarrow (s)BaO\text{-}NO_2$
$(s)BaO\text{-}NO_2 \rightarrow (s)BaO_2 + NO$	$(s)BaO\text{-}NO_2 \rightarrow (s)BaO_2 + NO$
$2NO_2 + (s)BaO_2 \rightarrow (s)Ba(NO_3)_2$	
Dispropornación del NO_2:	Formación del peróxido de bario (II):
$2NO_2 + (s)BaO \rightarrow (s)Ba(NO_3)_2 + NO$	$O\text{-}Pt^* + (s)BaO \rightarrow (s)BaO_2 + Pt^*$
$(s)Ba(NO_3)_2$	Formación de nitrito:
	$(s)BaO_2 + 2NO \rightarrow (s)Ba(NO_2)_2$
	Conversión de nitrito a nitrato:
	$(s)Ba(NO_2)_2 + 2OPt^* \rightarrow (s)Ba(NO_3)_2 + 2Pt^*$
	$(s)Ba(NO_2)_2$

[36]. Los subproductos que se forman durante las reacciones son muy importantes, ya que durante la reducción de los nitratos y nitritos se pueden formar diferentes especies, como N_2, NH_3 y N_2O junto con el agua. El objetivo del catalizador NSR cuando actúa de forma independiente, es maximizar la conversión de NO_x a N_2, evitando la formación de NH_3 y N_2O lo máximo posible.

En la literatura, se encuentran muchos estudios sobre el periodo de regeneración donde los NO_x se reducen por el H_2 [33, 36] y se han definido 3 rutas en la formación de N_2. La primera ruta fue estudiada por Nova y cols.

[36] y analizaron la reducción de los nitratos almacenados en un catalizador Pt-Ba/Al_2O_3 alimentando el H_2 en el periodo rico. Observaron que la formación de N_2 se da en dos pasos consecutivos donde en primer lugar ocurre la formación rápida del NH_3 mediante la reacción de nitratos y H_2 (Reacción 1.4). Seguido ocurre una reacción más lenta donde el NH_3 formado en la reacción anterior reacciona con los nitratos almacenados (Reacción 1.5):

$$Ba(NO_3)_2 + 8H_2 \rightarrow 2NH_3 + Ba(OH)_2 + 4H_2O \quad (1.4)$$

$$3Ba(NO_3)_2 + 10NH_3 \rightarrow 8N_2 + 3Ba(OH)_2 + 12H_2O \quad (1.5)$$

Pereda-Ayo y cols. [37-39] también estudiaron el comportamiento del catalizador monolítico Pt-Ba/Al_2O_3 durante el periodo rico, cuando se alimenta NO junto al H_2. Analizaron la distribución de N_2/N_2O/NH_3 a la salida del catalizador LNT a diferentes temperaturas (200-350 °C) y variando la concentración de H_2 (0,4-3 vol% H_2). En el estudio, se utilizaron los isotopos ^{14}NO y ^{15}NO durante el almacenamiento y regeneración, respectivamente, lo que permitió el seguimiento de dos nuevas rutas (ruta 2 y ruta 3) en la formación del N_2. La ruta 2 consiste en la reacción entre el ^{15}NO y el H_2 (Reacción 1.6) para formar NH_3, que continúa reaccionando con los nitratos almacenados (^{14}N) para formar nitrógeno ($^{14}N^{15}N$ y $^{15}N_2$) (Reacción 1.7):

$$2{}^{15}NO + 5H_2 \rightarrow 2{}^{15}NH_3 + 2H_2O \quad (1.6)$$

$$3Ba(^{14}NO_3)_2 + 10{}^{15}NH_3 \rightarrow 6{}^{14}N^{15}N + 2{}^{15}N^{15}N + 3BaO + 15H_2O \quad (1.7)$$

La tercera ruta para la formación de N_2 es la reacción directa entre ^{15}NO y H_2 para dar $^{15}N_2$ (Reacción 1.8). También se debe de tener en cuenta la reacción entre el $^{15}NH_3$ que viene de la Reacción 1.6 con el ^{15}NO para dar $^{15}N_2$ (Reacción 1.9).

$$2{}^{15}NO + 2H_2 \rightarrow {}^{15}N^{15}N + 2H_2O \quad (1.8)$$

$$4{}^{15}NH_3 + 6{}^{15}NO \rightarrow 5{}^{15}N^{15}N + 6H_2O \quad (1.9)$$

La dinámica del catalizador Pt-Ba/Al_2O_3 durante el periodo de regeneración está directamente relacionada con la concentración de H_2 y la

temperatura, pudiéndose distinguir distintas zonas de reacción en el reactor NSR [37]. La Figura 1.2 ilustra la propagación del H_2 y la interacción con los $^{14}NO_x$ almacenados y con el ^{15}NO que entra. En la zona del reactor en la que los centros de almacenamiento ya están regenerados (zona I), el ^{15}NO que entra reacciona con el H_2 para dar $^{15}NH_3$ o $^{15}N_2$ (Reacción 1.6 y 1.8). El $^{15}NH_3$ que se forma avanza a través del reactor hasta encontrar el frente de regeneración para reaccionar con $^{14}NO_x$ y dar $^{14}N^{15}N$ y $^{15}N_2$ (Reacción 1.7). Alternativamente, el H_2 que no ha sido consumido en la producción de NH_3 reacciona con los $^{14}NO_x$ liberados para formar $^{14}NH_3$. Este amoniaco puede reaccionar con $^{14}NO_x$ en centros de Pt para formar $^{14}N_2$ (Reacción 1.7). La selectividad de cada especie depende de la relación-concentración NO_x/H_2.

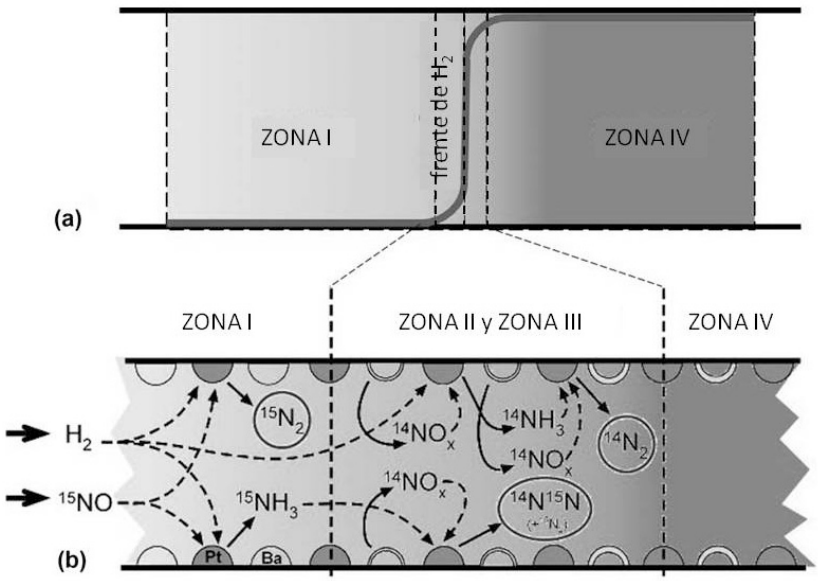

Figura 1.2. (a) Identificación de las distintas zonas que recorre el H_2 durante la regeneración del catalizador. (b) Esquema de los mecanismos de regeneración del catalizador NSR con hidrógeno. (El almacenamiento se realizó con ^{14}NO y la regeneración en presencia de ^{15}NO) [23].

1.1.3. Influencia de la presencia de H_2O y CO_2 en el comportamiento del catalizador NSR

La presencia de H_2O y CO_2 en la alimentación (como ocurre en la aplicación real) influye sobre la química de la reacción. Los experimentos realizados con H_2O y CO_2 evidencian la formación de especies hidróxido y carbonatos asociados a sitios de adsorción de compuestos alcalinos o alcalino-térreos [27, 30, 40-42] en la superficie del catalizador. Epling y cols. [43] evaluaron el impacto del agua y del CO_2 en un catalizador Pt-Ba/Al_2O_3 a distintas temperaturas y observaron que el almacenamiento de NO_x es mayor en ausencia de agua y CO_2. Esto se debe a que es más difícil almacenar NO_x en los centros de $Ba(OH)_2$ y $BaCO_3$ que en los de BaO [41]. También observaron que el efecto provocado por la alimentación conjunta de H_2O y CO_2 difiere del obtenido cuando se alimentan independientemente, ya que se modifica la estabilidad de $Ba(OH)_2$ y $BaCO_3$. Lietti y cols. [27] observaron que si el catalizador contiene las tres especies (BaO, $Ba(OH)_2$ y $BaCO_3$), el óxido de bario es el primero en almacenar los NO_x, después el hidróxido de bario y finalmente el carbonato de bario. El CO_2 tiene un mayor efecto de inhibición en la adsorción de NO_x que el agua. Además, las especies de carbonato pueden desplazar a las especies de hidróxido de bario cuando el agua y el CO_2 están presentes en la alimentación, minimizando el efecto del agua en la adsorción de NO_x [41, 43].

La presencia del agua reduce notablemente la eficacia de almacenamiento en todo el rango de temperatura [43]. A la inversa, el efecto negativo del CO_2 en el $Ba(NO_3)_2$ aumenta con la temperatura, lo que confirma que las especies de carbonato tienen mayor estabilidad que los hidróxidos de bario [43]. Toops y cols. [44] observaron que en presencia de agua disminuyen los nitratos porque la superficie de Al_2O_3 está saturada con grupos hidroxilos que limitan la adsorción de NO_x en la alúmina. Esto significa que la alúmina tiene mayor interacción con el agua que con NO_x y CO_2, reduciendo la capacidad de almacenamiento de los NO_x en el catalizador NSR.

La oxidación de NO a NO_2 durante el periodo pobre es un paso muy importante previamente al almacenamiento de los NO_x en los centros de almacenamiento. Sin embargo, la oxidación del NO queda inhibida en presencia de agua [45-47], porque el agua es adsorbida en los centros metálicos a bajas temperaturas [41, 45] bloqueando los sitios de platino para la adsorción del oxígeno. Sin embargo, Ren y cols. [48] demostraron que la presencia de agua en la oxidación de NO no influye en el almacenamiento de NO_x o en la conversión de los NO_x. Estas conclusiones concuerdan con los estudios realizados por Epling y cols. [43] que observaron una pequeña disminución en el almacenamiento de los NO_x en presencia de agua. Sin embargo, el almacenamiento de NO_x a temperaturas inferiores a 100 °C sí que está limitado por el agua.

La presencia de agua y CO_2 también afecta a la formación de amoniaco en el proceso NSR [41, 49]. El agua participa en la reacción de desplazamiento (WGS, Water Gas Shift) ($CO + H_2O \leftrightarrows CO_2 + H_2$), lo que permite la formación de H_2 durante la reacción. El hidrógeno producido tiene mayor capacidad de reducción que el CO. Simultáneamente, la formación de especies isocianatos promueve la selectividad a NH_3. Sin embargo, la ausencia de CO_2 mejora la conversión de los NO_x [49], con baja selectividad a NH_3.

En resumen, el CO_2 inhibe significativamente la adsorción de los NO_x porque la especie $BaCO_3$ tiene mayor estabilidad que los BaO y $Ba(OH)_2$. Por otro lado, el agua satura la superficie de la alúmina con grupos hidroxilos, lo que disminuye la disponibilidad y esto hace que haya un número fijo de centros de adsorción en la superficie de la alúmina para almacenar los NO_x. El agua también inhibe la oxidación de NO, aunque su efecto sobre el almacenamiento de los NO_x sobre los centros de bario sea limitado.

1.1.4. Efecto de la naturaleza del agente reductor en el proceso NSR

Varios estudios se han llevado a cabo con diferentes agentes reductores, como H_2, CO e hidrocarburos durante el periodo rico en el catalizador NSR y la combinación NSR-SCR, para estudiar la influencia de su concentración y de la temperatura de operación [50-52].

El H_2 es el agente reductor más eficaz para la reducción de los NO_x y para regenerar la superficie del catalizador, mientras que el CO y el C_3H_6 son menos eficaces, especialmente a bajas temperaturas. A altas temperaturas, los tres agentes reductores son comparables [53]. El CO puede trabajar como agente reductor directo de los NO_x mediante la reacción $2CO + 2NO \rightarrow N_2 + 2CO_2$ [53]; aunque también puede reducir los NO_x y regenerar la superficie del catalizador mediante la reacción de desplazamiento de agua ($CO + H_2O \leftrightarrows CO_2 + H_2$), donde el H_2 producido trabaja como agente reductor. Se conoce que la reacción de desplazamiento de agua ocurre sobre los metales preciosos tanto en los catalizadores NSR como en los catalizadores TWC [54-59]. En la literatura, se puede observar la actividad de los catalizadores $Pt/Ba/Al_2O_3$ y $Pt/K/Al_2O_3$ en las reacciones WGS [60, 61] y RWGS [27]. También se conoce que los catalizadores con Ce en su composición promueven la reacción de WGS.

El propileno es el agente reductor más estudiado, entre los hidrocarburos, durante el periodo rico con el catalizador NSR [15, 29, 62-65]. En la literatura, se ha informado que en el catalizador NSR se produce el craqueo o reformado del propileno con vapor de agua lo que proporciona moléculas más pequeñas y reactivas que actúan como reductores finales.

1.2. TECNOLOGÍA DE REDUCCIÓN CATALÍTICA SELECTIVA DE NO_x, NH_3-SCR

Los motores diésel funcionan por combustión de mezcla pobre con exceso de O_2. Hoy en día, no se dispone de catalizadores prácticos y efectivos para la

reducción selectiva de NO_x con CO o HCs en un ambiente oxidante, aunque se han venido comercializando durante décadas catalizadores selectivos utilizando amoniaco como reductor en el sector de efluentes procedentes de fuentes fijas.

Las reacciones catalíticas fundamentales en el proceso SCR se muestran a continuación (Reacciones 1.10, 1.11 y 1.12):

$$4NH_3 + 4NO + O_2 \rightarrow 4N_2 + 6H_2O \quad (1.10)$$

$$2NH_3 + NO + NO_2 \rightarrow 2N_2 + 3H_2O \quad (1.11)$$

$$4NH_3 + 3NO_2 \rightarrow 7/2N_2 + 6H_2O \quad (1.12)$$

La Reacción 1.10 se denomina generalmente "reacción SCR estándar". Como en los gases de escape siempre hay presencia de NO_2, (NO_2/NO_x hasta 10%) la Reacción 1.11 también es relevante y es, de hecho, la más rápida y favorecida de las reacciones de reducción de NO_x. Para promover esta reacción, denominada "reacción SCR rápida", se utiliza comúnmente un precatalizador de oxidación (DOC) para formar más NO_2 mediante la Reacción 1.13:

$$NO + 1/2O_2 \rightarrow NO_2 \quad (1.13)$$

Si se produce demasiado NO_2 en el DOC, $NO/NO_2<1$, se promociona la Reacción 1.12. Sin embargo, esta reacción no es deseada, debido a que el exceso de NO_2 puede producir N_2O, uno de los principales gases que genera el efecto invernadero:

$$4NH_3 + 4NO_2 \rightarrow 2N_2 + 2N_2O + 6H_2O \quad (1.14)$$

Si los reactivos no están bien mezclados, si se inyecta exceso de amoniaco para alcanzar alta eficiencia de eliminación de NO_x o si el amoniaco almacenado en el catalizador SCR se libera demasiado rápido, pueden detectarse concentraciones importantes de NH_3 a la salida del sistema. Para evitar este hecho, debe añadirse un catalizador de oxidación de amoniaco (ASC, Ammonia Slip Catalyst), que promueve la Reacción 1.15:

$$4NH_3 + 3O_2 \rightarrow 2N_2 + 6H_2O \qquad (1.15)$$

La tecnología SCR entró en Europa en el año 2003. Los sistemas actuales eliminaban hasta el 75% de los NO_x en el Ciclo Europeo Estándar de Conducción (NEDC, New European Driving Cycle), para ajustarse a las regulaciones de la norma Euro 4. Para cumplir las regulaciones de la norma Euro 6 (2014) la eficiencia media de eliminación de NO_x debe aproximarse al 95%. El objetivo para los próximos años es aumentar la eficiencia hasta el 98%, para lo que se han de mejorar diferentes aspectos del sistema de depuración. Probablemente, un futuro sistema SCR se compondrá de un dosificador de NH_3 y un conjunto de catalizadores compuesto por un DOC, un catalizador SCR y un ASC.

El esquema típico para un sistema de control de emisiones diésel con DPF (Diesel Exhaust Fluid) incorporado se muestra en la Figura 1.3, dosificándose la urea a partir del tanque DEF/AdBlue [66]. Además del sistema catalítico SCR (DOC, SCR, ASC, mezclador) y del DPF, los otros componentes principales

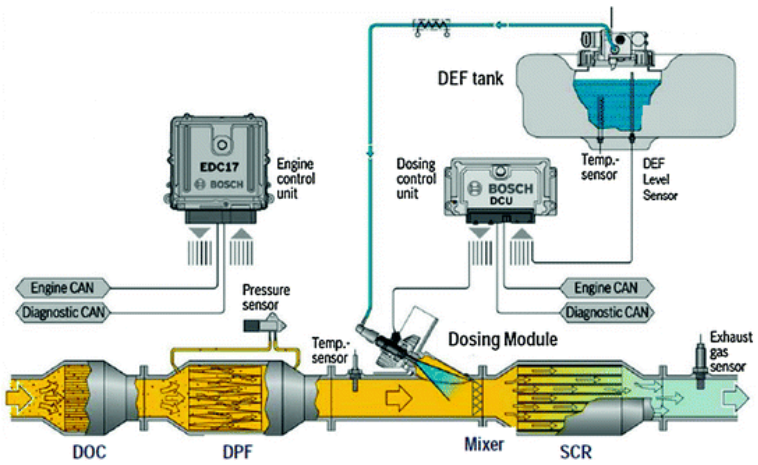

Figura 1.3. Esquema de un sistema comercial de reducción catalítica selectiva de NO_x, incluyendo catalizador de oxidación (DOC), filtro de partículas (DPF) y catalizador SCR [66].

del sistema son el tanque de almacenamiento (tanque DEF) y sistema de dosificación de urea, y el sistema de control para el funcionamiento adecuado de todo el sistema. Detalles más específicos de los diferentes componentes del sistema pueden encontrarse en la referencia [66].

1.2.1. Catalizador SCR

La parte más importante del dispositivo SCR es el catalizador SCR. Actualmente, se comercializan tres familias generales de catalizadores SCR: V_2O_5/WO_3, Cu/zeolita y Fe/zeolita. Walker [67] resumió las principales características de cada uno de estos catalizadores. Los catalizadores Cu/zeolita tienen el mejor comportamiento a baja temperatura, y en estado estacionario muestran muy poca sensibilidad a la concentración de NO_2. Sin embargo, son susceptibles a envenenamiento por azufre y requieren etapas de limpieza ocasionales a alta temperatura (>500 °C) para eliminar térmicamente los contaminantes. Estos catalizadores han sido significativamente mejorados en los últimos años, proponiéndolos como los catalizadores preferidos para sistemas de alta eficiencia.

Los catalizadores Fe/zeolita tienen el mejor comportamiento a temperaturas elevadas, pero es necesario el control del NO_2 en el gas de entrada para mejorar su comportamiento a baja temperatura. Por ello, es necesaria una mayor carga de metal precioso en el precatalizador DOC. Estos catalizadores no sufren envenenamiento por azufre, aunque se observa un envenenamiento moderado por hidrocarburos.

Los catalizadores de vanadio son los más baratos, pero tienen escasa durabilidad a alta temperatura (se deterioran a 550-600 °C) y, por tanto, no pueden utilizarse en sistemas que tengan DPF que necesite regeneración activa (T>650 °C). Al igual que Fe/zeolita, el comportamiento a baja temperatura depende de la disponibilidad de NO_2.

En la Figura 1.4, que muestra la sensibilidad de los tres tipos de catalizadores a la relación NO_2/NO_x en el gas de entrada, a 200 °C, se observa

que el catalizador Cu/zeolita presenta un mejor comportamiento $DeNO_x$ a baja temperatura con poca cantidad de NO_2 en el gas. Sin embargo, en un sistema estándar con DOC para la oxidación de los hidrocarburos, que también oxidará el NO a NO_2, los catalizadores de vanadio se comportan similarmente a Cu/zeolita en el rango de temperatura 225-275 °C, aunque los catalizadores Fe/zeolita sean menos activos. A temperaturas superiores, los catalizadores Cu/zeolita se comportan de forma muy similar a los catalizadores Fe/zeolita.

Las formulaciones de los catalizadores SCR y su diseño están evolucionando, para mejorar su comportamiento tanto a baja como a alta temperatura, aumentando la dispersión del catión metálico en la zeolita y utilizando el uso de estructuras zeolíticas más resistentes. Los efectos de envenenamiento por hidrocarburos y azufre se van comprendiendo mejor, lo que facilita su control, por ejemplo a través de una mejor modelización del proceso de deterioro y del control del tamaño de poro en la síntesis de zeolitas para evitar la entrada de los hidrocarburos a la estructura del catalizador.

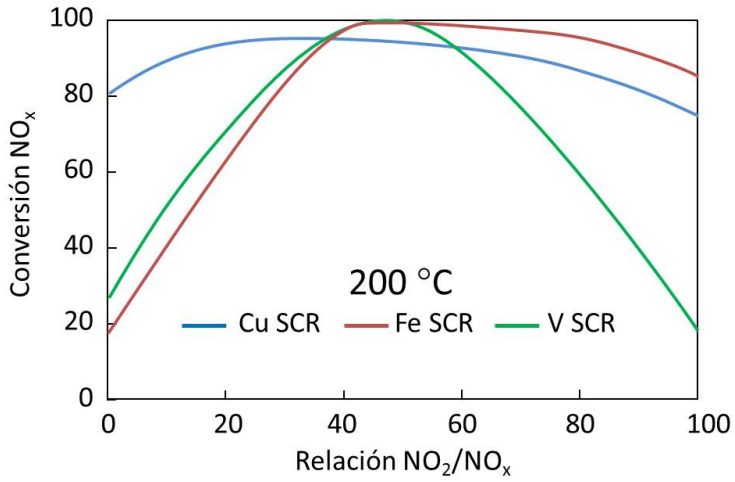

Figura 1.4. Sensibilidad a la alimentación de NO_2 sobre el comportamiento $DeNO_x$ de catalizadores SCR a 200 °C.

Los catalizadores de vanadio se utilizan en Europa, los mercados emergentes, y en algunas aplicaciones para la agricultura en EEUU, pero no en Japón por los requerimientos de durabilidad relacionados con la exposición a altas temperaturas cuando se regenera el DPF. Walker [68] ha presentado recientemente nuevas formulaciones Cu/zeolita que resisten el envejecimiento hidrotérmico hasta 900 °C y forman menos N_2O. Narula y cols. [69] muestran que es posible modificar sistemáticamente la estructura de la zeolita para alterar la densidad electrónica en los centros metálicos y facilitar la adsorción de amoniaco en la vecindad de estos centros. Estos mismos autores, en otra contribución [70] mostraron que mezclas físicas de Cu/zeolita y Fe/zeolita pueden mejorar el comportamiento a baja temperatura con respecto a catalizadores Cu/zeolita preparados por el método convencional; y cuando se añade lantano a la formulación binaria, el comportamiento mejora aún más.

En la actualidad, los catalizadores SCR se conforman depositados sobre estructuras monolíticas de 300-400 cpsi (48-64 celdas cm^{-2}). Heibel [71] comprobó que cuando el régimen está controlado por la transferencia de materia (230-350 °C), sustratos con 600 cpsi proporcionan velocidades de reacción un 35% más rápidos que sustratos de 400 cpsi. Mayor densidad de celda se está evaluando en programas avanzados para la mejora del comportamiento $DeNO_x$.

Los sistemas catalíticos SCR sufren envejecimiento, lo que necesita analizarse y comprenderse exhaustivamente, para alargar el periodo de vida útil de los catalizadores. Bartley y cols. [72] analizaron la capacidad de almacenamiento de NH_3 como una función del tiempo de envejecimiento y temperatura de un catalizador SCR. Estos investigadores modelizaron el envejecimiento utilizando isotermas de adsorción tipo Langmuir. Estos datos pueden utilizarse en algoritmos de control basados en el modelo para calcular la capacidad de almacenamiento de NH_3 de un catalizador SCR en operación real, conocido el histórico de tiempo y temperatura.

La Agencia de Protección Ambiental de EEUU (EPA, Environmental Protection Agency) ha reducido los límites para las emisiones de óxido nitroso (N_2O) para disminuir la emisión de gases de efecto invernadero de escapes de vehículos. Kamasamudram y cols. [73] muestran que el N_2O es muy estable y se forma mediante tres mecanismos en un catalizador SCR:

- Descomposición de nitrato amónico a baja temperatura (T<250 °C) mediante la Reacción 1.16:

$$NH_4NO_3 \rightarrow N_2O + H_2O \qquad (1.16)$$

- Oxidación de amoniaco a alta temperatura con Cu/zeolita por la Reacción 1.17:

$$2NH_3 \rightarrow N_2O + 3H_2O \qquad (1.17)$$

- Reacción de NO_2 en exceso (>50% NO_x) para formar nitrato amónico por la Reacción 1.18:

$$2NH_3 + 2NO_2 \rightarrow NH_4NO_3\downarrow + N_2 + H_2O \qquad (1.18)$$

el nitrato amónico formado se descompone inmediatamente mediante la Reacción 1.16 a temperaturas superiores a 200 °C.

Kamasamudram y cols. [73] mostraron que incrementando el contenido de Cu en el catalizador Cu/zeolita se disminuye la formación de N_2O por los dos primeros mecanismos, por lo que un mejor diseño y control del DOC puede prevenir el tercer mecanismo. Estos investigadores también mostraron que es posible reducir N_2O a N_2, pero estas reacciones de descomposición ocurren a mucha más alta temperatura que aquellas a las que se han formado.

Fickel y cols. [74] han descrito que zeolitas de estructura tipo chabazita, con pequeño tamaño de poro y con cobre incorporado muestran una mejor estabilidad hidrotérmica que las zeolitas de mayor tamaño de poro (como Cu/BETA y Cu/ZSM-5). Esta circunstancia ha hecho revivir el interés industrial en tamices moleculares que contienen metales para la eliminación de NO_x [75, 76]. En este sentido, Fickel y Lobo [77] han demostrado que la

mayor estabilidad hidrotérmica y la mejor actividad catalítica del catalizador Cu/CHA en la reacción SCR de NO_x se debe a la localización de los átomos de cobre, coordinados en unidades de dobles anillos de 6 miembros (D6-MR) presentes en las grandes cavidades de la estructura chabazita. Así, existen dos análogos de la estructura tipo chabazita: SSZ-13 y SAPO-34.

Estos catalizadores se han venido obteniendo mediante procedimientos de intercambio iónico en líquido post-síntesis, pero hoy en día se utilizan métodos de preparación más eficientes como el intercambio iónico en estado sólido (SSIE) o el intercambio iónico pre-síntesis (one-pot synthesis) que consiste en introducir el metal durante la síntesis de la zeolita.

El estudio realizado por Korhonen [76] descarta la existencia de dímeros de cobre en un catalizador SSZ-13 y concluye que las especies activas para la reacción SCR son iones de Cu^{2+} aislados cerca de los anillos de 6 miembros. Kwak [78] sugiere múltiples posiciones para los iones aislados en vez de únicamente los cercanos al anillo de 6 miembros, basándose en la existencia de dos tipos de cobre, detectados por H_2-TPR y FTIR, en un catalizador con bajo contenido de cobre. Gao [79] ha utilizado la técnica EPR para corroborar dos posiciones principales de intercambio para el Cu. Wang [80] ha observado que la velocidad de reacción SCR estándar por átomo de Cu mejora significativamente con la zeolita SAPO-34 cuando contiene iones aislados de Cu^{2+} con relación a la muestra que contiene clústeres de CuO en la extrared del catalizador.

Mientras que varios estudios han observado Cu^{2+} bajo condiciones de reacción, el estudio realizado por Bates [81], usando espectroscopía de rayos X (XAS) en operando, ha demostrado la presencia de iones Cu^{+} bajo condiciones estándar SCR, lo cual indica la existencia de un ciclo redox entre Cu^{+} y Cu^{2+} durante la reacción SCR.

1.2.2. Zeolitas de poro pequeño intercambiadas con Cu como catalizadores SCR

La demanda de catalizadores Cu/zeolita para la tecnología SCR con mayor durabilidad y estabilidad hidrotérmica, así como las limitaciones de las zeolitas convencionales, ha hecho que los investigadores busquen nuevas estructuras zeolíticas. En el año 1992, Ishihara y cols. [82, 83] estudiaron cobre intercambiado en SAPO-34, silicoaluminofosfato de poro pequeño con estructura chabazita (8 anillos). Estos autores observaron que la zeolita SAPO-34 proporciona mayor resistencia hidrotérmica y actividad catalítica SCR con propano, comparándola con Cu intercambiado en BETA, USY y ZSM-5. También observaron que este tipo de catalizadores son hidrotérmicamente más estables y activos para la descomposición del N_2O comparándolos con los catalizadores Cu/ZSM-5 [84-86]. En el año 2004, Zones y cols. [87] sintetizaron la chabazita de poro pequeño y propusieron utilizarla como soporte para los metales de transición, tales como el Cu, en la tecnología SCR.

En las reacciones SCR con hidrocarburos (HC-SCR) con catalizadores de metales de transición intercambiados en zeolitas se produce NH_3, que posteriormente es utilizado en la reacción NH_3-SCR para reducir los NO_x a N_2. Se comprende que si un catalizador es muy activo y duradero para las reacciones HC-SCR también lo será para las reacciones NH_3-SCR [88]. De hecho, Bull y cols. [89] publicaron que los catalizadores Cu/CHA, como Cu/SSZ-13, presentan buena actividad NH_3-SCR y estabilidad hidrotérmica. Andersen y cols. [90] observaron que el catalizador Cu/SAPO-34 mejoraba significativamente la estabilidad hidrotérmica para las aplicaciones NH_3-SCR.

Si se comparan las zeolitas BETA, ZSM-5 y CHA se observa que los catalizadores Cu/BETA y Cu/ZSM-5 presentan buena actividad SCR al inicio de la reacción. Sin embargo, cuando son envejecidas hidrotérmicamente a 750 °C durante 24 horas o 900 °C durante 1 hora, la Tabla 1.3 muestra que se desactivan severamente [23].

Tabla 1.3. Ejemplos de cobre soportado en zeolitas de poro pequeño para la tecnología SCR y la conversión de NO_x y la producción de N_2O a 250 °C [12].

Catalizadores	Estructura de la zeolita	Conversión de NO_x, %	Producción de N_2O, ppm
Cu/beta (Fresco)	BEA (12-anillos)	98	17
Cu/ZSM-5 (Fresco)	MFI (10-anillos)	98	7
Cu/SAPO-34 (Fresco)	CHA (8-anillos)	98	1
Cu/beta (750 °C/24 h)	BEA (12-anillos)	69	16
Cu/SAPO-34 (750 °C/24 h)	CHA (8-anillos)	99	3
Cu/SSZ-13 (750 °C/24 h)	CHA (8-anillos)	99	7
Cu/ZSM-34 (750 °C/24 h)	ERI (10-anillos)	98	3
Cu/beta (900 °C/1 h)	BEA (12-anillos)	58	22
Cu/ZSM-5 (900 °C/1 h)	MFI (10-anillos)	28	0
Cu/SAPO-34 (900 °C/1 h)	CHA (8-anillos)	97	2
Cu/SSZ-13 (900 °C/1 h)	CHA (8-anillos)	99	7

Las zeolitas SSZ-13 y SAPO-34 tienen la misma estructura cristalográfica, denominada CHA. Sin embargo, su composición es diferente. La zeolita SSZ-13 es una chabazita con altas cantidades de SiO_2 y una cantidad menor de Al_2O_3, mientras que la zeolita SAPO-34 es un silicoaluminofosfato que contiene cantidades casi equimolares de Al_2O_3 y P_2O_5, con una pequeña cantidad de SiO_2 sustituyendo parte del P_2O_5. A pesar de las diferencias que tienen las dos zeolitas, ambas presentan muy buena estabilidad hidrotérmica y actividad SCR, sugiriendo que es la propia estructura tipo CHA la que mejora la estabilidad hidrotérmica de los catalizadores Cu/CHA.

Otra característica importante de las zeolitas de poro pequeño es la limitada formación de N_2O. Se observa un breve aumento de N_2O cuando los catalizadores son envejecidos hidrotérmicamente, pero la producción total de N_2O sigue siendo bajo. Sin embargo, en los catalizadores Cu/BETA y Cu/ZSM-5

se observan altos niveles de formación de N_2O. El mecanismo de formación de N_2O en la tecnología SCR todavía no está bien definido, pero se ha observado que el tamaño de la cavidad de la estructura de la zeolita tiene una gran influencia en la formación del N_2O: poro pequeño < poro medio < poro grande [91]. El N_2O favorece fuertemente el efecto invernadero, por lo que debe minimizarse su formación, por lo que los catalizadores Cu/CHA presentan esta ventaja adicional.

La dimensión de los poros de la zeolita también regula el tamaño de molécula de gas que puede entrar en la red intracristalina. Con 8 anillos abiertos, la ventana de la zeolita de poro pequeño es suficientemente grande como para que entren gases como O_2, NO_x y NH_3, pero excluye la mayoría de HCs. Por ejemplo, la medida de la abertura de la zeolita CHA es 0,38 mm; mayor que el diámetro de las moléculas O_2 (0,35 nm), NO (0,32 nm), NO_2 (0,34 nm), o NH_3 (0,26 nm), pero más pequeña que cualquier hidrocarburo aromático como el tolueno (0,59 nm). El diámetro cinético de los hidrocarburos con cadenas cortas como el C_3H_6 (0,45 nm) o C_3H_8 (0,43 nm) es un poco más grande que el diámetro de poro de la zeolita CHA, por lo que estos HC podrán llegar a entrar en la zeolita con ciertas restricciones. Si se comparan las dimensiones de los poros de la zeolita BETA y ZSM-5, estas zeolitas tienen mayor tamaño de poro 0,66-0,72 nm y 0,54-0,56 nm, respectivamente; estas dimensiones son lo suficientemente grandes para que los HCs puedan entrar en su interior.

1.2.3. Química del proceso SCR con catalizadores Cu/zeolita

La reducción catalítica selectiva de mezclas gaseosas que contienen NO y NO_2 es un sistema complejo en el que intervienen simultáneamente múltiples reacciones. Para desarrollar nuevos catalizadores y convertidores SCR más eficientes es esencial conocer los aspectos mecanísticos de las reacciones principales. A continuación, se presentan las tres reacciones principales mencionadas anteriormente, que conducen al producto deseado N_2, además de otras reacciones secundarias.

La reacción SCR estándar (Reacción 1.10) se lleva a cabo coalimentando NO y NH_3 en presencia de oxígeno.

$$4NH_3 + 4NO + O_2 \rightarrow 4N_2 + 6H_2O \quad (1.10)$$

Varios estudios demuestran que la reducción de los NO_x aumenta cuando el NO y el NO_2 se alimentan equimolecularmente [92]. La reacción equimolecular de NO y el NO_2 con NH_3 se denomina reacción SCR rápida (Reacción 1.11):

$$2NH_3 + NO + NO_2 \rightarrow 2N_2 + 3H_2O \quad (1.11)$$

La tercera reacción importante es la reacción NO_2 SCR:

$$4NH_3 + 3NO_2 \rightarrow 7/2N_2 + 6H_2O \quad (1.12)$$

La Reacción 1.12 es importante, cuando los NO_x alimentados se componen sobre todo de NO_2 [93]. La participación del NO_2 en la reacción acelera la reducción de los NO_x sobre varios catalizadores [92], sin embargo complica la reacción química NH_3-SCR. El NO_2 es la especie clave en la reacción SCR para la reducción de los NO_x en presencia de NH_3, y la oxidación de NO a NO_2 es el paso limitante. Komatsu y cols. [94] estudiaron la reacción SCR estándar en catalizadores Cu/zeolita. En este estudio [94] observaron la formación de nitratos que reaccionan con el NO para formar NO_2. Posteriormente, el NO_2 reacciona con el NH_3 para formar N_2 y H_2O. Otros investigadores [95] sugirieron que en la reducción de NO y NO_2 con NH_3 se forman HNO_2 y HNO_3.

Aparte de las tres reacciones (Reacciones 1.10-1.12) mencionadas anteriormente, existen otras reacciones secundarias que consumen NH_3 ineficientemente o generan subproductos como N_2O, NH_4NO_3 y HNO_3.

La reacción de oxidación del amoniaco (Reacción 1.15) es una reacción secundaria importante que normalmente ocurre a temperaturas más altas de 350 °C, disminuyendo la disponibilidad del amoniaco para la reducción de los NO_x.

$$4NH_3 + 3O_2 \rightarrow 2N_2 + 6H_2O \quad (1.15)$$

Por otro lado, la oxidación de NO a NO_2 (Reacción 1.13) alcanza conversiones de equilibrio elevadas a temperaturas de 150-200 °C, que disminuyen al aumentar la temperatura (reacción exotérmica):

$$NO + 1/2O_2 \rightleftarrows NO_2 \quad (1.13)$$

La Reacción 1.13 es deseable debido a que el NO_2 que se forma es más fácil de reducir con el NH_3 que el NO (reacción SCR rápida vs. estándar). Por el contrario, la existencia de NO_2 complica el sistema de reacción; en particular, ocurre una formación neta de nitrato amónico a temperaturas intermedias (~275 °C) (Reacción 1.18).

$$2NH_3 + 2NO_2 \rightleftarrows N_2 + NH_4NO_3 + H_2O \quad (1.18)$$

En la bibliografía [96-101], se pueden observar mecanismos que describen la formación de NH_4NO_3. Koebel y cols. [97, 98] publicaron que la primera etapa para la formación de nitrato amónico es la dimerización del NO_2 (Reacción 1.19):

$$2NO_2 \rightleftarrows N_2O_4 \quad (1.19)$$

El N_2O_4 formado por la dimerización de NO_2 puede reaccionar con el H_2O para producir ácido nitroso y nítrico (Reacción 1.20):

$$N_2O_4 + H_2O \rightleftarrows HONO + HNO_3 \quad (1.20)$$

El HONO puede reaccionar con el amoniaco para formar nitrito amónico, que es inestable a temperaturas superiores a 100 °C. Cuando el nitrito amónico es descompuesto se forman N_2 y H_2O (Reacción 1.21).

$$NH_3 + HONO \rightleftarrows [NH_4NO_2] \rightarrow N_2 + H_2O \quad (1.21)$$

El NH_4NO_3 también se puede formar mediante la reacción del NH_3 con el HNO_3 (Reacción 1.22).

$$NH_3 + HNO_3 \rightleftarrows NH_4NO_3 \quad (1.22)$$

La reducción de nitratos por NO fue propuesta como etapa determinante de la velocidad de reacción en la química SCR con catalizadores basados en vanadio [99] (Ecuaciones 1.23 y 1.24).

$$NH_4NO_3 + NO \rightarrow NO_2 + N_2 + 2H_2O \quad (1.23)$$

$$HNO_3 + NO \rightleftarrows NO_2 + HONO \quad (1.24)$$

El nitrato amónico se descompone a N_2O a altas temperaturas (≥200 °C) (Reacción 1.16):

$$NH_4NO_3 \rightarrow N_2O + 2H_2O \quad (1.16)$$

El óxido nitroso (N_2O) es un gas de efecto invernadero como se ha mencionado en el apartado 1.2.1 y, por lo tanto, un subproducto indeseado que deberá ser controlado de forma estricta durante los años venideros. La formación de N_2O también ocurre mediante la Reacción 1.25:

$$4NH_3 + 4NO_2 + O_2 \rightarrow 4N_2O + 6H_2O \quad (1.25)$$

El N_2O se descompone a N_2 y O_2 a temperaturas más altas (Reacción 1.26):

$$2N_2O \rightarrow 2N_2 + O_2 \quad (1.26)$$

Finalmente, Devadas y cols. [102] estudiaron la desaparición del N_2O sobre Fe/ZSM-5, de acuerdo a la Reacción 1.27.

$$3N_2O + 2NH_3 \rightarrow 4N_2 + 3H_2O \quad (1.27)$$

1.2.3.1. Modelo cinético para el sistema de reacciones SCR

De-La-Torre y cols. [93] desarrollaron un modelo cinético global para la reacción NH_3-SCR sobre un catalizador Cu/CHA. Llevaron a cabo una selección de las etapas fundamentales del sistema generalizado descrito en la sección 1.2.3, tras el análisis de una serie preliminar de datos cinéticos obtenidos en un amplio rango de condiciones de operación. Para el estudio todas las líneas del sistema experimental fueron calorifugadas y por ello no consideraron la presencia de nitrato amónico en el sistema.

Para el modelo cinético global de la reacción NH_3-SCR se basaron en una selección de las etapas fundamentales, que consta de las siguientes reacciones: (I) oxidación de NH_3, (II) oxidación de NO, (III) reacción estándar SCR, (IV) reacción rápida SCR, (V) reacción lenta SCR, (VI) formación de N_2O y (VII) descomposición de N_2O. Para la definición de las ecuaciones de velocidad consideraron que el amoniaco participa en las reacciones I, III, IV, V y VI una vez adsorbido sobre los centros ácidos de la zeolita, mientras que el resto de las especies lo hace directamente desde la fase gas. La Tabla 1.4 muestra las etapas fundamentales junto a las correspondientes ecuaciones cinéticas.

La reacción de oxidación de NO a NO_2 (Reacción II) consideraron que ocurre en la fase gas, sin la intervención de ninguna especie adsorbida, con una cinética correspondiente a una etapa elemental y con conversiones de equilibrio limitadas en el intervalo de temperaturas estudiado.

Tabla 1.4. Ecuaciones SCR y sus expresiones cinéticas [93].

Reacción		Ecuación cinética
I.	$NH_3 + 3/4O_2 \rightarrow 1/2N_2 + 3/2H_2O$	$r_{\mathrm{I}} = \dfrac{k_{\mathrm{I}} C_{\mathrm{NH_3}} C_{\mathrm{O_2}}}{1 + k_{\mathrm{NH_3}} C_{\mathrm{NH_3}}}$
II.	$NO + 1/2O_2 \leftrightarrow NO_2$	$r_{\mathrm{II}} = k_{\mathrm{II}} \left(C_{\mathrm{NO}} C_{\mathrm{O_2}}^{0,5} - C_{\mathrm{NO_2}} / K_{\mathrm{NO}}^{\mathrm{eq.}} \right)$
III.	$NH_3 + NO + 1/4O_2 \rightarrow N_2 + 3/2H_2O$	$r_{\mathrm{III}} = \dfrac{k_{\mathrm{III}} C_{\mathrm{NH_3}} C_{\mathrm{NO}} C_{\mathrm{O_2}}}{1 + k_{\mathrm{NH_3}} C_{\mathrm{NH_3}}}$
IV.	$2NH_3 + NO + NO_2 \rightarrow 2N_2 + 3H_2O$	$r_{\mathrm{IV}} = \dfrac{k_{\mathrm{IV}} C_{\mathrm{NH_3}} C_{\mathrm{NO}} C_{\mathrm{NO_2}}}{1 + k_{\mathrm{NH_3}} C_{\mathrm{NH_3}}}$
V.	$4NH_3 + 3NO_2 \rightarrow 7/2N_2 + 6H_2O$	$r_{\mathrm{V}} = \dfrac{k_{\mathrm{V}} C_{\mathrm{NH_3}} C_{\mathrm{NO_2}}}{1 + k_{\mathrm{NH_3}} C_{\mathrm{NH_3}}}$
VI.	$3NH_3 + 4NO_2 \rightarrow 7/2N_2O + 9/2H_2O$	$r_{\mathrm{VI}} = \dfrac{k_{\mathrm{VI}} C_{\mathrm{NH_3}} C_{\mathrm{NO_2}}}{1 + k_{\mathrm{NH_3}} C_{\mathrm{NH_3}}}$
VII.	$2N_2O \rightarrow 2N_2 + O_2$	$r_{\mathrm{VII}} = k_{\mathrm{VII}} C_{\mathrm{N_2O}} C_{\mathrm{NO_2}}$

La constante de equilibrio $K_{NO}^{eq.}$ fue determinada mediante métodos termodinámicos a partir de los calores de formación de los componentes NO y NO_2 (Ecuación. 1.28):

$$K_{NO}^{eq.} = 8{,}31x10^{-4} \exp\left(\frac{5728}{RT}\right) \qquad (1.28)$$

La Reacción VI expresa la formación del subproducto indeseado N_2O, deducida de la combinación lineal de la Reacciones 1.12 y 1.27 del modelo general descrito anteriormente.

Para la descomposición directa del N_2O sugirieron diferentes esquemas de reacción de la bibliografía [103], donde el N_2O reacciona desde la fase gas generando N_2 en la fase gas y ad-átomos de oxigeno en la superficie del catalizador.

En el modelo SCR planteado, De-La-Torre y cols. [93] no consideraron inicialmente otra especie adsorbida distinta que el amoniaco. Sin embargo, al objeto de tener en cuenta la influencia del catalizador en la descomposición del N_2O, atendiendo a la participación de especies de oxígeno adsorbidas demostrada en algunos trabajos [104, 105], y con los resultados experimentales obtenidos por ellos mismos en una serie de experimentos preliminares de descomposición de N_2O, propusieron una ecuación cinética en la que intervienen especies precursoras de especies adsorbidas, bien en forma molecular o disociadas, en concreto N_2O y NO_2 (la eliminación de la especie NO_2 de la ecuación cinética no permite el ajuste del conjunto inicial de experimentos de descomposición de N_2O). Así, la etapa correspondiente a la descomposición de N_2O incluida en el modelo SCR global planteado es (Ecuación 1.29):

VII: $$r_{VII} = k_{VII} C_{N_2O} C_{NO_2} \qquad (1.29)$$

De-La-Torre y cols. [93] realizaron 176 experimentos para la estimación de los parámetros cinéticos de la reacción SCR. En primer lugar, se realizaron

experimentos alimentando NH_3 y NO_2, que permitieron analizar el subsistema compuesto por las Reacciones V, VI y VII, ya que en ausencia de O_2 y NO el resto de Reacciones (I-IV)son inexistentes. Una vez planteado el balance de materia diferencial para cada una de las especies del subsistema (NH_3, NO_2 y N_2O), resolvieron el sistema de ecuaciones diferenciales ordinarias para obtener los parámetros cinéticos (energía de activación y factor prexponencial) que minimizan la suma de los errores al cuadrado, considerando el error como la diferencia entre el valor de concentración experimental y el calculado. Obtuvieron un buen ajuste entre el modelo y los resultados experimentales en un amplio rango de condiciones de reacción.

De-La-Torre y cols. [93] dedujeron que no era posible plantear otro subsistema como el compuesto por las Reacciones V, VI y VII, cuyo análisis pudiera hacerse de forma independiente, ya que la introducción de NO activaba todas las reacciones (I-VII) del esquema global SCR. Por lo tanto, con una extensa experimentación realizando experimentos a distintas temperaturas, tiempos de contacto (W/Q) y variando la composición de entrada al reactor, lograron proponer un modelo capaz de seguir con mucha precisión las especies mayoritarias (NO y NH_3) y aceptablemente para el ajuste del resto de las especies.

En los resultados cinéticos obtenidos (Tabla 1.5) observaron una gran similitud en las energías de activación de las reacciones V-VII, que fueron estimadas previamente cuando en el sistema sólo se tuvieron en cuenta estas tres reacciones. Además, también verificaron valores similares de energías de activación con otros investigadores, especialmente para las reacciones III, IV y V. En la reacción estándar SCR la energía de activación obtenida por De-La-Torre y cols. [93] es de 91,5 kJ mol^{-1}, similar a la obtenida por Metkar y cols. [106] para Cu/CHA y también a la obtenida por Olsson y cols. [107] para Cu/ZSM-5. En la reacción rápida la energía de activación obtenida fue de 42,0 kJ mol^{-1} siendo menor que las obtenidas por Metkar y cols. [106] y Olsson y cols. [107]; 77,1 kJ mol^{-1} y 85,1 kJ mol^{-1}, respectivamente. Finalmente, para la

Tabla 1.5. Parámetros cinéticos del modelo globalizado basado en las siete etapas planteadas para la reducción catalítica selectiva de NO_x (reacciones I-VII) [93].

Constantes cinéticas	Factores preexponenciales		Energía de activación, kJ mol^{-1}	Intervalo de confianza (95%)
	Valor	Unidades		
k_I	$1{,}59\times10^{12}$	$m^6\ g^{-1}\ h^{-1}\ mol^{-1}$	108,11	± 0,40
k_{II}	$6{,}81\times10^{5}$	$m^{4,5}\ m^{-3}\ h^{-1}\ mol^{-0,5}$	12,39	± 3,01
k_{III}	$1{,}09\times10^{12}$	$m^9\ g^{-1}\ h^{-1}\ mol^{-2}$	91,45	± 1,58
k_{IV}	$9{,}40\times10^{9}$	$m^9\ g^{-1}\ h^{-1}\ mol^{-2}$	41,98	± 1,15
k_V	$3{,}07\times10^{12}$	$m^6\ g^{-1}\ h^{-1}\ mol^{-1}$	118,10	± 29,21
k_{VI}	$4{,}48\times10^{18}$	$m^6\ g^{-1}\ h^{-1}\ mol^{-1}$	152,34	± 1,44
k_{VII}	$2{,}45\times10^{28}$	$m^6\ g^{-1}\ h^{-1}\ mol^{-1}$	257,92	± 6,16
k_I	$1{,}59\times10^{12}$	$m^6\ g^{-1}\ h^{-1}\ mol^{-1}$	108,11	± 0,40
K_{NH_3}	$7{,}66\times10^{-7}$	$m^3\ mol^{-1}$	99,19[a]	-
K_{NO}	$8{,}61\times10^{-4}$	$m^{1,5}\ mol^{-0,5}$	57,28[a]	-

[a]En el caso de NH_3 y NO, este valor se corresponde con las entalpías del proceso de adsorción y la reacción de oxidación, respectivamente.

reacción NO_2 SCR la energía de activación obtenida fue de 118,1 kJ mol^{-1} y comparando con las energías obtenidas por los dos autores mencionados anteriormente [106, 107] era intermedia.

1.3. SISTEMAS COMBINADOS NSR-SCR (EN SERIE Y EN DOBLE CAPA)

Uno de los mayores inconvenientes de la tecnología NSR es que durante el periodo de regeneración, aparte del producto deseado N_2, también se produce NH_3. El amoniaco es nocivo para la salud y sus emisiones están estrictamente reguladas, por lo que deben implementarse estrategias adecuadas para convertir el amoniaco que se produce en el catalizador NSR en especies inocuas. La emisión del amoníaco en la norma Euro 6 está limitada a 10 ppm para motores diésel.

A finales de la década de los 90, Toyota intentó sacarle partido a la producción de amoniaco en el catalizador NSR, ya que éste es uno de los reductores más eficiente en condiciones oxidantes (periodo pobre). De hecho, en fuentes estacionarias (plantas de energía o incineradoras) la reducción de los NO_x se lleva a cabo mediante la reducción catalítica selectiva con amoniaco (NH_3-SCR) [108, 109]. Esta tecnología (SCR) también es utilizada para reducir los NO_x de fuentes móviles. Para ello, se obtiene amoniaco mediante la hidrólisis de la urea que es inyectada antes del catalizador SCR [110]. La tecnología NH_3-SCR se aplica en vehículos diésel pesados porque la instalación del tanque de urea es viable. Sin embargo, en los vehículos ligeros no se ha implementado por el alto coste del sistema de alimentación de urea [111] y el consumo extra de combustible adicional generado por el transporte de urea, así como por la escasa disponibilidad de espacio.

El concepto de acoplamiento NSR y SCR tiene muchas ventajas: (i) el NH_3 es producido en el mismo vehículo durante el periodo rico; (ii) el amoniaco que se forma en el catalizador NSR es utilizado en el catalizador SCR para reducir los NO_x y (iii) se reduce significativamente la emisión del amoniaco. En consecuencia, los fabricantes de vehículos están buscando la configuración óptima para dicho acoplamiento, lo que requiere una tecnología sofisticada. Estos avances se pueden observar en varias patentes [112-114]. Los sistemas combinados NSR-SCR se implementaron en el vehículo Mercedes E320 BlueTEC. Este vehículo utiliza una gran carga de platino para el catalizador NSR y Fe/zeolita para el catalizador SCR [115]. La tecnología BlueTEC está equipada con el catalizador de oxidación (DOC) para eliminar las emisiones de HC y CO. Además, el filtro de partículas (CDPF), que se encuentra entre los catalizadores NSR y SCR, es capaz de reducir las emisiones de partículas en más de un 90%.

Los sistemas combinados NSR-SCR trabajan en régimen transitorio alternando alimentaciones pobres y ricas, tal como lo hace la tecnología NSR. El beneficio de trabajar con el sistema combinado con respecto a la

configuración simple NSR es el aprovechamiento del NH_3 generado en el catalizador NSR para favorecer la reducción catalítica selectiva de NO_x en el catalizador SCR colocado a continuación (Figura 1.5). El mecanismo de formación de nitrógeno en el catalizador SCR es el mismo que se ha detallado en el apartado 1.2 para el sistema SCR estacionario. Sin embargo, el amoniaco sólo se forma en el catalizador NSR durante el periodo rico y así el NH_3 alcanza el catalizador SCR intermitentemente, contrariamente a lo que ocurre en la tecnología NH_3-SCR, donde la alimentación del agente reductor se realiza de forma continua. Así, el amoniaco tiene que ser adsorbido previamente en el catalizador SCR para posteriormente reaccionar con los NO_x que atraviesan el catalizador NSR sin ser almacenados.

En los sistemas simples NSR y combinados NSR-SCR la temperatura y la concentración del agente reductor son parámetros claves para su funcionamiento eficaz. Por ejemplo, en el sistema NSR-SCR se obtienen mejores resultados a baja temperatura y con alta concentración de hidrógeno,

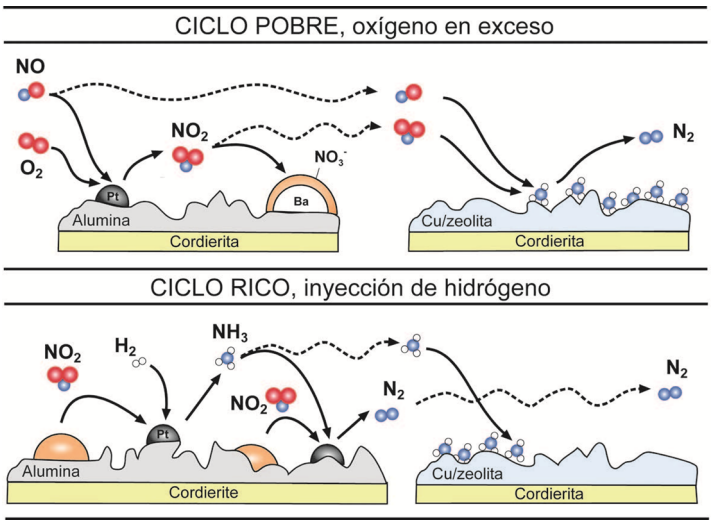

Figura 1.5. Esquema del funcionamiento de los catalizadores monolíticos NSR-SCR en serie durante el ciclo pobre y rico [9].

al ser en estas condiciones donde se promueve la formación del amoniaco en el catalizador NSR. Al aumentar la temperatura, la capacidad de producir NH_3 en el catalizador NSR se reduce y en consecuencia, disminuyen los beneficios de utilizar el sistema combinado NSR-SCR, a pesar de que aún se obtienen mejores resultados con la combinación NSR-SCR que con el catalizador NSR en configuración simple.

La configuración de doble capa en un único soporte monolítico es otra alternativa prometedora para la tecnología NSR-SCR. Nakatsuji y cols. [116] de Honda propusieron un sistema catalítico compuesto por un sólido ácido (zeolita con centros ácidos Brønsted) depositado sobre un catalizador Pt/OSC (OSC, catalizador de almacenamiento de oxígeno). Durante el periodo pobre los NO_x se almacenan en el OSC y durante el periodo rico el NH_3 formado se almacena en el catalizador sólido ácido. Durante el periodo pobre, el NH_3 adsorbido reduce los NO_x. El trabajo realizado por los investigadores de Honda suscitó mucho interés, aunque no proporcionaba mucha información acerca del catalizador ni del mecanismo de la reacción. El primer estudio que proporcionó información más detallada sobre el catalizador de doble capa LNT-SCR fue publicado por Liu y cols. [111, 117].

En este tipo de dispositivos de doble capa, el catalizador NSR se deposita sobre el sustrato como primera capa y el catalizador SCR se deposita sobre la capa NSR [111, 117-119]. La Figura 1.6 muestra esta disposición junto a un esquema representativo de la formación de nitrógeno. En este tipo de configuración, el catalizador NSR adsorbe los NO_x y convierte parte de ellos en amoniaco, mientras que la otra capa adsorbe el amoniaco formado para posteriormente reaccionar con los NO_x y producir N_2. Este dispositivo integrado permite la creación de un sistema de reducción de NO_x compacto y ligero para motores diésel. El sistema demuestra muy buena conversión de NO_x a baja temperatura (200 °C), pero baja conversión a temperaturas superiores a 350 °C.

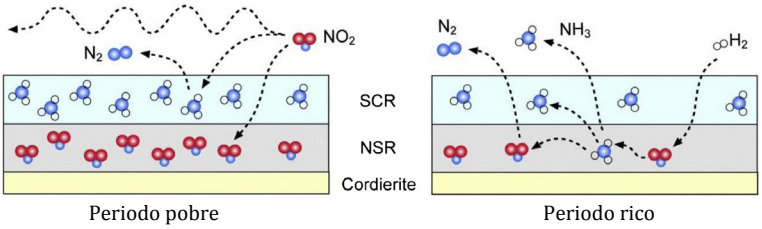

Figura 1.6. Esquema del funcionamiento de los catalizadores monolíticos de doble capa en ciclos pobres y ricos.

1.4. OBJETIVOS Y ESTRUCTURA DE LA TESIS

Las tecnologías NSR y SCR para la eliminación de NO_x procedentes de motores diésel o motores de mezcla pobre requieren una mejora de sus prestaciones catalíticas para satisfacer las normativas legislativas, cada vez más estrictas. Por ello, esta tesis sistematiza en primer lugar la síntesis de catalizadores NSR y SCR modelo, para posteriormente reformular dichos catalizadores y analizar su metodología de síntesis, sus propiedades físico-químicas, las condiciones operativas y su actividad catalítica y durabilidad para la eliminación de NO_x.

Como objetivo principal de la tesis, se pretende: desarrollar y optimizar sistemas NSR con producción interna de amoniaco y mejorar formulaciones SCR, con el fin de mejorar el rendimiento de sistemas combinados NSR-SCR. Esta investigación se ha desarrollado en el marco de los proyectos CTQ2012-32899 y CTQ2015-67597-C2-2-R.

El objetivo general se ha dividido en objetivos específicos para poder avanzar con las investigaciones planificadas en la tesis, tal como se define a continuación:

- Sintetizar catalizadores modelo NSR (Pt-BaO/Al_2O_3) y SCR (Cu/BETA) y caracterizar sus propiedades físico-químicas, así como determinar su

actividad catalítica para la eliminación de NO_x. Se estudiarán las tecnologías NSR y SCR individualmente, así como su combinación en sistemas hibridos NSR-SCR, conformados en forma granulada y depositados sobre estructuras monolíticas convencionales. También se estudian sistemas monolíticos de doble capa con tecnología combinada NSR-SCR, optimizando la relación de espesores de las capas NSR y SCR.

- Sintetizar catalizadores SCR utilizando zeolitas de poro pequeño, como la SAPO-34 con estructura CHA. Se utilizarán diferentes técnicas de preparación, como el intercambio iónico en fase acuosa y el intercambio iónico en fase sólida. Los sólidos resultantes se caracterizarán y se determinará su actividad en la reacción NH_3-SCR.
- Determinar las especies de NO_x adsorbidas durante el periodo pobre sobre catalizadores Pt-Ba-(Ce)/Al_2O_3 mediante DRIFTS y analizar la descomposición de las especies formadas durante la inyección de diferentes agentes reductores (H_2, CO o C_3H_6) durante el periodo rico. Por otro lado, se determinarán las especies adsorbidas sobre catalizadores Cu/SAPO-34 mediante FTIR durante la reacción NH_3-SCR. Los datos se correlacionarán con experimentos en bancada de reacción.
- Estudiar la influencia de la utilización de diferentes agentes reductores (H_2, CO, C_3H_6 o C_7H_8) durante la regeneración de catalizadores monolíticos NSR sobre la distribución de productos (N_2/NH_3/N_2O) en reactor. Estudiar la influencia de la colocación de un catalizador monolítico SCR aguas abajo del catalizador NSR en presencia de diferentes agentes reductores.

La estructura que se ha seguido para la presentación de los estudios realizados, los resultados obtenidos y la discusión de los mismos es la siguiente:

El Capítulo 1 proporciona una revisión detallada de la literatura sobre las tecnologías existentes para la eliminación de NO_x de las corrientes de escape de los motores diésel o de combustión pobre, funcionando con altas relaciones aire/combustible. Se discuten las conclusiones principales publicadas por

otros autores para las tecnologías NSR, SCR y sistemas NSR-SCR combinados o híbridos. Este análisis permite establecer la hipótesis que respalda los objetivos de la tesis.

En el Capítulo 2 se describen las diferentes técnicas analíticas empleadas para la caracterización de los catalizadores preparados. Por otro lado, se detalla el equipo de reacción experimental y el sistema de análisis para el estudio del comportamiento del catalizador.

En el Capítulo 3 se estudian los catalizadores NSR y SCR modelo. Los catalizadores SCR (Cu/BETA) se sintetizan mediante distintos procesos de intercambio iónico en fase acuosa para poder determinar la influencia del método de preparación. Los catalizadores Cu/BETA se caracterizan exhaustivamente para determinar la presencia de diferentes especies de cobre. En una primera aproximación se sintetizan catalizadores granulados que posteriormente se depositan sobre estructuras monolíticas. Se estudian las tecnologías NSR y SCR por separado y finalmente la combinación de ambas en dispositivos monolíticos NSR-SCR colocados en serie. También se sintetizan diferentes dispositivos de doble capa NSR/SCR, analizando la influencia que tiene el espesor de las capas.

En el Capítulo 4 se analiza la metodología de preparación de catalizadores Cu/SAPO-34 mediante intercambio iónico en estado sólido. En primer lugar, se estudia la influencia de la temperatura de calcinación y posteriormente, se prepararan varios catalizadores con distinta carga de cobre. Los catalizadores se caracterizan y se determina su actividad catalítica en reactor operando en régimen integral y diferencial. La actividad de los catalizadores evaluada mediante *TOF* se compara con la actividad de catalizadores Cu/SAPO-34 sintetizados mediante el método convencional de intercambio iónico en fase acuosa. También se determina la energía de activación de la reacción para los diferentes catalizadores sintetizados.

En el Capítulo 5 se estudian las especies adsorbidas durante las reacciones NSR y SCR utilizando catalizadores Pt-Ba-(Ce)/Al_2O_3 y Cu/SAPO-

34, respectivamente. Por un lado, se determinan las especies adsorbidas mediante DRIFTS cuando los catalizadores NSR se ponen en contacto con una corriente que contiene NO y O_2. Posteriormente, se sigue la evolución de la descomposición de las especies adsorbidas cuando los catalizadores se ponen en contacto con una corriente que contiene NO y un agente reductor (H_2, CO o C_3H_6). Se sigue la evolución de las especies adsorbidas en función de la corriente gaseosa con el tiempo y los experimentos se realizan a diferentes temperaturas, 200 °C, 300 °C y 400 °C. Por otro lado, mediante FTIR se estudian las especies adsorbidas sobre el catalizador Cu/SAPO-34 cuando se pone en contacto con corrientes gaseosas con diferente composición. En concreto, se estudia la adsorción de NO en presencia y ausencia de oxígeno, así como la adsorción de NH_3 también en presencia y ausencia de oxígeno. También se determinan las especies adsorbidas cuando se co-alimentan NH_3 y NO. Todos los experimentos se realizan siguiendo la evolución de las especies adsorbidas con el tiempo y a diferentes temperaturas, desde temperatura ambiente hasta 500 °C. También se realizan experimentos en bancada de reacción para correlacionar la evolución de los productos observados a la salida del reactor con las especies adsorbidas identificadas mediante FTIR.

En el Capítulo 6 se estudia la distribución de productos a la salida del convertidor monolítico NSR cuando se utilizan diferentes agentes reductores como H_2, CO, C_3H_6 y C_7H_8 durante el periodo rico. También se estudia la influencia de la adición de ceria en los catalizadores NSR. Por otro lado, se han preparado dos catalizadores monolíticos SCR (Cu/BETA y Cu/SAPO-34) para situarlos corriente abajo del catalizador NSR. El objetivo del estudio de los sistemas NSR-SCR ha sido analizar la influencia del tipo de zeolita y comparar los resultados obtenidos en la tecnología combinada NSR-SCR con los del catalizador simple NSR.

En el Capítulo 7 se presenta el resumen general del trabajo, así como las conclusiones generales que pueden extraerse del mismo. A la vista de los resultados y conclusiones obtenidos, se proponen posibles actuaciones futuras

para la continuación de la línea de investigación en el área de tecnologías para la eliminación de NO_x en corrientes de escape de motores de mezcla pobre en automóviles.

Finalmente, en los Capítulos 8 y 9 se presentan la nomenclatura y bibliografía utilizadas a lo largo de la memoria, respectivamente.

Capítulo 2

MATERIALES, MÉTODOS Y EQUIPOS

Capítulo 2

MATERIALES, MÉTODOS Y EQUIPOS

RESUMEN

En este capítulo se analizan los reactivos, los métodos de preparación de los catalizadores, las técnicas de caracterización y el sistema de reacción utilizados. Para la síntesis de los catalizadores SCR se utilizan las zeolitas BETA y SAPO-34 y para la tecnología NSR se sintetizan los catalizadores Pt-Ba/Al_2O_3 y Pt-Ba-Ce/Al_2O_3. Se describe la incorporación del bario, platino y del cobre mediante la impregnación o el intercambio iónico. También se describe el procedimiento de preparación utilizado para los catalizadores monolíticos Pt-Ba/Al_2O_3 y Cu/zeolita. Para el análisis físico-químico de los catalizadores se han utilizado las siguientes técnicas de caracterización, adsorción-desorción de nitrógeno, FRX, DRX, DRIFT, FTIR, SEM-TEM, UV-vis, EPR, H_2-TPR y NH_3-TPD. También se explica brevemente cada técnica y el procedimiento experimental. Además, se describen el sistema de reacción y los protocolos utilizados en los ensayos realizados con los catalizadores NSR o SCR en polvo y en monolitos. Se describe el sistema de reacción que permite la simulación del convertidor catalítico y las técnicas de análisis FTIR y QMS para determinar la distribución del producto a la salida de los dispositivos DeNO_x en condiciones muy similares a las de un automóvil.

Chapter 2

MATERIALS, METHODS AND EQUIPMENTS

ABSTRACT

General information about the chemicals, catalysts preparation methods and analytical and reaction techniques used is given in this chapter. BETA and CHA solids are used as starting materials for SCR catalyst synthesis. For NSR technology Pt-Ba/Al_2O_3 and Pt-Ba-Ce/Al_2O_3 catalysts are synthesized. Detailed description of platinum, barium and copper incorporation by impregnation or ion exchange is presented with different precursors. The preparation procedure of Pt-Ba/Al_2O_3 and Cu/zeolite monolithic catalysts is also included in this chapter. The following characterization techniques have been used in order to characterize the physico-chemical properties of the prepared catalysts, nitrogen adsorption-desorption, XRF, XRD, DRIFT, FTIR, SEM-TEM, UV-vis, EPR, H_2-TPR and NH_3-TPD. A brief description as well as the experimental procedure is reported for these techniques. In addition, the reaction system and protocols used for testing powder and monolith NSR or SCR catalysts are described. The experimental reactor bench allowing simulation of the converter under near real operation in the automobile practice, and the analysis techniques FTIR and QMS for determining the product distribution at the exit of $DeNO_x$ devices are also described.

2. MATERIALES, MÉTODOS Y EQUIPOS

En el presente capítulo se describen los materiales, métodos y equipos que se han utilizado durante el desarrollo de la tesis doctoral. Se detallan los reactivos utilizados para la síntesis y preparación de los catalizadores Pt-Ba/Al_2O_3 y Cu/zeolita en forma granulada y monolítica. Se especifican los gases empleados en la preparación, caracterización de materiales, así como en los ensayos de reacciones. Además, se resumen las bases teóricas, la metodología y la descripción de los equipos utilizados en la caracterización de los catalizadores preparados. Por último, se describen los equipos de reacción en los que se ha examinado el comportamiento de los catalizadores en las tecnologías NSR y SCR, tanto en sistemas monocatalíticos como en sistemas combinados. Se describe en detalle el sofisticado sistema de mezcla de gases para la preparación de las atmósferas de reacción, el sistema de control de las diferentes variables de operación y el sistema de análisis en línea que permite determinar con precisión la distribución de productos a la salida de los reactores.

2.1. MATERIALES Y REACTIVOS

2.1.1. Catalizadores NSR

Para la preparación del catalizador Pt-Ba/Al_2O_3 en los laboratorios de la Universidad del País Vasco, se ha utilizado γ-Al_2O_3 suministrada por la casa Saint Gobain con nombre comercial SA6173 para que actúe como soporte de las fases activas. La alúmina fue suministrada en forma de pastillas. La alúmina se ha sometido a un tratamiento previo de estabilización mediante calcinación en aire a 500 °C durante 4 horas en un horno de mufla. A continuación, se procede a realizar una molienda mecánica de la misma en un molino de bolas cerámico para obtener un tamaño de partícula menor.

Como sal precursora de Pt se ha empleado el nitrato de tetraminplatino (II), $Pt(NH_3)_4(NO_3)_2$, de la casa Alfa Aesar que presenta una pureza del 99,99% y un contenido de Pt del 50,4% en peso.

Se ha seleccionado el acetato de bario, $Ba(CH_3COO)_2$, como sal precursora del componente de almacenamiento elegido (Ba) para los catalizadores NSR. Su alta solubilidad en agua (590 g l^{-1} a 20 °C) en comparación al resto de sales de bario, junto a su relativamente fácil descomposición térmica, sin generación de residuos aniónicos halogenados, confieren a esta sal unas características especialmente adecuadas. El acetato de bario fue suministrado por la casa Sigma-Aldrich y presenta una pureza del 99% y un contenido de Ba del 53,7% en peso.

Para la preparación de los catalizadores Pt-Ba/Al_2O_3 y Pt-Ba-Ce/Al_2O_3 en los laboratorios de la Universidad Tecnológica de Chalmers se ha utilizado γ-Al_2O_3 de la casa Alfa Aesar, suministrada en forma de polvo con un tamaño de 20 nm. La alúmina se sometió a un tratamiento previo de estabilización mediante calcinación en aire a 750 °C durante 20 horas en un horno de mufla.

Como sal precursora de Pt se ha empleado el nitrato de tetraminplatino (II), $Pt(NH_3)_4(NO_3)_2$, de la casa Heraeus GmbH que presenta un contenido de Pt del 14,93% en peso.

El acetato de bario seleccionado ha sido el mismo que se utilizó para la preparación de los catalizadores en los laboratorios de la UPV/EHU. Cuando se han preparado catalizadores Pt-Ba-Ce/Al_2O_3, se ha utilizado como sal precursora el nitrato de cerio $Ce(NO_3)_3{\cdot}6H_2O$, de la casa Alfa Aesar con una pureza del 99,99%.

2.1.2. Catalizadores SCR

Para la síntesis de los catalizadores Cu/zeolita se han utilizado zeolitas NH_4-BETA y H-SAPO-34 de la casa Zeolyst International y ACS Material, respectivamente. Las zeolitas fueron suministradas en forma de polvo y según

las especificaciones del fabricante poseen una superficie BET de 680 m^2 g^{-1} para la zeolita BETA y 550 m^2 g^{-1} para la zeolita SAPO-34. La relación SiO_2/Al_2O_3 de la zeolita BETA es de 25 y la relación SiO_2:Al_2O_3:P_2O_5 de SAPO-34 es de 9,26:35,19:40,02, según las especificaciones del fabricante.

Para la preparación de catalizadores mediante intercambio iónico en fase líquida (LIE, liquid ion exchange) se ha empleado como sal precursora de Cu el acetato de cobre (II), $Cu(COOCH_3)_2$, de la casa Panreac que presenta una pureza del 98% y un contenido de cobre del 32% en peso. Para la síntesis de catalizadores mediante intercambio iónico en estado sólido (SSIE, solid state ion exchange) se ha utilizado como sal precursora oxido cúprico (CuO) de la casa Sigma-Aldrich. El CuO se encuentra en forma de polvo, en partículas de tamaño inferior a 50 nm según el fabricante.

En los catalizadores Cu/zeolita sintetizados mediante el intercambio iónico en líquido se llevó a cabo un intercambio intermedio con nitrato de sodio. El nitrato de sodio ($NaNO_3$) utilizado es de la casa Merck KGaA y su pureza es del 99,5%.

El sustrato monolítico de cordierita ha sido suministrado por Corning Celcor con una densidad de 62 celdas cm^{-2} (400 celdas in^{-2}). La forma geométrica de los canales es cuadrada con un espesor de pared de 150 μm, el diámetro del monolito es 17 mm y la largura de 21 mm. El sustrato monolítico se calcinó a una temperatura de 700 °C durante 4 horas como etapa previa de limpieza, antes de comenzar la síntesis del catalizador.

La bohemita (Disperal P2) utilizada como aglomerante para que la adherencia de las películas al monolito resulte altamente estable ha sido suministrada por Sasol Germany GmH.

Los gases empleados en las distintas técnicas de caracterización han sido H_2, N_2 y He de calidad 5,0 y botellas calibradas 5% O_2/He y 5%H_2/Ar, todos ellos suministrados por la empresa Praxair.

Los gases empleados en los ensayos de actividad han sido N_2 o Ar de 99,8% de pureza, CO_2 de 99,998% y NO de 99,9%, proporcionados por Air Liquide, y CO de 99,999% e H_2 de 99,999%, proporcionados por Praxair. Por otro lado, se han utilizado los siguientes gases en los laboratorios de la Universidad Tecnológica de Chalmers: 25% H_2/Ar, 10% CO/Ar, 4% C_3H_6/Ar y 3,145% NO/Ar suministrados por Air Liquide.

2.2. PREPARACIÓN DE CATALIZADORES NSR Y SCR

2.2.1. Preparación de catalizadores Pt-Ba/Al_2O_3 y Pt-Ba-Ce/Al_2O_3 granulados

2.2.1.1. Incorporación del metal por impregnación húmeda

Es un método sencillo y el más ampliamente empleado en la industria para la incorporación de metales en catalizadores. El proceso consiste en poner lentamente en contacto el sólido con una disolución de una concentración metálica determinada e ir evaporando el disolvente progresivamente. Se basa en la presencia de fuerzas de succión capilar que promueven el flujo de la disolución hacia el interior de los poros de la alúmina seca. Comúnmente se emplean volúmenes de disolución iguales al volumen de poros. En cambio, en este trabajo se ha optado por el empleo de mayores volúmenes de disolución de metal, con el fin de asegurar el mojado completo de todas las partículas de la alúmina y la homogeneidad en la distribución de la fase metálica.

La incorporación del metal se ha llevado a cabo en un rotavapor modelo R-114 de la casa Büchi, equipado con un baño termostatizado B-480 de la misma casa comercial, y un sistema de vacío. Se ha disuelto la cantidad correspondiente de precursor en agua y se ha añadido lentamente a la alúmina, agitando hasta que el disolvente se haya evaporado por completo. La temperatura y la presión del sistema se estabilizaron en 30 °C y 3 mm Hg, respectivamente. La muestra resultante se ha secado durante 2 horas a 110 °C

y se ha calcinado durante 4 horas a 500 °C. Posteriormente, se ha vuelto a repetir el mismo procedimiento, pero en este caso se ha añadido 15% de Ba a la muestra Pt/Al_2O_3. La muestra $Pt\text{-}Ba/Al_2O_3$ se ha secado durante 2 horas en la estufa a 110 °C y ha sido calcinada durante 4 horas a 500 °C.

2.2.1.2. Incorporación del metal por impregnación a humedad incipiente

En los laboratorios de la Universidad Tecnológica de Chalmers los catalizadores $Pt\text{-}Ba/Al_2O_3$ y $Pt\text{-}Ba\text{-}Ce/Al_2O_3$ se prepararon mediante impregnación a humedad incipiente. En primer lugar, se ha preparado una disolución de platino para añadirla gota a gota sobre la alúmina. Una vez que se ha obtenido una masa espesa homogénea la muestra se ha introducido a la estufa a 80 °C durante 20 horas y posteriormente se ha calcinado a 550 °C durante 2 horas en la mufla. El mismo proceso se ha repetido con el acetato de bario [120, 121].

2.2.2. Preparación de catalizadores Cu/zeolita granulados

2.2.2.1. Incorporación del metal por intercambio iónico en fase líquida (LIE; Liquid Ion Exchange)

Este método consiste en poner en contacto el soporte con una disolución de metal durante un largo periodo de tiempo, al final del cual el exceso de disolvente se separa por filtración. El proceso se basa en el intercambio iónico que sucede entre los centros cambiadores de la superficie del soporte sólido y los iones metálicos que se encuentran en la disolución.

La fuerza de intercambio iónico depende de la polarización y la carga iónica del catión/anión ($C^{4+}>C^{3+}>C^{2+}>C^{+}\approx H^{+}$; $SO_4^{2-}>I^{-}>Br^{-}>Cl^{-}>F^{-}$) [122]. Una de las principales ventajas que posee este método de preparación es la alta estabilidad del componente metálico frente a la sinterización en los tratamientos posteriores, debido a la fuerte interacción que se logra entre el metal y el soporte.

Los catalizadores Cu/zeolita se han preparado mediante intercambio iónico en fase líquida. En el caso de los catalizadores Cu/BETA, se han preparado cuatro muestras con distintas denominaciones; H/Cu (muestra1), NH_4/Cu (muestra 2), NH_4/Na/Cu (muestra 3) y H/Na/Cu (muestra 4). En la primera muestra se ha disuelto la cantidad correspondiente de precursor necesaria en 1,5 l de agua ultrapura, y se ha añadido la zeolita BETA (8 g l^{-1}) en foma protónica. En la segunda muestra, se ha preparado la misma disolución acuosa que en la primera muestra y se ha añadido la zeolita BETA en forma amónica. A continuación, en ambas muestras se ha ajustado el pH a 7 con amoniaco para favorecer el intercambio [123]. Las mezclas se han agitado durante 24 horas a 60 °C para posteriormente eliminar el disolvente por filtración. Por último, tras sucesivas limpiezas con agua ultrapura, se han secado a 110 °C durante una noche y se han calcinado a 500 °C durante 4 horas. En la tercera muestra, se ha disuelto la cantidad correspondiente de nitrato de sodio en 1,5 l de agua ultrapura y se ha añadido la zeolita BETA (8 g l^{-1}) en forma amónica. En la cuarta muestra, se ha preparado la misma disolución de nitrato de sodio y se ha mezclado con la zeolita BETA en forma protónica. En las muestras 3 y 4 el intercambio iónico con sodio en las dos muestras se ha llevado a cabo a temperatura ambiente y pH=6 y se ha agitado durante 24 horas. Posteriormente, se han filtrado las mezclas y las tortas formadas se han lavado con agua ultrapura y se han secado a 110 °C durante una noche. El intercambio iónico con nitrato de sodio se ha realizado dos veces. Una vez obtenida la torta de Na/BETA se ha calcinado a 550 °C durante 5 horas. Finalmente, se ha realizado el intercambio iónico entre la torta Na/BETA y el acetato de cobre en las mimas condiciones que en las muestras 1 y 2.

Los catalizadores Cu/SAPO-34 preparados mediante intercambio iónico en fase líquida se han preparado con el mismo proceso de preparación que la muestra cuatro (H/Na/Cu) descrito para el catalizador Cu/BETA.

2.2.2.2. Incorporación del metal por intercambio iónico en estado sólido (SSIE, Solid State Ion Exchange)

Para el intercambio iónico en estado sólido se prepara una mezcla física homogénea de la zeolita y el precursor de CuO en un mortero. Posteriormente, la mezcla se calcina en flujo de aire en un horno horizontal a distintas temperaturas (500, 600, 700, 750 y 800 °C) durante 12 horas [124, 125]. El proceso de intercambio iónico en fase sólida ocurre cuando la mezcla física se calienta a altas temperaturas, los metales se intercambian en la zeolita durante la calcinación. Además, cuando las zeolitas están en forma protónica o amónica, el método SSIE es adecuado porque los haluros de hidrógeno generados se eliminan fácilmente [126].

2.2.3. Preparación de catalizadores monolíticos

Para la preparación de los catalizadores monolíticos se ha llevado a cabo la incorporación de la película del material catalítico sobre el monolito cerámico mediante la técnica de recubrimiento (washcoating).

En los laboratorios del grupo TQSA los catalizadores monolíticos NSR y SCR se han preparado de la siguiente forma. En primer lugar, se ha preparado una suspensión acuosa del 40% del catalizador que se quiere depositar en el monolito. La suspensión se ha sometido a molienda húmeda en un molino de bolas para reducir el tamaño de las partículas por debajo de 3 μm, correspondiente al tamaño de poro de la cordierita. Con el material de tamaño de partícula reducido, se ha preparado una suspensión acuosa del 15%, en la que se sumerge el monolito durante un minuto. Fuera de la suspensión, el frente de paso del monolito se sopla con aire comprimido de forma controlada para eliminar el exceso de líquido retenido en los canales y luego se seca durante 30 minutos a 110 °C. Este proceso se repite hasta adherir el espesor deseado. Finalmente, el monolito se calcina a 550 °C durante 4 h para estabilizar el catalizador estructurado.

El procedimiento descrito es común para preparar tanto los catalizadores NSR como SCR.

Para la preparación de los monolitos de doble capa que se estudian en el Capítulo 3, la incorporación de las dos capas se realiza de forma sucesiva. En primer lugar, el monolito se sumerge en una suspensión de catalizador NSR y finalizada la estabilización de esta capa mediante calcinación se sumerge en una suspensión de catalizador SCR, para finalmente obtener un monolito de doble capa estabilizado.

Los monolitos preparados en los laboratorios de la Universidad de Chalmers también se han preparado mediante "washcoating". Para la preparación de estos monolitos se ha realizado una mezcla de 80% líquido (50% agua + 50% etanol) y 20% sólido (10% bohemita + 90% catalizador). Esta mezcla se introduce mediante una pipeta Pasteur en los canales del monolito, que luego se seca en flujo de aire caliente a 90 °C durante 1 minuto. El proceso se ha repetido hasta incorporar 250 mg de carga en el monolito. Finalmente, los monolitos se han calcinado a 500 °C durante 2 horas; con una rampa de 5 °C min^{-1}.

2.3. TÉCNICAS DE CARACTERIZACIÓN DE LOS CATALIZADORES

2.3.1. Adsorción física de gases

El método más extendido para el estudio de las propiedades texturales de los catalizadores es la adsorción física o fisisorción de gases. Esta técnica proporciona información relativa sobre el área superficial y la estructura de los poros [127].

Los sólidos presentan fuerzas a escala molecular sin compensar en los átomos o iones que componen la superficie exterior, lo que genera fuerzas de atracción con respecto a moléculas gaseosas (adsorbato). El proceso de adsorción física provoca que las moléculas de adsorbato tiendan a constituir una monocapa sobre la superficie del sólido. Por ello, para un sólido dado, la

cantidad de moléculas de adsorbato requerida para constituir una monocapa dependerá exclusivamente del tamaño de la propia molécula de adsorbato. El gas adsorbato más empleado es el N_2, operándose en experimentos isotermos a su temperatura normal de ebullición (-196 °C). En estas condiciones, el valor medio del área de la sección transversal de la molécula de N_2 es 0,162 nm^2. La representación de la cantidad de volumen de gas adsorbido una vez alcanzado el equilibrio, en función de la presión relativa del gas a adsorber recibe el nombre de isoterma. Su análisis matemático permite obtener el volumen necesario para lograr un recubrimiento del sólido en forma de monocapa y, en consecuencia, el cálculo de la superficie accesible del sólido.

En función de las características de dicho sólido, Brunauer, Emmett y Teller [128] propusieron cinco modelos diferentes de isoterma, a los que posteriormente, Sing [129] añadió un último modelo; las cuales se representan en la Figura 2.1.a. Sin embargo, en la caracterización de catalizadores, cuatro son los tipos de isotermas comúnmente encontrados [130]: tipo II, característica de sólidos macroporosos (tamaño de poro > 50 nm) o no porosos; tipo IV, correspondiente a sólidos mesoporosos con tamaño de poro comprendido entre 2 y 50 nm; tipo I, característica de sólidos microporosos, con tamaño de poro inferior a 2 nm; tipo VI, correspondiente con sólidos ultramicroporosos con tamaño de poro regular.

Las zeolitas BEA y CHA utilizadas como soporte catalítico para la reacción NH_3-SCR son sólidos microporosos y presentan isotermas tipo I. La alúmina utilizada para los catalizadores Pt-Ba/Al_2O_3 pertenece a la familia de los sólidos mesoporosos y su isoterma de adsorción es de tipo IV.

El ajuste a la ecuación de Brunauer, Emmett y Teller, conocida como ecuación BET, es el método más extendido para el cálculo del área superficial. En su forma linealizada y simplificada la isoterma BET se expresa mediante la Ecuación 2.1

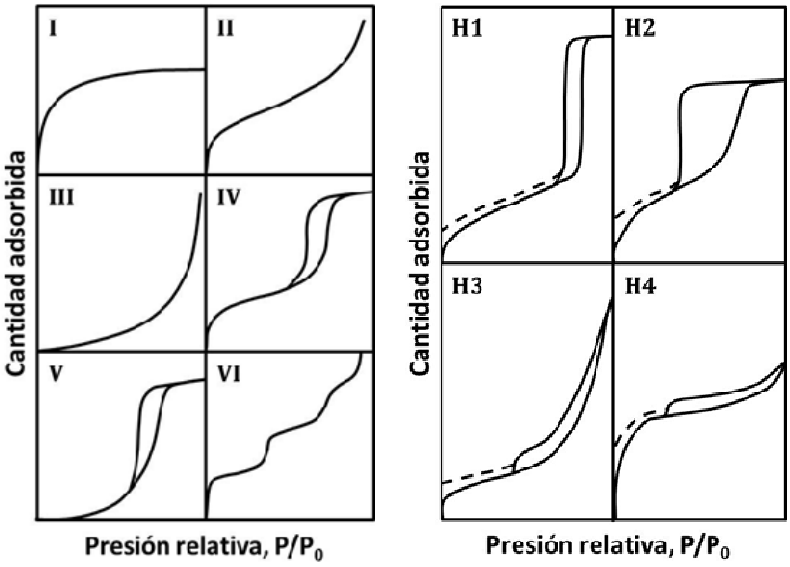

Figura 2.1. a) Representación esquemática de los seis tipos de isotermas de adsorción, según la IUPAC [131]. b) Forma de los posibles ciclos de histéresis, según la IUPAC [131].

$$\frac{P}{V_{\text{ads}}\left(P_0 - P\right)} = \frac{1}{V_{\text{m}}C} - \frac{C-1}{V_{\text{m}}C}\frac{P}{P_0} \tag{2.1}$$

donde V_{ads} (cm^3 g^{-1}) es el volumen de gas adsorbido por unidad de masa de sólido en equilibrio para una presión P (kPa) dada, V_{m} (cm^3 g^{-1}) es el volumen de adsorbato requerido para formar una monocapa, P_0 (kPa) es la presión de saturación del adsorbato en las condiciones de análisis y C es un parámetro asociado con las entalpías de adsorción y desorción del adsorbato [131]. El ajuste de los datos de la isoterma a la Ecuación 2.1, entre presiones relativas desde 0,05 a 0,2 permite el cálculo de los parámetros V_{m} y C a partir de la pendiente y la ordenada en el origen. Una vez determinado el parámetro V_{m}, el cálculo de la superficie específica (S_{BET}, m^2 g^{-1}) del sólido problema se realiza a través de la Ecuación 2.2

$$S_{\mathrm{BET}} = 10^{-18} \frac{V_{\mathrm{m}} N_{\mathrm{A}}}{m V_{\mathrm{mol}}} A_{\mathrm{m}} \qquad (2.2)$$

siendo N_A el número de Avogrado, V_{mol} el volumen molar del adsorbato ($cm^3\ mol^{-1}$), A_m el área de la sección transversal del adsorbato (nm^2) y m la masa del sólido problema empleada en la determinación de la isoterma (g).

Los procesos de condensación capilar que tienen lugar en el interior de los poros dificultan la retirada del gas adsorbido en los poros de menor tamaño, y en consecuencia, es posible que las ramas de adsorción y desorción de la isoterma no sean coincidentes, conduciendo al fenómeno denominado histéresis. La forma y presión relativa en las que aparezca la histéresis permite determinar las distribuciones de tamaño de poro. Según la IUPAC (Figura 2.1.b), existen cuatro tipos de histéresis dependiendo de si los poros son cilíndricos uniformes (H1), presentan cuello de botella (H2) o son en forma de rejilla uniforme (H4) o no uniforme (H3) [132, 133].

Uno de los métodos comúnmente empleados en la determinación del volumen de poro, V_P ($cm^3\ g^{-1}$), y de la distribución de tamaño de poro en muestras mesoporosas, es el propuesto por Barrett, Joyner y Halenda (método BJH) [134], Ecuación 2.3, basado en la ecuación de Kelvin para la condensación capilar que se aplica al análisis de la rama de desorción de la isoterma

$$r_{\mathrm{p}} = 10^{3} \frac{2\psi V_{\mathrm{ads}} \cos\upsilon}{RT \ln\left(\frac{P}{P_0}\right)} + e \qquad (2.3)$$

donde r_p es el radio de poro (nm), Ψ la tensión superficial del adsorbato ($N\ m^{-1}$), υ el ángulo de contacto de la fase condensada y las paredes del sólido, T la temperatura (K), R la constante de los gases perfectos (8,314 $J\ mol^{-1}\ K^{-1}$) y e el espesor de la capa adsorbida (nm).

Se ha aplicado el método BET para la evaluación de la superficie específica de las zeolitas BETA y SAPO-34 utilizadas en esta tesis.

Procedimiento experimental

Se han realizado experimentos isotermos de adsorción-desorción de N_2 a la temperatura normal de ebullición del N_2 (-196 °C) en un equipo de la casa Micromeritics modelo ASAP 2020, con el objeto de determinar la superficie específica de los distintos catalizadores preparados.

Para optimizar el análisis se seleccionaron masas de muestra de aproximadamente 35 m^2 de área superficial. Previo al análisis, las muestras se desgasificaron a vacío (< 1 Pa) y a 300 °C durante 2 horas, eliminándose la humedad, el aire y los posibles condensados susceptibles de interferir en la medida.

La toma de medidas que constituyen la isoterma es automática. La rama de adsorción se obtiene al añadir sucesivos volúmenes conocidos de N_2 y registrar los valores de presión de equilibrio, desde la presión más baja (< 1 Pa) hasta la de saturación del N_2 (~101,3 kPa). De toda esta rama se seleccionan 8 puntos en el intervalo de presiones relativas de N_2 entre 0,06 y 0,2 para el cálculo de S_{BET}.

Seguidamente se obtiene la rama de desorción, eliminando sucesivos volúmenes conocidos de N_2 y registrando los valores de presión de equilibrio hasta alcanzar el cierre de la histéresis. Se considera toda la rama de desorción, intervalo de presiones parciales 0,14-0,99, para el cálculo de la distribución de tamaño de poro según el método BJH. Para determinar la distribución de tamaño de poro de la zeolita por el método Horvarth-Kawazoe se seleccionaron los puntos de la isoterma desde su inicio hasta presiones relativas de 0,01.

2.3.2. Espectroscopía de fluorescencia de rayos X

La espectroscopía de fluorescencia de rayos X de dispersión por longitudes de onda (WDXRF, Wavelength Dispersive X-ray Fluorescence) es una técnica analítica empleada fundamentalmente para la determinación y cuantificación de los elementos presentes en muestras sólidas [135, 136]. Esta

técnica utiliza los rayos X que se generan en una muestra sometida a bombardeo electrónico para identificar los elementos presentes y establecer su concentración. Los rayos X se generan como consecuencia de choques inelásticos de los electrones incidentes que excitan los átomos de la muestra cediéndoles parte de su energía cinética. Cuando los átomos vuelven a su estado fundamental emiten la radiación X característica. La detección de estos rayos X se realiza mediante espectrómetros de dispersión de longitudes de onda o mediante espectrómetros de dispersión de energías.

Los espectrómetros de dispersión de longitudes de onda están basados en la selección de la longitud de onda característica al difractar la radiación incidente en un cristal monocromador de espaciado adecuado, y su posterior detección por un contador proporcional que mide la intensidad de los rayos X difractados.

Si la intensidad de la radiación electromagnética se representa frente a su longitud de onda (o energía), se obtiene el espectro de rayos X. Este espectro está constituido por una serie de picos, designados indistintamente como líneas, de intensidad variable, a los que se denomina rayos X característicos. Estas líneas se denominan en función de la capa a la que pertenezca el electrón arrancado (familias K, L, M) y el electrón proporcionado a esta capa (líneas α, β y γ). Los rayos X ocupan un pequeño intervalo de longitudes de onda en el espectro general de radicaciones electromagnéticas, entre 10^{-8} y 10^{-12} m, que corresponden al intervalo de energía entre 10^{-1}-10^{3} keV. La longitud de onda, λ, la frecuencia, ν y la energía, E, de cualquier radiación, están relacionados por la Ecuación 2.4.

$$E = h\nu = hc/\lambda \tag{2.4}$$

donde h es la constante de Planck y c la velocidad de la luz. La energía se expresa generalmente en estos procesos como eV. En estas condiciones:

$$E = 12397/\lambda \tag{2.5}$$

Procedimiento experimental

A partir de cada muestra en polvo, se ha preparado una perla de vidrio borado mediante fusión en un microhorno de inducción, mezclando el fundente Spectromelt A10 de la casa Merck y la muestra seca en proporciones aproximadas de 20:1.

El análisis químico de cada perla se ha realizado en atmósfera de vacío, empleando un espectrómetro secuencial de fluorescencia de rayos X por dispersión de longitud de onda (WDXRF), de la marca PANalytical, modelo AXIOS, dotado con un tubo de Rh, y tres detectores (flujo gaseoso, centelleo y sellado de Xe).

Para la confección de las rectas de calibrado se han utilizado patrones internacionales bien caracterizados de rocas y minerales. Se han analizado los elementos mayores habituales en los análisis de rocas, así como el CuO.

Los análisis y el procesamiento informático de los datos se han realizado en los Servicios Generales de Investigación SGIKER de la UPV/EHU.

2.3.3. Difracción de rayos X

Los rayos X sufren una serie de interacciones al atravesar la materia. Mientras parte de la energía es transmitida a través del medio, otra parte se transforma en calor, otra es re-irradiada y la restante es dispersada. La radiación dispersada de forma coherente, sin variar su longitud de onda, es la empleada por la técnica de difracción de rayos X (XRD, X-Ray Diffraction). Esta técnica permite estudiar la estructura interna de sólidos cristalinos.

La aplicación de la técnica XRD para el análisis cualitativo y cuantitativo de fases cristalinas está bien establecido [137]. En la materia cristalina, los átomos están dispuestos de una manera ordenada y periódica en el espacio, formando planos cristalinos. Los planos cristalinos de una misma familia están separados entre sí en un valor constante, d, denominado espaciado, que resulta del mismo orden de magnitud que la longitud de onda λ de los rayos X

(0,1-10 Å). Por ello, los rayos X pueden difractarse por las redes cristalinas de acuerdo con la Ley de Bragg (Ecuación 2.6)

$$n\lambda = 2d\,sen(\theta) \tag{2.6}$$

El método de análisis más extendido es el de muestras en polvo. Al estar la muestra en forma de partículas muy finas orientadas al azar, todas las orientaciones posibles quedan representadas en su superficie, y por tanto expuestas al haz de rayos X. Según gira la muestra, el ángulo de incidencia θ varia mientras el detector, a la vez, gira un ángulo doble (2θ), recogiendo un fondo continuo de radiación con una serie de máximos que corresponden a los rayos X difractados. Se obtiene un espectro llamado difractograma, cuyas posiciones 2θ e intensidades son características de cada fase cristalina. La comparación del difractograma experimental con los propios de cada fase cristalina, que están recogidos en una base de datos llamada PDF (Powder Diffraction File) establecida por el ICDD (International Centre for Diffraction Data), permite la identificación de las fases presentes en la muestra.

Esta técnica ha sido comúnmente aplicada para el cálculo de tamaños de cristales de metales dispersos en soportes catalíticos [138, 139], obteniéndose buenas concordancias con las medidas de dispersión determinadas mediante quimisorción. La técnica está limitada para partículas de tamaño superior a 3-4 nm, dado que las inferiores a este tamaño son prácticamente transparentes a la radiación X [140].

Procedimiento experimental

Las muestras catalíticas se han sometido a un proceso exhaustivo de molienda, asegurándose la obtención de polvo fino. Se coloca un vidrio plano sobre la cavidad del portamuestras, sobre el que se deposita una pequeña cantidad de muestra en polvo y unas gotas de acetona, de modo que al secarse ésta, el polvo queda adherido a la superficie del vidrio y aleatoriamente orientado.

Las medidas se han realizado en un difractómetro modelo PW1710 de la casa Philips, con geometría Bragg-Bretano, operando con la radiación Kα (1,541874 Å) del cobre. Las condiciones de medida han sido: barrido angular comprendido en el intervalo 5-80° para 2θ, tamaño de paso de 0,02° en 2θ y tiempo de paso de 1 s. El equipo está controlado por el software X´pert Data Collector. Para el tratamiento informático de los difractogramas obtenidos y la identificación de las fases presentes se ha empleado el software específico PANalytical X´pert HighScore, en combinación con la base de datos PDF2 del ICDD. Las intensidades de los picos obtenidos se han corregido para un valor de rendija fija.

Los análisis y el procesamiento informático de los datos se han realizado en los Servicios Generales de Investigación SGIKER de la UPV/EHU.

2.3.4. Espectroscopía infrarroja

La espectroscopía infrarroja (IR, InfraRed Spectroscopy) es la técnica espectroscópica más comúnmente utilizada, y generalmente la más efectiva, para la caracterización de la química superficial de catalizadores heterogéneos [141].

Esta técnica se basa en que una molécula comienza a vibrar de uno o varios determinados modos cuando es expuesta a radiación correspondiente a la región del IR, absorbiendo esta radiación para ciertas longitudes de onda características. La representación de la intensidad de la radiación IR detectada en función del número de onda (cm^{-1}) se denomina espectro IR. Su análisis permite la caracterización química de la muestra, dado que cada compuesto presenta un espectro IR característico.

Particularmente, en catálisis heterogénea, la espectroscopía IR se ha empleado comúnmente para la identificación de grupos funcionales superficiales presentes en los soportes, tales como hidroxilos, sulfatos y carbonatos. Además, dado que la técnica permite el seguimiento directo de las interacciones entre las moléculas que reaccionan y la superficie del

catalizador, se ha empleado para el estudio del mecanismo de reacciones catalíticas, analizando la naturaleza de los compuestos intermedios adsorbidos [142, 143]. Asimismo, empleándose moléculas sonda, la técnica se ha aplicado al estudio de la acidez de óxidos metálicos y zeolitas y a la caracterización de metales reducidos soportados [144, 145].

A pesar de que existe un amplio abanico de técnicas IR aplicables al estudio de la superficie de catalizadores, las más comúnmente empleadas son las de transmisión/absorción y la de reflectancia difusa [146].

Procedimiento experimental

La espectroscopía infrarroja se ha empleado para la identificación de las especies adsorbidas en la superficie de los catalizadores Pt-Ba/Al_2O_3 y Cu/zeolita. Los resultados obtenidos se muestran en el Capítulo 3 y 5.

Los espectros de absorción infrarrojos con transformada de Fourier (FTIR, Fourier Transformed InfraRed) se han realizado en un espectrofotómetro Protegé 460 de la casa Nicolet equipado con un detector de sulfato de triglicina deuterado (DTGS, Deuterated TriGlycine Sulfate) con lámina divisora de haz de KBr. Todos los espectros se han registrado en el intervalo de número de onda 4000-650 cm^{-1} promediándose 50 medidas con una resolución de 2 cm^{-1}. Estos ensayos se han llevado a cabo en los laboratorios del grupo TQSA.

Las muestras se soportan en una celda Specac de acero inoxidable 316 con ventanas de ZnSe. Dicha celda está provista con un horno y un controlador de temperatura que permite tratamientos térmicos in situ de la muestra hasta 500 °C. Un sistema externo de alimentación, constituido por una serie de controladores de flujo másico calibrados (N_2, NO, O_2, CO, CO_2, H_2 y NH_3) ha permitido especificar la composición gaseosa alimentada a la celda.

Las muestras se reducen a partículas muy finas mediante molienda en un mortero de ágata, para posteriormente conformar discos auto soportados (sin KBr) de 12 mm de diámetro. Dichos discos se preparan por empastillado a

presión elevada (2,5 10^5 kPa) en una prensa hidráulica modelo Specac. Se toman y registran masas de muestra apropiadas para conseguir una densidad superficial de los discos de aproximadamente 15 mg cm^{-2}. Su disposición en la celda fue perpendicular al haz IR.

Para el estudio de la superficie de los catalizadores Cu/BETA (Capítulo 3) se han llevado a cabo los experimentos a 30 °C y alimentando 40 ppm de NO y 30 ppm NO_2 con N_2 con un caudal total de 500 mL min^{-1}. Por otra parte, también se han llevado a cabo experimentos donde se ha analizado la adsorción de NO y CO con reducciones intermedias, de acuerdo al siguiente protocolo: en primer lugar el catalizador fue reducido con un caudal de 5% H_2/N_2 con una rampa de temperatura de 5 °C min^{-1} hasta 200, 250, 300, 350, 400, 450 y 500 °C. Una vez que se ha reducido el catalizador a la temperatura deseada se ha bajado la temperatura hasta 30 °C para adsorber NO (470 ppm NO en N_2) o CO (390 ppm CO en N_2). Los gases se alimentan hasta saturar el catalizador.

Para el estudio de la superficie de los catalizadores Cu/SAPO-34 en el Capítulo 5 se han introducido 660 ppm de NO, 660 de NH_3 y 6% de O_2 en N_2 con un caudal total de 500 mL min^{-1}. Entre experimento y experimento el catalizador se ha limpiado con N_2 a 500 °C. Posteriormente, la temperatura se disminuye para llevar a cabo un nuevo experimento. La adsorción de los distintos gases se ha analizado a 100, 200, 300, 400 y 500 °C.

En el Capítulo 5 también se lleva a cabo el estudio superficial de los catalizadores Pt-Ba/Al_2O_3 y Pt-Ba-Ce/Al_2O_3 en los laboratorios de la Universidad Tecnológica de Chalmers mediante un equipo DRIFT. El equipo utilizado ha sido BioRad FTS 6000 equipado con una celda con ventanas de KBr (Harrick Scientific, Praying Mantis) donde se pone la muestra en polvo. La temperatura se regula mediante un controlador Eurotherm 2416. Mediante los controladores másicos de la casa Bronkhorst Hi-Tech se suministraban los gases a la celda. En este caso para llevar a cabo los experimentos, en primer lugar la superficie del catalizador fue tratada a 500 °C durante 30 minutos con

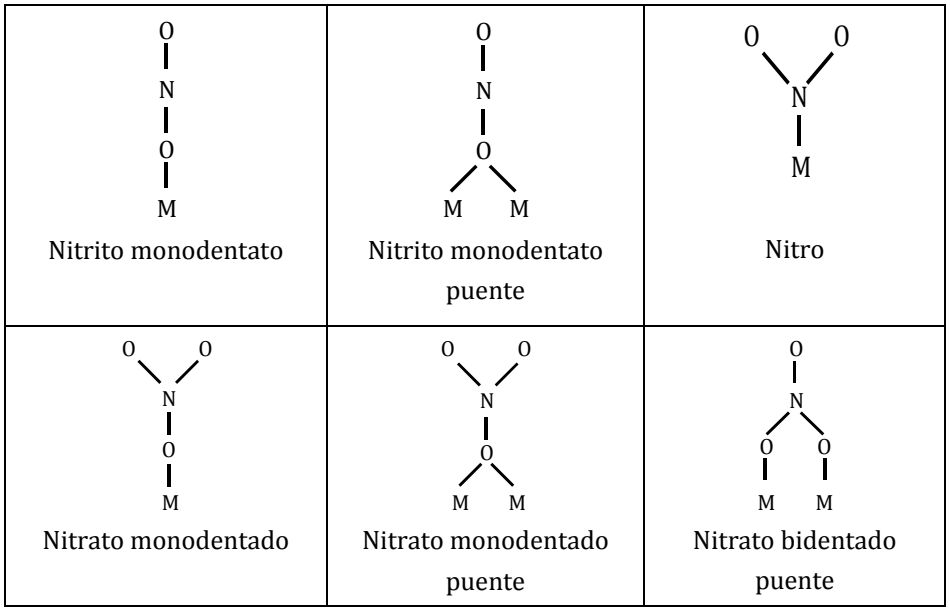

Figura 2.2. Posibles estructuras de las especies NO_2^- y NO_3^- adsorbidas sobre la superficie de óxidos metálicos.

1000 ppm de NO y 8% de O_2 y posteriormente 15 minutos de H_2 en argón. El caudal total utilizado para todos los experimentos fue de 100 ml min^{-1}. Durante los experimentos se introdujeron 1000 ppm de NO y 8% de O_2 para identificar las especies del periodo pobre y 1000 ppm de NO junto un agente reductor (1000 ppm de H_2 o 1000 ppm de CO o 1111 ppm de C_3H_6) para la identificación de las especies durante el periodo rico. Los espectros fueron registrados a 200, 300 y 400 °C.

En la Figura 2.2 se pueden observar algunas de las especies nitrito y nitrato identificadas durante el estudio.

2.3.5. Microscopía electrónica

La microscopía electrónica comprende un conjunto de técnicas que proporcionan información relativa a las propiedades texturales y estructurales y a la constitución química de los catalizadores, resultando una

importante herramienta de caracterización de los mismos [147, 148]. La principal ventaja reside en la posibilidad de enfocar el haz de electrones en áreas muy reducidas de la muestra y es una técnica ampliamente utilizada en el análisis del tamaño de partículas metálicas en catalizadores soportados [137].

2.3.5.1. Microscopía electrónica de barrido

La microscopía electrónica de barrido (SEM, Scanning Electron Microscopy), utiliza un haz de electrones de alta energía que barre la superficie de una muestra permitiendo la obtención de imágenes en dos dimensiones que proporcionan información sobre la morfología de la superficie de una muestra o la composición de la misma. Como fuente de electrones de alta energía se suelen utilizar filamentos de W o de LaF6, que producen la emisión de electrones por efecto termoiónico. Estos electrones son acelerados y dirigidos hacia la muestra por una serie de lentes electromagnéticas que tienen como finalidad la obtención de un haz de electrones lo más estrecho posible que sea capaz de hacer un barrido de la superficie de la muestra.

Cuando los electrones interaccionan con la muestra se producen distintos fenómenos que dan lugar a diferentes tipos de señales que pueden ser detectadas y analizadas en un microscopio electrónico de barrido. De entre estos tipos de señales, las más utilizadas en el microscopio son los electrones secundarios (sensibles a la morfología superficial de la muestra) y los electrones retrodispersados (sensibles a la composición de la muestra). Estos microscopios pueden incluir también un detector de energía dispersiva de rayos X (EDX) que permite analizar los rayos X emitidos por la muestra cuando se produce una transición electrónica entre dos niveles de un átomo después de interaccionar con el haz de electrones, señal que es característica de cada elemento de la muestra.

Procedimiento experimental

Las muestras se han analizado con un microscopio electrónico de barrido JEOL JSM-7000-F equipado con una fuente de emisión de campo tipo Schottky y un espectrómetro EDX Oxford Instruments Inca Energy 350. Se ha trabajado con un voltaje de aceleración de 20 kV y corrientes de haz en el entorno de 1nA. Se han obtenido varias imágenes de electrones retrodispersados y espectros EDX de cada una de las muestras que permite la identificación y el análisis elemental semicuantitativo de un área determinada de la muestra. En este caso, tanto la preparación de las muestras como la adquisición de las imágenes SEM se llevó a cabo en los Servicios Generales de Investigación SGIKER de la UPV/EHU.

Mediante la espectroscopía de barrido se estudió el espesor y la composición de los monolitos. Para ello los monolitos se introdujeron en una probeta de resina epoxi, se cortaron con una sierra de precisión (Buehler ISOMET 1000), se lijaron mediante discos de diamantes y con suspensiones de diamantes de varios tamaños la superficie se pulió. Finalmente, los monolitos se introdujeron en una suspensión de alúmina con tamaño de partícula de 0,05 μm. El pulido se llevó a cabo en una pulidora de Buehler Beta. Posteriormente, los monolitos fueron metalizados y observados mediante el microscopio.

Los catalizadores Cu/SAPO-34 analizados en el Capítulo 4 también se analizaron mediante SEM. Para ello, las muestras se depositaron sobre una cinta adhesiva conductora de carbono y se recubrieron por evaporación en vacío con una capa de 20 nm de carbono para hacerlas conductoras.

2.3.5.2. Microscopía electrónica de transmisión

La microscopía electrónica de transmisión (TEM, Transmission Electron Microscopy) proporciona información sobre propiedades texturales y estructurales. Esta técnica se basa en la irradiación de la muestra con un haz de electrones, los cuales son emitidos por un filamento y acelerados por una

diferencia de potencial. Los electrones se enfocan a través de unas lentes para formar un haz paralelo que incide sobre la muestra. Cuando los electrones atraviesan la muestra, éstos se dispersan y son enfocados con una lente de objetivo. A continuación, se amplifican con una lente y finalmente forman la imagen deseada. La principal ventaja reside en la posibilidad de enfocar el haz de electrones en áreas muy reducidas de la muestra.

El microscopio electrónico ofrece la posibilidad de realizar un microanálisis mediante la técnica EDX (EDX, Energy Dispersive X-ray Spectroscopy). Dicha técnica permite determinar la composición química de la muestra a través de los rayos X emitidos por los elementos que la componen.

Procedimiento experimental

El equipo utilizado para el estudio de las muestras ha sido un microscopio electrónico de transmisión Philips SuperTwin CM200 equipado con un filamento de LaB6 y sistema de microanálisis EDAX EDS. Los análisis se han llevado a cabo a 200 kV, en los Servicios Generales de Análisis de SGIKER de la UPV/EHU.

Para la correcta medición es necesaria una preparación previa de las muestras, que consiste en suspender en etanol una pequeña cantidad del catalizador en polvo y disgregarlo durante 15 minutos con la ayuda de un baño de ultrasonidos. Posteriormente, se han depositado unas gotas de esta suspensión en el portamuestras, que consiste en una rejilla circular de cobre (300 mesh) recubierta por una capa enrejada de carbón amorfo.

El microscopio utilizado en la Universidad Tecnológica de Chalmers para el estudio de las muestras Pt-Ba(-Ce)/Al_2O_3 ha sido el microscopio FEI Titan 80-300. Este microscopio tiene un monocromador de alta resolución EELS (0,11 eV de resolución) y un filtro de 866 GIF Tridiem de alta resolución. Las lentes del condensador tienen un corrector de aberración esférica que proporciona una resolución de 70 pm en imágenes STEM de alta resolución y permite una espectroscopía de alta resolución espacial. El microscopio tiene

un bi prisma para la holografía de electrones fuera del eje y una lente de Lorentz para holografía de baja magnificación y experimentos libres de campo magnético. La tomografía se puede llevar a cabo en modo TEM y STEM, incluido STEM anular de campo oscuro de ángulo alto.

2.3.6. Espectroscopía de reflectancia difusa ultravioleta-visible

Los iones y complejos de los metales de transición poseen la propiedad de absorber determinadas longitudes de onda del espectro electromagnético. En la región visible, ultravioleta e infrarrojo cercanos, las bandas de absorción de los espectros de iones y complejos de metales de transición son, con frecuencia, anchas y están enormemente influenciadas por los factores químicos del entorno. Los espectros de absorción de este tipo de radiación permiten obtener información sobre la estructura y el enlace de los compuestos.

La absorción de los metales de transición está originada por la excitación de un electrón de un orbital d del átomo metálico, que pasa del estado fundamental a un estado excitado. El espectro de absorción que presenta un compuesto depende del estado de oxidación del metal, del número y la clase de átomos o iones que se enlazan directamente a él y de la geometría de coordinación.

Procedimiento experimental

Para obtener los espectros de absorción de los catalizadores preparados en esta tesis doctoral se ha utilizado la espectroscopia DR UV-Vis, que permite medir espectros de absorción de muestras policristalinas. Un haz de radiación que incide sobre una superficie rugosa se ve reflejado difusamente. La radiación reflejada difusamente se detecta a través de una célula fotosensible, y por comparación con la intensidad de un patrón de referencia se obtiene el porcentaje de reflectancia.

Las medidas de espectroscopia DR UV-Vis se han realizado en los Servicios Generales de Investigación SGIKER de la UPV/EHU, en un

espectrofotómetro Cary 5000 de la marca Varian. Las muestras han sido deshidratadas en la estufa a 110 °C antes de ser analizadas. Los espectros se han registrado a temperatura ambiente en un intervalo de número de onda comprendido entre 200 y 2500 nm.

2.3.7. Espectroscopía de resonancia paramagnética electrónica

Esta técnica estudia las diferencias de energía debidas a la interacción de un electrón desapareado en una muestra bajo un campo magnético, B_0. Este efecto es el denominado efecto Zeeman. Por tanto, la posesión de un momento neto de espín electrónico es la única condición necesaria (y suficiente) que debe cumplir un material para poder ser estudiado por espectroscopia EPR. Son numerosos los sistemas que satisfacen esta condición, como radicales libres en estado sólido, líquido o gaseoso, la mayoría de los iones de transición y tierras raras o defectos en los cristales iónicos [149].

Debido a que el electrón desapareado tiene un momento magnético, se verá afectado cuando esté bajo un campo magnético, teniendo únicamente dos estados de energía permitidos. Por un lado, uno de baja energía cuando el momento del electrón, μ, esté alineado con el campo magnético, y por otro lado un estado de alta energía cuando μ esté alineado en contra del campo magnético (Figura 2.3). La diferencia entre las energías de estos dos estados, causada por la interacción del spin electrónico y el campo magnético viene dada por la Ecuación 2.7

$$\Delta E = g\mu_B B_0 \Delta m_s = g\mu_B B_0 \qquad (2.7)$$

donde g es el factor de Landé, μ_B es el magnetón de Bohr, que es la unidad natural del momento magnético intrínseco de un electrón, y Δm_S es la variación en el estado de spin (Δm_S=1 para transiciones permitidas).

Los estudios de EPR proporcionan información sobre la geometría del entorno de los iones paramagnéticos, así como sobre la existencia de posibles interacciones magnéticas entre los mismos.

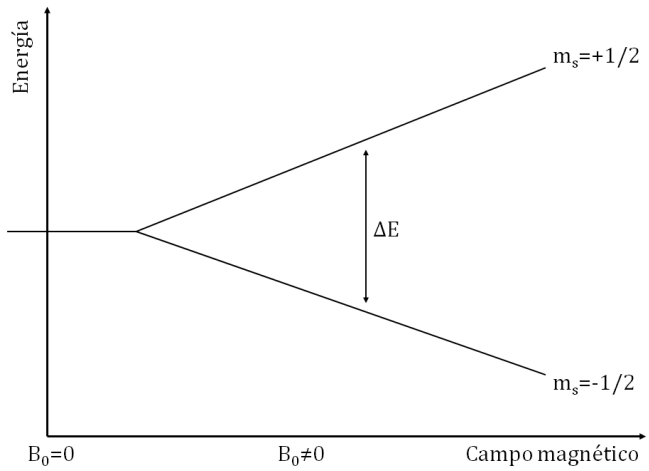

Figura 2.3. Divergencia de las energías de los dos estados de spin de un electrón desapareado al variar el campo magnético.

Procedimiento experimental

Los espectros de las muestras se han analizado en un espectrómetro Bruker ELEXSYS 500, equipado con una cavidad resonante de alta resolución ER-4123-SHQ, y operando en banda X. El campo magnético se ha calibrado con una probeta de RMN, y la frecuencia en el interior de la cavidad se ha determinado con un contador de microondas integrado. La temperatura se ha estabilizado con un regulador (ITC4) de la marca Oxford Instrument.

Los análisis de las muestras se han llevado a cabo en el departamento de Química Inorgánica de la Universidad del País Vasco.

2.3.8. Reducción a temperatura programada con H_2

La actividad de muchos catalizadores, y en especial la de los óxidos, está asociada a sus propiedades redox. En el caso de las reacciones de oxidación, la reducibilidad del óxido metálico está directamente relacionada con su capacidad de oxidación, ya que en las condiciones de reacción, el óxido

metálico se somete a reducción y reoxidación simultáneamente. El análisis de la reducibilidad de los catalizadores da información acerca del número y naturaleza de las especies reducibles presentes en una muestra, tanto cualitativa como cuantitativamente. Para el caso de los catalizadores soportados, también da información sobre la interacción de la especie reducible con el soporte [138, 139].

En un análisis TPR la muestra se reduce mediante un gas reductor, generalmente diluido, haciéndolo circular a través de un reactor tubular, en el que la muestra permanece en un lecho fijo. Se procede a un calentamiento de la muestra a velocidad constante, comenzando desde una temperatura inferior a la de reducción. El consumo de gas reductor se evalúa mediante la integración de las áreas de las curvas señal/tiempo obtenidas durante el análisis. En función de la reducibilidad de los componentes presentes en la muestra, se obtienen una serie de picos a unas determinadas temperaturas.

Procedimiento experimental

Los análisis TPR se han llevado a cabo en un equipo Micromeritics AutoChem II, provisto de un detector de conductividad térmica. La muestra (0,25 g) se coloca en un reactor de cuarzo en forma de U. En primer lugar, se introduce una corriente de helio (50 cm^3 min^{-1}) a temperatura ambiente, después se introduce la mezcla 5% H_2/Ar de 50 cm^3 min^{-1} y se aumenta la temperatura hasta 900 °C con una rampa de temperatura de 10 °C min^{-1}. Finalmente, se enfría la muestra hasta 30 °C bajo una corriente de Ar de 20 cm^3 min^{-1}.

2.3.9. Desorción de NH_3 a temperatura programada

La acidez superficial es una de las propiedades catalíticas más importante de los sólidos ácidos, ya que es la responsable de un elevado número de reacciones químicas de interés industrial, tales como la deshidrogenación de alcoholes, hidrogenación y polimerización de olefinas, craqueo de hidrocarburos, etc. La caracterización de la acidez se realiza básicamente

determinando la naturaleza de los centros ácidos (Brønsted/Lewis), su densidad y su fuerza, para lo cual existen diferentes métodos y técnicas. En esta tesis se han analizado los centros ácidos mediante desorción de amoniaco a temperatura programada (TPD, Temperature Programmed Desorption).

Un experimento estándar de TPD consiste en someter a una muestra colocada en un reactor, sobre la que previamente se ha adsorbido un gas activo, a una rampa de temperatura mientras se barre la muestra con un gas inerte [138, 139]. Con un flujo de gas portador adecuado, la respuesta del detector colocado a la salida del reactor será proporcional a la velocidad de desorción del adsorbato, siempre que la difusión o readsorción de los gases no sea limitante. De esta forma, se obtiene un perfil de cantidad desorbida en función de la temperatura, cuya forma está relacionada con el proceso de desorción, y proporciona información acerca de la interacción entre el compuesto activo y la muestra estudiada.

El adsorbato empleado dependerá de la propiedad de la muestra que se quiera estudiar. Así, para la evaluación de la acidez se pueden emplear varios adsorbatos que se adsorben exclusivamente sobre los centros ácidos de la muestra, como el amoniaco, la piridina, la n-butilamina o el benzonitrilo. De todos ellos, el amoniaco es uno de los compuestos más empleados debido a que es una molécula de carácter básico, de pequeño tamaño y que presenta una gran estabilidad térmica. Debido a su basicidad relativamente fuerte, el amoniaco se adsorbe sobre todos los centros ácidos, pero la temperatura a la que se desorbe depende de la fuerza ácida de estos centros. El TPD de NH_3 es una de las técnicas más empleadas en la medida de la acidez global de las zeolitas.

Procedimiento experimental

Los experimentos de TPD de NH_3 se han llevado a cabo en un equipo Micromeritics AutoChem II provisto de un detector de conductividad térmica (TCD thermal conductivity detector). La muestra (0,08 g) se coloca en un

reactor de cuarzo en forma de U, y es sometida al siguiente protocolo de análisis:

- Limpieza del catalizador bajo una corriente de N_2 de 50 cm^3 min^{-1} y una rampa de temperatura de 20 °C min^{-1} hasta 550 °C.
- Mantener 30 minutos a 550 °C y bajar la temperatura a 100 °C.
- La etapa de adsorción se realiza introduciendo amoniaco en helio (13 cm^3 min^{-1}) a 100 °C hasta saturación de la muestra.
- Con el fin de eliminar las moléculas de NH_3 fisisorbidas, se expone la muestra a una corriente de helio de 50 cm^3 min^{-1} durante 2 horas a 100 °C.
- Finalmente, la desorción del amoniaco quimisorbido en la muestra se realiza elevando la temperatura desde 100 a 550 °C con una rampa de calentamiento de 10 °C min^{-1} en una corriente de helio de 50 cm^3 min^{-1}. La muestra se mantiene a 550 °C durante 30 minutos para desorber completamente el amoniaco residual.

Durante estas dos últimas etapas, el detector TCD cuantifica la cantidad de amoniaco desorbido en cada instante del experimento, lo cual permite obtener un registro de amoniaco desorbido en función del tiempo y la temperatura.

2.3.10. Sistema de reacción

El estudio de la actividad y durabilidad de los catalizadores evaluados requiere la elección de un equipo adecuado que permita llevar a cabo las reacciones y seguir su evolución. El reactor debe permitir un buen control de las condiciones de operación y la obtención de resultados de actividad de forma repetitiva. Por su parte, el sistema de análisis debe permitir el seguimiento del curso de la reacción de manera fiable, repetitiva y lo más inmediata posible.

Se ha trabajado con dos reactores a escala de laboratorio que permiten trabajar en las condiciones de presión y temperatura necesarias para el desarrollo de las reacciones, y que consiguen que la alimentación llegue al lecho catalítico o monolito de forma estable y homogénea. Por otro lado, las características mecánicas y operativas del reactor evitan los gradientes de temperatura y permiten despreciar los controles de las etapas de transferencia de materia.

De este modo, los experimentos de reducción catalítica selectiva de NO_x (SCR), almacenamiento y reducción de NO_x (NSR) y los experimentos combinandos de ambos sistemas (NSR-SCR) se han realizado en el sistema de reacción disponible en los laboratorios del grupo TQSA en una bancada de reacción con control automatizado de las variable de proceso y diseñada para el tratamiento de corrientes de hasta 6 l min^{-1}. Por otro lado, los catalizadores NSR y SCR preparados en los laboratorios de la Universidad Tecnológica de Chalmers se han estudiado en un reactor horizontal de cuarzo.

2.3.10.1. Sistema de reacción de la Universidad Tecnológica de Chalmers

Los experimentos se realizaron en un reactor de flujo que consistía en un tubo de cuarzo horizontal con un cable calefactor aislado (Figura 2.4). La velocidad de flujo total utilizada en todos los experimentos fue de 1800 ml min^{-1} y se utilizó argón como gas portador. Todos los gases fueron introducidos por los controladores de flujo másico (MFC) y el sistema CEM de Bronkhorst se utilizó para controlar el flujo de agua. Se analizó la actividad de los catalizadores NSR y de los sistemas NSR-SCR. Se usaron dos termopares para medir y controlar la temperatura. Un termopar se colocó 10 mm delante del catalizador y el otro se colocó dentro del catalizador, a 60 mm de la parte final de los catalizadores NSR. Para la configuración NSR-SCR combinada, el catalizador SCR se colocó aguas abajo del NSR separado por 2 cm. En el caso de la configuración doble, se colocó un termopar dentro del catalizador SCR corriente abajo (es decir, en las muestras Cu/BETA o Cu/SAPO-34) y el otro termopar se colocó entre los dos monolitos (10 mm delante del monolito SCR).

La concentración de gas de salida se analizó mediante el FTIR MKS MultiGasTM 2030 HS y el espectrómetro de masas cuádruplo Hiden. Antes de cada experimento, las muestras frescas fueron estabilizadas a 600 °C durante 2 horas con una mezcla gaseosa de 400 ppm de NO, 8% de O_2, 5% de CO_2 y 5% de H_2O durante el período pobre y 400 ppm de NO, 5% de H_2O, 5 % de CO_2 y 1% de H_2 durante el período rico. Después de la estabilización, los monolitos fueron pretratados a 500 °C siguiendo las siguientes secuencias: a) introducción de 8% de O_2, 5% de H_2O y 5% de CO_2 durante 15 minutos; b) introducción de 5% de H_2O y 5% de CO_2 durante 5 min; c) introducción de 1% de H_2, 5% de H_2O y 5% de CO_2 durante 15 minutos; y d) introducción de 5% de H_2O y 5% de CO_2 durante 5 minutos. Se llevaron a cabo ciclos alternando alimentaciones pobres y ricas en combustible a 200 °C, 300 °C, 400 °C y 500 °C. La composición del gas del periodo pobre fue de 400 ppm de NO, 8% de O_2, 5% de CO_2 y 5% de H_2O y la del periodo rico de 400 ppm de NO, 1% de H_2, 5% de CO_2 y 5% de H_2O. Se realizaron cinco ciclos pobre/rico (240s/60s) para cada concentración y temperatura del agente reductor.

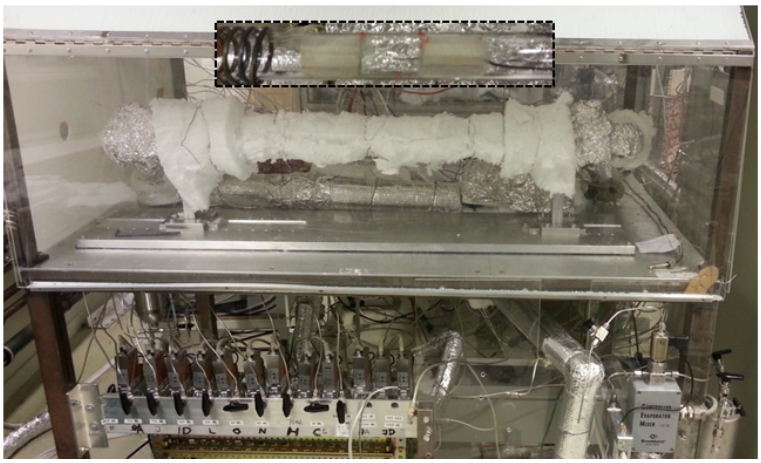

Figura 2.4. Imagen del sistema de reacción utilizado para los catalizadores NSR y SCR en la Universidad Tecnológica de Chalmers.

Se llevaron a cabo ciclos alternando alimentaciones pobres y ricas en combustible con el catalizador NSR y con la configuración NSR-SCR combinada alimentando diferentes reductores (H_2, CO, C_3H_6 y C_7H_8) con diferente concentración durante el período rico. Específicamente, el H_2 y CO fueron alimentados con las siguientes concentraciones: 0,1; 0,5 y 1%, mientras que la concentración correspondiente fue dividida por 9 y 18 en el caso de C_3H_6 y C_7H_8, respectivamente, para mantener constante la capacidad de reducción y para obtener resultados comparables entre diferentes reductores de acuerdo a la estequiometria de las siguientes reacciones (Reacciones 2.8-2.11):

$$H_2 + 1/2O_2 \rightarrow H_2O \quad (2.8)$$

$$CO + 1/2O_2 \rightarrow CO_2 \quad (2.9)$$

$$C_3H_6 + 9/2O_2 \rightarrow 3CO_2 + 3H_2O \quad (2.10)$$

$$C_7H_8 + 9O_2 \rightarrow 7CO_2 + 4H_2O \quad (2.11)$$

2.3.10.2. Sistema de reacción del grupo TQSA de la Universidad del País Vasco, UPV/EHU

La bancada de reacción ha sido construida bajo diseño propio en el grupo TQSA. El resultado es un equipo experimental que reduce al mínimo el tiempo necesario para alcanzar el estado estacionario y permite la rápida obtención de datos experimentales. En el equipamiento utilizado para la valoración experimental del comportamiento de los catalizadores monolíticos en mezclas complejas de reacción, se distinguen tres secciones: el sistema de alimentación, el sistema de reacción y el sistema de análisis.

Sistema de alimentación

El sistema de alimentación está diseñado con el objetivo principal de simular los gases de escape de los automóviles tanto en condiciones continuas, típicas del proceso SCR, como en condiciones cíclicas de operación, típicas de los procesos NSR y NSR-SCR.

El sistema de alimentación consta de 11 líneas por las que se pueden alimentar los siguientes gases: N_2, Ar, CO, CO_2, SO_2, C_3H_6, NO, O_2 y H_2. La alimentación correspondiente al CO y C_3H_6 se encuentra dividida en dos líneas; una para caudales elevados hasta 150 ml min^{-1} y otra para caudales más bajos de hasta 4 ml min^{-1}.

La Figura 2.5 muestra una imagen del sistema de alimentación con las 11 líneas de gases. Las seis primeras corresponden a gases que serán alimentados de forma continua al reactor, es decir, tanto en los experimentos SCR como durante el conjunto de los dos periodos de almacenamiento y reducción de NO_x. Las 5 líneas siguientes corresponden a gases que podrán ser alimentados

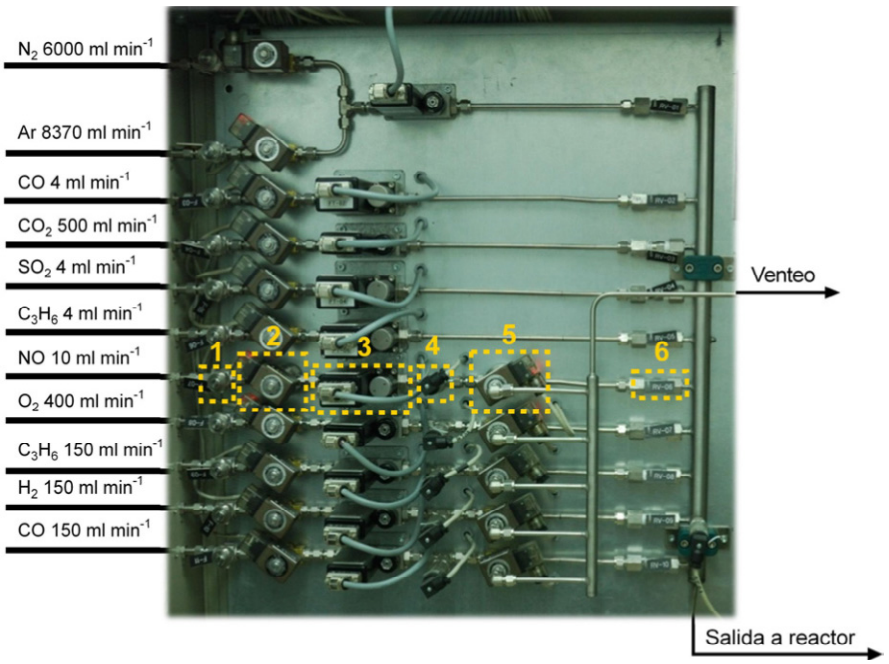

Figura 2.5. Sistema de alimentación utilizado para el control de la composición de las corrientes que simulan mezclas de escape pseudo-reales provenientes de motores de mezcla pobre, para su alimentación a los reactores de la bancada de reacción experimental de la Universidad del País Vasco.

de forma alternativa entre periodos. Nótese que las líneas de alimentación de oxígeno e hidrógeno se corresponden con estas últimas, para así poder simular condiciones oxidantes y reductoras durante los ciclos pobres y rico, respectivamente. Cada una de estas líneas de alimentación está compuesta por seis elementos que se han numerado en la Figura 2.5. A la entrada de cada línea, se ha colocado un filtro (1) para evitar la entrada de partículas al sistema de reacción y análisis. A continuación una electroválvula de dos vías Parker Lucifer (2) permite la entrada del gas al sistema, y el caudal se regula mediante controladores de flujo másico Brooks, MFC 5850 TR o Bronkhorst (3). Un transductor de presión Nuova Fima Bravo (4), con una presión máxima de medida de 1,5 bar, mide la presión de la línea antes de una electroválvula de tres vías, también de la marca Parker Lucifer (5), que dirige el flujo de gas al colector que conduce los gases al reactor o bien al colector de venteo. Por último, antes del colector de reacción, se ha colocado una válvula anti-retorno (6).

La acción de las electroválvulas de dos y tres vías, así como la del controlador de flujo másico se realiza a través de un PLC Siemens que permite el registro y control de más de 500 variables. El control de supervisión y adquisición de datos (SCADA) permite a través de un ordenador supervisar y controlar las distintas variables de proceso a distancia, proporcionando comunicación con los dispositivos del sistema (controladores autónomos) y controlando el proceso de forma automática mediante un software especializado, específicamente programado para la aplicación. Una de las pantallas de la interfaz se muestra en la Figura 2.6, indicando el estado de las válvulas, caudales y presión de las líneas. En la parte inferior izquierda también se controla y registra la temperatura en distintos puntos del horno de reacción y en el propio catalizador. El modo de operación varía en función de si se trabaja con la disposición NSR o NSR-SCR.

En caso de querer alimentar agua a la reacción, es necesario redireccionar la corriente hacia un evaporador-mezclador controlador CEM (Bronkhorst)

capaz de controlar la temperatura de evaporación y de homogeneizar la corriente gaseosa. Asimismo, todas las líneas de alimentación requieren ser calorifugadas para evitar condensaciones de agua no deseadas.

El modo de operación en un experimento típico NSR y NSR-SCR que alimenta Ar, O_2 y NO durante el periodo pobre y Ar, H_2 y NO durante el periodo rico es el siguiente. En primer lugar, se actúa sobre las válvulas de dos vías para permitir el paso de los gases que se requieren y se introduce el punto de consigna para el caudal requerido de cada uno de ellos. Durante el periodo de almacenamiento, llegará al colector de reacción el gas inerte, oxígeno y NO, mientras que el caudal de hidrógeno será venteado a través de la electroválvula de tres vías (5). Por el contrario, durante el periodo de reducción, la electroválvula situada en la línea del hidrógeno permitirá su paso

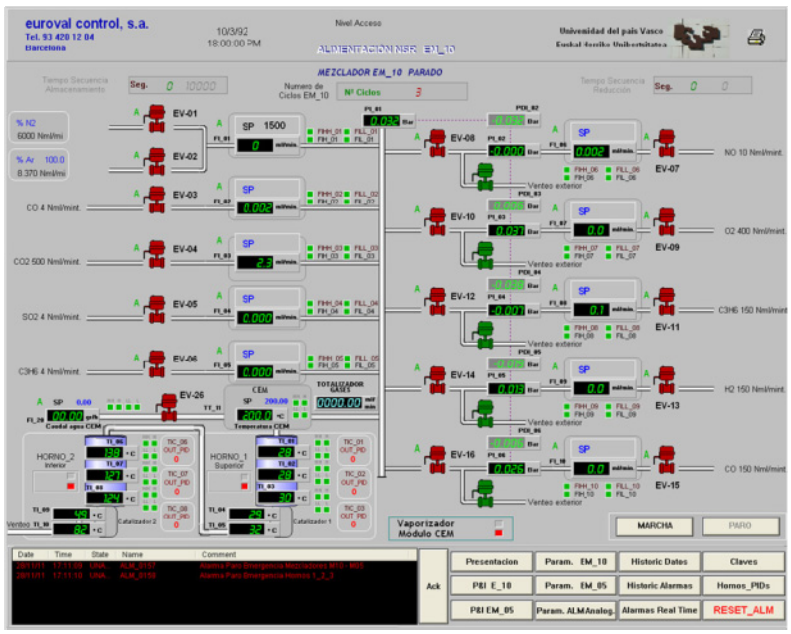

Figura 2.6. Interfaz del sistema de control (SCADA) de la bancada de reacción, gestionado a través de un controlador PLC Siemens.

al colector de reacción mientras que la electroválvula situada en la línea del oxígeno permutará para dirigir el gas a venteo. La línea del gas inerte se introduce al colector de reacción por la parte superior para que arrastre los gases introducidos con menor caudal y permita realizar una mezcla homogénea. Este doble sistema alimentación-venteo permite el equilibrio de presión entre las dos líneas, evitando saltos bruscos de presión y caudal en la alimentación al reactor.

Por otro lado, durante los experimentos SCR, dado que el funcionamiento se realiza en estado estacionario, la alimentación de NO, NH_3, O_2 y Ar se realiza de forma continua, sin necesidad de modificación alguna entre distintos periodos de operación.

Sistema de reacción

El equipo de reacción consta de dos líneas, con dos hornos donde se encuentran tres controladores de temperatura, dos reactores tubulares de acero inoxidable y una pieza en "T" pasante, para cada línea. Dado que se han realizado distintos tipos de experimentos, los experimentos de reacción requerirán el uso de 1 ó 2 líneas, en función de si se trata de experimentos únicos SCR o NSR o si se trata de experimentos combinados NSR-SCR. Además, en función de la estructura catalítica a utilizar (granulado o monolítico), se utilizarán diferentes tipos de reactores, según se detalla en los siguientes apartados. En general, ambas líneas consisten en un reactor tubular con circulación de gases en sentido descendente, constituido por cinco elementos: un horno, un tubo exterior, un tubo interior y dos chavetas de sujeción y centrado. La temperatura en diferentes zonas del reactor se controla a través del sistema SCADA (Figura 2.7).

i) Equipo de reacción para catalizadores granulados

Para estudiar los catalizadores granulados preparados, se utiliza un reactor tubular, asociable a comportamiento de flujo de pistón, por el que el

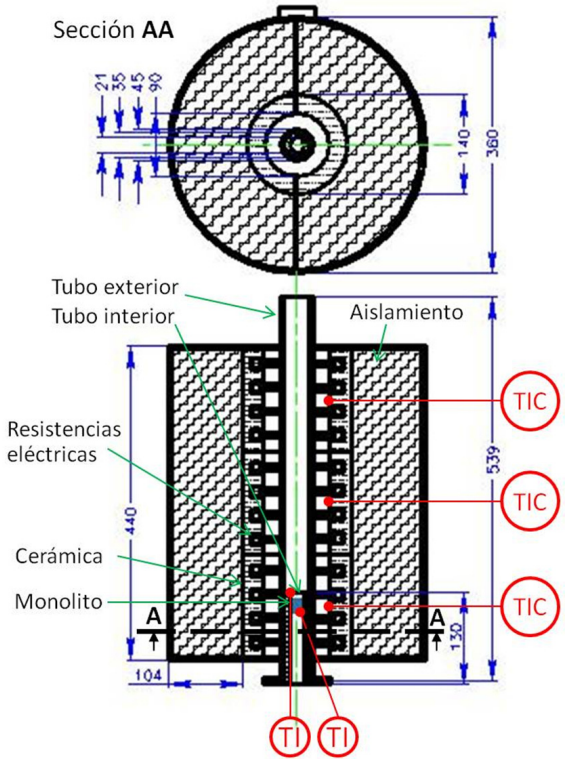

Figura 2.7. Vistas de planta y frontal de los hornos de reacción, con el reactor acogido en su interior. Distancias expresadas en milímetros.

flujo de gases circula de manera descendente y está compuesto por los siguientes elementos principales:

- Un horno de geometría cilíndrica, cuyas dimensiones son D_{ext} = 360 cm, D_{int} =140 mm, L = 440 mm y presenta 3 resistencias rodeadas de material aislante para el establecimiento de la temperatura de reacción deseada mediante el sistema de control SCADA. Además presenta un recubrimiento metálico para su protección. La temperatura de las tres zonas se controla a través del software de control, Figura 2.6.
- Tubo externo, en el cual se introduce posteriormente el tubo de reacción con las siguientes dimensiones: D_{ext} = 35 mm, D_{int} = 21 mm, L = 230 mm.

- Tubo de reacción con el catalizador granulado en su interior, de dimensiones D_{ext} = 21 mm, D_{int} = 13 mm y L=230 mm. Este tubo de reacción se fija por la parte inferior del sistema de reacción quedando la cámara de reacción herméticamente cerrada mediante el empleo de una serie de juntas y bridas.
- También se dispone de un termopar que proporciona en todo momento la temperatura en lecho catalítico.

ii) Equipo de reacción para catalizadores monolíticos

Para el análisis del comportamiento de los catalizadores monolíticos preparados se utiliza un reactor tubular, a través del cual los gases circulan de forma descendente. Los elementos que lo componen son los siguientes:

- Un horno cilíndrico de dimensiones D_{ext} = 360 mm, D_{int} = 140 mm y L = 440 mm. El horno consta de tres resistencias, encargadas de establecer la temperatura de reacción deseada mediante el sistema de control SCADA, rodeadas de material aislante y con un recubrimiento metálico para su protección.
- Un tubo externo de dimensiones D_{ext} = 45 mm, D_{int} = 35 mm y L = 130 mm, en el que se sitúa el tubo de reacción.
- Un tubo de reacción de dimensiones D_{ext} = 35 mm, D_{int} = 21 mm y L = 130 mm, en cuyo interior se sitúa el monolito. El tubo de reacción se fija por la parte inferior del sistema de reacción gracias al empleo de una serie de juntas y bridas, quedando la cámara de reacción herméticamente cerrada.
- Tres termopares, que permiten conocer en todo momento la temperatura de las tres zonas del horno: la zona superior, la zona intermedia y la zona inferior. Los termopares son de tipo K y en este caso la temperatura de las tres zonas también se controla a través del software de control, Figura 2.6.

- Un termopar, que mide continuamente la temperatura a la que se encuentra el monolito tanto a la entrada como a la salida, de forma que es posible conocer en todo momento la temperatura real de reacción.

Sistema de análisis en serie FTIR-QMS

Todos los elementos del sistema de análisis en serie FTIR-QMS se han montado en un armario, modelo Tempered de la casa RETEX. El sistema de análisis consta de un sistema de toma de muestra del analizador FTIR, el propio analizador FTIR, y un espectrómetro de masas situado a continuación del FTIR. Además, el FTIR dispone de una célula de ZrO_2 para el análisis de oxígeno, sirviendo esta señal para la equiparación de los tiempos entre los analizadores FTIR y QMS.

La medida de los gases se ha realizado mediante un analizador FTIR MultiGas Analyzer 2030 de la casa MKS, capaz de determinar la concentración de más de 30 gases simultáneamente (excepto especies homonucleares como el O_2, N_2 o H_2) desde 10 ppb hasta 100%, incluso con un contenido en vapor agua de hasta 30% en la corriente de gas a analizar.

Esta técnica se basa en que una molécula comienza a vibrar de uno o varios determinados modos cuando es expuesta a radiación correspondiente a la región del IR, absorbiendo esta radiación para ciertas longitudes de onda características. La representación de la intensidad de la radiación IR detectada en función del número de onda (cm^{-1}) se denomina espectro IR. Su análisis permite la caracterización química de la muestra, dado que cada compuesto presenta un espectro IR característico [150].

El espectrómetro MultiGas Analyzer 2030 emplea un intervalo de número de onda entre 400–5000 cm^{-1}, es decir, trabaja en la región del infrarrojo medio y posee una resolución espectral superior a 0,5 cm^{-1}. Como la mayoría de los instrumentos de infrarrojo de transformada de Fourier disponibles comercialmente se basa en el interferómetro de Michelson y utiliza la transformada de Fourier para el tratamiento de los datos [151]. El volumen de

la celda de análisis es de 200 ml y consta de unas ventanas de KBr y superficies ópticas (espejos) de aluminio niquelado con baño de oro donde la radiación infrarroja se refleja repetidamente hasta recorrer una longitud de 5,11 m. Para que el gas no condense en las paredes de la celdilla a temperatura ambiente, ésta es termoestatizada realizando así la medida del espectro infrarrojo a 190 °C.

Idealmente, la fuente de radiación infrarroja debe ser continua en un amplio intervalo de longitudes de onda y su intensidad no debe variar apreciablemente en ese intervalo. En este caso, se ha utilizado una fuente Globar que consiste en una varilla cilíndrica de carburo de silicio con electrodos de aluminio en los extremos, que se calienta eléctricamente y la temperatura de trabajo es de 1200 °C, ya que a partir de esta temperatura comienza a haber problemas de oxidación y pérdida de material. Por otro lado, el sistema de análisis utiliza un detector fotoconductor refrigerado de teluro de mercurio y cadmio (LN_2-cooled MCT).

El procedimiento más habitual para determinar la transmitancia o la absorbancia con un espectrómetro FTIR consiste, en primer lugar, en establecer el fondo de escala como referencia. Para ello se introduce en el equipo una corriente de nitrógeno para eliminar el agua y el CO_2 presente en el interior, ya que estos compuestos interfieren el espectro. Posteriormente, es necesario enfriar el detector MTC añadiendo nitrógeno líquido y así disminuir el nivel de ruido. Finalmente, se realiza la medida de la muestra. Se calcula la relación entre los datos espectrales de la muestra y referencia y se obtiene la transmitancia o absorbancia a distintas frecuencias.

Chapter 3

INFLUENCE OF Cu SPECIATION IN Cu/BETA ON DeNO$_x$ PERFORMANCE IN NH$_3$-SCR AND COMBINED NSR-SCR SYSTEMS

Chapter 3

INFLUENCE OF Cu SPECIATION IN Cu/BETA ON $DeNO_x$ PERFORMANCE IN NH_3-SCR AND COMBINED NSR-SCR SYSTEMS

ABSTRACT

NSR and SCR technologies are studied separately and combined in series and in dual-layer monoliths in this chapter. Cu/BETA catalysts are prepared starting from protonic or ammonic BEA zeolite following liquid ion exchange with copper. Alternatively, an intermediate ion exchange with Na ions is performed before copper ion exchange. Cu/BETA catalysts are extensively characterized by XRF, N_2 adsorption–desorption, FTIR of NO and CO adsorption, EPR, H_2-TPR, TEM and SEM in order to identify copper oxidation state (Cu^+ or Cu^{2+}) and copper species (agglomerated or Cu ions with different interaction with the support). Cu/BETA catalyst prepared from ammonic BETA zeolite with intermediate Na ion exchange followed by copper ion exchange results in the most active catalyst in the NH_3-SCR reaction, which is related to the coexistence of Cu^+ and Cu^{2+} ions and to a more accessible location of such ions in the zeolite matrix. This catalyst is washcoated onto a monolithic substrate with an optimum loading of 0.32 g cm^{-3}, in order to be placed downstream a NO_x storage and reduction (NSR) monolithic catalyst, prepared by washcoating Pt-Ba/Al_2O_3 powder with an optimum loading of 0.25 g cm^{-3}. NSR-SCR catalyst in sequential beds results in a very active system with a NO_x removal of 97% and a N_2 selectivity of 96% at 275 °C. NSR/SCR catalyst prepared in a unique dual-layer device shows that top SCR layer loading can be tuned in order to improve $DeNO_x$ performance. Optimum SCR layer loading is observed for 0.02 g cm^{-3}, enhancing the NO_x to N_2 efficiency of single NSR.

Capítulo 3

INFLUENCIA DE LA ESPECIACIÓN DE Cu EN CATALIZADORES Cu/BETA SOBRE EL COMPORTAMIENTO DeNO$_x$ EN NH$_3$-SCR Y SISTEMAS COMBINADOS NSR-SCR

RESUMEN

En el presente capítulo se han estudiado las tecnologías NSR y SCR por separado y la combinación de ambas en serie y en un solo monolito de doble capa. Para el estudio de la tecnología SCR se han preparado cuatro muestras Cu/BETA mediante el método de intercambio iónico en fase líquida. Las dos primeras muestras Cu/BETA se han preparado a partir de la zeolita BETA en estado protónico o amónico seguido de un intercambio iónico con cobre. Alternativamente, se han preparado otras dos muestras Cu/BETA con un intercambio intermedio con Na antes de realizar el intercambio con cobre. Los catalizadores Cu/BETA han sido caracterizados exhaustivamente mediante XRF, adsorción-desorcion de N_2, FTIR con adsorción de NO y CO, EPR, H_2-TPR, TEM y SEM para identificar el estado de oxidación del cobre y las especies de cobre. El catalizador Cu/BETA preparado mediante la zeolita BETA en estado amónico con intercambio iónico intermedio con Na y seguido del intercambio iónico con cobre resulta el catalizador más activo para la reacción NH_3-SCR. Esto se debe a la coexistencia de iones Cu^+ y Cu^{2+} y a la mayor accesibilidad de los iones en la matriz de la zeolita. El catalizador SCR también ha sido preparado en un monolito de cordierita con un espesor óptimo de 0,32 g cm^{-3}. Por otro lado, se ha optimizado el espesor de un catalizador modelo Pt-Ba/Al_2O_3 depositado sobre un monolito de cordierita, siendo el espesor óptimo 0,25 g cm^{-3}. Los catalizadores NSR y SCR preparados han sido analizados en serie y se ha observado que el sistema presenta buena actividad con una eliminación del 97% de NO_x y un 96% de selectividad a N_2 a 275 °C. Mediante el catalizador NSR/SCR en doble capa se ha observado que el espesor del catalizador SCR puede ser optimizado para mejorar la actividad. El espesor óptimo de la capa SCR es 0,02 g cm^{-3}.

3. INFLUENCE OF Cu SPECIATION IN Cu/BETA ON DeNO$_x$ PERFORMANCE IN NH$_3$-SCR AND COMBINED NSR-SCR SYSTEMS

The use of diesel engines and lean burn gasoline engines in vehicles application is increasing due to their higher fuel efficiency and lower CO_2 emissions compared to stoichiometric gasoline engines. However, the introduction of excess oxygen for fuel combustion produces an oxygen rich exhaust and makes NO_x reduction a challenging endeavor, because well-established three-way catalysts (TWC) are inefficient in such oxygen rich environment [105]. Two different approaches have been developed in order to mitigate NO_x emissions from diesel and lean burn engines, lean NO_x trap (LNT)—also denominated NO_x storage and reduction (NSR) catalysts— and selective catalytic reduction (SCR) catalysts [152].

Model NSR catalysts consist of a cordierite monolith washcoated with porous alumina on which an alkali or alkali-earth oxide (e.g. BaO) and a noble metal (Pt) are deposited. The NSR technology runs the engine under cyclic fuel lean and fuel rich conditions, producing net oxidizing and reducing environments, respectively. Usually, lean period duration is in the order of few minutes while rich period duration is few seconds. During the lean period NO_x are stored in barium sites in the form of nitrates and nitrites and during the rich period the stored NO_x are released and reduced to N_2, NH_3 and N_2O. One of the main drawbacks of the NSR technology is the emission of ammonia in the gas exhaust when using H_2 as reductant [153].

On the other hand, SCR technology runs the engine under continuous lean mode and needs an external source of reductant. Ammonia, obtained from the hydrolysis of urea, is used as reducing agent and is continuously added to the engine exhaust. Cu exchanged ZSM-5 was first reported to be an effective catalyst for NO_x reduction on lean exhaust [154]. Later, Cu^{2+} ion-exchanged BETA zeolite (Cu/BETA) was shown to have excellent activity in the SCR of

NO_x with NH_3 [79], and metal exchanged BEA zeolites are generally found to have greater hydrothermal stability than similar ZSM-5 catalysts [109].

Recently, a new approach has been proposed in order to mitigate NO_x emissions from diesel engines which combine NSR and SCR catalysts in consecutive reactors, firstly patented by researchers at Ford Motor Co. [155]. In the combined, sequential NSR-SCR technology, the limitation of NH_3 formation at the outlet of NSR catalyst is converted into an advantage. NH_3 is trapped or stored on acidic sites of the metal-exchanged zeolite and then is utilized to reduce NO_x that slips from the NSR during the subsequent lean period. The aim is to generate in the NSR as much NH_3 as needed to completely reduce NO_x, releasing to the atmosphere only innocuous compounds, such as nitrogen and water.

A dual-layer configuration is a potential alternative to the sequence of NSR-SCR monoliths. Nakatsuji et al. [116] from Honda proposed a catalyst system comprising a solid acid (Brønsted acid-based zeolite) on top of Pt/OSC (oxygen storage catalyst). While Honda's work provoked interest in this approach, it did not provide sufficient information about the catalyst or understanding of the fundamental work of the NSR-SCR dual-layer catalyst. The first fundamental study to provide insight and understanding of the dynamic performance of a dual-layer NSR-SCR was reported by Liu et al. [111, 117]. The dual-layer catalysts exhibited high N_2 selectivity and low NH_3 selectivity over the temperature range of 150–300 °C. In a dual-layer catalyst system the NSR and SCR catalysts are in intimate contact although the operating principle remains essentially the same as sequential NSR-SCR system. When the SCR layer is coated on top of the NSR layer, NO_x that diffuses into the SCR catalyst during the lean period may either react with NH_3 or diffuse to the underlying NSR layer where it is stored, and then may be reduced to N_2 or NH_3 during the next fuel-rich period [117]. These findings by Liu et al. [111, 117] were interpreted in terms of the individual performance features of the NSR and SCR systems. With coupled systems, since only a

fraction of the fed NO_x has to be reduced on the NSR, a fraction of the expensive NSR catalyst may be replaced by the less expensive SCR catalyst.

The objective of the current chapter is to gain insight and understanding on $DeNO_x$ performance features of NSR-SCR coupled systems in terms of the nature and distribution of Cu active species in the SCR catalyst, when two sequential monoliths and one dual-layer monolith are configured. We investigate the influence of Cu^{2+}, Cu^{+} and CuO species in the based-zeolite SCR catalyst by using different preparation procedures. Different loadings of the resultant most active SCR catalyst were washcoated on monoliths and the influence of the washcoat layer thickness on the $DeNO_x$ performance was studied. Also the NSR catalyst washcoat layer thickness was varied, and the NO_x removal and $N_2/NH_3/N_2O$ selectivities achieved with coupled NSR-SCR are compared for the sequential doubled monoliths and the single dual-layer monolith.

3.1. Cu/BETA CATALYST CHARACTERIZATION

3.1.1. Composition and textural properties

As described in the experimental section, four Cu/BETA samples were prepared following different preparation procedures to be tested in the NH_3-SCR reaction. Table 3.1 resumes the principal physicochemical properties of

Table 3.1. Physico-chemical properties of the prepared catalyst.

Sample	Cu wt., %	Na wt., %	Si/Al	Cu/Al	Cu ion exchange efficiency, %	Surface area, $m^2\ g^{-1}$
H/Cu	2.6	-	12.1	0.39	65	519
NH_4/Cu	3.2	-	12.0	0.49	80	516
NH_4/Na/Cu	3.4	0.27	11.8	0.51	85	511
H/Na/Cu	3.3	0.30	11.9	0.50	82.5	508

the prepared samples. The sample prepared by Cu ion exchange over protonic BETA zeolite (H/Cu) presented a Cu loading of 2.6 wt.%, as determined by XRF, which means that 65% of the initial Cu present in solution was incorporated to the zeolite structure leading to a Cu/Al ratio of 0.39. Performing the same ion exchange procedure over an ammonic BETA zeolite (NH_4/Cu) a slightly higher Cu loading (3.2 wt.%) was obtained, and thus, the ion exchange efficiency increased to 80% with a Cu/Al ratio of 0.49. Finally, it is worth to note that irrespective of the initial state of the zeolite support (i.e. ammonic or protonic), if an intermediate ion exchange with Na^+ ions is performed over the bare zeolite, the following ion exchange with Cu^{2+} is performed with higher efficiency. The resulting sample, i.e. NH_4/Na/Cu and H/Na/Cu, presented a Cu loading of 3.4% and 3.3%, which results in an exchange efficiency of 85% (Cu/Al = 0.51) and 82.5% (Cu/Al = 0.50), respectively. Cu/Al ratios around 0.5 are representative of fully exchanged zeolites, considering that copper exchange as Cu^{2+} occurs over two neighbor Al^{3+} pairs. On the other hand, the samples prepared by intermediate ion exchange of Na^+ ions presented a final Na content of 0.27 and 0.30% for NH_4/Na/Cu and H/Na/Cu catalysts, respectively, while the presence of Na was not detected for H/Cu and NH_4/Cu catalysts.

The surface area of the bare BETA zeolite resulted in 530 $m^2\ g^{-1}$ which decreased to 520–510 $m^2\ g^{-1}$ due to the incorporation of copper. The surface area decrease (≈20 $m^2\ g^{-1}$) can be considered low and indicates that copper has been preferentially incorporated as copper ions instead of copper aggregates, because for the latter a greater surface area decrease would has been expected due to pore blockage [118, 156].

3.1.2. Cu^{2+} and Cu^+ ions identification by FTIR

FTIR adsorption experiments of probe molecules is considered as one of the most commonly used characterization techniques for Cu/zeolites [116]; in fact, NO molecule is traditionally used to probe the oxidation state of copper cations in zeolites, due to its ability to form stable nitrosyl adducts with both

Cu^{2+} and Cu^{+} cations [157]. Figure 3.1 shows the FT-IR spectra of the prepared catalysts when submitted to a feed stream composed of 40 ppm of NO and 30 ppm of NO_2 balanced with 500 ml min^{-1} N_2. The interaction of NO and NO_2 with Cu^{2+} and Cu^{+} cations led to the formation of several absorption bands at different wavenumbers. Three IR features were common for all prepared samples: 1622 cm^{-1} with a shoulder at 1631 cm^{-1} and 1600 cm^{-1}, ascribed to NO_2 adsorbed on Cu^{2+} [158-160], 1575 cm^{-1} which is due to the formation of superficial nitrates [160, 161] and 1908 cm^{-1} which is due to the interaction

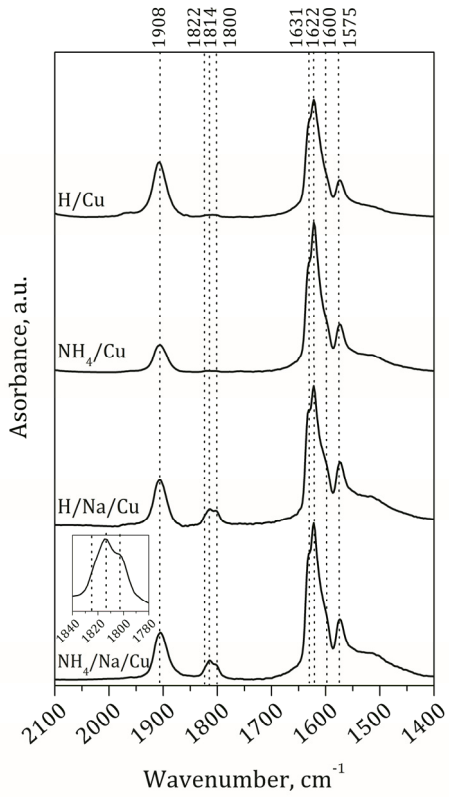

Figure 3.1. FTIR spectra of Cu/BETA samples after exposure to 40 ppm NO and 30 ppm NO_2 using N_2 as balance gas with a total flow rate of 500 ml min^{-1} at room temperature for 30 minutes.

between NO and isolated Cu^{2+} ions having a square pyramidal configuration [159]. Interestingly, only Cu/BETA samples prepared by intermediate ion exchange of Na^+, i.e. NH_4/Na/Cu and H/Na/Cu, presented an IR feature at 1814 cm^{-1} with two shoulders at 1803 and 1823 cm^{-1}, which is attributed to Cu^+-NO species. Thus, the preparation procedure affects notably the relative abundance of Cu^+/Cu^{2+} ions over the zeolite support. Copper ion exchange over (H^+) or (NH_4^+) BETA zeolite resulted in Cu/BETA samples in which almost all copper remained as Cu^{2+}. On the other hand, an intermediate ion exchange with Na^+ ions led to a sample in which Cu^+ and Cu^{2+} ions coexist. Furthermore, the presence of 3 different contributions for Cu^+-NO (inset of Figure 3.1) and Cu^{2+}-NO_2 interactions suggest the presence of different types of exchanged Cu species.

In order to gain insight into the reduction process of Cu ions, additional CO and NO adsorption experiments were carried out. The sample was in situ reduced in a 5% H_2/N_2 stream with a total flow of 500 ml min^{-1} at different temperatures (200–500 °C, 50 °C stepwise) and afterwards NO or CO was dosed at room temperature. Figure 3.2a shows the FTIR spectra obtained for the NH_4/Na/Cu sample after being exposed for 15 min to a feed stream composed of 470 ppm of NO and N_2. As previously explained in Figure 3.1, four principal absorption peaks were detected at 1908 cm^{-1} (Cu^{2+}-NO), 1814 cm^{-1} (Cu^+-NO), 1622 cm^{-1} (Cu^{2+}-NO_2) and 1575 cm^{-1} (nitrates). Note that the absorption intensity due to Cu^{2+}-NO_2 interaction (1622 cm^{-1}) and due to the presence of nitrates (1575 cm^{-1}) is considerably lower compared to that observed in Figure 3.1. Although NO_2 has not been fed to the reactor in these experiments, this component is a common impurity of pure NO and thus the introduction of few ppm of NO_2 cannot be disregarded, giving way to the appearance of weak absorption bands due to Cu^{2+}-NO_2 and nitrates. Intermediate reduction step below 350 °C did not alter the absorption spectra, which means that Cu^{2+} and Cu^+ ions remain unaltered (not reduced). On the other hand, the reduction step at 400 °C decreased the area below the IR feature located at 1908 cm^{-1} and 1814 cm^{-1}. Thus, above 400 °C the reduction

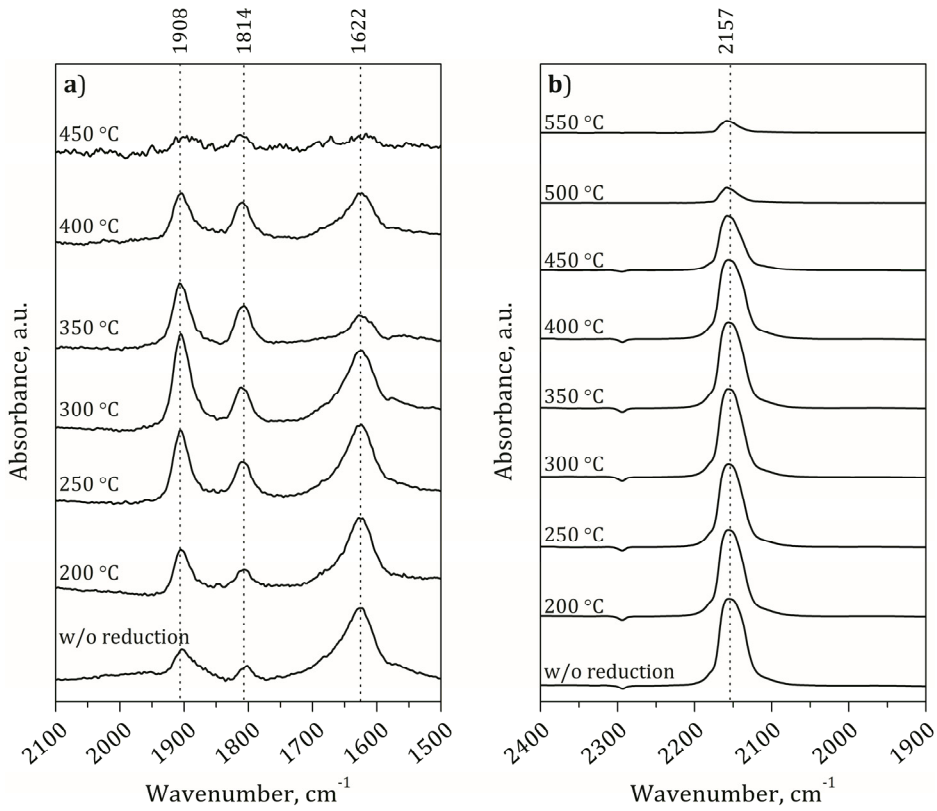

Figure 3.2. FTIR spectra of NH_4/Na/Cu sample after NO (a) and CO (b) adsorption at room temperature. Intermediate reduction steps (5% H_2/N_2) at different temperature levels have been performed between NO and CO adsorption experiments at room temperature.

of Cu^{2+} and Cu^{+} ions to Cu^{0} occurs. Finally, reduction temperature of 450 °C dramatically decreased the intensity of both Cu^{2+} and Cu^{+} interacting with NO. It is known that at room temperature NO is reactive and therefore does not act solely as a probe during FTIR analysis [161]. Consequently, similar experiments were carried out but dosing 390 ppm of CO instead of NO (Figure 3.2b), which only permitted us to follow the Cu^{+}-CO interaction, as Cu^{2+}-CO complexes are very unstable and difficult to detect [157]. The conclusion arisen from those experiments is in line with NO adsorption experiments, i.e.

the signal intensity of Cu^{+}-CO (2157 cm^{-1}) interaction remained unaltered until 350 °C and afterwards decreasing intensities were detected as increasing reduction temperature, which again evidences that reduction of Cu^{+} ions occurred at high temperature (T>400 °C).

3.1.3. Cu^{2+} ions identification by EPR

EPR analysis (electron paramagnetic spectroscopy) is an excellent technique for quantitatively identifying the amount of isolated Cu^{2+} ions [157, 162, 163], as other copper species, i.e. copper aggregates or Cu^{+} ions, are EPR silent [164]. Figure 3.3 shows the EPR spectra of the prepared samples at room temperature, and the inset figure the corresponding analysis of NH_4/Cu sample at low temperature (4 K). The signal intensity of collected spectra confirmed the presence of isolated Cu^{2+} ions for all prepared samples. Furthermore, all samples presented two contributions to the negative peak at high field. This feature is attributed to a significant fraction of copper being

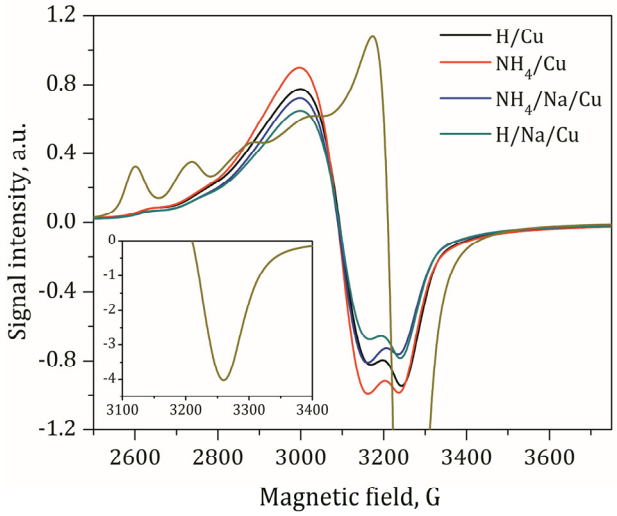

Figure 3.3. EPR spectra of prepared Cu/BETA samples at room temperature and low temperature (4 K) EPR spectra for NH_4/Cu sample.

able to detach from the framework and obtain full rotational freedom when H_2O is adsorbed on the sample [157]. In our experiments, samples were exposed to air at room temperature before EPR analysis, and thus water adsorption is very likely, giving way to the appearance of aforementioned two contributions. In order to decrease Cu^{2+} ions mobility additional EPR measurements were performed at low temperature (4 K). Those analysis revealed only a single contribution at high field for all catalysts, and in the low field region, hyperfine structures are much better resolved, unequivocally confirming the presence of Cu^{2+} ions. Although three different types of copper ions were detected by FTIR (Figure 3.2), in the fully hydrated samples, only a single hyperfine structure is found by EPR. Previous studies pointed out that EPR is unable to differentiate hydrated Cu^{2+} ions at different locations [79].

The total Cu^{2+} signal intensity was calculated as the double integral of the EPR signal at room temperature. The following trend was observed for Cu^{2+} signal intensity in the prepared samples: NH_4/Cu > H/Cu > NH_4/Na/Cu > H/Na/Cu. The loss of the EPR signal can be attributed to the presence of CuO aggregates or Cu^{+} ions, both EPR silent as already reported. As it will be shown later, the quantity of CuO aggregates (quantified by H_2-TPR experiments) is roughly the same for all catalysts and thus EPR signal decrease can be assigned solely to the presence of Cu^{+} ions. Note that FTIR experiments did not reveal the presence of Cu^{+} ions for H/Cu and NH_4/Cu and thus all copper ions present in those catalysts are Cu^{2+} and the lower intensity observed for H/Cu catalyst is due to the lower copper loading. On the other hand, considering that copper loading is almost the same for the rest of the prepared samples, comparison of the double integral of the EPR signal of NH_4/Na/Cu and H/Na/Cu samples with respect to NH_4/Cu, permitted us to quantify a signal decrease of around 20% for samples prepared by intermediate ion exchange of Na, which was attributed to the presence of Cu^{+} ions, in line with FTIR results.

3.1.4. Redox properties and copper particle size

Figure 3.4 shows the evolution of H_2 consumption during temperature programmed reduction experiments. Two H_2 consumption peaks were observed for all catalysts, i.e. low temperature and high temperature reduction peaks. There is no agreement in literature for the assignment of those peaks. Some authors [79, 164-166] claimed that the low temperature peak is due to the reduction of Cu^{2+} to Cu^{+}, at intermediate temperature the reduction of Cu_xO_y clusters occurs, while at high temperature the reduction of Cu^{+} to Cu^{0} takes place. On the other hand, some other authors [167-169]

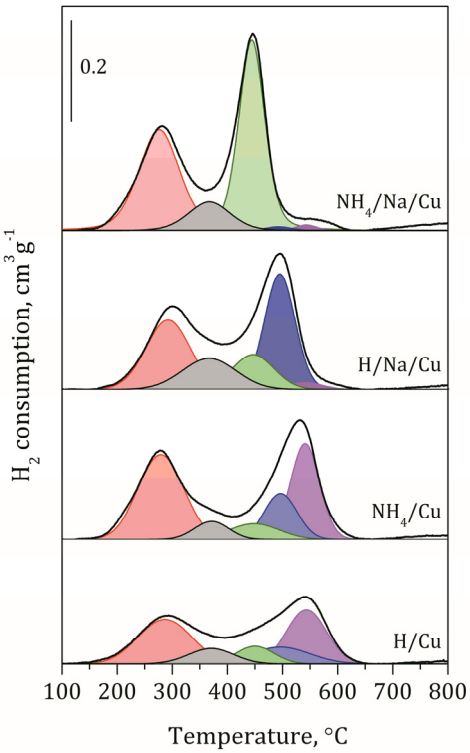

Figure 3.4. H_2 consumption profile during temperature programmed reduction experiment carried out in 5% H_2/Ar with a temperature ramp of 10 °C min^{-1}.

believed that low temperature H_2 consumption corresponds to the reduction of CuO aggregates while Cu^{2+} ions reduction occur at higher temperature.

Taking into account the reduction behavior of Cu^{+} and Cu^{2+} ions studied by FTIR, the high temperature reduction peak has been assigned to the reduction of Cu ions. On the other hand, considering that reduction of pure nanosized CuO takes place around 260 °C [167], it seems reasonable to assign the low temperature H_2 consumption peak to the reduction of CuO particles. Thus, the H_2 consumption profile shown in Figure 3.4 has been deconvoluted in 5 different contributions located at 280, 365, 450, 495 and 545 °C and assigned to reduction of external CuO clusters, CuO clusters located in the zeolite channels, and three different copper ions, respectively, attending to the three different contributions observed by FTIR, with reduction temperatures above 400 °C (Figure 3.2). These different Cu ions contributions are probably due to Cu^{2+}/Cu^{+} located at different exchangeable positions of the zeolite framework, or could probably be the result of different coordination environments of Cu ions, i.e. octahedral, square bipyramidal and distorted elongated bipyramidal, as previous works have already suggested [157, 170]. Stronger interaction with zeolite framework, and thus, higher reduction temperature is expected from octahedral to square bipyramidal and distorted elongated bipyramidal configuration, with reduction temperatures tentatively assigned at 450, 495 and 545 °C, respectively.

The integration of deconvoluted H_2 consumption peaks permitted us to quantify the amount of each species in the prepared samples (Table 3.2). The amount of CuO aggregates, which comprises CuO external clusters and intrachannel nanosized CuO particles with reduction peaks located at 280 and 365 °C, respectively, was similar for all samples, accounting for around 45% of the total H_2 consumption. On the contrary, the amount of different types of Cu ions changed radically among the prepared samples. NH_4/Na/Cu sample presented almost total Cu ions of type (I), which are the most easily reducible ions (450 °C), while the contribution of copper ions of type (II) and (III) was

Table 3.2. Quantification of Cu species in the prepared samples.

Sample	Cu species, %				
	CuO clusters	CuO nanoparticles	Cu ions (I)	Cu ions (II)	Cu ions (III)
H/Cu	30	11	14	10	35
NH_4/Cu	30	16	8	6	40
NH_4/Na/Cu	39	11	48	1	1
H/Na/Cu	30	16	14	38	2

almost negligible. The most abundant copper ions for H/Na/Cu sample was type (II) with a reduction temperature of 495 °C, while type (III) was mayor for H/Cu and NH_4/Cu, with the highest reduction temperature (545 °C). Previous studies [171, 172] have also observed lower reduction temperature

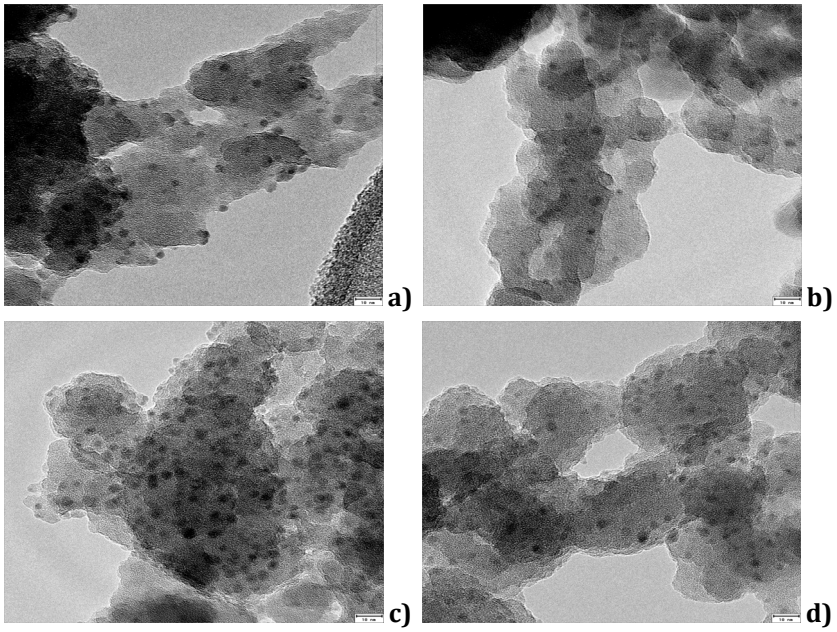

Figure 3.5. TEM images of a) H/Cu, b) NH_4/Na/Cu, c) NH_4/Na/Cu and d) H/Na/Cu catalysts.

of Cu ions in the presence of Na as cocation, which was attributed to the inhibition effect of copper reduction caused by the acidic sites when H^+ is the counter cation or to a different location of copper ions. Considering that Cu ions reduction temperature is lower for NH_4/Na/Cu with respect to H/Na/Cu (Figure 3.4) and that the Na content in both samples is similar or even slightly higher for the latter (Table 3.1), we are assuming that copper location is also playing a significant role in the reduction temperature of Cu ions.

Figure 3.5 shows TEM images obtained for all Cu/BETA samples in which external CuO cluster are visible with a mean size of 5 nm. Figure 3.5 confirms that all catalysts presented similar CuO clusters, as already discussed from H_2-TPR results.

3.2. NH_3-SCR PERFORMANCE OF Cu/BETA CATALYSTS

3.2.1. Granulated samples

Figure 3.6 illustrates the SCR activity of four Cu/BETA prepared samples, including the NO and NH_3 conversion and product selectivity (N_2, N_2O and NO_2) with increasing temperature. The NO and NH_3 conversion and product selectivities were calculated by Equations 3.1-3.5.

$$X_{NO}(\%) = \frac{F_{NO}^{in} - F_{NO}^{out}}{F_{NO}^{in}} \times 100 \quad (3.1)$$

$$X_{NH_3}(\%) = \frac{F_{NH_3}^{in} - F_{NH_3}^{out}}{F_{NH_3}^{in}} \times 100 \quad (3.2)$$

$$S_{NO_2}(\%) = \frac{F_{NO_2}^{out}}{F_{NO}^{in} X_{NO} + F_{NH_3}^{in} X_{NH_3}} \times 100 \quad (3.3)$$

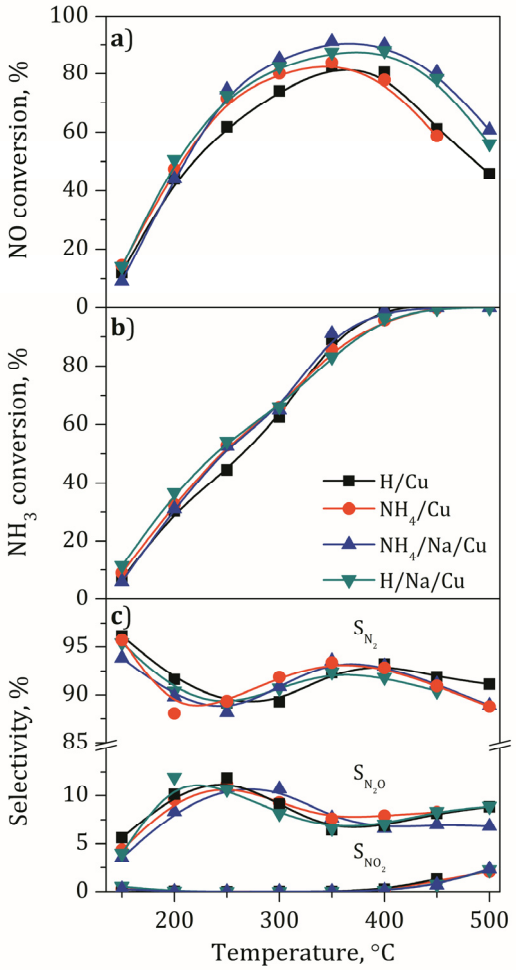

Figure 3.6. NO and NH_3 conversion and selectivity to N_2, N_2O and NO_2 as a function of the reaction temperature for the prepared Cu/BETA powder catalysts during NH_3-SCR reactions. Feed stream: 660 ppm NO, 660 ppm NH_3, and 6% O_2 using Ar as balance gas with a total flow rate of 2600 ml min^{-1}. *GHSV*= 86,500 h^{-1}.

$$S_{N_2O}(\%) = \frac{2F_{N_2O}^{out}}{F_{NO}^{in}X_{NO} + F_{NH_3}^{in}X_{NH_3}} \times 100 \quad (3.4)$$

$$S_{N_2}(\%) = \frac{2F_{N_2}^{out}}{F_{NO}^{in}X_{NO} + F_{NH_3}^{in}X_{NH_3}} \times 100 \quad (3.5)$$

As can be observed in Figure 3.6, among the prepared catalysts, H/Cu achieved the lowest activity for NO reduction, i.e. 81%, with a temperature window for conversion higher than 80% of 45 °C (340–380 °C). NH_4/Cu sample achieved a slightly higher NO conversion (83%) and a temperature window of 75 °C (305–380 °C). Note that no significant differences were observed in the physicochemical properties of both samples, absence of Cu^+ (FTIR of NO) and similar type of Cu^{2+} ions (H_2-TPR), and thus, the higher activity of NH_4/Cu sample was only related to the higher Cu loading (3.2%) with respect to H/Cu (2.6%). NH_4/Na/Cu sample was the most active for NO reduction (90%) with a temperature window of 170 °C (280–450 °C). Two reasons seem to be affecting the superior activity of this catalyst [118]. On the one hand, the coexistence of Cu^+ and Cu^{2+} improves the redox properties of the sample which has been found to be closely related with the SCR activity. This has been observed by Corma et al. [158] and by Sultana et al. [171]. On the other hand, the reduction temperature of Cu ions (Figure 3.4) was comparably lower for this sample which can be related to more accessible copper ions. Finally, the maximum NO reduction activity for H/Na/Cu sample was 87% with a temperature window of 150 °C (290–440 °C), which results slightly lower SCR activity than that observed for NH_4/Na/Cu. Although the Cu^{2+}/Cu^+ ratio was the same for both catalysts as determined by EPR, the reduction of copper ions in H/Na/Cu was obtained at higher temperatures, suggesting less accessible copper sites which results in a lower SCR activity.

Thus, the best SCR performance was obtained with NH_4/Na/Cu sample which was prepared by first ion exchanging Na^+ over ammonic BETA zeolite and subsequent ion exchange with Cu. The coexistence of Cu^{2+} and Cu^+ and

easily reducible copper ions (accessible location) led to a highly active SCR sample.

3.2.2. Monolithic samples. Determination of the optimal washcoat thickness

Figure 3.7 shows NO and NH_3 conversion and selectivity to N_2, N_2O and NO_2 for different loadings (from 0.07 to 0.32 g cm^{-3}) of NH_4/Na/Cu sample washcoated onto a monolithic substrate. As it can be observed, washcoat loading has a remarkable impact in the $DeNO_x$ performance. Low loaded catalyst (0.07 g cm^{-3}), achieved a poor maximum conversion of 55% and also high N_2O selectivity of 50% at 250 °C.

The monolithic catalysts with washcoat loadings of 0.14 and 0.27 g cm^{-3} presented a better SCR activity. These two catalysts achieved NO conversion of 61 and 70 % and N_2O selectivity of 45 and 21%, respectively at 250 °C. The washcoat loading also improves the selectivity to N_2 which accounts for 55% and 79% for loadings of 0.14 g cm^{-3} and 0.27 g cm^{-3}, respectively. In all the monoliths it is observed that when the temperature is increased the NO conversion decreased abruptly, being even negative for temperatures higher than 300 °C. Above that temperature, total NH_3 conversion is obtained (Figure 3.7b) and oxidation reactions start to prevail over SCR reactions and thus, at such conditions it makes sense to define the selectivity to NO (Equation 3.6) because rather than a reactive it becomes a product of the oxidation of ammonia.

$$S_{NO}(\%) = \frac{F_{NO}^{out} - F_{NO}^{in}}{F_{NO}^{in} X_{NO} + F_{NH_3}^{in} X_{NH_3}} \times 100 \qquad (3.6)$$

Clearly it can be observed that at high temperature NH_3 reacts with oxygen to form preferably NO rather than NO_2, which reaches a selectivity of 80%. The best NH_3-SCR behaviour among prepared monolithic catalyst was observed for 0.32 g cm^{-3} loaded catalyst, which corresponds to a washcoat

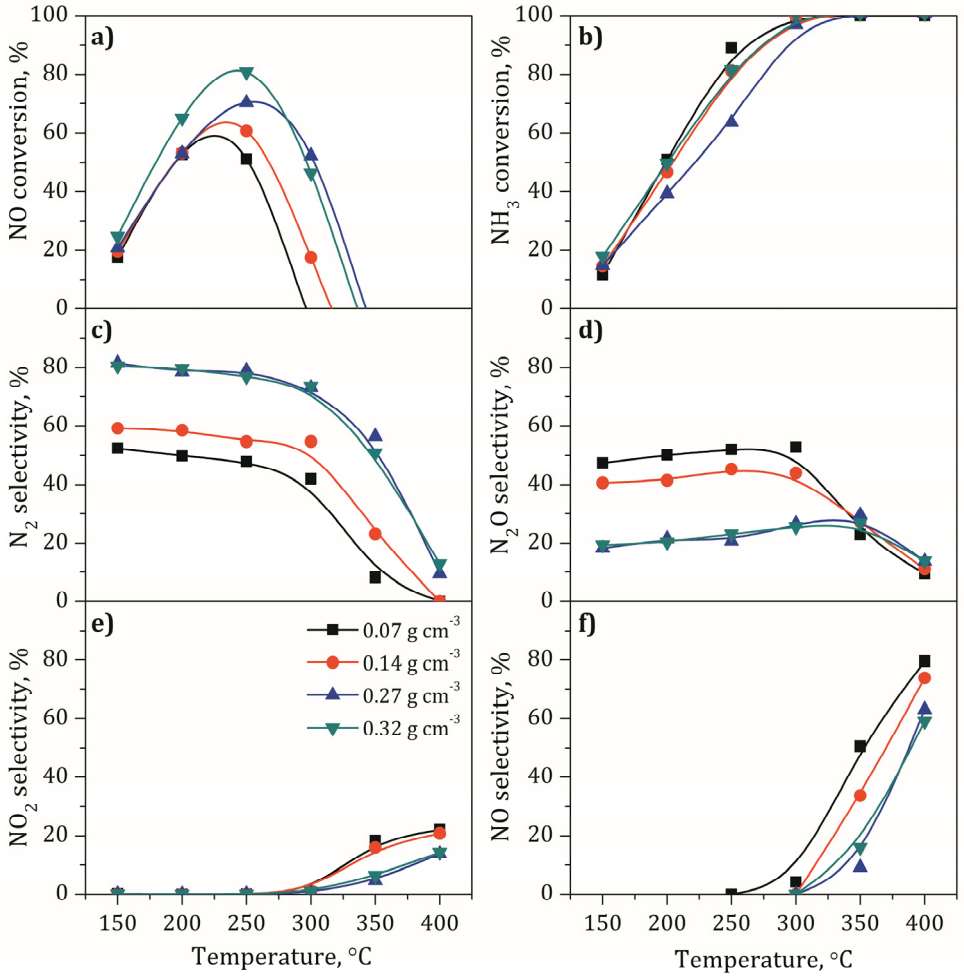

Figure 3.7. NO and NH_3 conversion and selectivity to N_2, N_2O, NO and NO_2 as a function of the reaction temperature for NH_4/Na/Cu catalyst washcoated onto monolithic substrates with different loadings (from 0.07 to 0.32 g cm $^{-3}$) onto a monolithic substrate during NH_3-SCR reaction. Feed stream: 660 ppm NO, 660 ppm NH_3, 6% and O_2 using Ar as balance gas with a total flow rate of 2600 ml min^{-1}. *GHSV*= 36,000 h^{-1}.

thickness of 70 μm. This catalyst achieved maximum NO conversion of 80% at 250 °C with a nitrogen selectivity of 80%. Although this catalyst presented better high temperature performance than the rest, its activity was markedly reduced with increasing temperature above 300 °C due to the enhancement of oxidation reactions as previously discussed.

3.3. DETERMINATION OF THE OPTIMAL Pt-Ba/Al_2O_3 WASHCOAT THICKNESS ON MONOLITHIC NSR CATALYST

Six bare cordierite monoliths were washcoated with increasing amounts of Pt-Ba/Al_2O_3, leading to catalyst loadings within the range 0.07–0.35 g cm^{-3}. Figure 3.8a shows the NO_x storage and reduction behaviour of the prepared monoliths during two consecutive storage and reduction cycles at 350 °C. During the lean period, the NO entering the reactor is oxidized to NO_2 by platinum sites which favors NO_x storage on barium sites as nitrates and nitrites [24, 30, 173]. As increasing lean period time, NO_x storage sites become progressively saturated and thus, NO concentration at the reactor outlet increased. The saturation of barium sites was much more evident for monoliths with low catalyst loading, i.e. 0.07 g cm^{-3}, leading to a NO_x outlet concentration above 400 ppm at the end of the lean period. Higher catalyst loading progressively reduced the NO_x emitted at the reactor outlet, resulting in an increasing NO_x trapping efficiency, which was calculated following the procedure explained elsewhere [37, 38], equivalent to the area comprised between the inlet and outlet NO_x concentration curves during the lean period in Figure 3.8a.

During the rich period, the stored NO_x react with H_2 to produce N_2, NH_3, N_2O and H_2O. Although the amount of stored NO_x changed notably with increasing the catalyst loading, this trend was not observed for NH_3 formation at the reactor outlet, which was hardly influenced by the catalyst loading (Figure 3.8b). It is worth noting that irrespective of the catalyst loading, the

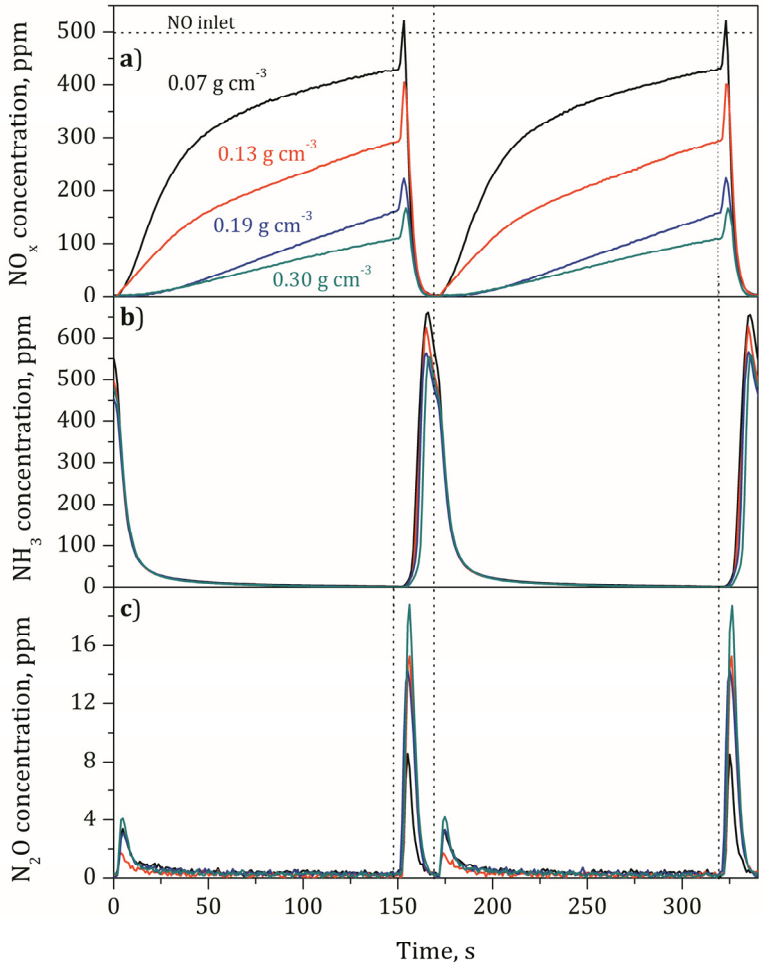

Figure 3.8. NO, NH_3 and N_2O concentration profile at the reactor exit during two consecutive NO_x storage and reduction cycles at 300 °C for different washcoat loadings: 0.07, 0.13, 0.19 and 0.30 g cm^{-3}. (Lean period, 150 s: 500 ppm NO, 6% O_2. Rich period, 20 s: 500 ppm NO, 3% H_2 using in both periods Ar as a balance gas with a total flow rate of 2600 ml min^{-1}. *GHSV*= 36,000 h^{-1}.

amount of N_2O at the reactor outlet was almost negligible, with a maximum concentration of 20 ppm (Figure 3.8c).

The activity of the catalyst during lean and rich periods was evaluated by the following parameters, as defined by Pereda-Ayo et al. [38]:

(a) The NO_x trapping efficiency:

$$NSC(\%) = \frac{NO_x^{stored}}{NO_L^{in}} \times 100 = \frac{F_{NO}^{in} t_L - \int_0^{t_L} F_{NO_x}(t)dt}{F_{NO}^{in} t_L} \times 100 \quad (3.7)$$

where F_{NO} is the NO molar flow (mol min^{-1}) at the reactor inlet, F_{NOx} is the NO_x molar flow (mol min^{-1}) at the reactor outlet and t_L (min) is the length of the lean period.

(b) NO_x reduction conversion (X_R) during the reduction period is calculated by Equation 3.8:

$$X_R(\%) = \frac{\left[NO_x^{stored} + \left(NO^{in}\right)_R\right] - \left(NO_x^{out}\right)_R}{\left[NO_x^{stored} + \left(NO^{in}\right)_R\right]} \times 100 = \frac{\left[F_{NO}^{in} t_L - \int_0^{t_L} F_{NO_x}(t)dt + F_{NO}^{in} t_R\right] - \int_{t_L}^{t_L + t_R} F_{NO_x}(t)dt}{\left[F_{NO}^{in} t_L - \int_0^{t_L} F_{NO_x}(t)dt + F_{NO}^{in} t_R\right]} \times 100 \quad (3.8)$$

It is considered that the total amount of NO_x to be reduced accounts for the NO_x stored in the previous lean period plus the NO continuously added during the rich period $(NO^{in})_R$. On the other hand, $(NO_x^{out})_R$ refers to the amount of NO_x coming out from the reactor during the reduction period (t_R).

(c) Selectivity to N_2O, NH_3 and N_2

The selectivity to NH_3 (Equation 3.9) and N_2O (Equation 3.10) is defined as the amount of N_2O/NH_3 at the reactor outlet whenever was detected (mainly during the rich period and the first part of the subsequent lean period) related to the total amount of reacted NO_x.

$$S_{NH_3}(\%) = \frac{NH_3^{out}}{NO_{x,L}^{stored} + NO_R^{in} - NO_{x,R}^{out}} \times 100 = \frac{\int_0^{t_L+t_R} F_{NH_3}(t)dt}{X_R\left(F_{NO}^{in} t_L - \int_0^{t_R} F_{NO_x}(t)dt + F_{NO}^{in} t_R\right)} \times 100 \quad (3.9)$$

$$S_{N_2O}(\%) = \frac{2N_2O^{out}}{NO_{x,L}^{stored} + NO_R^{in} - NO_{x,R}^{out}} \times 100 = \frac{2\int_0^{t_L+t_R} F_{N_2O}(t)dt}{X_R\left(F_{NO}^{in} t_L - \int_0^{t_R} F_{NO_x}(t)dt + F_{NO}^{in} t_R\right)} \times 100 \quad (3.10)$$

Once a cycle-to-cycle steady state is reached, the stored NO_x plus the NO fed during the rich cycle will react to form NH_3, N_2 or N_2O and a small quantity could also be released as NO_x without being reduced.

$$NO_x^{stored} + \left(NO^{in}\right)_R = NH_3^{out} + 2N_2^{out} + 2N_2O^{out} + \left(NO_x^{out}\right)_R \quad (3.11)$$

Starting from the above described equation (Equation 3.11), the nitrogen selectivity can be calculated by balance.

$$2N_2^{out} = NO_x^{stored} + \left(NO^{in}\right)_R - NH_3^{out} - 2N_2O^{out} - \left(NO_x^{out}\right)_R \quad (3.12)$$

$$S_{N_2}(\%) = \frac{F_{NO}^{in} t_L - \int_0^{t_L} F_{NO_x}(t)dt + F_{NO}^{in} t_R - \int_0^{t_L+t_R} F_{NH_3}(t)dt - 2\int_0^{t_L+t_R} F_{N_2O}(t)dt - \int_{t_L}^{t_L+t_R} F_{NO_x}(t)dt}{2X_R\left(\int_0^{t_L}\left[F_{NO}^0 - F_{NO_x}(t)dt + F_{NO}^0 t_R\right]\right)} \times 100 \quad (3.13)$$

Figure 3.9 shows the evolution of NO_x storage capacity (*NSC*) (Figure 3.9a), NH_3 selectivity (Figure 3.9b) and N_2 and N_2O selectivity (Figure 3.9c) with increasing catalyst loading at 200, 275, 350 and 425 °C. The *NSC* increases almost linearly for low catalyst loadings and then progressively tends to saturate for high catalyst loadings, with a maximum *NSC* around 85%. As can be observed, the NO_x storage capacity is slightly higher for 350 °C with

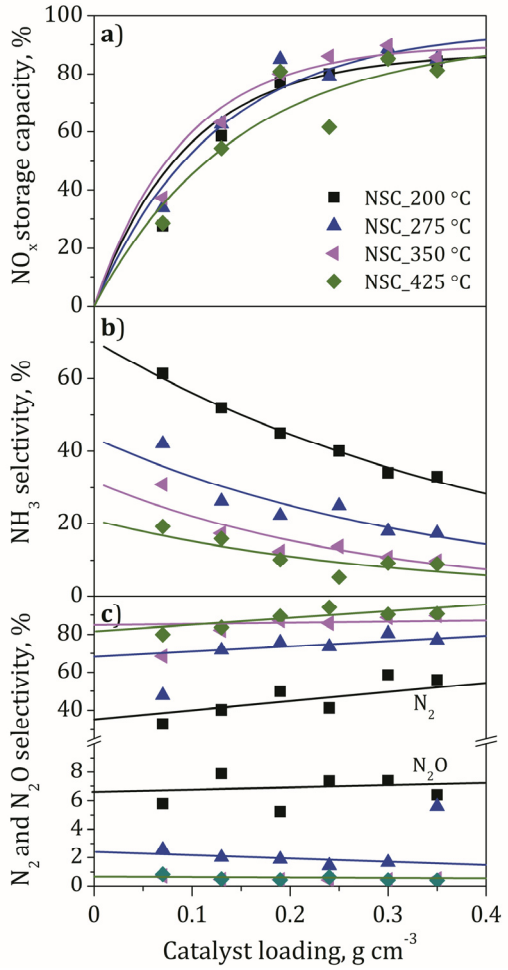

Figure 3.9. NO_x storage capacity (a), NH_3 selectivity (b) and N_2 and N_2O selectivities (c) as a function of the washcoat loading for different reaction temperatures. (Lean period, 150 s: 500 ppm NO, 6% O_2. Rich period, 20 s: 500 ppm NO, 3% H_2 using in both periods Ar as a balance gas with a total flow rate of 2600 ml min^{-1}. *GHSV*= 36,000 h^{-1}.

respect to 200 °C, in line with reference [38]. At such low temperature (200 °C), the extension of NO to NO_2 oxidation reaction is low and thus the

NSC is penalized. On the other hand, the NO-to-NO_2 conversion is maximum at 350 °C [38] which facilitates NO_x adsorption via NO_2 [17].

Figure 3.9b shows that NH_3 selectivity decreases with catalyst loading and temperature, which can be explained based on mechanistic features of NSR process. As it is known, nitrogen formation in NSR catalysts occurs via intermediate NH_3 formation. The first step is the reaction between hydrogen and stored nitrates to form NH_3 which then further reacts with stored nitrates located downstream to form N_2 [33, 36, 39, 174]. The reaction between intermediate ammonia and stored nitrates to form nitrogen is greatly enhanced with increasing temperature, and thus, it results in NH_3 selectivity diminution with increasing temperature. On the other hand, NH_3 selectivity decrease (in favor of nitrogen) was also observed for increasing catalyst loading or washcoat thickness. A very thin washcoat (7 μm, 0.07 g cm^{-3}) means that intermediate NH_3 has lower probability to meet additional stored nitrates while it is diffusing along the washcoat depth to reach the monolith channel, resulting in NH_3 selectivity of 61.3% at 200 °C. On the contrary, a thick washcoat (62 μm, 0.35 g cm^{-3}) increases the probability of meeting additional nitrates to react with and consequently the selectivity to NH_3 decreases considerably to 33%. A compromise between catalyst loading and NSR activity must be considered in order to select the optimum catalyst loading, which results in 0.25 g cm^{-3} (40 μm), for NSR-SCR applications.

3.4. $DeNO_x$ PERFORMANCE OF COMBINED NSR-SCR SYSTEMS: SEQUENTIAL CONFIGURATION vs. DUAL LAYER MONOLITHS

In this section the NO_x removal with NSR-SCR technology configured in sequential monolithic reactors or in a single dual layer reactor is analyzed. Figure 3.10 shows SEM images of the prepared single NSR, single SCR and NSR\SCR dual-layer catalysts. NSR catalyst was synthesized with a washcoat loading of 0.25 g cm^{-3}, whereas SCR catalyst with 0.32 g cm^{-3}, based on optimized charges determined in previous sections. Washcoat thickness of 40

and 70 μm were observed for NSR and SCR monolithic catalysts, respectively. Dual layer catalysts consisted of a bottom NSR layer with a loading of 0.25 g cm^{-3} (around 40 μm depth) and an upper SCR layer with increasing loadings of 0.02 g cm^{-3} (7 μm), 0.05 g cm^{-3} (26 μm) and 0.07 g cm^{-3} (34 μm).

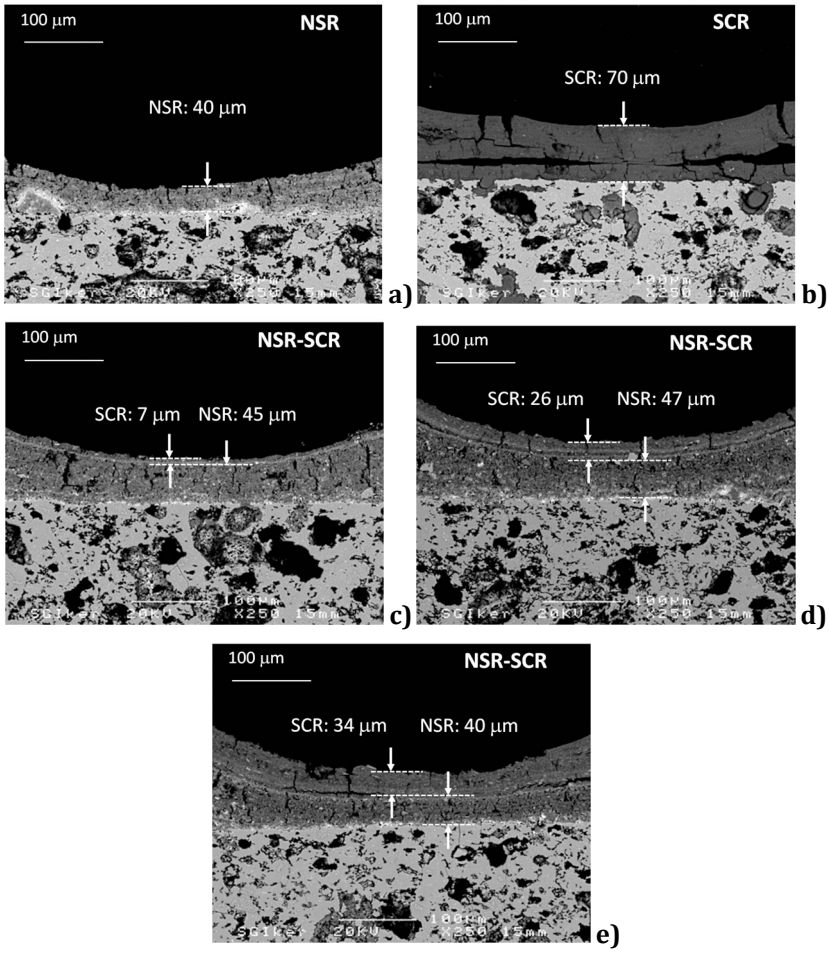

Figure 3.10. SEM images of NSR (a) and SCR (b) monolithic catalysts with optimum catalyst loading and dual-layer NSR/SCR monolithic catalyst with increasing top layer SCR loading 0.02 (c), 0.05 (d) and 0.07 g cm^{-3} (e).

The beneficial effect of placing an SCR catalyst downstream NSR is clearly evidenced in Figure 3.11, as it was already reported in literature [105, 119, 175, 176]. NSR-SCR combined systems in sequential beds reduced significantly NH_3 emissions at the reactor exit from 35% for the single NSR to 15% at 200 °C. Less NH_3 is emitted from combined NSR-SCR system due to NH_3 storage in the acidic sites of zeolite, which participates in the reduction of additional NO_x in the subsequent lean period, and thus, achieves a superior $DeNO_x$ performance, particularly at low temperatures where NH_3 production at NSR outlet is notable. The optimal operating temperature for combined NSR-SCR catalyst in sequential monolithic beds was 275 °C, with NO_x removal of 97% and product selectivity of 1% NH_3, 3% N_2O and 96% N_2.

$DeNO_x$ performance of dual-layer NSR\SCR catalyst is strongly dependent on the SCR layer loading deposited on top of the NSR. Dual-layer monolith with the lowest amount of SCR layer loading (0.02 g cm^{-3}) improved the NO_x conversion observed for the single NSR in the temperature range of 220–400 °C, reaching a maximum NO_x conversion of 84%. In contrast, further increase of the top SCR layer loading (0.05 g cm^{-3}) has a negative impact on the NO_x conversion due to higher diffusional resistance of the top SCR layer that prevents NO_x from reaching Ba adsorption sites located in the bottom NSR layer and thus decreases NO_x conversion to 78%. Dual layer catalyst with the highest amount of SCR top layer (0.07 g cm^{-3}) further decreases NO_x conversion to 72%.

As shown in Figure 3.11 for thicker SCR layer, the NO_x conversion achieved by the dual-layer catalyst can be lower than that achieved by the single NSR catalyst. This confirms the unexpected finding firstly reported by Liu et al. [111] for dual-layer catalyst with Cu/ZSM5 as the top SCR layer. This counterintuitive result comes from an interaction between the two layers. At temperature below 200 °C, on one hand the Cu/BETA steady-state activity for SCR reaction is not so high (Figure 3.7); however, the zeolite still can store NH_3 produced in the NSR layer (Figure 3.9). On the other hand, the dual-layer

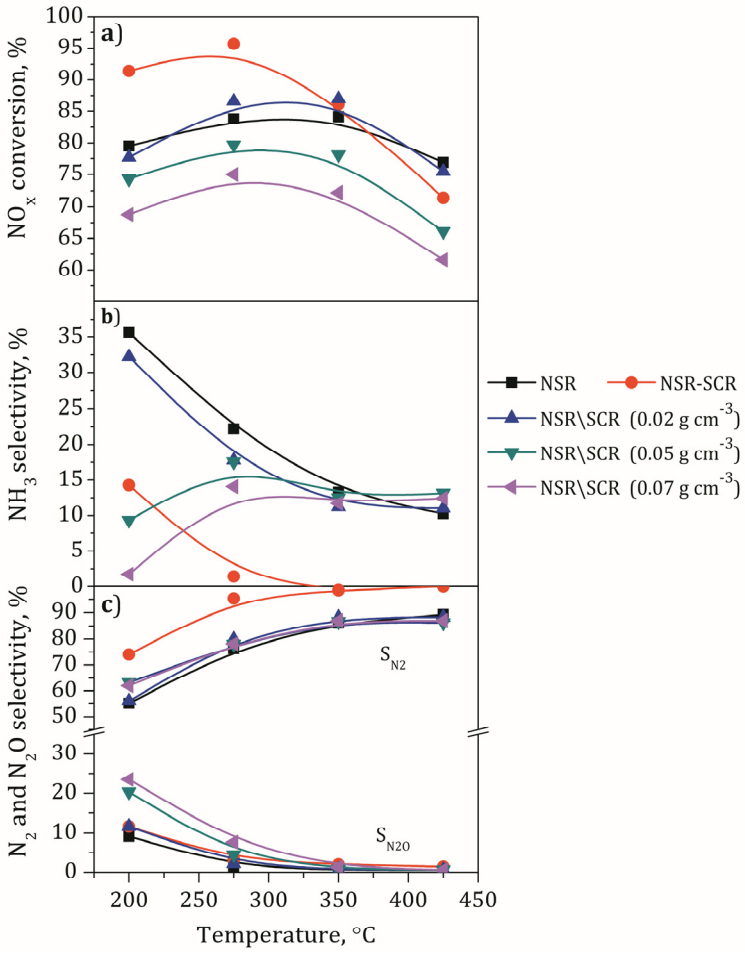

Figure 3.11. NO_x (a) and NH_3 (b) conversion and N_2 and N_2O (c) selectivities as a function of the reaction temperature for single NSR, NSR-SCR in consecutive reactors and dual-layer NSR\SCR catalysts with increasing top layer SCR loading 0.02, 0.05 and 0.07 g cm^{-3}. Feed stream: Lean period, 150 s: 500 ppm NO, 6% O_2. Rich period, 20 s: 500 ppm NO, 3% H_2 using in both periods Ar as balance gas with a total flow rate of 2600 ml min^{-1}. *GHSV*= 36,000 h^{-1}.

catalyst achieves more N_2O selectivity than the single NSR catalyst (Figure 3.11). The N_2O can be formed by either one or both of possible pathways [111]: (i) the formation and decomposition of NH_4NO_3, which requires formation of NO_2 by NO oxidation, (ii) the adsorption and oxidation of NH_3 on the Pt-crystallites of the NSR catalyst. NO and NH_3 oxidation experiments on the Pt-Ba/Al_2O_3 catalyst achieved conversion of 14% and 30%, respectively, at 200 °C [39]; and also considering that NH_4NO_3 decomposition is slow below 250 °C [96] the second route would probably be more viable to form N_2O at low temperatures. Above 250 °C, however, complete NH_3 conversion is achieved in the SCR layer with increasing NO_x (NO_2+NO) selectivity instead of the SCR reaction (Figure 3.7).

Regarding NH_3 selectivity, it can be observed that low loaded (0.02 g cm^{-3}) SCR dual-layer catalysts reduced NH_3 emissions in the whole temperature range with respect to the single NSR. Further increase of the SCR layer loading to 0.05 g cm^{-3} causes a significant decrease in the NH_3 selectivity, i.e. NH_3 formed in the bottom NSR layer is efficiently adsorbed on the top SCR layer while it diffuses towards the monolith channel, reducing ammonia selectivity below 10% at 200 °C. NH_3 selectivity as low as 2% can be achieved by increasing SCR catalyst loading to 0.07 g cm^{-3} at 200 °C. At higher temperatures, NH_3 selectivity increases due to NH_3 adsorption efficiency decrease and eventually reaches the same NH_3 selectivity than that observed for the single NSR, which means that at such operating conditions (above 350 °C) NH_3 adsorption is almost negligible, in accordance with NH_3-TPD results for BETA zeolite [177]. Also, increasing amounts of N_2O are observed with increasing SCR layer loading, especially at lower temperatures.

Thus, top layer SCR catalyst loading can be tuned in order to improve $DeNO_x$ performance of dual-layer NSR\SCR catalysts. Low SCR layer loaded catalyst (0.02 g cm^{-3}, 7 μm) can improve $DeNO_x$ performance of single NSR at intermediate temperatures (220–400 °C). For temperatures lower than 200 °C dual-layer catalysts performance is penalized due to limited NH_3-SCR activity

of Cu/BETA catalyst, which could be improved by the utilization of zeolites with small pore size such as chabazite as will be studied in Chapter 4 [166, 178, 179]. On the other hand, at temperatures higher than 400 °C, N_2 production is promoted instead of NH_3 in the bottom NSR layer and besides, the limited quantity of NH_3 produced cannot be efficiently adsorbed in the top SCR layer, which causes a reductant deficiency for activating NH_3-SCR reaction.

3.5. OVERALL VIEW AND CONCLUSIONS

The preparation procedure of Cu/BETA catalysts affects notably the physicochemical properties of the final solids. Copper ion exchange over protonic or ammonic BEA zeolite resulted in Cu/BETA catalysts (H/Cu and NH_4/Cu) in which almost all copper remained as Cu^{2+}. On the other hand, an intermediate ion exchange with Na^+ ions led to Cu/BETA catalysts (NH_4/Na/Cu and H/Na/Cu) in which Cu^+ and Cu^{2+} coexist. H_2-TPR experiments revealed that the amount of CuO aggregates was similar for all prepared catalysts, accounting for about 45% of the total H_2 consumption. NO adsorption experiments followed by FTIR revealed the presence of 3 types of Cu ions and thus, hydrogen consumption assigned to this species was deconvoluted in three contributions located at 450, 495 and 545 °C. It was found that NH_4/Na/Cu catalyst presented the most easily reducible ions, while copper ions with intermediate reduction temperature were more abundant in H/Na/Cu catalyst, and finally, copper ions with the highest reduction temperature were predominant in NH_4/Cu and H/Cu catalyst. The superior NH_3-SCR activity of NH_4/Na/Cu catalyst was attributed to the coexistence of Cu^{2+} and Cu^+ ions and also to the ease of ions reduction, which in turn could be related with a more accessible location of such ions. Optimum loading of 0.32 g cm^{-3} of NH_4/Na/Cu catalyst deposited onto a monolithic substrate was determined. However, monolithic catalyst presented a more limited NH_3-SCR performance in comparison with powder catalyst, particularly at high

temperatures, where NH_3 oxidation to NO prevailed over selective catalytic reduction reactions.

Different strategies were considered for combined NSR-SCR technology study, i.e. sequential monolithic reactors or single dual layer configuration. Top layer SCR catalyst loading can be tuned in order to improve $DeNO_x$ performance of dual-layer NSR\SCR catalysts. Increasing top layer SCR catalyst loading increases the storage capacity of NH_3 generated in the bottom NSR layer while it diffuses towards the monolith channel, and thus reduces NH_3 selectivity, particularly at low temperatures. On the other hand, increasing top layer SCR catalyst loading increases the diffusional resistance that prevents NO_x from reaching Ba adsorption sites located in the bottom NSR layer. Thus, optimum SCR layer loading was observed for 0.02 g cm^{-3} in order to balance the aforementioned two effects, enhancing the NO_x to N_2 efficiency of the single NSR catalyst. However, significantly higher NO_x to N_2 conversion was achieved with NSR and SCR monolithic catalysts placed in sequential beds, achieving a NO_x removal of 97% with a N_2 selectivity of 96% at 275 °C.

Chapter 4

MICROPOROUS Cu/SAPO-34 CATALYSTS PREPARED BY SSIE AND LIE FOR IMPROVING NH_3-SCR ACTIVITY

Chapter 4

MICROPOROUS Cu/SAPO-34 CATALYSTS PREPARED BY SSIE AND LIE FOR IMPROVING NH_3-SCR ACTIVITY

ABSTRACT

Cu/SAPO-34 catalysts are prepared using two methods: solid state ion exchange (SSIE) and liquid ion exchange (LIE). SSIE is conducted by calcining a physical mixture of the H-SAPO-34 zeolite and CuO nanoparticles at elevated temperatures (500-800 °C). The conventional LIE method is conducted by exchanging the Na/SAPO-34 with $Cu(COOCH_3)_2$ aqueous solution with a final calcination step at 500 °C. Catalysts are characterized by N_2 adsorption-desorption, ammonia temperature programmed desorption (NH_3-TPD), scanning electron microscopy (SEM), electron paramagnetic resonance (EPR), temperature programmed reduction (H_2-TPR) and ultraviolet-visible spectroscopy (UV-Vis), specially focusing on Cu species identification. The activity performance for NO removal by selective catalytic reduction with NH_3 (NH_3-SCR) is evaluated in a plug flow reactor running under differential and integral regimes. Cu/SAPO-34 catalysts synthesized by SSIE at 700 °C achieved the highest reaction rate which was correlated with a higher proportion of Cu^{2+} ions. Lower temperatures during SSIE synthesis do not conveniently disperse the copper, while higher temperatures promote agglomeration of copper ions and reduce the stability of the zeolite framework. The SSIE catalysts achieve higher TOF values than LIE catalysts for similar copper content, i.e. 1.9% and 2.2%, respectively. These results provide evidence that Cu ions are successfully exchanged into the Cu/SAPO-34 catalysts synthesized by SSIE, which allows the formation of active copper ions. Which in turn promotes NH_3-SCR of NO_x and results in higher TOF values than catalysts synthesized by conventional LIE.

Capítulo 4

CATALIZADORES MICROPOROSOS Cu/SAPO-34 PREPARADOS MEDIANTE SSIE Y LIE PARA MEJORAR LA ACTIVIDAD NH_3-SCR

RESUMEN

Se han preparado catalizadores Cu/SAPO-34 mediante dos métodos de preparación: intercambio iónico en estado sólido (SSIE) e intercambio iónico en fase acuosa (LIE). El método de preparación SSIE consiste en calcinar a alta temperatura (500-800 °C) la mezcla física preparada mediante la zeolita H-SAPO-34 y el precursor CuO. El método convencional LIE consiste en realizar el intercambio en fase acuosa entre el Na/SAPO-34 y $Cu(COOCH_3)_2$ para posteriormente calcinarlo a 500 °C. Los catalizadores han sido caracterizados para la determinación de las especies de cobre mediante adsorción-desorción de N_2, desorción a temperatura programada con NH_3 (NH_3-TPD), microscopia electrónica de barrido (SEM), resonancia paramagnética electrónica (EPR), reducción a temperatura programada (H_2-TPR) y espectroscopia ultravioleta-visible (UV-vis). La reducción de los NO_x en la reacción NH_3-SCR se ha realizado en un reactor tubular operando en régimen diferencial e integral. El catalizador Cu/SAPO-34 preparado mediante SSIE y calcinado a 700 °C es el que mayor actividad tiene debido a que posee una mayor proporción de iones Cu^{2+}. Los catalizadores SSIE calcinados a menores temperaturas tienen menor actividad por la baja dispersión del cobre. Por otro lado, los catalizadores SSIE calcinados a mayor temperatura tienen menor actividad por la aglomeración de los iones de cobre reduciendo la estabilidad en la estructura de la zeolita. Si se compara un catalizador SSIE con un catalizador LIE con similar carga de cobre, el catalizador SSIE presenta mayores valores de TOF. Esto indica que en los catalizadores SSIE los iones de cobre están intercambiados exitosamente en la zeolita en forma de especies iónicas muy activas para catalizar la reacción NH_3-SCR.

4. MICROPOROUS Cu/SAPO-34 CATALYSTS PREPARED BY SSIE AND LIE FOR IMPROVING NH_3-SCR ACTIVITY

The catalysts with small pore zeolites such as Cu/CHA present good NH_3-SCR activity and good hydrothermal stability at high temperatures [91, 180]. Many factors can be found to influence NO_x removal of Cu/SAPO-34 catalysts, such as the synthesis methods, the zeolite composition, the copper amount and the calcination conditions. The most common and conventional method to prepare the Cu/zeolite catalysts is liquid ion exchange (LIE). A drawback of this method is that the exchange procedure has to be repeated several times to obtain high ion exchange levels.

An alternative method to introduce metal ions into zeolite is by solid-state ion-exchange (SSIE). This method consists in physicaly mixing metal salt or oxide and the zeolite. Then, the mixture is heated at high temperature, typically 700-800 °C, which results in the diffusion of the metal ions into the zeolite. The high temperature required to initiate the metal exchange restricts SSIE to thermally stable zeolites. However, even the stable chabazite structure shows some damage after SSIE at 800 °C [181].

This chapter analyzes the $DeNO_x$ behavior of Cu/SAPO-34 catalyst as prepared by solid state ion exchange (SSIE) and liquid ion exchange (LIE). First, the influence of the temperature at which SSIE is carried out will be studied. Then, copper loading effects will be analyzed in Cu/SAPO-34 catalysts prepared by LIE and SSIE.

4.1. SOLID STATE ION EXCHANGE (SSIE). SELECTION OF THE CALCINATION TEMPERATURE

4.1.1. Catalysts characterization

Several 4% Cu/SAPO-34 catalysts were prepared by physically mixing CuO and H-SAPO-34 and submitted to high temperature, namely 500, 600,

650, 700, 750 and 800 °C in order to favor the solid state ion exchange. As a reference, an additional physical mixture of CuO and H-SAPO-34 sample was prepared without being calcined (WO/C). The Cu loading of the catalysts was maintained at 4% for the SSIE temperature analysis in this section.

4.1.1.1. Composition and textural properties

Table 4.1 resumes the composition and the specific surface area of the prepared samples. As it can be observed, the mayor compounds are P and Al and Si in a minor extent, as for aluminosilicophosphates (H-SAPO-34). Also, Fe, Mg, Na and Ca are found as impurities.

As can be observed, all catalyst presented very similar copper loading around 4.2%. The interaction between copper and the zeolite reduces the specific surface area from 600 $m^2\ g^{-1}$ to 450 $m^2\ g^{-1}$ for samples calcined at temperatures below 700 °C, assigned to pore blockage by copper aggregates. A further increase in the calcination temperature above 750 °C lead to a clear decrease of the specific surface area, which resulted in 403 and 270 $m^2\ g^{-1}$ for 750 and 800 °C, respectively. The specific surface area reduction is directly

Table 4.1. Composition, copper loading and BET surface area of samples prepared by SSIE at different temperatures.

SSIE temperature, °C	Composition wt., %									S_{BET}, $m^2\ g^{-1}$
	Si	Al	Fe	Mg	Ca	Na	P	O	Cu	
H-SAPO-34	4.5	19.4	0.6	0.1	0.1	0	18.2	57.0	-	600
500	5.7	20.1	0.6	0.1	0.8	0	18.6	49.9	4.3	452
600	5.4	20.3	0.6	0.1	0.7	0	18.7	49.9	4.3	463
650	5.1	20.1	0.6	0.1	0.6	0	18.9	50.0	4.2	458
700	5.3	20.3	0.6	0.1	0.7	0	18.9	50.0	4.2	447
750	5.1	20.2	0.6	0.1	0.6	0	18.9	50.0	4.2	403
800	5.2	20.2	0.6	0.1	0.6	0.1	18.9	49.9	4.4	270

related with a partial destruction of the zeolite framework, as will be evidenced in the following section.

4.1.1.2. Phase identification and copper particle size

XRD was used to monitor the integrity of the H-SAPO-34 structures after SSIE due to the severe thermal treatment used during the synthesis. Figure 4.1 represents X-ray diffraction patterns of the prepared catalysts along with the uncalcined sample and the bare zeolite.

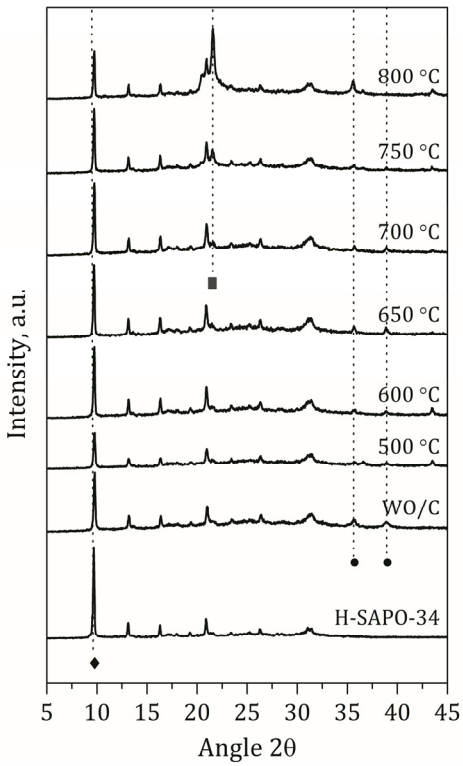

Figure 4.1. XRD diffractograms of H-SAPO-34 zeolite and 4% Cu/SAPO-34 catalysts prepared by SSIE.

XRD patterns of the bare zeolite and catalysts prepared at temperatures lower than 700 °C are very similar, which assures that the zeolite structure and crystallinity is maintained unaltered after SSIE. The unique exception with respect to H-SAPO-34 diffraction pattern is the presence of peaks located at 35.5 and 38.5° 2θ attributed to the presence of copper oxide [91]. This fact indicates that, at least, some fraction of copper is not ion exchanged and remains as copper aggregates, because copper ions are not detectable by XRD [180, 181]. On the other hand, XRD patterns of samples calcined at temperatures higher than 700 °C presented an additional phase with a characteristic diffraction peak situated at 21°. This peak, ascribed to silicon dioxide (SiO_2) [86, 126], was evident for Cu/SAPO-34 sample calcined at 750 °C and became the main diffraction peak for the sample treated at 800 °C. Thus, it can be concluded that the chemical structure stability of H-SAPO-34 zeolite starts to be significantly affected by temperatures higher than 750 °C, leading to some silicon segregation from the zeolite framework.

SEM images were recorded in order to examine the morphology of H-SAPO-34 zeolite and determine the size of copper aggregates in the prepared samples. As can be observed in Figure 4.2, perfect cubic crystals (in light grey) were observed irrespective of the calcination temperature, which is in line with the large crystallinity of H-SAPO-34 detected by XRD. The size of those crystals was rather homogeneous, in the range 2-5 μm, in accordance with previous results [126, 180, 182]. Large and numerous copper aggregates (detectable by lighter areas due to the higher atomic number of copper) could be easily observed for the sample calcined at 500 °C (Figure 4.2a). The number and size of those aggregates was progressively reduced while increasing calcination temperature, as can be observed in Figure 4.2e for 4% Cu/SAPO-34 sample calcined at 750 °C. Thus, it can be concluded that increasing SSIE temperature treatment enhances the ability to disperse copper aggregates, forming smaller Cu_xO_y clusters or even copper ions (Cu^{2+}), which are not detectable by SEM. However, it was evidenced that irrespective

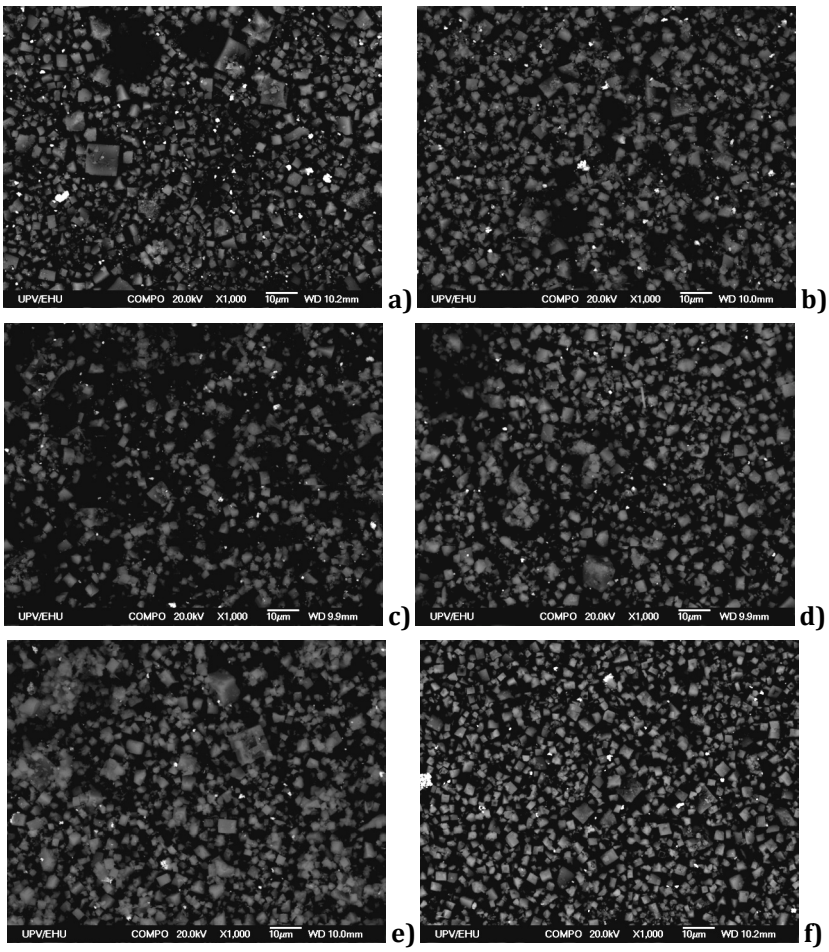

Figure 4.2. SEM images for 4% Cu/SAPO-34 catalyst prepared by SSIE at a) 500 °C, b) 600 °C, c) 650 °C, d) 700 °C, e) 750 °C and f) 800 °C.

of the thermal treatment temperature, this procedure was not able to accomplish complete dispersion of copper because easily detectable copper aggregates located outside the pores of the zeolite were still visible after SSIE.

4.1.1.3. Cu^{2+} identification by EPR

Electron paramagnetic resonance (EPR) has been extensively used in order to specifically characterize isolated Cu^{2+} ions [79, 126, 157, 183], as aggregated CuO species and Cu^{+} ions are EPR silent [184-186]. Figure 4.3 shows EPR spectra for 4% Cu/SAPO-34 catalysts prepared at different SSIE temperatures, along with the CuO and H-SAPO-34 physical mixture as reference. All samples presented a characteristic feature at low fields (around 1500 G, not shown) attributed to the presence of Fe^{3+} ions [187, 188]. The intensity of this signal changed among samples, indicating that the quantity of iron was not homogeneous and consequently made more challenging the quantification of Cu^{2+} ions content. Qualitatively, the obtained spectra presented a unique feature in the high field region at 3270 G whereas copper hyperfine features are evident at low field and the intensity of both, low and high field features, clearly increased with SSIE temperature. It is worth to note

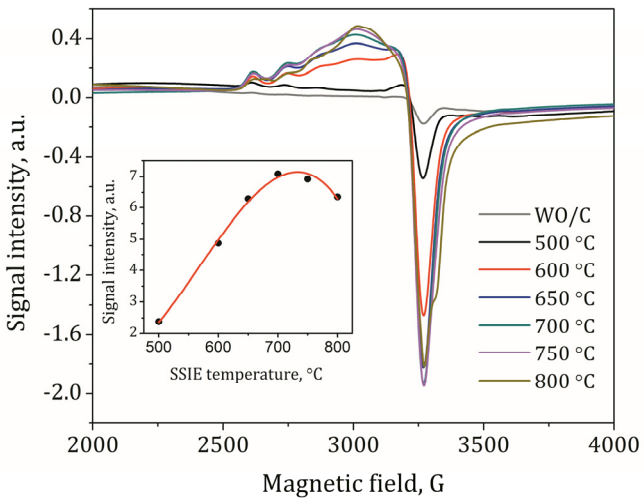

Figure 4.3. EPR spectra for 4% Cu/SAPO-34 catalyst prepared by SSIE at different temperatures. The inset figure represents the signal intensity calculated by double integral of the original signal in the 2500-3500 field range.

that the detection of an additional feature at high field (3315 G) for the sample calcined at 800 °C suggests the presence of two different types of copper ions.

The double integration of the signal presented in Figure 4.3 in the magnetic field range of 2500-3500 G is shown in the inset figure and allows a semiquantitative comparison among the prepared samples. As can be observed, the signal intensity due to the presence of isolated Cu^{2+} ions increases monotonically with increasing SSIE temperature up to 700 °C. Afterwards, the signal intensity tends to saturate or even decrease, which points out that a further temperature increase above 700 °C does not result in the formation of higher amount of copper ions.

4.1.1.4. Redox properties and copper species quantification

Figure 4.4 shows H_2 consumption profiles during temperature programmed reduction (H_2-TPR) experiments for 4% Cu/SAPO-34 catalysts prepared by SSIE at different calcination temperatures. Generally, the reduction of Cu^{2+} ions in zeolites takes place through two consecutive steps, i.e. Cu^{2+} ions reduction to Cu^{+} and subsequent reduction of Cu^{+} ions to Cu^{0} [164, 171, 185, 189]. Moreover, it has been reported that the reduction of CuO nanoparticles to Cu^{0} occurs in a single step at around 300 °C [164, 190]. However, in accordance with the results reported by Wang et al. [167], we experimentally determined that a physical mixture of CuO and H-SAPO-34 zeolite presented a unique reduction peak located at somewhat lower temperature, c.a. 260 °C (Figure 4.4a), undoubtedly assigned to the reduction of CuO aggregates to Cu^{0}.

SSIE procedure at 500 °C did not modify the redox behavior of the sample with respect to the physical mixture. However, some changes started to be evident for the sample submitted to SSIE at 600 °C, i.e. a small H_2 consumption peak centered around 320 °C started to develop. Reduction of Cu^{2+} ions to Cu^{+} has been reported to occur at temperatures lower than 250 °C [180, 185, 191] whereas subsequent reduction of Cu^{+} ions to Cu^{0} occurs at higher

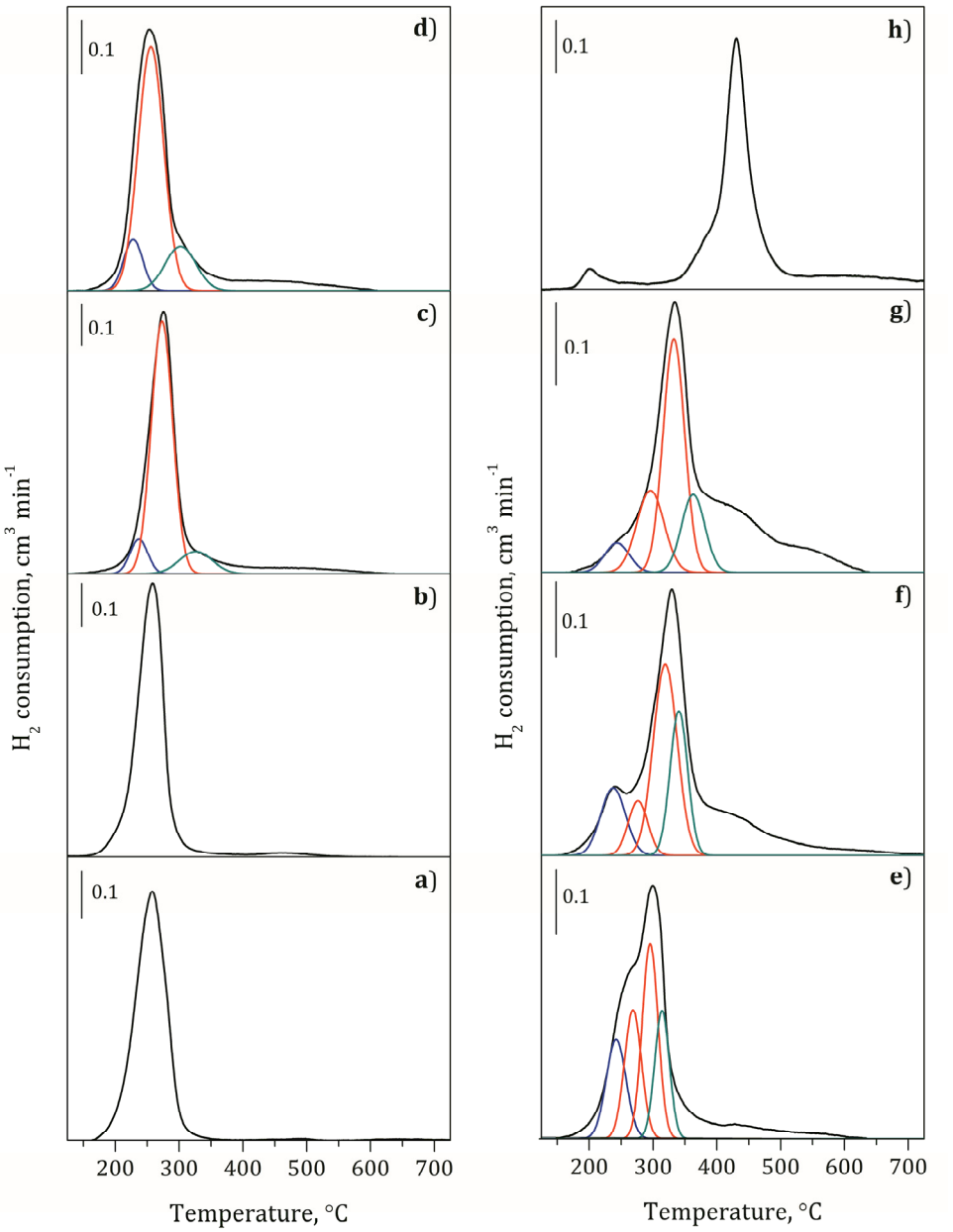

Figure 4.4. H_2 consumption profiles during H_2-TPR experiments for 4% Cu/SAPO-34 catalyst prepared by SSIE at different temperatures: b) 500 °C, c) 600 °C, d) 650 °C, e) 700 °C, f) 750 °C, g) 800 °C. Experiments with a physical mixture of CuO and H-SAPO-34 without been calcined (WO/C) (a) and copper aluminate (h) are also included as a reference.

temperatures. Thus, we are considering that the reduction of Cu^{2+} ions to Cu^{+} occurs around 230 °C, reduction of large copper aggregates around 260 °C and final reduction of Cu^{+} ions takes place at 320 °C. Note that the coexistence of copper ions (Cu^{2+}) and CuO aggregates has been already evidenced by EPR and SEM, respectively, in the prepared samples.

It was not straightforward to determine the size and amplitude of the low temperature H_2 consumption contribution due to Cu^{2+} ions reduction to Cu^{+}. However, the observed H_2/Cu ratio for the whole H_2-TPR experiment (Table 4.2) is very close to 1 in all cases, which indicates that all copper exist in the oxidation state of +2 in the original sample and thus the area of the low temperature contribution ($Cu^{2+}\rightarrow Cu^{+}$) located at 230 °C should be very close to the area of the high temperature contribution ($Cu^{+}\rightarrow Cu^{0}$) located at 320 °C.

Samples treated at temperatures higher than 700 °C required an additional contribution in order to adequately describe the observed H_2 consumption profile. In particular, this contribution was located at 300 °C and was assigned to the reduction of nanosize copper clusters (Cu_xO_y) [164] which interact more strongly with the support and consequently require a higher temperature than large copper aggregates (260 °C) to get reduced. This observation is in agreement with results previously reported by Gao et al. [126] who attributed the temperature shift of the major reduction peak to higher temperatures due to changes in dispersion of the CuO nanoparticles.

Finally, samples treated at temperatures higher than 600 °C presented an additional H_2 consumption contribution centered around 450 °C with a long tail up to 650 °C. This contribution was assigned to the reduction of highly stable copper ions in copper aluminate ($CuAl_2O_4$) phase, which formation has already been reported for copper zeolites under specific preparation conditions [126, 192]. In order to verify this assignation, bulk $CuAl_2O_4$ was synthesized by mixing nanopowder CuO and γ-Al_2O_3 and calcining the physical mixture at 1000 °C. The H_2-TPR experiment included in Figure 4.4h revealed a

Table 4.2. Quantification of H_2 consumption attributed to the reduction of different copper species along with copper species distribution and H_2/Cu ratio.

Sample	H_2 consumption due to, μmol g^{-1}					Cu species distribution, %					H_2/Cu
	Cu^{2+} → Cu^{+}	CuO → Cu^0, aggregates	CuO → Cu^0, clusters	Cu^{+} → Cu^0	$CuAl_2O_4$	Cu^{2+}	CuO aggregates	CuO clusters	Cu^{+}	$CuAl_2O_4$	
WO/C	-	538.3	-	-	-	-	100	-	-	-	0.93
500 °C	-	643.1	-	-	-	-	100	-	-	-	0.94
600 °C	61.8	472.0	-	75.8	78.6	18	67	-	4	11	0.99
650 °C	83.2	382.5	-	93.9	88.5	25	58	-	3	13	1
700 °C	107.2	136.0	175.1	113.9	106.4	33	21	27	2	16	0.91
750 °C	89.2	50.4	244.6	101.7	150.6	27	8	38	4	23	0.93
800 °C	56.4	59.9	269.4	75.7	177.9	17	9	41	6	29	0.85

main hydrogen consumption peak at 430 °C for $CuAl_2O_4$, which validates the previous assignation. It is worth to note that the presence of $CuAl_2O_4$ started to be significant for temperatures higher than 750 °C, in line with the detection of some segregated silicon oxide from the zeolite framework by XRD. Thus, it seems that such a high temperature is able to produce a partial destruction of the zeolite framework leading to some recombination of atoms to form SiO_2 and $CuAl_2O_4$ along with the original H-SAPO-34. Furthermore, the formation of $CuAl_2O_4$ can also be well correlated with the detection of two different types of Cu^{2+} ions by EPR for samples treated at 750 and 800 °C.

The integration of H_2 consumption peaks observed in Figure 4.4 in the time domain permitted us to calculate the amount of hydrogen (μmol H_2 g^{-1}) dedicated to the reduction of copper ions in sequential steps, reduction of copper aggregates and copper clusters, and reduction of copper aluminate. Furthermore, it was possible to determine the relative abundance of different types of copper species in the original sample (Table 4.2) based on the reduction stoichiometry. For example, the sample treated at 700 °C presented a hydrogen consumption due to Cu^{2+} ions reduction to Cu^{+} of 107.2 μmol H_2 g^{-1}, which means that 214.4 μmol Cu^{2+} g^{-1} were present in the original sample based on the reduction stoichiometry ($Cu^{2+} + 1/2H_2 \rightarrow Cu^{+} + H^{+}$). Then, 136.0 and 175.1 μmol H_2 g^{-1} were dedicated to the reduction of copper aggregates and copper clusters, respectively, both with the same reduction stoichiometry, i.e. ($CuO + H_2 \rightarrow Cu^0 + H_2O$), resulting in a content of copper aggregates and clusters of 136.0 and 175.1 μmol H_2 g^{-1}, respectively. The amount of hydrogen devoted to the reduction Cu^{+} ions to metallic copper was 113.9 μmol H_2 g^{-1}. However, the calculation of the amount of Cu^{+} ions in the original sample requires the substraction of the hydrogen consumption due to the reduction of Cu^{+} ions that derive from Cu^{2+} ions reduction. Thus, hydrogen consumption attributed to Cu^{+} ions reduction can be calculated by 113.9 μmol H_2 – 107.2 μmol H_2 = 6.7 μmol H_2 g^{-1} and taking into account the reduction stoichiometry ($Cu^{+} + 1/2H_2 \rightarrow Cu^0 + H^{+}$), the

content of Cu^{+} ions results in 13.3 μmol g^{-1}. Finally, the hydrogen consumption due to the reduction of copper aluminate was 106.4 μmol H_2 g^{-1} and consequently this also was the amount of copper aluminate, based on the reduction stoichiometry ($CuAl_2O_4 + H_2 \rightarrow Cu^0 + Al_2O_3 + H_2O$).

The proportion of different types of copper species is tabulated in Table 4.2. As can be observed, SSIE carried out at 500 °C is not able to produce any change with respect to non-calcined sample and all copper remained as aggregates. A further increase in the calcination temperature up to 600 °C results in the formation of copper ions in detriment of large aggregates. The proportion of Cu^{2+} ions progressively increased with SSIE temperature, reaching a maximum value of 33% at 700 °C, in line with EPR results, and meanwhile the proportion of CuO aggregates was reduced complementarily. Small copper clusters begin to be detectable for SSIE temperatures of 700 °C and onwards. A further temperature increase up to 800 °C penalized the formation of copper ions probably because such a high temperature is able to promote copper ions agglomeration in order to form small copper clusters inside the zeolite framework. The proportion of Cu^{+} ions was below 6% for all prepared samples, in line with experimentally detected H_2/Cu values situated very close to one. Finally, copper aluminate started to be detectable at calcination temperatures of 600 °C, and increasing SSIE temperature resulted in a progressive promotion of its formation reaching a maximum value of 29% at 800 °C. To sum up, it can be concluded that a progressive increase in the temperature at which SSIE is carried out up to 700 °C favors the formation of copper ions while a further temperature increase promotes the formation of small copper clusters and copper aluminate.

UV-Vis DRS spectra were analyzed to complete the analysis of copper species in the prepared samples by SSIE [157, 184]. The overall spectra (Figure 4.5) are similar to those reported for Cu/zeolites such as Cu/SSZ-13 [124], or Cu/SAPO-34 [182, 193, 194]. Two main characteristic absorption bands for all of the samples were observed. The one centered at ca. 240 nm is

attributed to a charge transfer band of the zeolite [182, 195], and a broad band in the region of 300–800 nm was attributed to the presence of CuO [124], as evidenced by the UV-Vis spectra of the sample prepared by physical mixture of CuO and H-SAPO-34 and also by the bulk CuO sample. This broad band is composed of several bands at ca. 355 nm and 456 nm assigned to the charge transfer bands of O-Cu-O and Cu-O-Cu complexes, respectively [196, 197] and a broad absorption band at 600-800 nm assigned to the electron d–d transitions of Cu^{2+} in distorted octahedral coordination surrounded by oxygen in dispersed CuO particles [182, 197]. As can be observed, the physical mixture of CuO and H-SAPO-34 presents a broad absorption band in the ultraviolet visible and near infrared region, i.e. 300-800 nm. The absorption intensity was progressively reduced as increasing the SSIE temperature, until it became minimum for treating temperatures of 700 °C, revealing that the population of aggregated CuO species was progressively reduced. Finally, SSIE temperatures of 750 and 800 °C presented higher absorption intensity around 350-600 nm, assigned to the presence of copper aluminate [124].

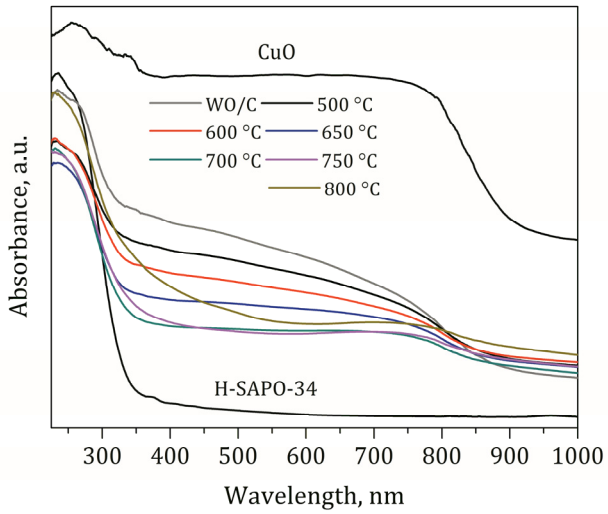

Figure 4.5. UV-vis spectra of SSIE catalysts calcined at different temperatures.

4.1.1.5. Acidity

NH_3-TPD is frequently used to determine the number and strength of the acid sites in catalysts. The NH_3-TPD profiles of bare H-SAPO-34 and 4% Cu/SAPO-34 catalysts are shown in Figure 4.6.

The H-SAPO-34 zeolite can be deconvoluted into four peaks [166, 185] and Cu/SAPO-34 catalysts can be deconvoluted into different peaks depending on the calcination temperatures. Peak 1 at lower temperatures is assigned to the weak Brønsted acid sites at surface hydroxyls [184, 198], and peaks 2, 3 and 4 at higher temperatures are related to the structural Brønsted acid sites referred to moderate and strong acidity. Peaks 5 and 6 were ascribed to the NH_3 desorbed from the strong Lewis sites created by copper species.

Table 4.3 includes the total acidity of the samples determined from Figure 4.6. As can be observed, the total acidity of the samples progressively increased as increasing SSIE temperature up to 650 °C. This fact was ascribed to the formation of Cu^{2+} ions, providing the catalyst with higher amount of Lewis acid sites in order to store NH_3 [167, 182, 184, 199]. However, total acidity of the samples tends to decrease when SSIE was carried out at temperatures higher than 650 °C. Note that total acidity of the sample prepared by SSIE at 800 °C was even lower than that observed for the bare zeolite. We suggest, in accordance with XRD results, that such a high temperature is able to produce a partial destruction of the zeolite framework (evidenced by SiO_2 segregation) which ultimately reduces the population of Brønsted acid sites and leads to a lower NH_3 adsorption capacity.

Table 4.3. Total acidity of samples prepared by SSIE at different temperatures.

Sample	H-SAPO-34	500 °C	600 °C	650 °C	700 °C	750 °C	800 °C
Acidity, μmol NH_3 g^{-1}	1384	1449	1532	1613	1571	1232	853

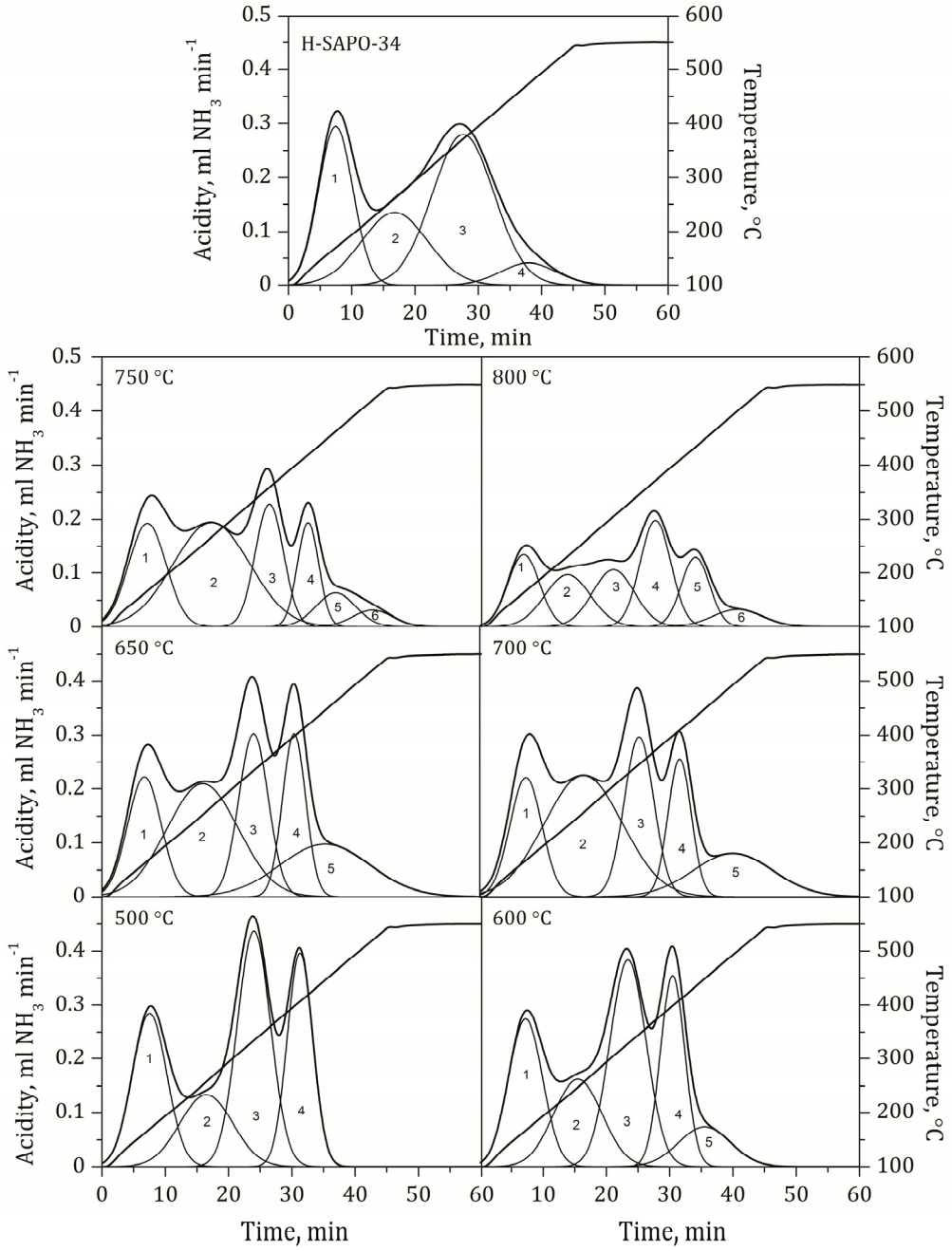

Figure 4.6. NH_3-TPD results of bare H-SAPO-34 and 4% Cu/SAPO-34 catalysts prepared by SSIE method at different calcination temperatures.

4.1.2. NH_3-SCR performance

4.1.2.1. Influence of the reaction temperature on the activity and selectivity

Figure 4.7 illustrates NO and NH_3 conversions and selectivity towards N_2, N_2O and NO_2 as a function of the reaction temperature during NH_3-SCR experiments carried out with 4% Cu/SAPO-34 catalysts prepared by SSIE at different temperatures. The catalysts were exposed to 660 ppm NO, 660 ppm NH_3 and 6% O_2 using Ar as balance gas with a total flow rate of 2600 ml min^{-1}. As can be observed, the catalyst prepared at 500 °C presents a very limited NH_3-SCR performance, reaching maximum NO conversion of 58% at 300 °C (Figure 4.7a). Increasing the temperature at which SSIE is performed results in a noteworthy enhancement of NO conversion. In fact, 4% Cu/SAPO-34 catalyst prepared at 600 °C obtained a maximum NO conversion of 98% at 300 °C. This NH_3-SCR activity enhancement can be related to the formation of copper ions in detriment of large aggregates, and this, points out that those copper ions are more active than aggregates. A further increase in the SSIE temperature up to 750 °C results in a broadening of the NO conversion performance, increasing low and high temperature NH_3-SCR activity. Although the content of large copper aggregates and small copper clusters changed markedly in the samples calcined at 650, 700 and 750 °C, almost identical NH_3-SCR activity was achieved due to comparable amount of copper ions, situated in the range of 26-33%. A further temperature increase up to 800 °C favored the migration of copper ions into the partially destroyed zeolite matrix to form $CuAl_2O_4$, which reduces the availability of copper species at the surface to activate the NH_3-SCR reaction, and consequently, achieved a lower NH_3-SCR activity specifically at low temperatures. Furthermore, the lower catalytic activity of the sample calcined at 800 °C could also be correlated with its lower specific surface area and lower acidity (Table 4.1 and 4.3).

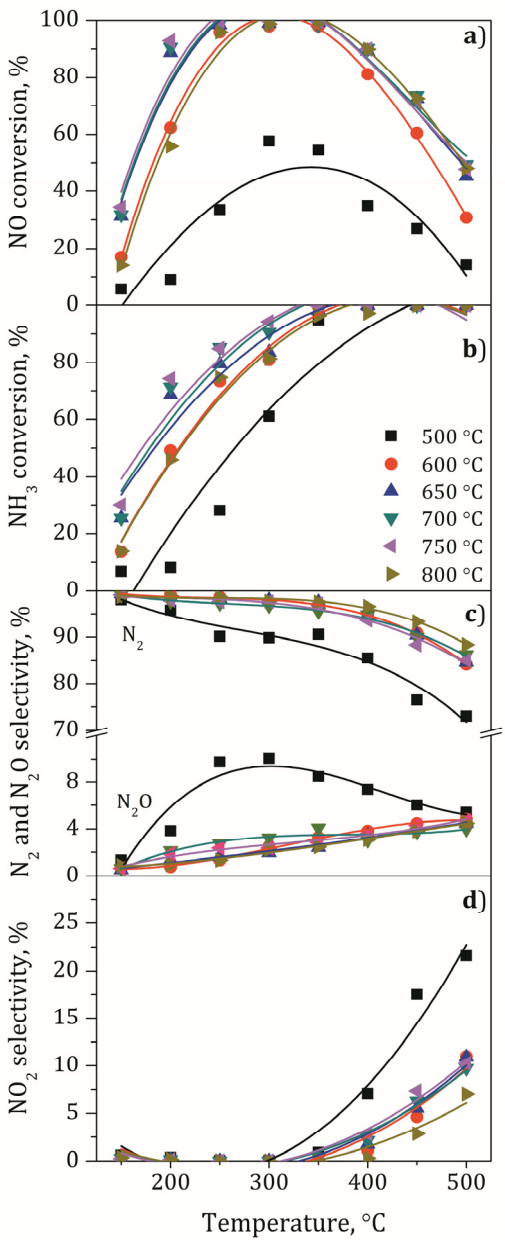

Figure 4.7. Evaluation of NH_3-SCR performance for samples prepared by SSIE at different temperature: a) NO conversion, b) NH_3 conversion, c) N_2 and N_2O selectivity and d) NO_2 selectivity. Reaction conditions: 660 ppm NO, 660 ppm NH_3 and 6% O_2 using Ar as a balance gas with a total flow rate of 2600 ml min^{-1} and 0.8 g of catalyst.

The NH_3 conversion (Figure 4.7b) follows a similar trend to that observed for NO, but specifically it can be observed that the sample prepared at 750 °C presents the highest NH_3 conversion in the whole studied temperature range. At high temperature the NH_3 oxidation reaction starts to prevail and thus total NH_3 conversion is obtained for temperatures of 400 °C and onwards for all the prepared catalysts [175, 200]. The reaction between NH_3 and oxygen reduces the availability of reductant, and consequently NO conversion starts to decrease for temperatures higher than 400 °C, as already observed in Figure 4.7a.

Figure 4.7c shows the selectivity to N_2 and N_2O whereas Figure 4.7d presents the selectivity to NO_2 in the studied temperature range. As can be observed, all prepared samples presented a high selectivity to nitrogen and a limited selectivity to N_2O. Selectivity to N_2 and N_2O are complementary up to 350 °C, while for higher temperatures the formation of NO_2 due to NO oxidation started to be significant. Focusing on N_2O selectivity, it can be observed a growing tendency as increasing reaction temperature but always below 5%. Specifically, the sample prepared at 500 °C presented a significantly higher N_2O selectivity showing a maximum of 10% around 300 °C, which is related to the decomposition of ammonium nitrate [201, 202]. Besides, this sample also presented a notably higher NO_2 selectivity, as high as 22% at 500 °C. Thus, it can be suggested that copper species also have a notable effect in the NH_3-SCR product distribution. Large copper aggregates favor the formation of N_2O and enhance the oxidation capacity of the sample promoting the selectivity to NO_2. On the other hand, copper ions, even if they are in a minor relative abundance with respect to aggregates or clusters, are able to drive the NH_3-SCR reaction selectively towards nitrogen.

4.1.2.2. Determination of the apparent activation energy and the turnover frequency

In order to better discern the NH_3-SCR activity of the prepared samples, additional reaction experiments were carried out in differential reactor regime. Before these experiments, internal and external diffusion resistances were analyzed (Figure 4.8). The experiments to evaluate the internal mass transfer resistance were carried out with 0.4 g of Cu/SAPO-34 catalyst and a gas stream composition of 660 ppm NO, 660 ppm NH_3 and 6% O_2 with a total flow rate of 2600 ml min^{-1} at 300 °C. The absence of internal mass transfer resistance can be assured for particle sizes lower than 0.3-0.5 mm (Figure 4.8a).

On the other hand, the experiments to evaluate the external mass transfer resistance were carried out varying the total flow rate and catalyst mass in order to maintain a constant W/F_{NO}^{in}, i.e. 94.9 g h mol^{-1}. The composition of the gas stream was 660 ppm NO, 660 ppm NH_3 and 6% O_2. Total flow rates above 2000 ml min^{-1} assured the absence of external mass transfer resistance (Figure 4.8b).

In order to determine the activation energy and turnover frequency (*TOF*) values for SSIE catalyst additional reaction experiments were carried out under differential regime. The experimental conditions were *GHSV*≃1,500,000 h^{-1}, $W/F_{NO}^{in} \simeq$ 14.4 $g_{cat.}$ h mol^{-1} and the NO conversion was below 15% in the whole studied temperature range. Then, the internal and external diffusion resistance experiments confirmed that under these experimental conditions the observed reaction rate is determined under a kinetically controlled regime (Figure 4.8). Thus, the reaction rate can be determined in a plug flow reactor, from the mass balance (Equation 4.1) applied in a differential catalyst weight element.

$$-dF_{NO} = \left(-r_{NO}\right) dW \tag{4.1}$$

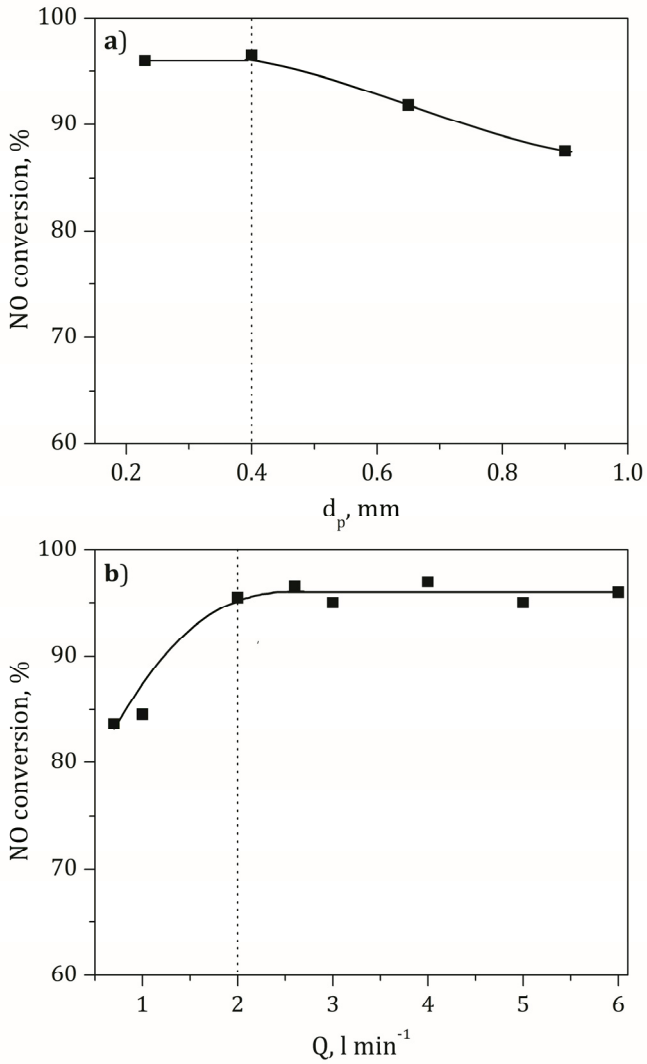

Figure 4.8. Evolution of NO conversion with catalyst particle size and total flow rate for evaluating internal (a) and external (b) mass transfer resistances.

$$-r_{NO} = -\frac{dF_{NO}}{dW} = F_{NO}^{in}\frac{dX_{NO}}{dW} = \frac{dX_{NO}}{d\left(W/F_{NO}^{in}\right)} \tag{4.2}$$

Under differential regime, when the NO conversion is below 15%, the reaction rate can be assumed uniform inside the short (differential) reactor, then the initial mean reaction rate approximates to Equation 4.3.

$$-r_{NO}^{0} = \frac{x_{NO}}{W/F_{NO}^{in}} \tag{4.3}$$

On the other hand, considering the usual functional kinetic equation, the initial reaction rate is dependent of temperature and concentration of reactants at the reactor inlet (Equation 4.4).

$$-r_{NO}^{0} = k(T)f(C_{NO}^{0}C_{NH_3}^{0}C_{O_2}^{0}) \tag{4.4}$$

Introducing the dependence of the kinetic constant with temperature (Arrhenius equation) and after rearrangement, Equation 4.5 is deduced.

$$-r_{NO}^{0} = A\exp\left(-\frac{E_a}{RT}\right)f\left(C_{NO}^{0}C_{NH_3}^{0}C_{O_2}^{0}\right) = A_{ap}\exp\left(-\frac{E_a}{RT}\right) \tag{4.5}$$

which can be linearized as $\ln\left(-r_{NO}^{0}\right)$ vs. $1/T$ allowing calculation of an apparent activation energy (E_a).

The reaction rate normalized per mol of copper has also been calculated in order to compare the activity of the prepared samples, $-r_{NO}^{'}$ (mol NO $molCu^{-1}h^{-1}$). Also, turnover frequency (*TOF*) has been studied (Equation 4.6) based on the amount of isolated copper ions (Cu^{2+} and Cu^{+}) or alternatively based on the amount of only Cu^{2+} ions.

$$TOF\left(\frac{\text{molNO}}{\text{molCuh}}\right) = \frac{-r_{NO}}{N_{Cu_{ion}}/W} \tag{4.6}$$

Table 4.4 shows the experimental values obtained for the conversion of NO_x at different temperatures for SSIE 4% Cu/SAPO-34 catalyst. Also, the reaction rate normalized per mol of copper, the apparent activation energy deduced from Figure 4.9 and turnover frequencies based on the amount of copper ions or Cu^{2+} ions are collected.

Figure 4.9 shows the Arrhenius plot in order to calculate the apparent activation energy and as can be observed, irrespective of the temperature at which SSIE was carried out, the apparent activation energy resulted in around 40 kJ mol^{-1} (with the exception of 500 °C), which means that the NH_3-SCR reaction proceeds through the same reaction mechanism. The observed activation energy is very close to that reported by Hu et al. [203] with Cu/SAPO-34 catalysts prepared by one pot synthesis and different crystal size of zeolite, i.e. 44.8 kJ mol^{-1}. Besides, Hu et al. [203] collected different activation energies from other works [164, 167, 182, 185, 204, 205] using Cu/SAPO-34 catalysts at different reaction temperature (100-225 °C) and copper loading (0.35-6.78 wt.%) revealing that all were situated between 34 and 45 kJ mol^{-1}. Specifically, the sample prepared by SSIE at 500 °C presented lower activation energy of 28 kJ mol^{-1}. Specific experiments were carried out with this sample to verify the absence of internal diffusion limitations. Changes in the activation energy at low temperatures (<250 °C) was also reported by Gao et al. [183], who justified this observation by assuming that different type of active centers or locations were affecting the kinetic analysis. In this sense, we can speculate that the different activation energy observed for the sample prepared by SSIE at 500 °C is due to the presence of large copper aggregates as the unique active center.

In order to complete the kinetic analysis, the reaction rate normalized per mol of copper and turnover frequencies (*TOF*) were calculated (Equation 4.6 and Table 4.4). Some papers [80, 182, 206] have used the reaction rate normalized per mol of copper to compare the NH_3-SCR activity, whereas some other papers [79, 203] have used the turnover frequency based on the amount

Table 4.4. Apparent activation energy (E_a) and turnover frequency (*TOF*) values calculated in differential reactor regime for SSIE catalysts. $W/F_{NO}^{in} \approx 14.4$ g h mol^{-1}.

Catalyst	T, °C	X_{NO}, %	$-r'_{NO}$, mol NO h^{-1} mol$_{Cu}^{-1}$	E_a, kJ mol^{-1}	*TOF*, h^{-1}	
					Cu ions	Cu^{2+} ions
SSIE 500 °C	230	6.7	6.3	28		
	240	7.4	7.1			
	250	8.3	8.1			
	260	9.5	9.2			
	270	10.3	10.1			
	280	11.6	11.5			
	290	13.1	13.0			
	300	14.5	14.4			
SSIE 600 °C	180	5.7	5.9	37	26.6	32.6
	190	6.6	6.8		31.0	37.9
	200	7.9	8.2		37.1	45.3
	210	10.6	10.9		49.5	60.5
	220	12.3	12.7		57.7	70.5
	230	14.7	15.1		68.8	84.1
SSIE 650 °C	180	6.4	6.7	42	24.1	26.9
	189	7.5	7.8		27.9	31.3
	201	9.5	9.9		35.6	39.9
	210	12.6	13.2		47.2	52.8
	220	16.4	16.5		58.9	66.0
SSIE 700 °C	170	8.6	8.1	38	23.2	24.6
	180	10.8	11.3		32.2	34.2
	190	11.9	12.5		35.8	37.9
	200	15.5	16.2		46.2	48.9
SSIE 750 °C	180	7.1	7.5	38	24.1	27.7
	190	8.3	8.8		28.3	32.5
	200	10.2	10.7		34.7	39.8
	210	13.0	13.8		44.1	50.6
	220	16.0	16.8		54.3	62.4
SSIE 800 °C	190	6.6	6.7	42	29.2	39.5
	200	7.5	7.6		33.0	44.7
	210	10.5	10.7		46.3	62.6
	220	13.4	13.5		58.8	79.5
	230	15.5	14.8		64.2	86.8

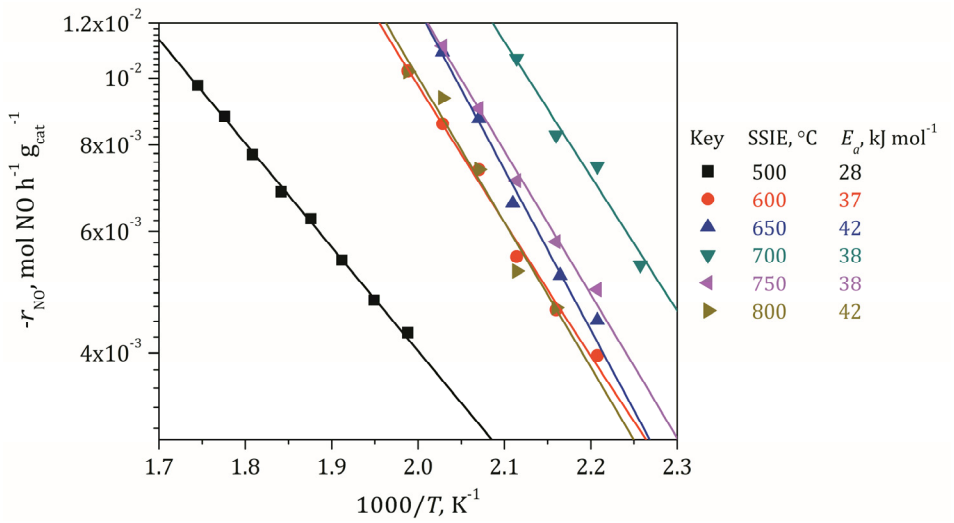

Figure 4.9. Arrhenius plot for the determination of the activation energy for samples prepared by SSIE at different temperature. Reaction conditions: 660 ppm NO, 660 ppm NH_3 and 6% O_2 using Ar as a balance gas with a total flow rate of 6000 ml min^{-1} and 0.15 g of catalyst.

of the copper ions. In the present study, we have calculated both kinetic parameters. On one hand, the moles of NO converted per hour (in differential reaction regime) have been divided by the total moles of Cu in the catalyst to calculate ($-r'_{NO}$). On the other hand, the moles of NO converted per hour have been divided by the total amount of copper ions (Cu^{2+} and Cu^{+}) or Cu^{2+} quantitatively determined by H_2-TPR (Table 4.2), resulting in the *TOF* values reported in Table 4.4.

Figure 4.10a shows the evolution of ($-r'_{NO}$) at 200 °C for catalyst prepared by SSIE at different temperatures. As can be observed, the evolution of ($-r'_{NO}$) with SSIE temperature presents a maximum for a catalyst calcined at 700 °C (16.2 h^{-1}). Note that ($-r'_{NO}$) profile is very well correlated with the proportion of copper ions, which resulted maximum (33% Cu^{2+}) for the sample prepared

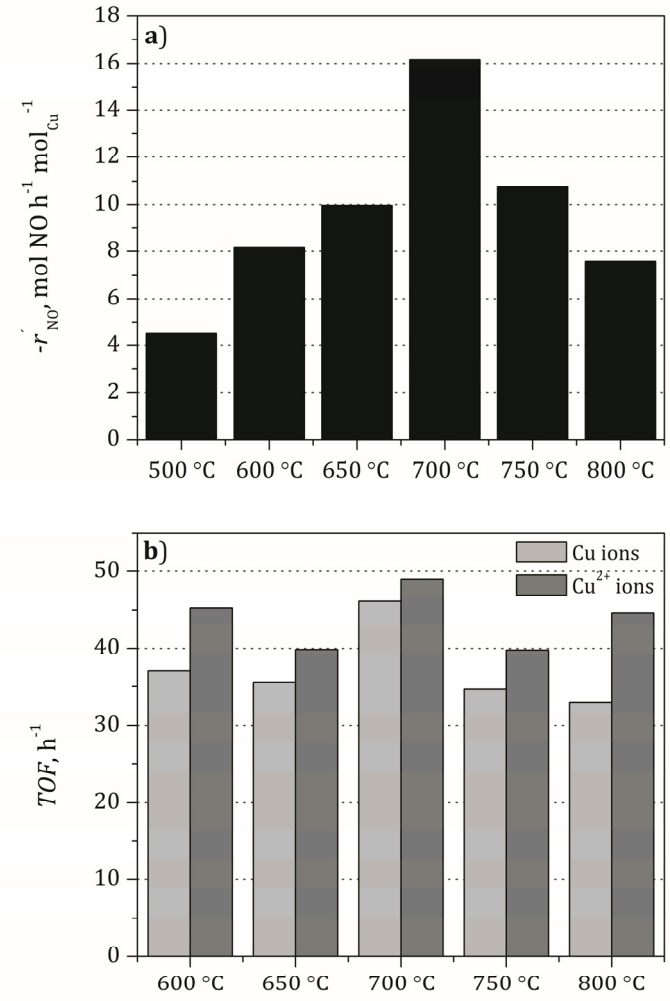

Figure 4.10. Evolution of reaction rate and turnover frequencies at 200 °C as a function of SSIE temperature when reaction rate is referred to the total amount of copper (a) and when *TOF* is referred to the amount of copper ions quantified by H_2-TPR (b). Reaction conditions: 660 ppm NO, 660 ppm NH_3, 6% O_2 using Ar as a balance gas with a total flow rate of 6000 ml $min^{-1}$and 0.15 g of catalyst.

at 700 °C. Thus, it can be deduced that Cu^{2+} ions are the main active species for NH_3-SCR, although large copper aggregates also presented some activity based on ($-r'_{NO}$) calculation for the sample calcined at 500 °C (4.4 h^{-1}). Figure 4.10b shows the evolution of *TOF* referred to the amount of copper ions or Cu^{2+} ions for the prepared samples except for that calcined at 500 °C due to the absence of copper ions. As can be observed, similar *TOF* values are obtained, which suggest that copper ions are the main active specie for NH_3-SCR.

4.2. COPPER LOADING EFFECTS ON Cu/SAPO-34 CATALYST PREPARED BY LIE AND SSIE

In the following section, four Cu/SAPO-34 catalysts were prepared by liquid ion exchange (LIE) and subsequent calcination at 500 °C. Different copper concentrations were used in the starting solution in order to get nominal contents of 1, 2, 4 and 10% copper in the prepared samples. On the other hand, five Cu/SAPO-34 catalysts were prepared by SSIE at the optimal synthesis temperature deduced in the previous section, i.e. 700 °C, with a nominal copper loading of 2, 4, 6, 8 and 10 wt.%.

4.2.1. Catalyst characterization

4.2.1.1. Composition and textural properties

Table 4.5 resumes the composition, the copper loading and BET surface area of the prepared samples by SSIE and LIE. As can be observed in Table 4.5, Si, Al and P contents are similar for Cu/SAPO-34 catalysts prepared by LIE and SSIE. On the other hand, small quantities of Na can be detected for catalyst prepared by LIE, due to the intermediate exchange with sodium nitrate. It is worth to note that actual copper contents are similar to the nominal values for SSIE catalysts, whereas copper incorporation by LIE is not favored for high loadings.

Table 4.5. Copper loading, composition and BET surface area of samples prepared by LIE and SSIE.

Preparation method	Nominal Cu loading, %	Composition wt., %						Surface area, $m^2\ g^{-1}$
		Cu	Si	Al	P	Na	O	
H-SAPO-34	-	-	4.5	19.4	18.2	0.1	57.0	600
LIE	1	1.1	4.9	21.4	20.0	0.4	51.3	504
	2	1.7	4.9	21.2	19.9	0.3	51.0	517
	4	2.2	4.9	21.0	19.7	0.3	50.8	509
	10	3.6	4.8	20.7	19.4	0.2	50.3	489
SSIE	2	1.9	5.2	21.6	19.2	0	50.9	483
	4	3.7	5.1	20.7	19.0	0	50.1	397
	6	5.8	4.9	20.0	18.3	0	49.1	322
	8	7.9	4.9	19.4	17.8	0	48.3	190
	10	9.8	5.0	18.8	17.0	0	47.5	44

BET surface area slightly decreases after LIE procedure with respect to bare zeolite (600 $m^2\ g^{-1}$). However, Cu loading does not have a great impact on surface area, which is maintained in the range 472-517 $m^2\ g^{-1}$, with a slight tendency to decrease with increasing the Cu loading. When samples with similar Cu content prepared by LIE and SSIE are compared, it can be observed that specific surface area is notably higher for samples prepared by LIE. Specifically, the sample prepared by LIE with the actual copper loading of 3.6% presented a specific surface area of 489 $m^2\ g^{-1}$, which is notably higher than that presented by the sample prepared by SSIE with an actual copper loading of 3.7%, 397 $m^2\ g^{-1}$. Note that specific surface area critically decreases for copper loadings higher than 4% in samples prepared by SSIE. In fact, the specific surface area of the sample with a nominal copper loading of 10% decreases to 44 $m^2\ g^{-1}$.

4.2.1.2. Phase identification and copper particle size

Figure 4.11 shows XRD diffraction patterns of prepared LIE and SSIE samples. XRD patterns confirmed that H-SAPO-34 framework was maintained unaltered after LIE, without significant crystallinity loss, irrespective of Cu loading. Furthermore, CuO characteristic diffraction peaks, located at 35.5 and 38.5° 2θ, were not detected even for high copper loaded catalyst, suggesting that isolated copper ions or highly dispersed Cu_xO_y clusters, both beyond XRD detection limit [180, 181], are the predominant copper species in the samples prepared by LIE. On the other hand, all catalysts prepared by SSIE presented

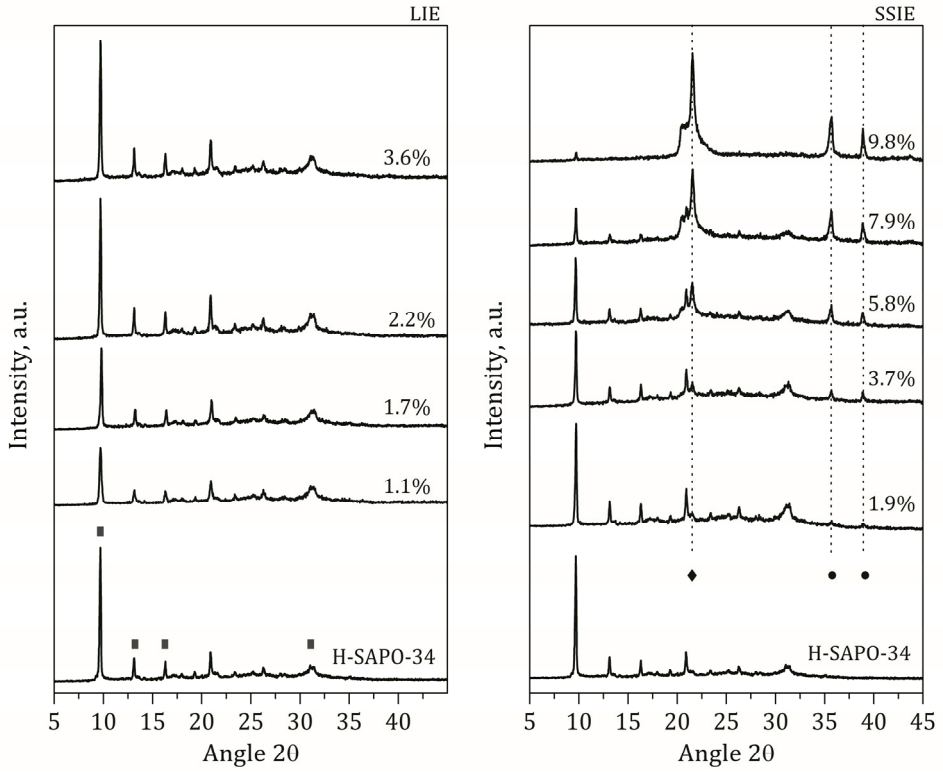

Figure 4.11. XRD diffractograms of LIE (a) and SSIE (b) catalysts with different copper loading.

diffraction peaks attributed to CuO with increasing intensity as increasing copper loading. Besides, all catalysts presented some SiO_2 segregation detected at 21° 2θ. The intensity of that diffraction peak increased with copper loading, revealing that high copper content notably favors the collapse of the zeolite structure, which can also be evidenced by the almost total disappearance of the main diffraction peak of H-SAPO-34 situated at 10° 2θ.

Figure 4.12 shows SEM images of catalysts prepared by LIE and SSIE. On one hand, it was difficult to find copper aggregates by SEM in low copper loaded samples prepared by LIE. In particular, only two large CuO aggregates with a particle size around 1 μm were observed for 1.7% Cu/SAPO-34 catalyst (Figure 4.12a). The picture changed radically for 3.6% Cu/SAPO-34 catalyst, where a very large number of CuO particles were easily distinguishable

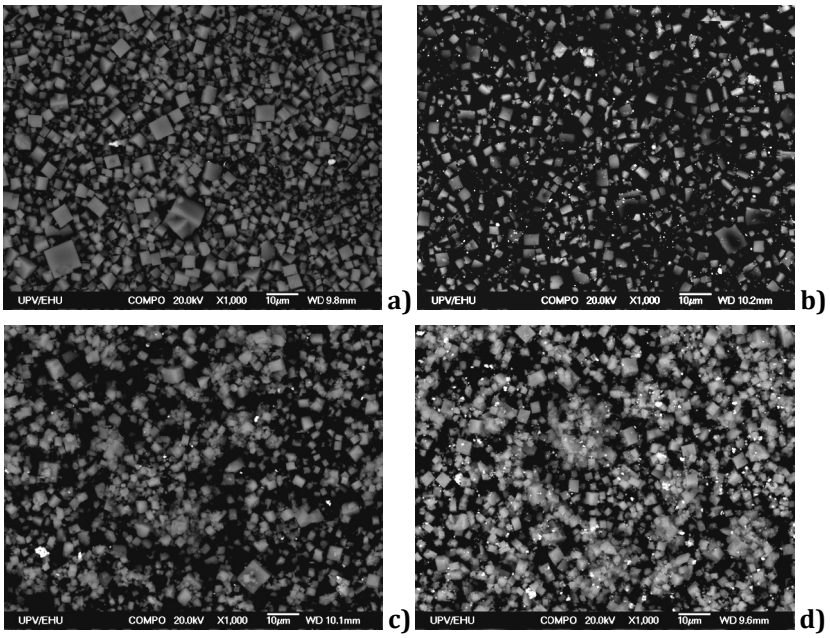

Figure 4.12. SEM images for Cu/SAPO-34 catalyst prepared by LIE with a copper loading of 1.7% (a) and 3.6% (b) and SSIE with a copper loading of 1.9% (c) and 9.8% (d).

(Figure 4.12b). On the other hand, numerous large copper particles were evident even for low copper loaded catalyst prepared by SSIE (1.9% Cu/SAPO-34, Figure 4.12c), and the number of those aggregates further increased with copper loading (9.8% Cu/SAPO-34, Figure 4.12d). From Figure 4.12 it can be also inferred that SSIE reduces the cristallinity of the zeolite (as already observed by XRD), as the perfect cubic crystals observed for catalysts prepared by LIE tend to became much more irregular after the temperature treatment during SSIE.

4.2.1.3. Cu^{2+} identification by EPR

EPR spectra for samples prepared by LIE and SSIE are displayed in Figure 4.13a and Figure 4.13b, respectively. Catalysts prepared by LIE presented a unique feature at high field and well resolved copper hyperfine features at low fields. On the contrary, samples prepared by SSIE presented an additional feature at high field (3323 G) for samples with a copper loading above 6%, whose intensity increases with copper loading and can be related to the presence of copper aluminate. The copper ions signal intensity calculated by the double integral can be observed in the inset of each figure. As can be observed, Cu^{2+} signal intensity increases linearly for samples prepared by LIE up to a copper loading of 1.7 wt.%, whereas for higher copper loadings, the signal intensity tends to saturate, indicating that almost all the exchangeable locations of the zeolite have already been occupied and only few more copper ions can be included by LIE. A similar trend was observed for samples prepared by SSIE, but instead the signal intensity increased linearly up to a copper loading of 3.7 wt. %. A higher copper loading did not result in a signal intensity increase, which also reveals an upper limit in order to incorporate copper ions by SSIE.

4.2.1.4. Redox properties and copper species quantification

Figure 4.14 shows H_2 consumption profiles during temperature programmed reduction (H_2-TPR) experiments for Cu/SAPO-34 catalysts

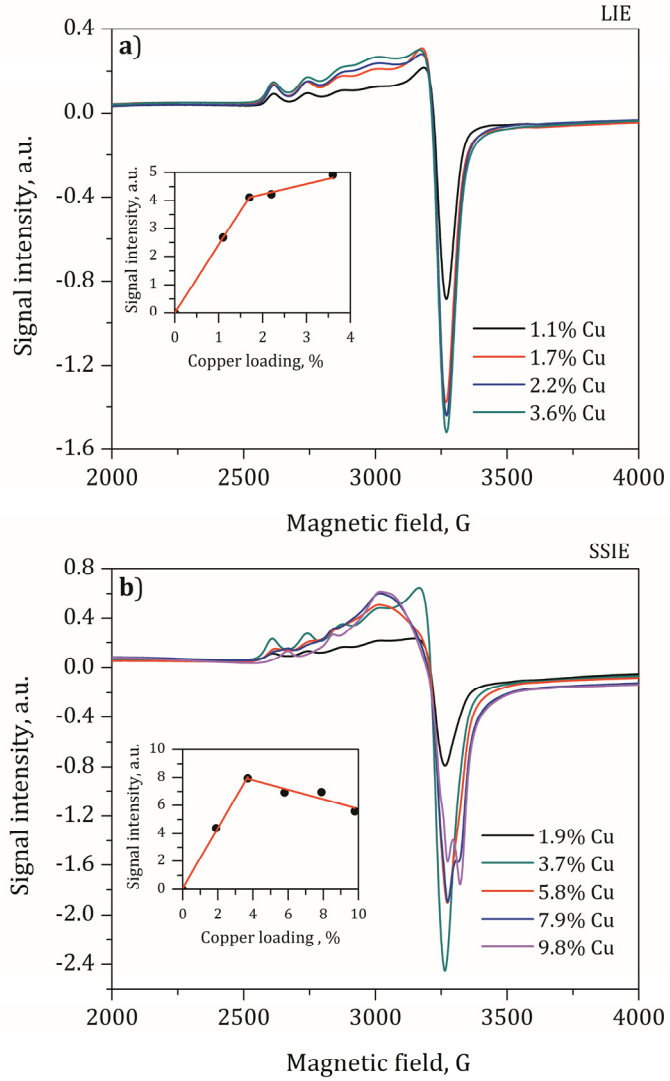

Figure 4.13. EPR spectra for Cu/SAPO-34 catalyst prepared by LIE (a) and SSIE (b) with varying copper loading. The inset figures represent the signal intensity calculated by double integral of the original signal in the 2500-3500 field range.

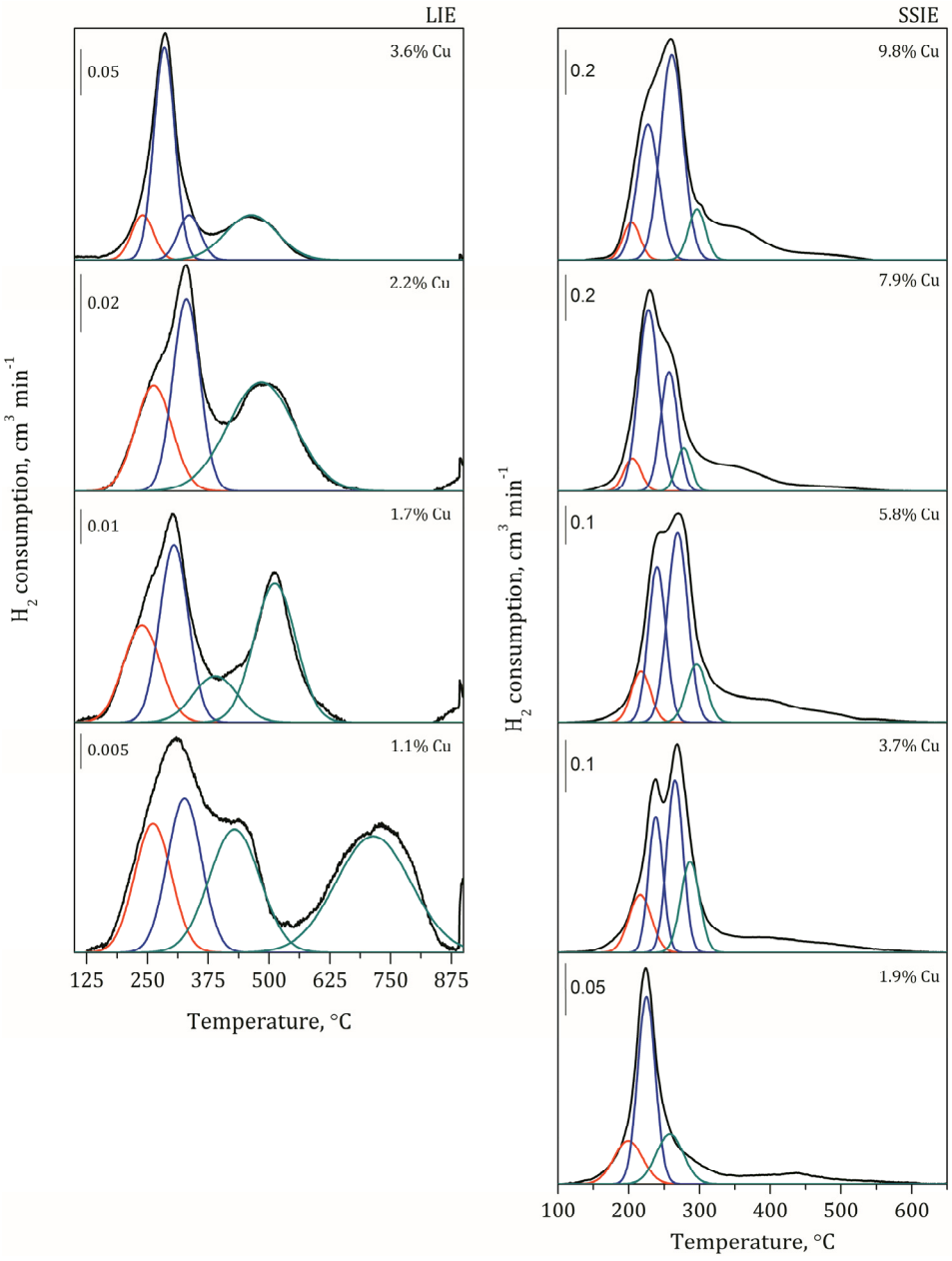

Figure 4.14. H_2 consumption profiles during H_2-TPR experiments for Cu/SAPO-34 catalyst prepared by LIE (left) and SSIE (right) with different copper loading.

prepared by LIE and SSIE with different copper loading. Focusing on samples prepared by LIE and following the previous assignation, the low temperature peak (240 °C) was ascribed to the reduction of Cu^{2+} ions to Cu^{+}. At higher temperature (300 °C) reduction of small copper clusters to metallic copper occurred in a single step ($CuO \rightarrow Cu^0$) and for high copper loading samples, additional hydrogen consumption was observed at somewhat lower temperatures (280 °C) due to reduction of large copper aggregates. Final reduction of Cu^{+} ions to Cu^0 was affected by copper loading. Cu/SAPO-34 catalyst with copper loadings higher than 1.7% presented a single reduction contribution around 480 °C. On the other hand, two contributions were needed in order to describe $Cu^{+} \rightarrow Cu^0$ reduction in low copper loaded Cu/SAPO-34 catalysts and furthermore Cu^{+} ions reduction required higher temperatures. In fact, highly stable Cu^{+} ions (namely H-Cu^{+}) reduction occurred at temperatures as high as 790 °C for 1.1% Cu/SAPO-34 catalyst, which has already been reported in literature [207, 208]. Torre-Abreu et al. [189] have also reported the ease of Cu^{+} ions reduction with increasing copper loading.

Table 4.6 shows hydrogen consumption quantification for each reduction step in LIE catalysts, i.e. $Cu^{2+} \rightarrow Cu^{+}$, $CuO \rightarrow Cu^0$ and $Cu^{+} \rightarrow Cu^0$ and the proportion of copper species based on previous H_2 consumption and reduction stoichiometry. Isolated Cu^{2+} and Cu^{+} ions were predominant in low copper loading samples, whereas the proportion of CuO clusters progressively increased at the expense of copper ions while copper content was increased. This fact reveals a limited quantity of exchangeable sites in H-SAPO-34 zeolite in order to accommodate copper ions, in line with EPR results.

Figure 4.14 also includes H_2-TPR experiments for Cu/SAPO-34 samples prepared through SSIE with different copper loading. The H_2 consumption contributions have been assigned, as in the previous section with SSIE catalysts calcined at different temperatures, to reduction of Cu^{2+} ions to Cu^{+}, reduction of large CuO aggregates to Cu^0, reduction of small CuO clusters to

Table 4.6. Quantification of H_2 consumption attributed to the reduction of different copper species along with copper species distribution and the H_2/Cu ratio for catalysts prepared by LIE.

Preparation method	Cu wt., %	H_2 consumption due to, μmol g^{-1}			Cu species distribution, %			H_2/Cu
		$Cu^{2+} \rightarrow Cu^0$	$CuO \rightarrow Cu^0$	$Cu^{+} \rightarrow Cu^0$	Cu^{2+}	CuO	Cu^{+}	
LIE	1.1	21.3	25.5	64.2	28	17	56	0.57
	1.7	61.1	84.5	136.1	34	24	42	0.87
	2.2	63.2	90.4	125.3	37	27	36	0.83
	3.6	58.9	292.3	133.8	21	52	27	0.87

Cu^0 and reduction of Cu^+ ions to Cu^0 with increasing reduction temperature. Figure 4.14 allows a proper comparison between hydrogen reduction profiles of samples prepared by LIE and SSIE. The main difference between both preparation methods is that reduction of Cu^{2+} and more notably reduction of Cu^+ ions, occurred at lower temperature for samples prepared by SSIE. We suggest that LIE preparation methodology incorporates more specifically copper ions at exchangeable sites with a higher interaction with the support, e.g. at 6dr windows of CHA structure, which hinders their reduction. On the other hand, SSIE preparation methodology incorporates copper ions at CHA cages, which facilitates their reduction. Table 4.7 also includes the copper species distribution for samples prepared by SSIE. As can be observed, low copper content sample presents the highest proportion of copper ions, although small copper clusters are the predominant species. With increasing copper loading the proportion of copper ions decreased in favor of copper aggregates and clusters. Finally, the proportion of $CuAl_2O_4$ is similar because the same calcination protocol was used for all prepared samples and, as deduced from the previous section, copper aluminate formation is only promoted by the temperature at which the SSIE procedure took place. In this sense, copper aluminate is not detected in samples prepared by LIE due to the lower calcination temperature, i.e. 500 °C.

UV-vis DRS spectra were analyzed in the prepared LIE and SSIE samples with different copper loading, whose spectra are shown in Figure 4.15. As previously observed in Figure 4.5, two characteristic absorption bands were observed. The adsorption band at 240 nm is attributed to a charge transfer band of the zeolite. Other absorption band attributed to CuO (300-800 nm) could be observed. This band (300-800 nm) increases with copper loading for LIE and SSIE catalysts. The absorbance of this band is higher for SSIE catalysts than LIE catalysts due to the higher amount of copper aggregates. On the other hand, electron d-d transitions of Cu^{2+} in distorted octahedral coordination surrounded by oxygen in dispersed CuO particles can be observed in the wavelength range of 600-800 nm. The absorbance of this region increases

Table 4.7. Quantification of H_2 consumption attributed to the reduction of different copper species along with copper species distribution and the H_2/Cu ratio for catalysts prepared by SSIE.

Preparation method	Cu wt., %	H_2 consumption due to, μmol g^{-1}					Cu species distribution, %					H_2/Cu
		$Cu^{2+} \rightarrow Cu^0$	$CuO \rightarrow Cu^0$, aggregates	$CuO \rightarrow Cu^0$, clusters	$Cu^+ \rightarrow Cu^0$	$CuAl_2O_4$	Cu^{2+}	CuO, aggregates	CuO, clusters	Cu^+	$CuAl_2O_4$	
SSIE	1.9	40.3	115.4	-	46.3	38.8	33	47	-	5	16	0.80
	3.7	78.5	133.9	176.2	109.5	88.3	25	22	29	10	14	0.93
	5.8	84.3	299.7	264.4	90.1	173.5	18	33	29	1	19	0.87
	7.9	89.9	492.9	376.7	116	182.8	14	38	29	4	14	0.89
	9.8	92.1	430.3	512.1	120.4	290.2	13	29	35	4	20	0.90

with copper loading for catalysts prepared by LIE and SSIE, revealing a preferential formation of copper aggregates.

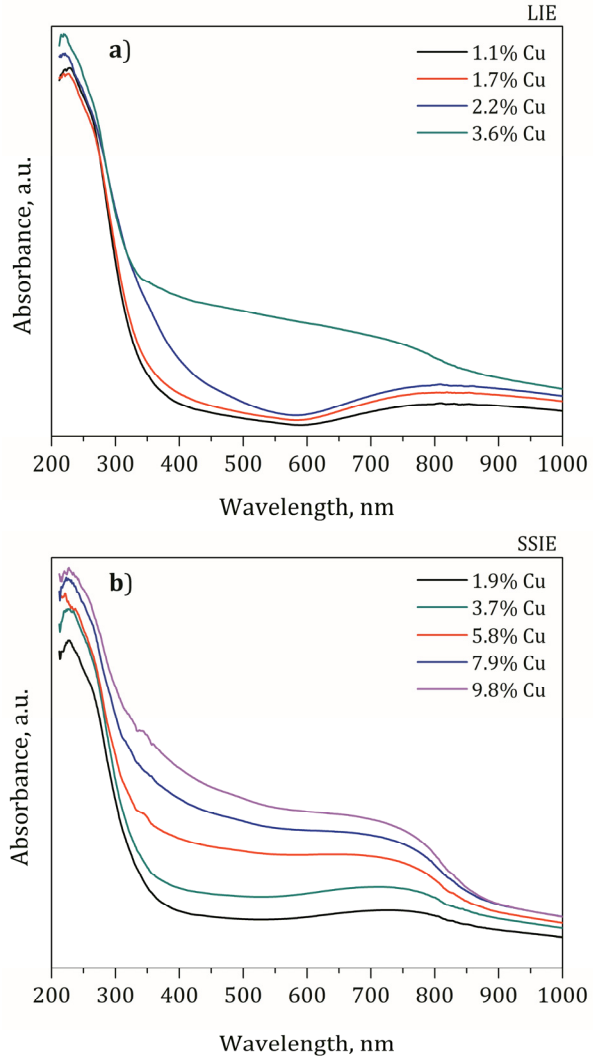

Figure 4.15. UV-vis spectra of LIE (a) and SSIE (b) catalysts.

4.2.1.5. Acidity

Figure 4.16 shows NH_3 desorption profiles for Cu/SAPO-34 catalysts prepared by LIE and SSIE with different copper loading. It can be observed that in all LIE samples there is an NH_3 desorption peak at low temperature related to weak Brønsted acid sites at surface hydroxyls. When the copper amount was increased, two NH_3 desorption peaks appeared, which were related to Lewis acid sites.

In SSIE catalysts the NH_3 desorption peaks at low and high temperatures decreased with the copper loading. The partial blockage of the pores of the support by CuO species decreased the accessibility to Lewis and Brønsted acid sites.

Table 4.8 shows the total acidity of LIE and SSIE samples determined by NH_3-TPD experiments. As can be seen for LIE catalysts, the total acidity increased with copper loading up to 2.2% Cu. This fact is attributed to the formation of Cu^{2+} ions which increased the amount of Lewis acid sites that participate in the storage of NH_3. However, the total acidity of the samples started to decrease for higher copper loadings due to the preferential formation of CuO agregates (Table 4.8).

Table 4.8. Total acidity of samples prepared by LIE and SSIE methods.

LIE	
Catalyst	Acidity, μmol NH_3 g^{-1}
1.1 % Cu	1112.2
1.7 % Cu	1652.9
2.2 % Cu	1647.1
3.6 % Cu	1543.2

SSIE	
Catalyst	Acidity, μmol NH_3 g^{-1}
1.9% Cu	1402.7
3.7% Cu	1348.5
5.8% Cu	1533.3
7.9% Cu	990
9.8% Cu	399.3

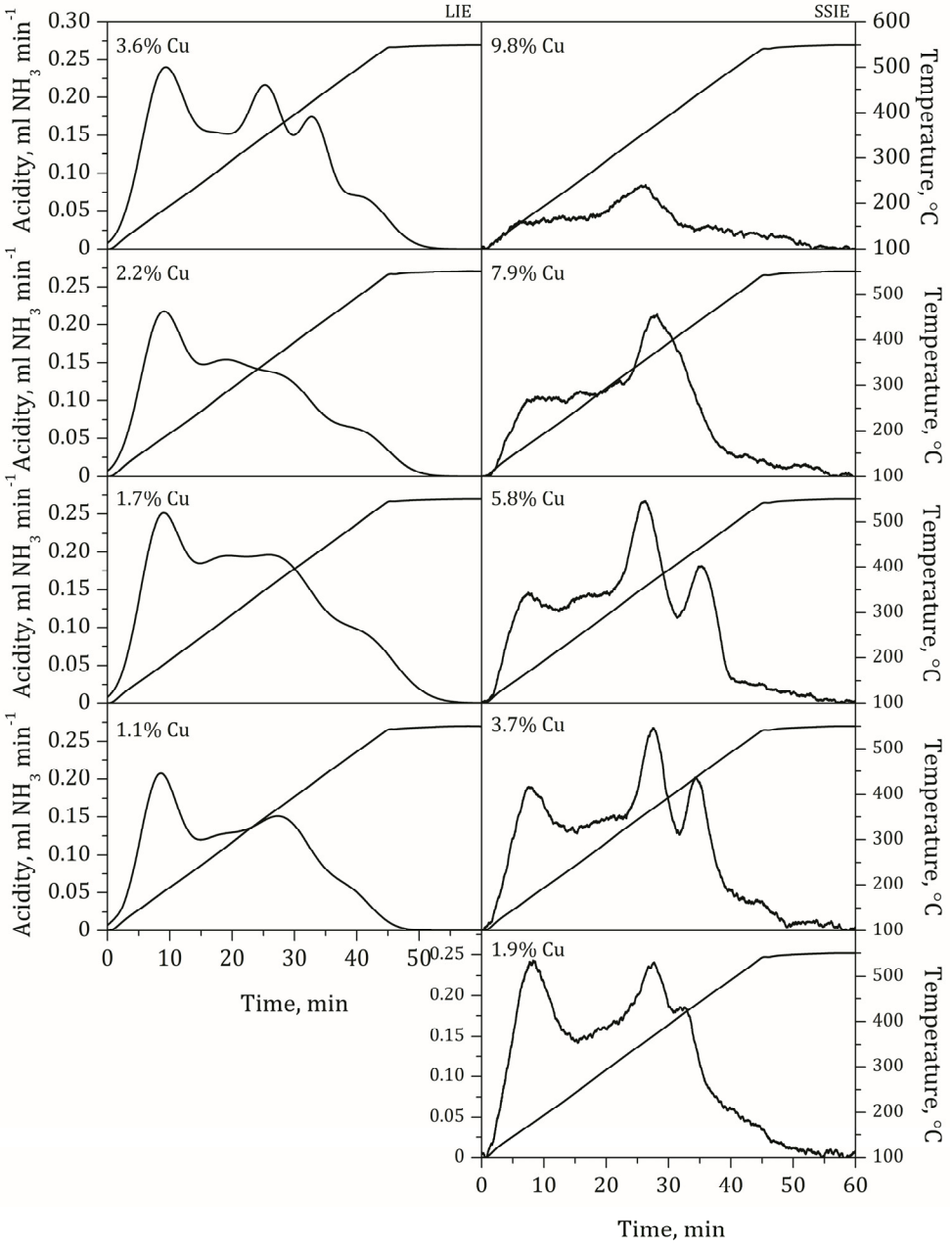

Figure 4.16. NH_3-TPD results of Cu/SAPO-34 catalysts prepared by LIE (left) and SSIE (right) methods.

The acidity of the samples prepared by SSIE was maintained almost constant for copper loadings of 1.9, 3.7 and 5.8. Higher loadings penalized the acidity due to the partial destruction of the zeolite framework as observed by XRD.

4.2.2. NH_3-SCR performance

4.2.2.1. Influence of the reaction temperature on the activity and selectivity

The NH_3-SCR activity of samples prepared by LIE and SSIE with different copper loading has been collected in Figure 4.17. The catalysts were exposed to 660 ppm NO, 660 ppm NH_3 and 6% O_2 using Ar as balance gas with a total flow rate of 2600 ml min^{-1}. A clear promotion of low temperature NH_3-SCR activity can be observed for LIE catalyst with increasing copper loading from 1.1% to 2.2%, as already reported in a previous work [168] for BETA and ZSM-5 zeolites. The promotion of low temperature NH_3-SCR activity for SSIE catalyst with increasing copper loading was not so evident and only a slight promotion of NO conversion was observed from 1.9% to 3.7% of Cu. It is worth to note that SSIE preparation methodology resulted in more active Cu/SAPO-34 catalyst for low temperature NH_3-SCR in comparison to those prepared by LIE. For example, at 200 °C, NO conversion was 41% for 1.7% Cu/SAPO-34 catalyst prepared by LIE, whereas NO conversion increased up to 74% for 1.9% Cu/SAPO-34 catalyst prepared by SSIE. On the contrary, catalysts prepared by LIE presented a better high temperature NH_3-SCR performance than SSIE. This behavior can be explained by the different copper species present in catalysts prepared by both methodologies. On one hand, the main copper specie for catalysts prepared by SSIE methodology is CuO (aggregates or clusters), which can catalyze the oxidation of NO to NO_2 readily at low temperature and thus activate the fast NH_3-SCR reaction. However, the promotion of the oxidation capacity implies some other drawbacks, as NH_3

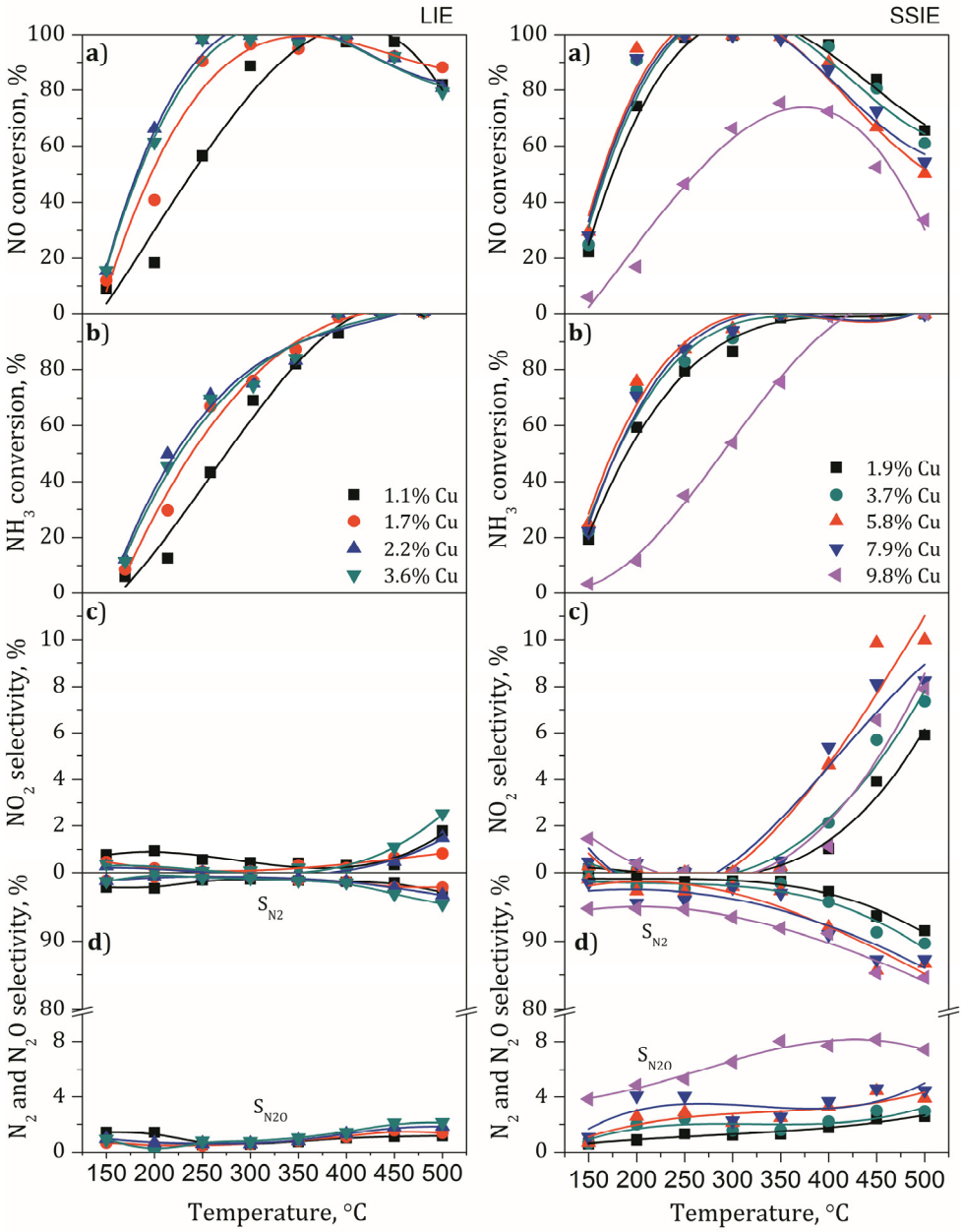

Figure 4.17. Evaluation of NH_3-SCR performance for samples prepared by LIE and SSIE with different copper loading. a) NO conversion, b) NH_3 conversion, c) NO_2 d) N_2 and N_2O selectivity. Reaction conditions: 660 ppm NO, 660 ppm NH_3 and 6% O_2 using Ar as a balance gas with a total flow rate of 2600 ml min^{-1}. *GHSV*=86,500 h^{-1}.

oxidation starting to be significant at intermediate temperatures and thus penalizing high temperature NH_3-SCR activity. On the other hand, copper ions are the main copper species for catalysts prepared by LIE, specifically those with low copper loading. Copper ions are not so active in catalyzing the oxidation of NO to NO_2 and consequently are less active at low temperature, but on the other hand, higher NH_3-SCR activity was maintained at high temperature.

As can be observed in Figure 4.17c, the SSIE catalysts present a higher selectivity to NO_2 than LIE catalysts and this is clearly observed above 350 °C. The reason for higher NO_2 selectivity in SSIE catalysts is the higher oxidation capacity and the higher copper amount in SSIE catalysts than in LIE catalysts. Focusing on N_2O and N_2 selectivities (Figure 4.17d), it can be observed a growing tendency as increasing reaction temperature but always below 4% for LIE and below 9% for SSIE catalysts. Specifically, the 9.8% Cu/SAPO-34 (SSIE) sample presented a higher N_2O selectivity which is related to the higher amount of larger copper aggregates. The selectivity to N_2 for LIE catalysts is above 95% and for SSIE is above 84% at all range of temperature. As it could be observed for selectivities of N_2O and NO_2, the LIE catalysts show better selectivity to N_2 due to the higher amount of copper ions than aggregates.

4.2.2.2. Determination of the activation energy and the turnover frequency

The NH_3-SCR reaction activation energy for samples prepared by LIE and SSIE with different copper loadings were calculated from experiments carried out at differential reactor regime as it was explained in 4.1.2.2. section. Table 4.9 and 4.10 show the obtained results of NO conversion and the reaction rate to obtain the apparent activation energy (E_a) and turnover frequency (*TOF*) values for LIE catalysts and SSIE catalysts, respectively. The catalysts were exposed to 660 ppm NO, 660 ppm NH_3 and 6% O_2 using Ar as balance gas with a total flow rate of 6000 ml min^{-1} Ar. The results can be observed in Figure 4.18. The activation energy was situated around 40-47 kJ mol^{-1} for samples prepared by LIE whereas a slightly lower values were observed for SSIE,

Table 4.9. The experimental values for catalysts prepared by LIE to obtain the apparent activation energy and *TOF* values. $W / F_{NO}^{in} \approx 14.4$ g h mol^{-1}.

Catalyst	T, °C	X_{NO}, %	$-r'_{NO}$, mol NO h^{-1} mol$_{Cu}^{-1}$	E_a, kJ mol^{-1}	*TOF*, h^{-1}	
					Cu ions	Cu^{2+} ions
1.1% Cu/SAPO-34	190	4.9	17.5	19	20.8	62.3
	200	5.1	17.9		21.4	64.1
	210	5.9	21.1		25.1	75.4
	220	6.1	22.3		26.5	79.6
	230	7.0	25.7		30.6	91.8
1.7% Cu/SAPO-34	190	5.2	12.8	42	16.9	37.7
	200	6.1	15.1		19.9	44.4
	210	7.5	18.6		24.5	54.7
	220	9.8	24.2		31.8	71.1
	230	12.2	30.3		39.8	89.0
2.2% Cu/SAPO-34	190	4.7	9.1	47	12.5	24.6
	200	5.4	10.6		14.5	28.7
	210	7.2	14.1		19.3	38.0
	220	10.1	19.9		27.2	53.7
	230	14.8	23.1		31.7	62.5
3.6% Cu/SAPO-34	190	6.6	8.0	47	16.7	38.2
	200	7.7	9.3		19.5	44.5
	210	9.4	11.4		23.8	54.4
	220	12.4	15.1		31.5	72.1
	230	17.5	21.3		44.4	101.4

Table 4.10. The experimental values for catalysts prepared by SSIE to obtain the apparent activation energy and *TOF* values. $W/F_{NO}^{in} \approx 14.4$ g h mol^{-1}.

Catalyst	T, °C	X_{NO}, %	$-r'_{NO}$, mol NO h^{-1} mol$_{Cu}^{-1}$	E_a, kJ mol^{-1}	*TOF*, h^{-1}	
					Cu ions	Cu^{2+} ions
1.9% Cu/SAPO-34	170	6.9	15.8	37	41.5	47.8
	180	7.9	18.1		47.7	54.9
	190	9.3	21.3		56.1	64.6
	200	11.9	27.6		72.5	83.5
	210	15.6	35.9		94.6	108.9
3.7% Cu/SAPO-34	170	8.7	10.4	38	29.6	41.4
	180	10.4	12.4		35.4	49.6
	190	12.9	15.5		44.1	61.8
	200	16.7	19.9		56.8	79.5
5.8% Cu/SAPO-34	170	7.3	5.6	34	29.5	31.1
	180	8.8	6.7		35.1	37.1
	190	11.1	8.5		44.7	47.1
	200	13.1	9.9		52.4	55.3
	210	16.2	12.4		65.1	68.7
7.9% Cu/SAPO-34	170	7.1	4.0	36	22.3	28.7
	180	8.9	5.0		27.9	35.9
	190	10.9	6.1		34.1	43.9
	200	13.4	7.5		41.9	53.9
9.9% Cu/SAPO-34	190	3.9	1.8	32	10.4	13.6
	200	5.1	2.3		13.4	17.5
	210	5.9	2.6		15.5	20.3
	220	6.8	3.0		17.7	23.4
	230	7.9	3.5		20.7	27.1

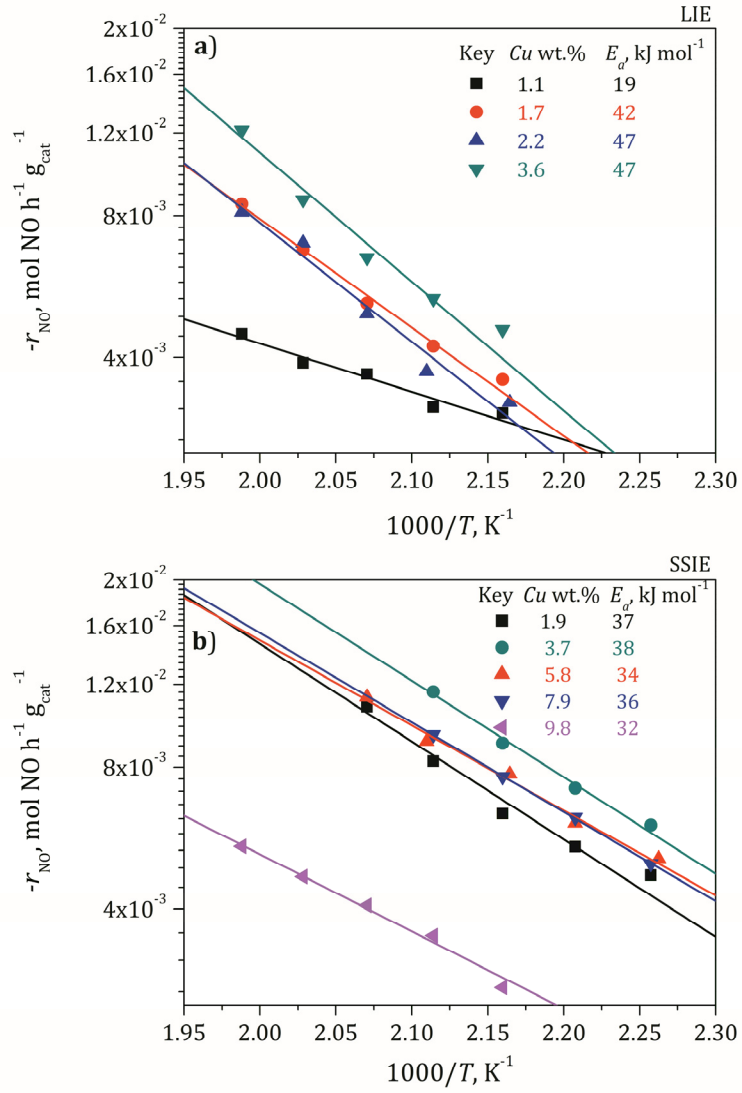

Figure 4.18. The NH_3-SCR reaction activation energy for samples prepared by LIE (a) and SSIE (b) with different copper loadings. Reaction conditions: 660 ppm NO, 660 ppm NH_3 and 6% O_2 using Ar as a balance gas with a total flow rate of 6000 ml min^{-1} and 0.15 g of catalyst.

around 32-38 kJ mol^{-1}. Specifically, the sample prepared by LIE with a copper loading of 1.1% presented a notably lower activation energy, i.e. 19 kJ mol^{-1}, which could be as a consequence of a different reaction mechanism due to such a low copper content.

Finally, Figure 4.19 shows the reaction rate normalized per mol of copper ($-r'_{NO}$) and the turnover frequency values (*TOF*) referred to the amount of

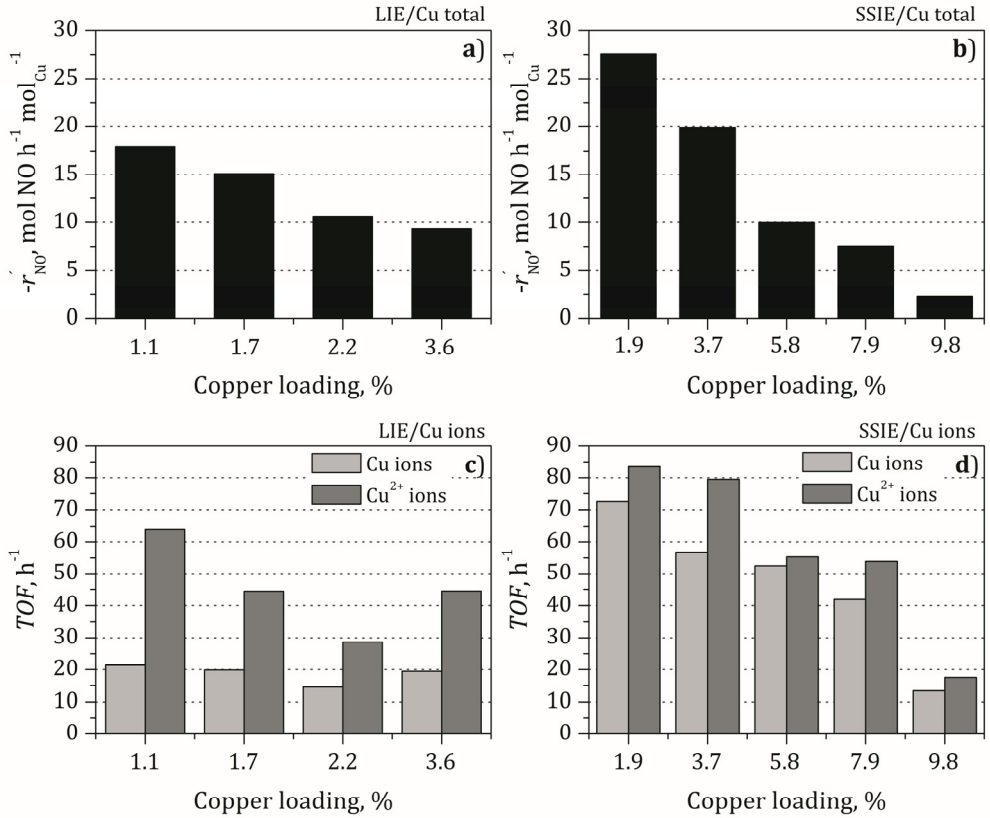

Figure 4.19. Evolution of reaction rate and turnover frequencies at 200 °C as a function of copper loading for samples prepared by LIE (a, c) and SSIE (b, d) when reaction rate is referred to the total amount of copper and when *TOF* is referred to the amount of copper ions quantified by H_2-TPR.

copper ions (Cu^{2+} and Cu^{+}) or Cu^{2+} ions at 200 °C for samples prepared by LIE and SSIE. Focusing on samples prepared by LIE, it can be observed a clear decrease of ($-r'_{NO}$) with increasing copper loading. This fact can be explained by the progressive increase in the proportion of copper aggregates with low SCR activity with respect to copper ions. The same trend can be observed for catalysts prepared by SSIE, although the observed reaction rates are higher, specifically for samples with low copper content. Thus, Cu/SAPO-34 catalysts prepared by SSIE present a higher NH_3-SCR activity than those prepared by LIE.

The observed *TOF* values are very similar irrespective of the copper loading when referred to the amount of copper ions in catalysts prepared by LIE, i.e. 19.8 h^{-1}. On the other hand, *TOF* values decreased with copper loading for catalysts prepared by SSIE due to the progressive decrease of the exposed surface area. Note that the *TOF* values are significantly higher for catalysts prepared by SSIE than LIE. The highest *TOF* value is observed for Cu/SAPO-34 catalyst prepared by SSIE with a copper loading of 1.9% (72.5 h^{-1}). The higher *TOF* for catalysts prepared by SSIE can be related to the preferential formation of Cu^{2+} ions, whereas the lower *TOF* for catalysts prepared by LIE can be related to the preferential formation of Cu^{+} ions, which can be considered less active than Cu^{2+} to assist the NH_3-SCR based on these results.

The *TOF* values are still higher for catalysts prepared by SSIE than LIE when referred to the amount of Cu^{2+} ions. This fact can be explained by the different locations of copper ions into the exchangeable sites of the zeolite [126]. It can be suggested that Cu^{2+} ions in SSIE catalysts are located at more accessible locations which promote the specific activity of Cu^{2+} ions with respect to catalysts prepared by LIE.

4.3. OVERALL VIEW AND CONCLUSIONS

Increasing the temperature at which solid state ion exchange (SSIE) was carried out from 500 °C up to 700 °C enhanced the ability to disperse copper aggregates and promoted the formation of isolated copper ions. In fact, all copper species were detected as aggregates for the sample treated at 500 °C, whereas the proportion of copper ions increased up to 33% in detriment of aggregates for the sample calcined at 700 °C. A further increase in the SSIE temperature negatively affected the stability of H-SAPO-34 zeolite framework, leading to some silicon segregation and the loss of specific surface area and acidity. Besides, copper ions tend to agglomerate to form small copper clusters inside the zeolite matrix and the formation of copper aluminate was favored.

The activation energy of the NH_3-SCR reaction was observed to be in the range of 37-42 kJ mol^{-1}. Only the sample prepared at 500 °C presented a somewhat lower activation energy of 28 kJ mol^{-1}, which suggested some changes in the reaction mechanism ascribed to the absence of copper ions. The Cu/SAPO-34 catalyst prepared at 700 °C by SSIE presented the best NH_3-SCR performance revealed by the highest reaction rate ($-r'_{NO}$) when referred to the total amount of copper in the sample, which was attributed to a higher content of Cu^{2+} ions. However, when calculation is per mol of copper ions (*TOF*), very similar values were obtained irrespective of the SSIE temperature, which further suggested that copper ions are the main active specie for NH_3-SCR.

The SAPO-34 zeolite presents a limited capacity in order to incorporate copper by liquid ion exchange (LIE). The signal intensity due to Cu^{2+} ions increased linearly up to a copper content of 1.7 wt.%, whereas the signal intensity tend to saturate for higher copper loadings, indicating that almost all the exchangeable locations of the zeolite were already occupied. Thus, copper is preferably incorporated as copper aggregates instead of copper ions for high copper loadings. On the other hand, SSIE permitted to incorporate copper

in a larger extent. However, the signal intensity due to Cu^{2+} ions was maximum for a copper loading of 3.7wt.% and did not further increase with copper loading, revealing again an upper limit to incorporate copper ions by SSIE.

The NH_3-SCR reaction activation energy for samples prepared by LIE and SSIE with different copper loading was in the range of 40-47 kJ mol^{-1} and 32-38 kJ mol^{-1}, respectively. Specifically, the sample prepared by LIE with a copper loading of 1.1wt.% presented a lower activation energy, i.e. 19 kJ mol^{-1}, which could be as a consequence of a different reaction mechanism due to such a low copper loading. The highest reaction rate values were observed for Cu/SAPO-34 catalysts with low copper loading prepared by either LIE or SSIE due to the preference formation of copper ions instead of aggregates. When calculation is per mol of copper ions (*TOF)*, very similar values were recorded irrespective of copper loading for catalysts prepared by LIE. Contrarily, a decreasing tendency in *TOF* was observed for samples prepared by SSIE with increasing copper loading due to a notable penalization of specific surface area.

It was observed that *TOF* values were higher for catalyst prepared by SSIE rather than LIE. We speculate that LIE preparation methodology incorporates copper ions more specifically at exchangeable sites with a higher interaction with the support, e.g. at 6dr windows of CHA structure. On the other hand, SSIE preparation methodology incorporates copper ions more randomly, at accessible locations, which promotes NH_3-SCR.

Chapter 5

IDENTIFICATION OF ADSORBED SPECIES DURING NO_x STORAGE AND REDUCTION AND SELECTIVE CATALYTIC REDUCTION

Chapter 5

IDENTIFICATION OF ADSORBED SPECIES DURING NO_x STORAGE AND REDUCTION AND SELECTIVE CATALYTIC REDUCTION

ABSTRACT

DRIFT experiments were carried out for determining adsorbed species during NO_x storage and reduction with Pt-Ba-(Ce)/Al_2O_3 catalysts. Adsorbed species during selective catalytic reduction of NO_x with NH_3 were also determined by FTIR using Cu/SAPO-34 catalyst.

DRIFT spectra were recorded during NO adsorption in the presence of oxygen at different temperature with time on stream. Nitrites and nitrates coexist in the catalyst surface at low temperature and short time on stream. On the other hand, nitrates were identified as the only NO_x adsorbed species at high temperature. The decomposition of NO_x adsorbed species was analyzed feeding different reductants, namely H_2, CO and C_3H_6. DRIFT spectra were recorded at different temperatures with increasing time on stream.

On the other hand, the adsorption of NO, NO_2 and NH_3 in the presence and absence of oxygen over Cu/SAPO-34 catalyst were studied by FTIR. Transient experiments were also carried out by first saturating the catalyst with NO and then feeding NH_3, or vice versa, in the presence or absence of oxygen. Finally, reactor experiments were carried out trying to correlate the temporal evolution of reactants and products with the adsorbed species observed by FTIR.

Capítulo 5

IDENTIFICACIÓN DE ESPECIES ADSORBIDAS DURANTE EL ALMACENAMIENTO Y REDUCCIÓN DE NO_x Y DURANTE LA REDUCCIÓN CATALÍTICA SELECTIVA

RESUMEN

Se han realizado experimentos DRIFT para determinar las especies adsorbidas durante el almacenamiento y reducción de NO_x en los catalizadores Pt-Ba-(Ce)/Al_2O_3. Las especies adsorbidas durante la reducción catalítica selectiva de NO_x con NH_3 también se han estudiado mediante FTIR en el catalizador Cu/SAPO-34.

Se han registrado distintos espectros DRIFT durante la adsorción de NO en presencia de oxigeno a diferentes temperaturas con el tiempo. A baja temperatura, en la superficie del catalizador coexisten nitritos y nitratos. Por otra parte, a alta temperatura solamente se han identificado los nitratos. La descomposición de los NO_x adsorbidos se ha analizado alimentando H_2, CO y C_3H_6 como agentes reductores. Los espectros DRIFT se han tomado a diferentes temperaturas e incrementando el tiempo.

Por otro lado, se ha estudiado mediante FTIR la adsorción de NO, NO_2 y NH_3 en presencia y ausencia de oxigeno en el catalizador Cu/SAPO-34. También se han llevado a cabo experimentos en estado transitorio donde en primer lugar el catalizador se satura con NO y después con NH_3 o viceversa, en presencia y en ausencia de oxigeno. Finalmente, se han realizado experimentos en el reactor para poder correlacionar la evolución temporal de los reactivos y productos con las especies adsorbidas observadas en el FTIR.

5. IDENTIFICATION OF ADSORBED SPECIES DURING NO_x STORAGE AND REDUCTION AND SELECTIVE CATALYTIC REDUCTION

Infrared spectroscopy is possibly one of the most widely used techniques in the characterization of heterogeneous catalysts [209]. There are numerous examples of its use in obtaining qualitative information regarding bulk phase vibrations in solids such as oxides, hydroxides, carbides, carbonates and other surface terminating groups such as hydroxyls. Bulk and surface species such as carbonates, acetates and acrylates, nitrates [210] and sulfates [211] can be also identified. Probe molecules such as ammonia and pyridine are also widely used to determine acidic groups on oxide surfaces by FTIR, or the use of CO and NO to study the speciation of metals, oxides and sulphides [212] on supported catalysts.

Two are the main objectives of this chapter. On the one hand, adsorbed species on the catalyst surface during the NO_x storage period (fuel lean cycle) will be identified by DRIFTS for Pt-Ba/Al_2O_3 and Pt-Ba-Ce/Al_2O_3 catalysts. Afterwards, during the reduction period (fuel rich cycle), the decomposition reactions of NO_x ad-species will be studied under the environment of different reducing agents (H_2, CO or C_3H_6). On the other hand, adsorbed species during selective catalytic reduction of NO with NH_3 will be identified by FTIR using Cu/SAPO-34 catalyst under steady state or transient experiments and different gas stream compositions. Reactor experiments will be also performed trying to correlate the evolution of reactants and products with the adsorbed species observed by FTIR.

5.1. IDENTIFICATION OF ADSORBED SPECIES DURING NO_x STORAGE AND REDUCTION

In order to identify adsorbed species in the NO_x storage and reduction (NSR) catalyst surface, DRIFTS experiments were carried out during NO_x

storage (lean period) and NO_x reduction (rich period) at 200, 300 and 400 ºC using Pt-Ba/Al_2O_3 and Pt-Ba-Ce/Al_2O_3 catalysts. During catalysts preparation, the incorporation sequence for the active phases over alumina was first ceria, second platinum and finally barium, with intermediate calcination steps. Platinum and barium loading was 2% and 14%, respectively, whereas in the case of ceria containing catalyst, CeO_2 loading was 20%. In order to focus the attention in the NO_x adsorbed species, CO_2 and H_2O were not admitted in the feed-stream, as those gases would be adsorbed in the catalyst surface and would make more difficult the interpretation of data.

5.1.1. NO adsorption in the presence of oxygen on Pt-Ba-(Ce)/Al_2O_3 catalysts

In order to identify NO_x adsorbed species during the lean period, the catalyst was contacted with a gas stream composed of 1000 ppm of NO and 8% of O_2, using Ar as balance gas with a total flow rate of 100 ml min^{-1}. Table 5.1 shows the IR bands and the assignment to different surface nitrate and nitrite species based on the literature reports. Figure 5.1 shows the absorbance of Pt-Ba/Al_2O_3 and Pt-Ba-Ce/Al_2O_3 catalysts in the region of interest for identifying NO_x adsorbed species, i.e. 1640-1200 cm^{-1}.

Table 5.1. IR bands detected during NO+O_2 adsorption experiments and their assignments.

IR band, cm^{-1}		Assignment	Reference
Pt-Ba/Al_2O_3	Pt-Ba-Ce/Al_2O_3		
1247-1222	1241-1222	Bridged bidentate nitrite	[6, 173, 213]
1432-1312	1570-1307	Monodentate nitrate	[173, 213]
1640-1313	1570-1469	Bidentate nitrates	[173, 213]
1454, 1400	1530, 1400, 1307	Nitrates	[173, 213]

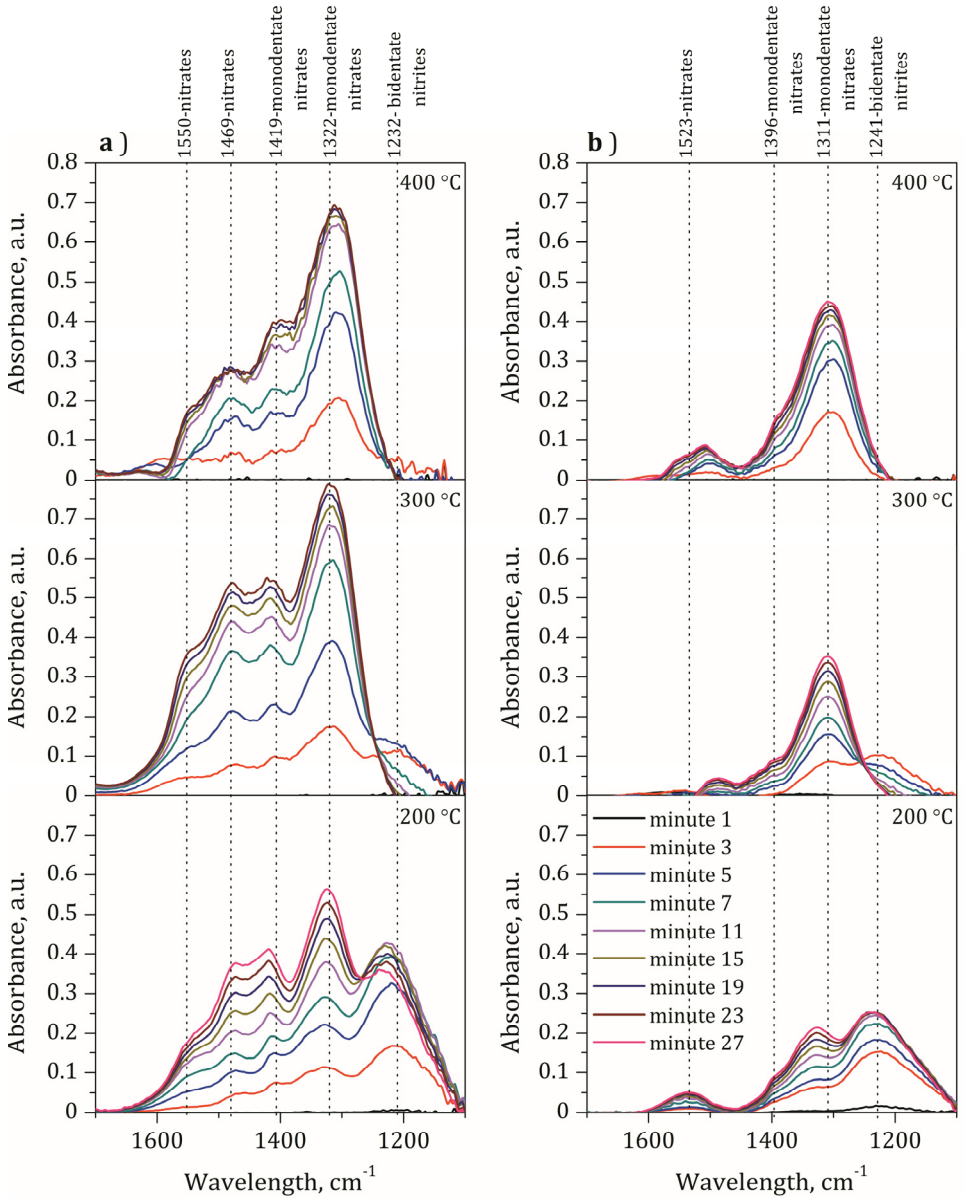

Figure 5.1. NO adsorption in Pt-Ba/Al_2O_3 (a) and Pt-Ba-Ce/Al_2O_3 (b) catalysts at 200, 300 and 400 °C. Feed stream: 1000 ppm NO and 8% O_2 using Ar as a balance gas with a total flow rate of 100 ml min^{-1} during 30 minutes.

Bridged bidentate nitrites, which absorption band is located at 1232 cm^{-1} [6, 173, 213], are the dominant NO_x ad-species at 200 °C and short time on stream, i.e. below 7 minutes, for Pt-Ba/Al_2O_3 catalyst. Nitrites formation involves two sequential steps [214]:

$$BaO + Pt\text{-}O \rightarrow BaO_2 + Pt \quad (5.1)$$

$$BaO_2 + 2NO \rightarrow Ba(NO_2)_2 \quad (5.2)$$

First, barium oxide in close contact with platinum reacts with oxygen ad-atoms chemisorbed in Pt to form barium peroxide (Equation 5.1). Then, barium peroxide reacts with gas phase NO in order to form barium nitrite (Equation 5.2). On the other hand, monodentate nitrates (asymmetric and symmetric), which absorption band is located at 1322 and 1419 cm^{-1} [173], respectively, are also present in the catalyst surface for short time on stream, although with a lower absorption intensity with respect to nitrites. Finally, nitrates located at 1469 and 1550 cm^{-1} [173] are also noticeable in the catalyst surface for short time on stream. The formation of nitrates has been well described by the NO_2 disproportionation reaction [30, 214], which requires a previous oxidation of NO to NO_2 assisted by platinum (Equation 5.3 and 5.4):

$$NO + 1/2O_2 \rightleftarrows NO_2 \quad (5.3)$$

$$3NO_2 + BaO \rightarrow Ba(NO_3)_2 + 2Pt \quad (5.4)$$

For longer time on stream, 11 minutes and onwards, the absorbance of bridged bidentate nitrites (1232 cm^{-1}) does not further increase and even tends to decrease. This fact can be explained by the progressive oxidation of nitrites to nitrates catalyzed by platinum as increasing time on stream:

$$Ba(NO_2)_2 + 2Pt\text{-}O \rightarrow Ba(NO_3)_2 + 2Pt \quad (5.5)$$

Due to the previous reaction (Equation 5.5), the absorbance of monodentate nitrates (1322 and 1419 cm^{-1}) increase progressively until it became dominant.

At higher temperature (300 °C), the presence of nitrites (1232 cm^{-1}) is only detected for short time on stream (below 5 minutes). Then, the absorbance intensity is progressively reduced until it becomes negligible for longer time on stream, revealing the absence of nitrites on the catalyst surface. On the other hand, the absorption intensity of all bands ascribed to nitrates (1322, 1419, 1469 and 1550 cm^{-1}) increased progressively with increasing time on stream. Note that the absorption intensity of asymmetric nitrates (1322 cm^{-1}) after 27 minutes of time on stream is notably higher at 300 °C with respect to 200 °C, revealing that a temperature increase promotes the formation of superficial nitrates on the Pt-Ba/Al_2O_3 catalyst surface. This fact can be due to the higher oxidation capacity of the catalysts, which promotes the oxidation of NO to NO_2 and consequently enhances the formation of nitrates through Equation 5.4. Furthermore, the nitrates absorption intensity growth with increasing time on stream is faster at 300 °C and reaches maximum absorption intensity for shorter time on stream, which evidences a faster NO_x adsorption kinetics [173].

At 400 °C nitrites are not detected even for short time on stream, due to the higher oxidation capacity of the catalyst which promotes nitrates formation instead of nitrites. Note that the absorption intensity due to the presence of nitrates reaches its maximum after 11 minutes of time on stream, which means that the NO_x adsorption kinetics is further enhanced at 400 °C. However, the maximum absorption intensity is slightly lower at 400 °C with respect to 300 °C, due to the lower stability of nitrates which start to decompose at 350 °C [213].

The adsorption of NO_x over Pt-Ba-Ce/Al_2O_3 catalyst could be carried out over barium oxide or alternatively over ceria, which also presents the ability to take part as NO_x storage site [173]. However, specific absorption bands due to the adsorption of NO_x over ceria (1074, 1100 and 1182 cm^{-1}) [173] were not detected in the DRIFTS spectra. On the other hand, at low temperature (200 °C), it seems that the presence of ceria enhances the stability of nitrites

associated to the barium phase, that is to say, inhibits the oxidation of nitrites to nitrates as already observed for Pt-Ba/Al_2O_3. One possible explanation is that ceria could encapsulate platinum during the calcination step of Pt-Ce/Al_2O_3 sample due to a strong metal support interaction, which finally reduces the exposed metallic surface area. After barium incorporation, ceria impedes the close contact between Pt and BaO, which is considered a necessary step in order to favor the oxidation of nitrites by oxygen ad-atoms chemisorbed in a neighborhood Pt at low temperature (Equation 5.5). This explanation was corroborated by TEM images shown in Figure 5.2 for Pt-Ba/Al_2O_3 and Pt-Ba-Ce/Al_2O_3 catalysts. Platinum particles are evident in the case of ceria free NSR catalysts, whereas Pt particles are not detected for Pt-Ba-Ce/Al_2O_3 catalysts, confirming that the presence of ceria could promote the encapsulation of the noble metal and thus avoid a close contact between Pt and Ba. Consequently, nitrites (1241 cm^{-1}) are the dominant NO_x ad-species even for long time on stream for Pt-Ba-Ce/Al_2O_3 catalyst. Asymmetric nitrates (1311 cm^{-1}) are also evident, whereas the intensity of nitrates located at (1396, 1523 and 1550 cm^{-1}) is significantly lower with respect to Pt-Ba/Al_2O_3. At higher temperature (300 °C), the oxidation capacity of the catalyst is promoted and the presence of gas phase NO_2 facilitates the formation of nitrates, which are the dominant species at high temperature.

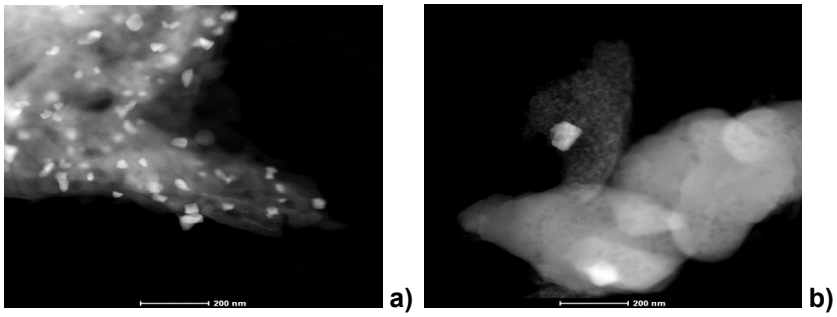

Figure 5.2. TEM images of Pt-Ba/Al_2O_3 (a) and Pt-Ba-Ce/Al_2O_3 (b) catalysts.

5.1.2. Decomposition of adsorbed NO_x species under different reducing environments

In order to identify the surface species formed over Pt-Ba/Al_2O_3 and Pt-Ba-Ce/Al_2O_3 catalysts during NO_x reduction, DRIFTS measurements were conducted in a net reducing atmosphere. Prior to the analysis, the catalysts were saturated with NO_x by admitting to the gas cell a gas stream composed of 1000 ppm NO and 8% O_2 using Ar as balance gas with a total flow rate of 100 ml min^{-1}. The time on stream was extended for 30 minutes, which guarantees that the catalyst surface is saturated with nitrites and nitrates, as already observed in the previous section. Afterwards, the composition of the gas stream was changed and for the subsequent 30 minutes of reduction period different gas streams were admitted to the gas cell [215]. In order to determine the reduction ability of different reducing agents and its influence over the decomposition reactions of nitrates and nitrites, different gas streams were simulated. The concentration of reductants is comparable according to stoichiometry (Equations 2.10-2.13): i) 1% H_2/Ar; ii) 1% CO/Ar; and iii) 0.11% C_3H_6/Ar. During the reduction period 1000 ppm of NO were also admitted to the gas cell irrespective of the reductant used. Experiments were carried out at 200, 300 and 400 ºC.

5.1.2.1. Decomposition of NO_x ad-species with hydrogen

Figure 5.3 and Figure 5.4 show the evolution of DRIFTS spectra while increasing time on stream in a reducing atmosphere including hydrogen as reductant. As can be observed, the signal intensity due to nitrites and nitrates located in the wavelength region of 1250-1232 cm^{-1} and 1640-1322 cm^{-1}, respectively, decreases rapidly once the reducing gas is admitted to the gas cell. The decomposition of nitrates in order to form nitrogen can be described by the following equation:

$$Ba(NO_3)_2 + 5H_2 \rightarrow BaO + N_2 + 5H_2O \qquad (5.6)$$

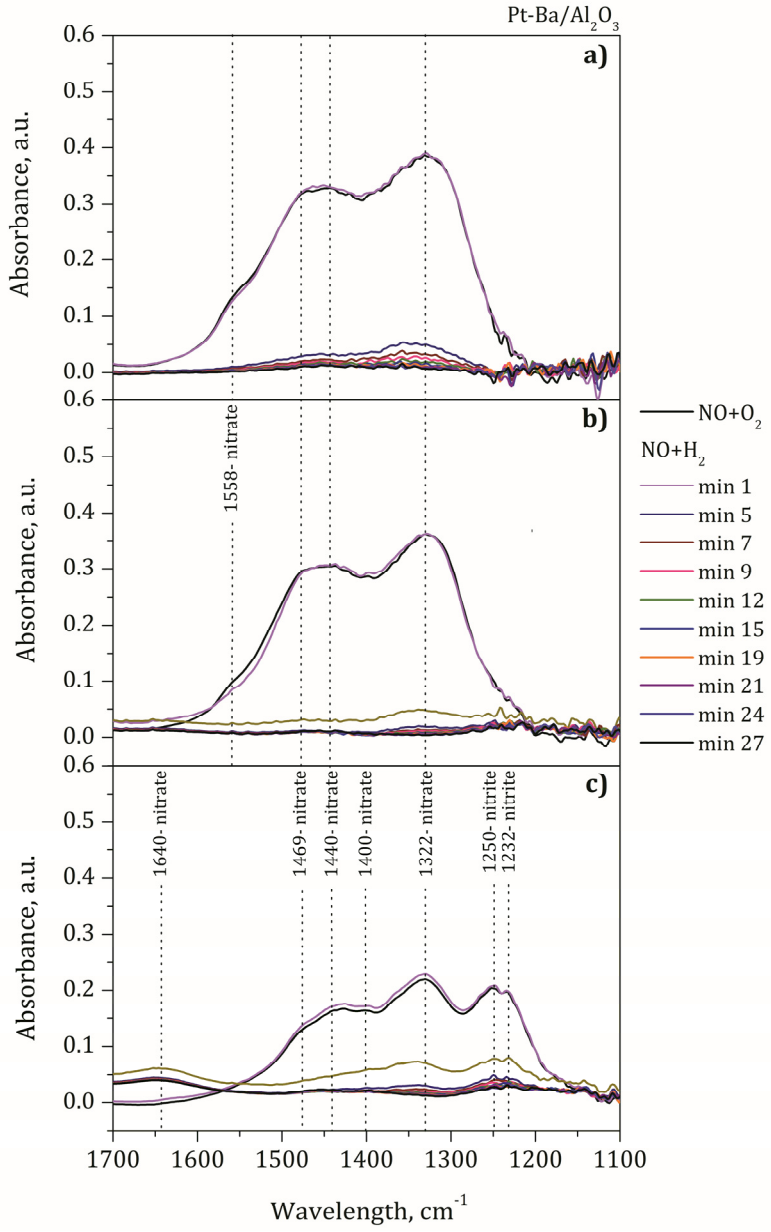

Figure 5.3. Decomposition of NO_x ad-species in the presence of NO and H_2 in Pt-Ba/Al_2O_3 catalyst at 400 °C (a), 300 (b) and 200 (c) °C. Feed stream: i) lean period: 1000 ppm NO, 8% O_2 with a total flow rate of 100 ml min^{-1} Ar during 30 minutes and ii) rich period: 1000 ppm NO and 1000 ppm H_2 with a total flow rate of 100 ml min^{-1} Ar during 30 minutes.

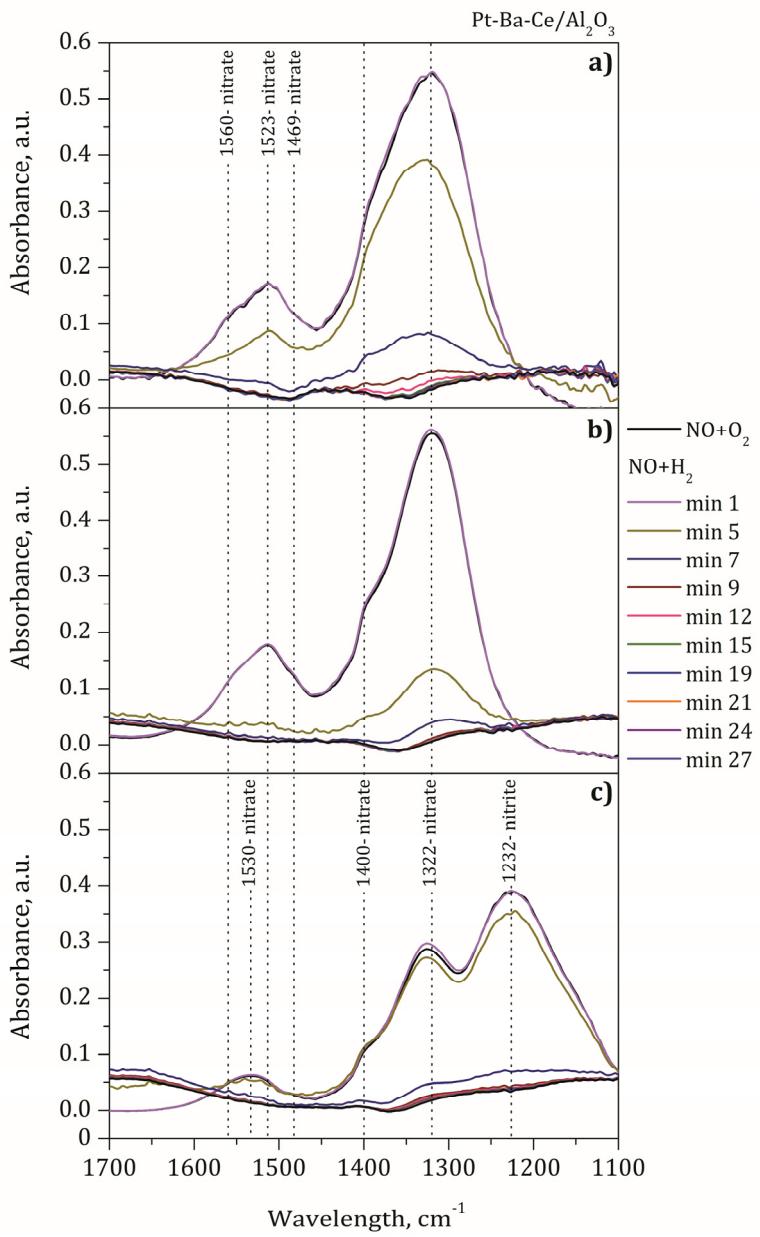

Figure 5.4. Decomposition of NO_x ad-species in the presence of NO and H_2 in Pt-Ba-Ce/Al_2O_3 catalyst at 400 °C (a), 300 (b) and 200 (c). Feed stream: i) lean period: 1000 ppm of NO and 8% of O_2 with a total flow rate of 100 ml min^{-1} Ar during 30 minutes and ii) rich period: 1000 ppm of NO and 1000 ppm of H_2 with a total flow rate of 100 ml min^{-1} Ar.

The decomposition of nitrites and nitrates is slightly slower at 200 °C, and especially for ceria containing catalysts, due to the absence of an intimate contact between Pt and Ba, as observed in Figure 5.2. Some authors [216] have also suggested that nitrates adsorbed over ceria are more difficult to reduce than nitrates on barium. However, it can be observed that 9 minutes of time on stream is enough to completely remove NO_x ad-species from the catalyst surface for Pt-Ba/Al_2O_3 and Pt-Ba-Ce/Al_2O_3 catalysts, irrespective of the catalyst temperature.

5.1.2.2. Decomposition of NO_x ad-species with carbon monoxide

Figure 5.5 and Figure 5.6 show the evolution of DRIFTS spectra while increasing time on stream in a reducing atmosphere including 1000 ppm of CO as reductant using Ar as balance gas with a total flow rate of 100 ml min^{-1} for Pt-Ba/Al_2O_3 and Pt-Ba-Ce/Al_2O_3 samples. Table 5.2 summarizes the IR bands detected during the decomposition of NO_x ad-species when feeding carbon monoxide at 200, 300 and 400 °C.

When CO is admitted to the gas cell at 200 °C, the intensity of the bands located at 1236 cm^{-1} and 1421 cm^{-1} ascribed to nitrites and nitrates, respectively, start to decrease immediately. The reduction of adsorbed

Table 5.2. IR bands detected during NO+CO adsorption experiments and their assignments.

IR band, cm^{-1}		Assignment	Reference
Pt-Ba/Al_2O_3	Pt-Ba-Ce/Al_2O_3		
1577-1560	1577-1560	Carbonates on barium ($BaCO_3$)	[215-218]
2080-2063	2080-2046	CO over Pt (Pt^0-CO)	[216-220]
2175-2171	2167	Isocyanate on barium (NCO-Ba)	[217, 218, 220]
2233-2221	2233-2231	Isocyanate on alumina (NCO-Al)	[217, 218]

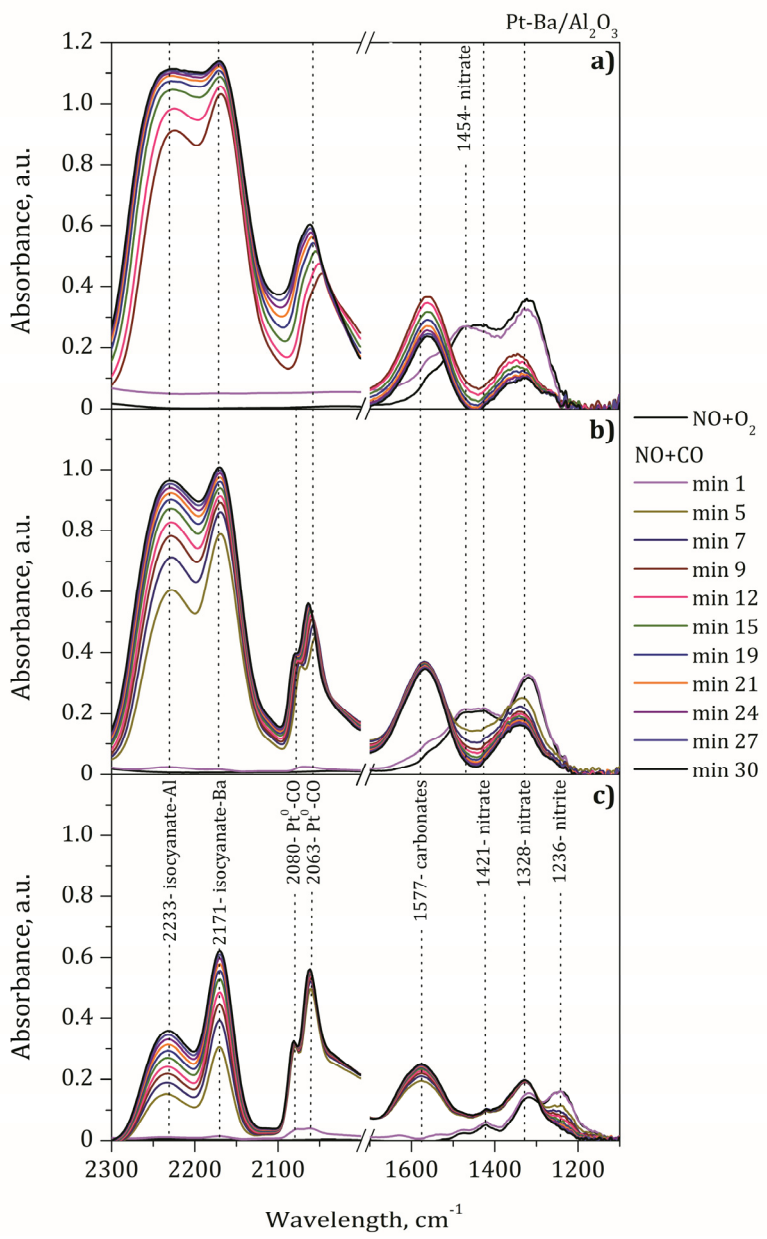

Figure 5.5. Decomposition of NO_x ad-species in the presence of NO and CO in Pt-Ba/Al_2O_3 catalyst at 400 °C (a), 300 (b) and 200 (c). Feed stream: i) lean period: 1000 ppm of NO and 8% of O_2 with a total flow rate of 100 ml min^{-1} Ar during 30 minutes and ii) rich period: 1000 ppm of NO and 1000 ppm of CO with a total flow rate of 100 ml min^{-1} Ar during 30 minutes.

nitrates by CO has been described by the occurrence of the following reaction [219]:

$$Ba(NO_3)_2 + 5CO \rightarrow N_2 + BaCO_3 + 4CO_2 \quad (5.7)$$

However, it was worth to note that the signal of the bands at 1236 cm^{-1} and 1421 cm^{-1}, was still detectable even for times on stream as long as 30 minutes, which reveals that nitrites and nitrates were not completely removed from the catalyst surface. Thus, it can be concluded that CO is not as efficient as H_2 for the decomposition of stored nitrites and nitrates at low temperature (200 °C).

On the contrary, the signal intensity of the band located at 1328 cm^{-1} ascribed to nitrates increases with time on stream. This fact was attributed to the simultaneous formation of barium carbonates while CO decomposes superficial nitrates, in line with Equation 5.7. Some of the bands ascribed to barium carbonate overlap with the previous bands assigned to nitrates [219, 220], e.g. the band located at 1328 cm^{-1}. However, the formation of superficial carbonates is also evident because a new band located at 1577 cm^{-1} appears which is not overlapped with nitrite and nitrate signals. Consequently, it can be deduced that the catalyst surface consists of a mixture of nitrates and nitrites and carbonates at the end of the reduction period.

Along with the previous signals ascribed to nitrites, nitrates and carbonates, two mayor signals located at 2171 and 2233 cm^{-1} evolved with increasing reduction time with CO, assigned to adsorbed cyanate/isocyanate species [217, 221]. Specifically, the band around 2171 cm^{-1} was assigned to NCO species adsorbed on BaO [220, 222] and the band around 2233 cm^{-1} was assigned to NCO species adsorbed on alumina [217]. As can be observed in Figure 5.5, the signal attributed to cyanate or isocyanate species progressively increased with increasing time on stream. The formation of isocyanate species can be described by the following reaction (Reaction 5.8):

$$Ba(NO_3)_2 + 8CO \rightarrow Ba(NCO)_2 + 4CO_2 \quad (5.8)$$

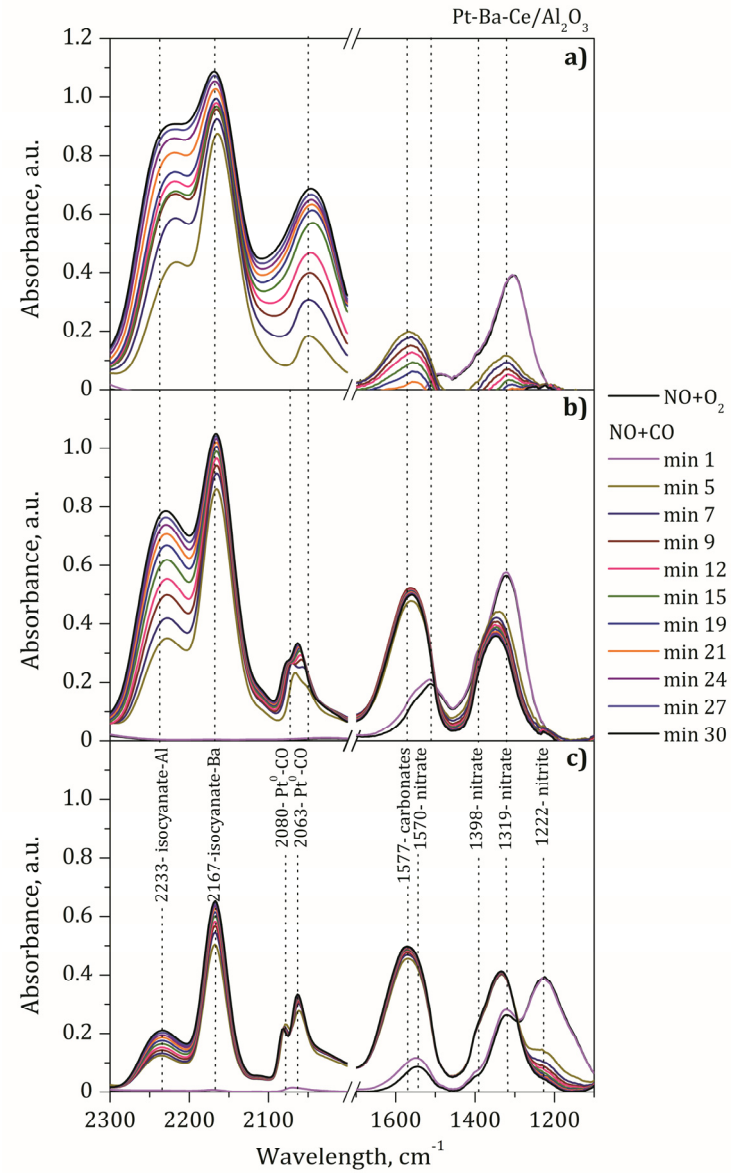

Figure 5.6. Decomposition of NO_x ad-species in the presence of NO and CO in Pt-Ba-Ce/Al_2O_3 catalyst at 400 °C (a), 300 (b) and 200 (c). Feed stream: i) lean period: 1000 ppm of NO and 8% of O_2 with a total flow rate of 100 ml min^{-1} Ar during 30 minutes and ii) rich period: 1000 ppm of NO and 1000 ppm of CO with a total flow rate of 100 ml min^{-1} Ar during 30 minutes.

The isocyanate species adsorbed over barium can further react with adjacent nitrates in order to form nitrogen, according to Reaction 5.9:

$$5Ba(NCO)_2 + 3Ba(NO_3)_2 \rightarrow 8N_2 + 8BaCO_3 + 2CO_2 \quad (5.9)$$

In the presence of H_2O, NCO species are rapidly hydrolyze according to Reaction 5.10, forming NH_3 and CO_2. However, as DRIFTS spectra have been taken in the absence of H_2O, NCO species adsorbed over barium or alumina are stable and remain adsorbed on the catalyst surface at the end of the reduction period.

$$Ba(NCO)_2 + 3H_2O \rightarrow BaO + 2NH_3 + 2CO_2 \quad (5.10)$$

An additional prominent band can be detected in the DRIFTS spectra shown in Figure 5.5 located at 2063 cm^{-1} with a shoulder at 2080 cm^{-1}. This band appears just at the beginning of the rich period (after 1 minute of time on stream) and is ascribed to CO adsorbed over platinum [219, 220]. The Pt-CO bond is stable and maintains its absorbance intensity during the whole reduction period.

The same absorption bands can be detected in the DRIFTS spectra for ceria containing catalyst, i.e. Pt-Ba-Ce/Al_2O_3 (Figure 5.6), at low temperature (200 °C). However, some differences are noticeable. On the one hand, the signal intensity due to cyanate species adsorbed over alumina (2233 cm^{-1}) is slightly lower in the case of ceria containing catalyst. It is suggested that the incorporation of 20 wt.% of ceria and 14 wt.% of barium covers almost completely the alumina surface and thus the possibility to adsorb cyanate species over alumina is decreased. On the other hand, it is also observable that the signal intensity due to CO adsorption over Pt is lower in the case of ceria containing catalyst. As already reported, the SMSI between Pt and CeO_2 could reduce the exposed metallic surface area and consequently the signal intensity due to carbon monoxide adsorption on Pt is reduced.

At higher temperature (300 °C) the Pt-Ba/Al_2O_3 catalyst surface is mostly populated by nitrates before the reduction period, in line with the results

observed in the previous section. Again, the signals ascribed to nitrates located at 1421 and 1328 cm^{-1} decrease rapidly with the beginning of the reduction period while carbonates signal developed at 1577 cm^{-1}. Now, the intensity of the band located at 1328 cm^{-1}, which is influenced by the presence of nitrates and carbonates, decreases with increasing time on stream, as opposite to that observed at 200 °C. Thus, the presence of nitrates at the beginning of the reduction period is higher at 300 °C, and after the reduction period, the presence of carbonates is comparable to that observed at lower temperature.

At higher temperature, i.e. 400 °C, the signal ascribed to nitrates (1328 cm^{-1}) decreases with increases time on stream, but notably faster than at 300 °C, revealing faster nitrates decomposition kinetics. On the contrary, the signal intensity due to carbonates on barium (1577 cm^{-1}) increases more progressively than that observed at 300 °C, suggesting that carbonates formation is not favored at high temperature. Similar conclusions can be extracted from DRIFTS spectra obtained for Pt-Ba-Ce/Al_2O_3 catalyst.

5.1.2.3. Decomposition of NO_x ad-species with propylene

Figure 5.7 and Figure 5.8 show the evolution of DRIFTS spectra while increasing time on stream in a reducing atmosphere including 0.11% of propylene as reductant for Pt-Ba/Al_2O_3 and Pt-Ba-Ce/Al_2O_3 samples. Table 5.3 summarizes the IR bands observed in these experiments. The initial DRIFTS spectra shows the typical bands ascribed to nitrites (1247 cm^{-1}) and nitrates (1432 and 1313 cm^{-1}) once the Pt-Ba/Al_2O_3 catalyst has been saturated with NO_x at 200 °C. In addition, some superficial carbonates were also detected at 1618 and 1562 cm^{-1} before the rich period started. Once the gas stream was switched to a reducing environment including C_3H_6, the bands ascribed to superficial nitrites and nitrates were hardly affected, revealing that propylene

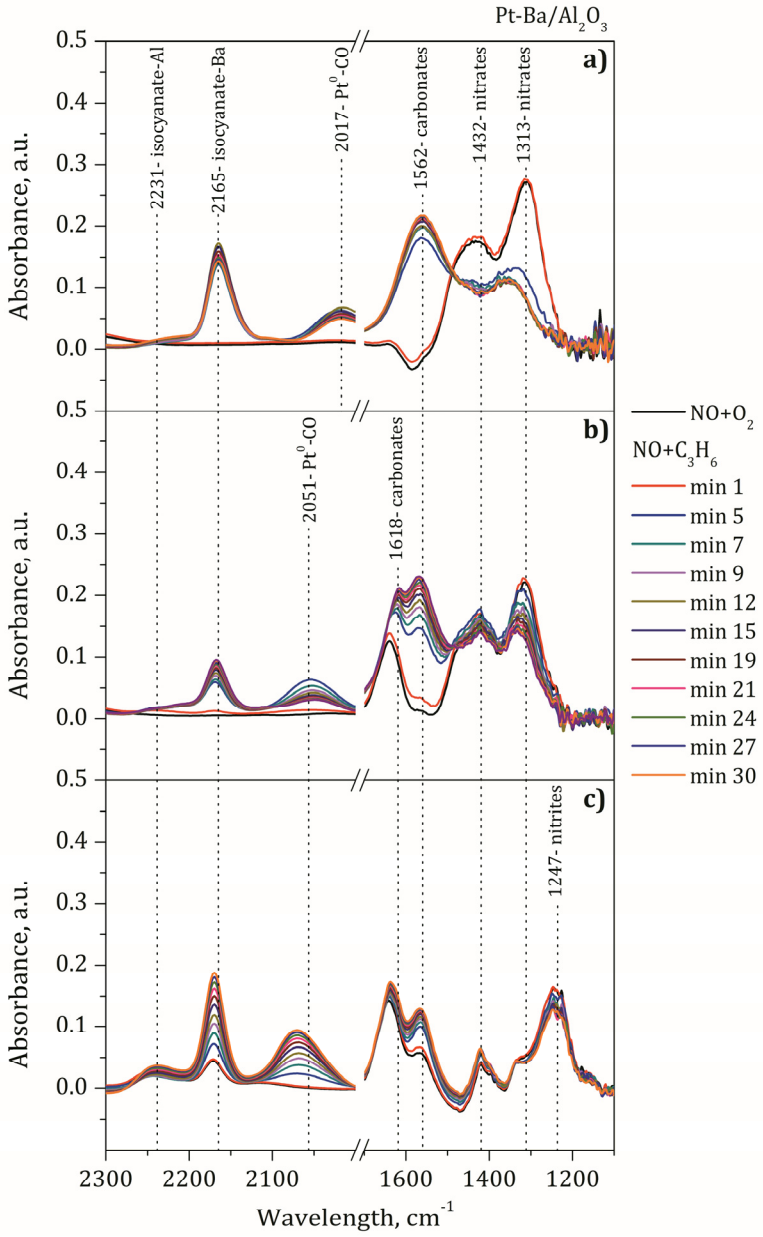

Figure 5.7. Decomposition of NO_x ad-species in the presence of NO and C_3H_6 in Pt-Ba/Al_2O_3 catalyst at 400 °C (a), 300 (b) and 200 (c). Feed stream: i) lean period: 1000 ppm of NO and 8% of O_2 with a total flow rate of 100 ml min^{-1} Ar during 30 minutes and ii) rich period: 1000 ppm of NO and 1111 ppm of C_3H_6 with a total flow rate of 100 ml min^{-1} Ar during 30 minutes.

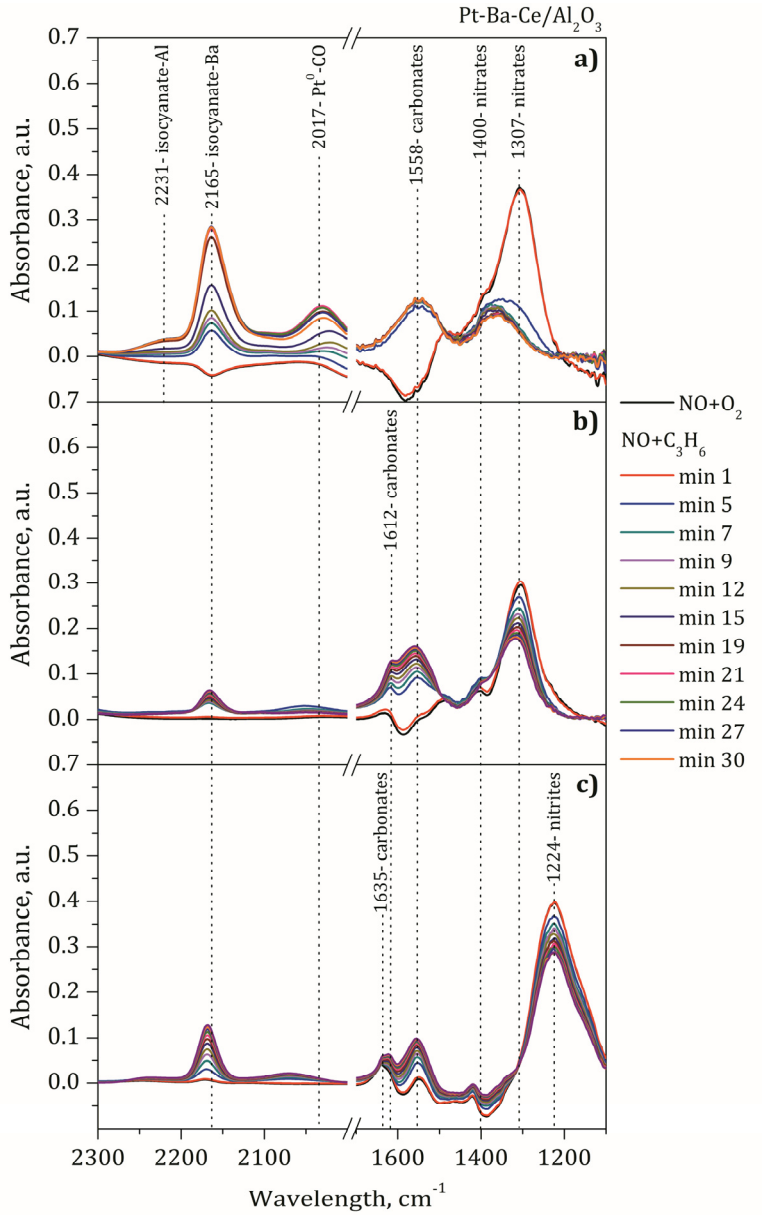

Figure 5.8. Decomposition of NO_x ad-species in the presence of NO and C_3H_6 in Pt-Ba-Ce/Al_2O_3 catalyst at 400 °C (a), 300 (b) and 200 (c). Feed stream: i) lean period: 1000 ppm of NO and 8% of O_2 with a total flow rate of 100 ml min^{-1} Ar during 30 minutes and ii) rich period: 1000 ppm of NO and 1111 ppm of C_3H_6 with a total flow rate of 100 ml min^{-1} Ar during 30 minutes.

Table 5.3. IR bands detected during NO + C_3H_6 adsorption experiments and their assignments.

IR band, cm^{-1}		Assignment	Reference
Pt-Ba/Al_2O_3	Pt-Ba-Ce/Al_2O_3		
1618-1562	1635-1556	Carbonates on barium ($BaCO_3$)	[215-218]
2051-2017	2044-2017	CO over Pt (Pt^0-CO)	[216- 220]
2167-2165	2167-2165	Isocyanante on BaO (NCO-Ba)	[217, 218, 220]
2231	2231	Isocyanante on alumina (NCO-Al)	[217, 218]

is not active enough to promote the decomposition of NO_x adsorbed species at 200 °C.

On the contrary, the signal intensity due to carbonates (1618 and 1562 cm^{-1}) increased with increasing time on stream probably due to some oxidation of propylene with adsorbed oxygen in the catalyst which forms CO_2 and H_2O, the former being adsorbed in the basic sites of the catalyst in the form of carbonates. Additionally, it seems that a fraction of propylene is not fully oxidized and results in a partial oxidation that produces carbon monoxide, as deduced from the increasing intensity of the band located around 2051 cm^{-1} and attributed to CO adsorbed on Pt. Meanwhile, the formation of CO also promotes the appearance of adsorbed cyanate species over barium (2165 cm^{-1}) and alumina (2231 cm^{-1}), although with a lower intensity with respect to that observed when using CO as reductant (Figure 5.5 and Figure 5.6). Similar species and similar evolution is observed when admitting C_3H_6 during the rich period using Pt-Ba-Ce/Al_2O_3 catalyst. In line with previous results, the intensity of the signal due to CO adsorption over Pt is lower in the case of ceria containing catalysts due to a lower exposed metallic surface area.

Similar trends can be observed when analyzing DRIFTS spectra at 300 °C. The unique exception is that the catalyst surface is now mainly populated by nitrates instead of nitrites before the reducing period. Once again, C_3H_6 is not able to significantly reduce the intensity of nitrates, and after 30 minutes of time on stream, the catalyst surface consists of a mixture of nitrates and carbonates. Finally, at 400 °C, it can be observed that the signal located at 1432 cm^{-1} ascribed to nitrates, which is not interfered by carbonates, is reduced at some extent. Thus, C_3H_6 starts to be effective for NO_x decomposition and reduction only for high temperatures, although NO_x removal from the catalyst surface is not complete.

5.2. IDENTIFICATION OF ADSORBED SPECIES DURING SELECTIVE CATALYTIC REDUCTION

In order to identify the adsorbed species during NH_3-SCR on Cu/SAPO-34 catalyst, Fourier Transform Infrared (FTIR) spectroscopy analysis were carried out under different gas stream compositions. Reactor experiments were also performed trying to correlate the evolution of reactants and products with the observed adsorbed species by FTIR. The following experiments were carried out in FTIR and bench reactor admitting a fixed gas stream composition until steady state was obtained for studying: i) NO adsorption in the presence and absence of oxygen; ii) NH_3 adsorption in the presence and absence of oxygen; iii) NO and NH_3 coadsorption under standard SCR reaction conditions. Alternatively, transient experiments were also performed alternating the composition of the gas stream admitted to the reactor. The first experiment consisted on admitting a gas stream containing NH_3 until saturation and afterwards NH_3 gas replaced by NO and FTIR spectra were taken with increasing time on stream. Similar experiments were also carried out in the opposite order, i.e. first admitting NO until saturation and then NH_3. Both experiments were repeated in the presence of oxygen in the

gas stream. The aforementioned experiments were carried out at different temperatures, 100, 200, 300 and 400 °C.

It is very important a clear understanding of the reaction process and the NH_3-SCR mechanism to enhance catalytic activity. It was reported that Cu-active sites were formed on isolated Cu^{2+} and Cu clusters and also it was reported that Cu^{2+} species were the active sites for NH_3 adsorption. The adsorbed NH_3 could be converted to coordinated NH_3 and NH_4^+ and then it can react with NO_x complexes. Suarez et al. [223] have defined that the adsorbed NO_2 and nitrates species have a very important role in the SCR reaction. However, this study was focused on the NO_x removal from stationary source. Other researchers [224, 225] found that nitrates and nitrites are the principal NO_x adsorption species that react with coordinated NH_3 and NH_4^+ for NO_x elimination from diesel engine exhausts. Also, they proposed the nitrates as the key intermediates, but the reaction between the NO_x and NH_3 species is still ambiguous. In the following section we gain understanding on the NH_3-SCR mechanism by observing the adsorbed species in the catalyst surface with different gas stream compositions, under stationary or transient experiments.

5.2.1. Identification of adsorbed species under stationary gas stream

5.2.1.1. NO adsorption in the presence and absence of oxygen

First, FTIR experiments were carried out by contacting a gas stream composed of 660 ppm NO balanced with 500 ml min^{-1} N_2 (thus, in the absence of oxygen) with the Cu/SAPO-34 catalyst for 30 minutes. Experiments were carried out at room temperature (28 °C), 100, 200, 300 and 400 °C. However, only the FTIR spectra recorded at 28 and 100 °C are displayed in Figure 5.9, as the signal intensity due to NO ad-species at higher temperature resulted in almost negligible signal, revealing a very low interaction between NO and the Cu/SAPO-34 catalyst. The Table 5.4 summarizes the IR bands detected when NO is adsorbed on Cu/SAPO-34 catalyst.

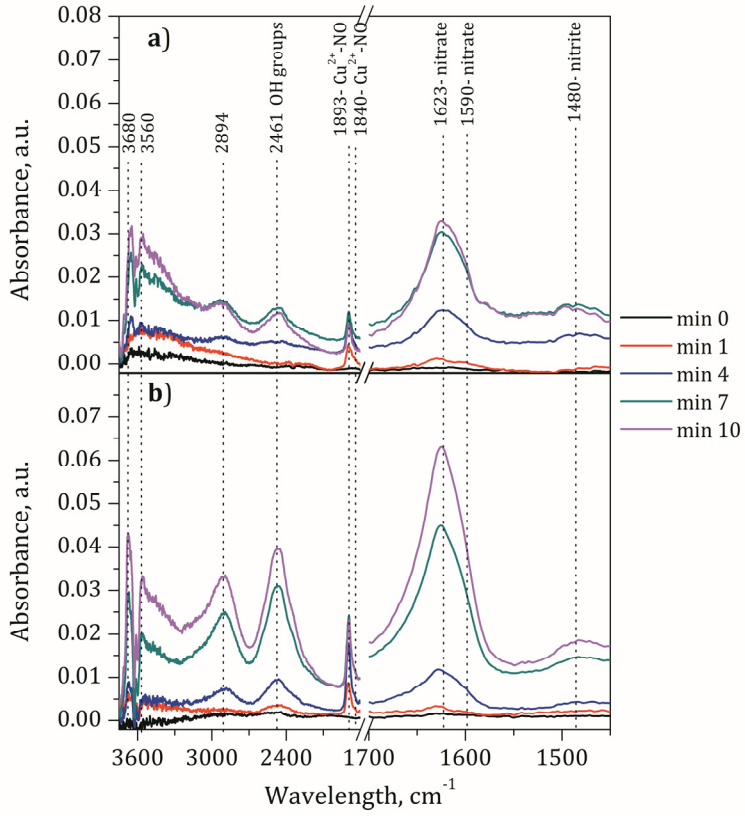

Figure 5.9. FTIR spectra during NO adsorption over Cu/SAPO-34 catalyst at 100 °C (a) and 28 °C (b) with increasing time on stream up to 30 minutes in the absence of oxygen. Feed stream: 660 ppm NO in 500 ml min^{-1} N_2 during 30 minutes.

The bands around 1650 and 1500 cm^{-1} were assigned to nitrates and nitrites, respectively, adsorbed primarily on the transition metal active sites of the catalyst [224, 226-229]. Specifically, the bands located at 1623 and 1590 cm^{-1} were attributed to nitrates and the band located at 1480 cm^{-1} was assigned to nitrites [226, 227]. Note that the signal intensity due to nitrates was significantly more intense than nitrites, revealing that the adsorption of NO proceeds preferentially through the formation of nitrates. Additionally, a band located at 1893 cm^{-1} was detected, which is assigned to the adsorption of

Table 5.4. Overview of the IR bands detected during NO adsorption on Cu/SAPO-34 and their assignments.

IR band, cm^{-1}	Assignment	Reference
1500	Nitrite	[224, 226-229]
1590	Bidentate nitrate	[226, 227]
1623	Bridging bidentate nitrate	[226, 227]
1840, 1893	NO adsorbed on Cu^{2+} (Cu^{2+}-NO)	[226, 227]
2461, 2894, 3560, 3680	OH groups	[224, 226, 227, 229]

NO on Cu^{2+} sites. On the other hand, due to the absence of IR features around 1800-1812 cm^{-1}, attributed to the adsorption of NO over Cu^{+}, the presence of copper (I) ions can be disregarded. Finally, in the OH stretching region (4000 cm^{-1} to 2400 cm^{-1}), bands at 3680, 3560, 2894 and 2461 cm^{-1} were observed and attributed to perturbed Si-OH, P-OH and OH groups associated with extra-framework Al and Cu, respectively [224, 226-229].

When the temperature was increased from 28 to 100 °C, the same bands were detected but with lower intensity, which reveals that NO adsorption as nitrites and nitrates is not favored with increasing temperature in the absence of gas phase oxygen.

Afterwards, the catalyst was exposed to a gas stream composed of 660 ppm NO and 6% O_2 balanced with 500 ml min^{-1} N_2 for 30 minutes to investigate whether the presence of oxygen affects the formation of NO_x ad-species. It is important to study the adsorption of NO with O_2 because under such conditions NO could be oxidize to NO_2 and oxygen keeps copper ions in a high oxidation state. Figure 5.10 shows the FTIR spectra when NO and O_2 are fed at 100, 200 and 300 °C.

As already observed in Figure 5.9, the IR feature in Figure 5.10 located around 1650-1500 cm^{-1} can be assigned to different nitrates and nitrites species. However, it is difficult to identify these peaks due to the very similar

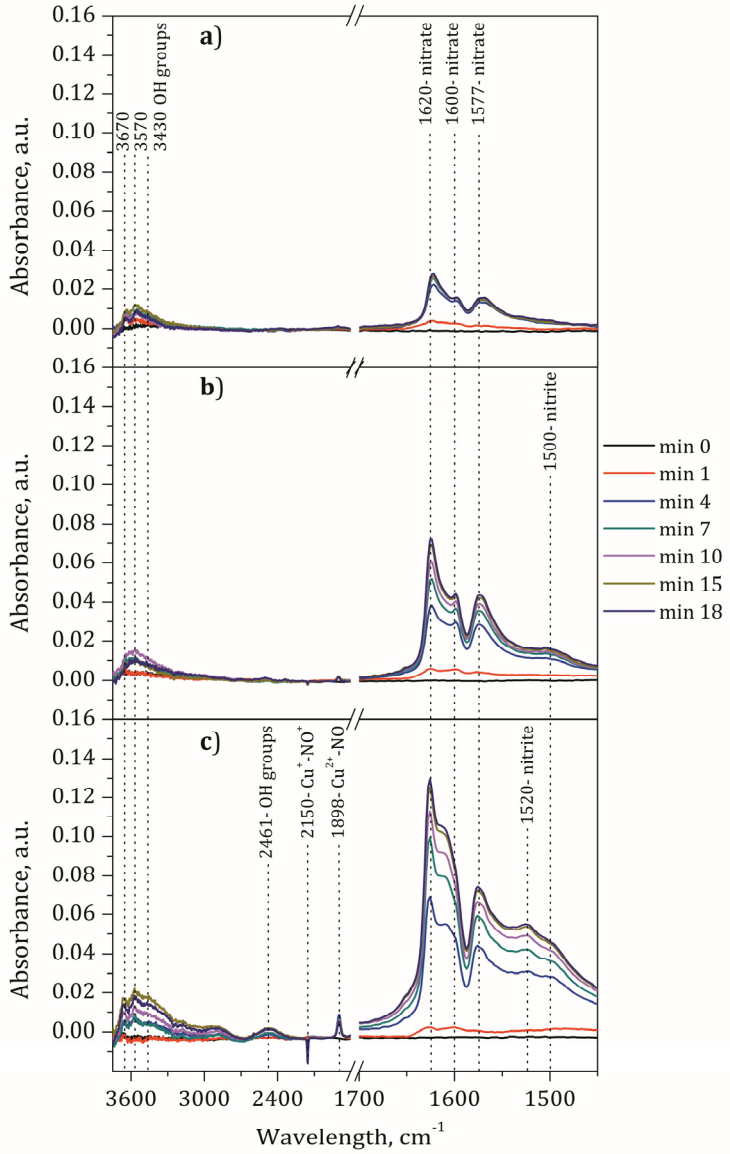

Figure 5.10. FTIR spectra during NO adsorption in the presence of O_2 over Cu/SAPO-34 catalyst at 300 °C (a), 200 (b) and 100 (c) °C with increasing time on stream up to 30 minutes. Feed stream: 660 ppm of NO and 6% of O_2 using N_2 as balance gas with a total flow rate of 500 ml min^{-1}.

vibrations of the different nitrate species. Tentatively, the identified bands could be attributed to monodentate nitrates (1600 cm^{-1}), bidentate nitrates (1577 cm^{-1}) and nitrites (1500 cm^{-1}) [226, 227]. The band located around 1890 cm^{-1} was assigned to NO adsorption on Cu^{2+} sites. At low temperature (28 °C), two different contributions were observed, located at 1892 cm^{-1} and 1860 cm^{-1}, which revealed the existence of different types of Cu^{2+} species, probably located at different exchangeable sites of the zeolite framework. Again, no features corresponding to NO adsorbed on Cu^{+} sites were observed around 1800 cm^{-1}. There is no agreement in the literature regarding the assignation of the band located at 2150 cm^{-1}. Some authors attributed that signal to NO^{+} paired with Cu^{+}, or alternatively to NO^{+} adsorbed on acid sites of the zeolite. In any case, a decreasing intensity was observed when increasing the time on stream due to the decomposition of some stable Cu^{+}-NO adduct. The summary of all these IR bands can be seen in Table 5.5.

A decreasing signal intensity of nitrites and nitrates was observed with increasing temperature, again revealing that the stability of NO_x ad-species decreases with temperature. Specifically, nitrites are less stable and their absorption intensity is reduced at a higher extent than nitrates. Comparing the

Table 5.5. Overview of the IR bands detected during NO adsorption in the presence of oxygen on Cu/SAPO-34 and their assignments.

IR band, cm^{-1}	Assignment	Reference
1500	Nitrites	[224, 226-229]
1577	Bidentate nitrates	[226, 227]
1607	Monodentate nitrates	[226, 227]
1860, 1892	Mononitrosyl species on Cu^{2+} sites (Cu^{2+}-NO)	[226, 227]
2150	NO^{+} paired with Cu^{+} ion on acid site (Cu^{+}-NO^{+})	[226, 227]
2461, 2894, 3570, 3670	OH groups	[224, 226, 227, 229]

FTIR spectra in the presence or absence of oxygen, it can be deduced that the intensity of the signals attributed to nitrates and nitrites is notably higher in the presence of oxygen. Nitrates signal is almost negligible for temperatures higher than 200 °C in the absence of O_2, whereas nitrates are observable for temperatures as high as 400 °C in the presence of O_2.

5.2.1.2. NO_2 adsorption in the absence of oxygen

In this section the adsorption of NO_2 over Cu/SAPO-34 was studied in the absence of oxygen. The catalyst was contacted with a gas stream composed of 660 ppm of NO_2 using N_2 as balance gas with a total flow rate of 500 ml min^{-1}. FTIR spectra were recorded with increasing time on stream until catalyst saturation at different temperatures, i.e. 100, 200, 300 and 400 °C. As an example, Figure 5.11 shows the evolution of the signal intensity due to different adsorbed species in the catalyst surface at 100 °C. The main

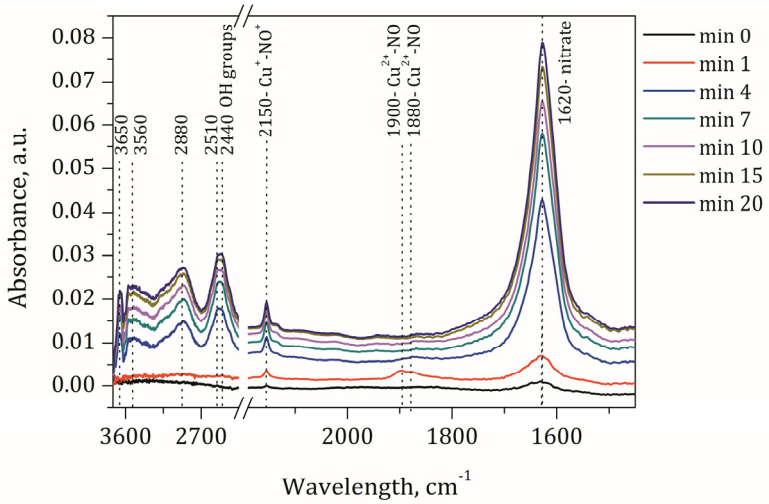

Figure 5.11. FTIR spectra during NO_2 adsorption over Cu/SAPO-34 catalyst at 100 °C with increasing time on stream up to 30 minutes. Feed stream: 660 ppm of NO_2 using N_2 as balance gas with a total flow rate of 500 ml min^{-1}.

difference with respect to the spectra recorded when the catalyst is contacted with NO in the presence or absence of O_2 is that the adsorption of NO_2 results in the formation of nitrates located at 1620 cm^{-1} as the only adsorbed specie. Nor nitrates located at different wavelengths (1577, 1590 or 1607 cm^{-1}) neither nitrites (1481 or 1500 cm^{-1}) were observed in the obtained spectra irrespective of the catalyst temperature. As already observed, the signal intensity due to the adsorption of NO_2 ad-species decreased with increasing temperature. Comparing the signal intensity of bridging nitrates (1620 cm^{-1}) when the catalyst was contacted with NO, $NO+O_2$ or NO_2, it can be observed the following intensity order: $NO<NO_2<NO+O_2$. Thus, it could be concluded that the formed nitrates are more stable when the catalyst is contacted with a gas stream containing NO in the presence of oxygen.

5.2.1.3. NH_3 adsorption in the presence and absence of oxygen

Ammonia has been used as a probe molecule to identify the different types of surface acidic sites in this study, which is also one important feature in the NH_3-SCR reaction. Figure 5.12 illustrates the FTIR spectra of Cu/SAPO-34 when the catalyst is contacted with a gas stream composed of 660 ppm of NH_3 and using N_2 as balance gas with a total flow rate of 500 ml min^{-1} N_2 at 100, 200 and 300 °C. Table 5.6 summarizes the IR bands identified when NH_3 is admitted to the gas cell.

Five bands at 3740, 3670, 3360, 3280 and 3190 cm^{-1} and three bands at 1620, 1440 and 1290 cm^{-1} were observed after the sample was treated with NH_3 containing gas stream. In the N-H stretching region, the bands at 3360, and 3280 cm^{-1} can be assigned to ammonium ions, while the band at 3190 cm^{-1} can be assigned to Cu^+-NH_3 species on the exchanged sites [224, 230].

The band around 1450 cm^{-1} was due to the bending vibration of NH_4^+ on the Brønsted acidic sites, while the bands at 1620 and 1290 cm^{-1} can be assigned to molecularly adsorbed NH_3 on Lewis acid sites (cooper ion sites). It has been cited that Lewis acid sites are primarily composed of the transition

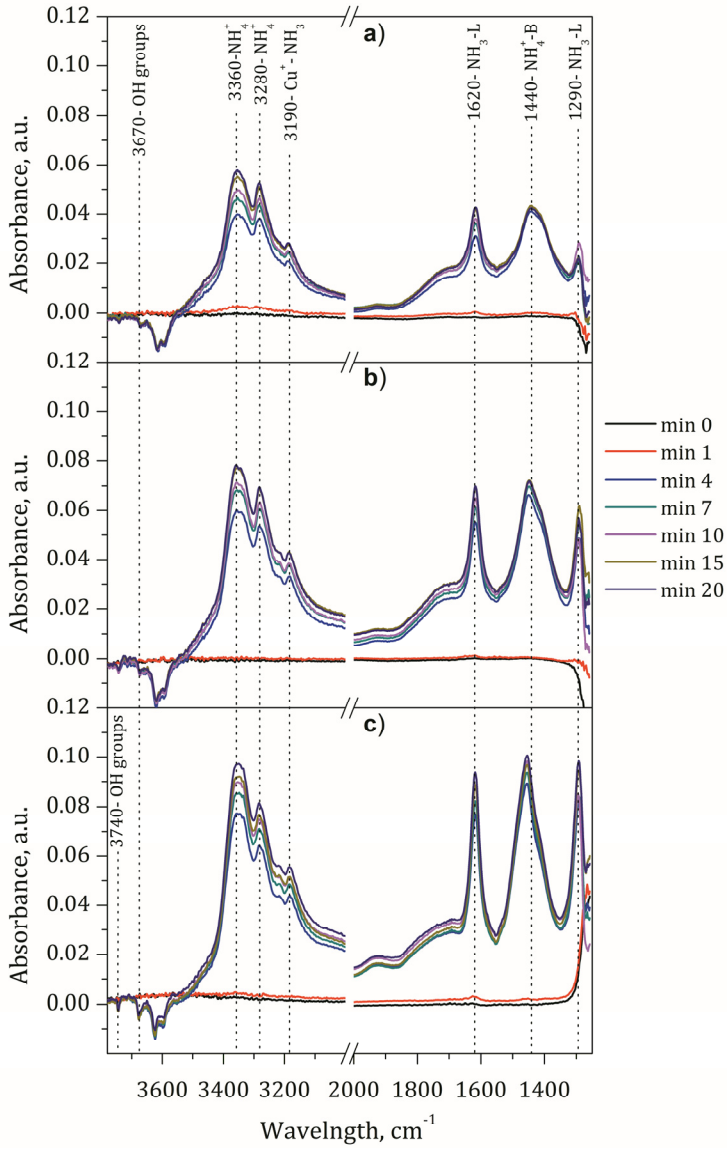

Figure 5.12. FTIR spectra during NH_3 adsorption over Cu/SAPO-34 catalyst at 300 (a), 200 (b) and 100 (c) °C with increasing time on stream up to 30 minutes in the absence of oxygen. Feed stream: 660 ppm of NH_3 using N_2 as balance gas with a total flow rate of 500 ml min^{-1}.

Table 5.6. Overview of the IR bands detected during NH_3 adsorption on Cu/SAPO-34 and their assignments.

IR band, cm^{-1}	Assignment	References
3360, 3280	Ammonium ions in N-H stretching region (NH_4^+)	[80, 224, 226, 228, 230, 231]
3180	Cu^+-NH_3 species on the exchanged sites (Cu^+-NH_3)	[80, 224, 226, 228, 230, 231]
3740	Si-OH on the external surface	[80, 224, 226, 228, 230, 231]
3670	P-OH on the external surface	[80, 224, 226, 228, 230, 231]
1450	NH_4^+-Brønsted acid sites (NH_4^+-B)	[80, 224, 226, 228, 230, 231]
1610, 1290	Molecularly adsorbed NH_3 on Lewis acid sites (NH_3-L)	[80, 224, 226, 228, 230, 231]

metal ions in metal ion exchanged zeolites [80, 224], while some extra-framework Al, mostly located at the external surface of the zeolite, may also contribute to the number of Lewis acid sites [224]. The negative peak at 3670 cm^{-1} was assigned to the occupation of P-OH sites by NH_3, reducing the corresponding OH stretching vibrations [224]. A band at 3740 cm^{-1} was also detected upon exposure to NH_3 at room temperature at 100 °C. This band can be assigned to NH_3 adsorbed onto Si-OH groups. This, however, was not observed in the NH_3 adsorption spectra taken at temperatures higher than 200 °C because of the weak adsorption strength of NH_3 on this site [224]. The intensity of the bands decreased when increasing the temperature indicating that the ammonia adsorption is restricted for high temperature [228].

The NH_3 desorption process was also followed by a temperature programmed desorption (NH_3-TPD) experiment to study the NH_3 adsorption strength and acid properties of the Cu/SAPO-34 sample. The NH_3-TPD was carried out by first admitting to the gas cell 660 ppm of NH_3 using N_2 as

balance gas with a total flow rate of 500 ml min^{-1} until catalyst saturation at 28 °C. After the NH_3 adsorption, the temperature was increased until 450 °C with a temperature ramp of 5 °C min^{-1} in 500 ml min^{-1} of N_2. Figure 5.13 shows representative FTIR spectra collected from room temperature up to 450 °C during NH_3-TPD experiment. At the beginning of the temperature ramp, the intensity of all bands decreased because of NH_3 desorption. Firstly, the band at 1455 cm^{-1}, which was assigned to ammonia adsorbed on Brønsted acid sites as ammonium ions (NH_4^+), decreases gradually until it disappeared at 450 °C. On the other hand, the band at 1620 cm^{-1}, attributed to the ammonia adsorbed on Lewis acid sites, also decreases but it was still detectable at 450 °C. Adsorbed NH_3 started to desorb from both type of acid sites readily from 28 °C, however, the NH_3 associated with Brønsted acid sites decreased more rapidly than the Lewis acid sites with increasing temperature, which indicates that NH_3 adsorbed on Lewis acid sites was more strongly bonded than on Brønsted acid sites. Simultaneously, the bridged OH groups are generally restored, as

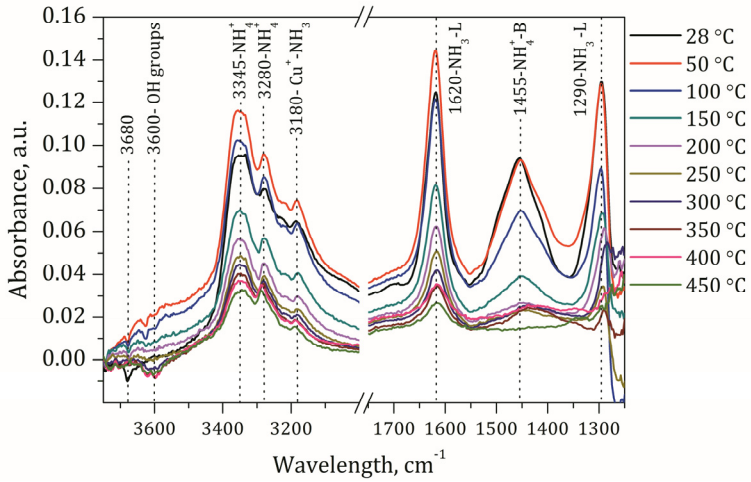

Figure 5.13. FTIR spectra during NH_3 desorption while increasing temperature (from 28 to 450 °C) over Cu/SAPO-34. Feed stream during NH_3 adsorption step: 660 ppm of NH_3 using N_2 as balance gas with a total flow rate of 500 ml min^{-1}. Feed stream during the TPD: 500 ml min^{-1} of N_2.

indicated by the growth of the negative bands at 3680 and 3600 cm^{-1} especially at temperatures higher than 400 °C [231].

To observe the influence of the presence of oxygen in the adsorption of NH_3 on the acid sites of the catalyst, FTIR spectra were taken with increasing time on stream while a gas stream of 500 ml min^{-1} composed of 660 ppm NH_3 and 6% O_2 was admitted to the gas cell. Figure 5.14 shows the evolution of the absorbance intensity with increasing time on stream at 100, 200 and 300 °C. Table 5.7 summarizes the IR bands when NH_3 and O_2 were fed together.

As can be observed in Figure 5.14 the adsorption bands are similar disregarded of the presence or absence of oxygen. The main difference is the relative intensity of the bands attributed to Brønsted and Lewis acid sites. In the presence of O_2, the band assigned to Brønsted acid sites (1440 cm^{-1}) is lower than that of Lewis acid sites (1620 cm^{-1}), which indicates that NH_3 adsorption is promoted over Lewis acid sites in the presence of oxygen.

Table 5.7. Overview of the IR bands detected during NH_3 adsorption in the presence of oxygen on Cu/SAPO-34 and their assignments.

IR band, cm^{-1}	Assignment	References
3350, 3271	Ammonium ions in N-H stretching region (NH_4^+)	[80, 224, 226, 228, 230, 231]
3180	Cu^+-NH_3 species on the exchanged sites (Cu^+-NH_3)	[80, 224, 226, 228, 230, 231]
3740	Si-OH on the external surface	[80, 224, 226, 228, 230, 231]
3670	P-OH on the external surface	[80, 224, 226, 228, 230, 231]
1440	NH_4^+-Brønsted acid sites (NH_4^+-B)	[80, 224, 226, 228, 230, 231]
1620, 1290	Molecularly adsorbed NH_3 on Lewis acid sites (NH_3-L)	[80, 224, 226, 228, 230, 231]

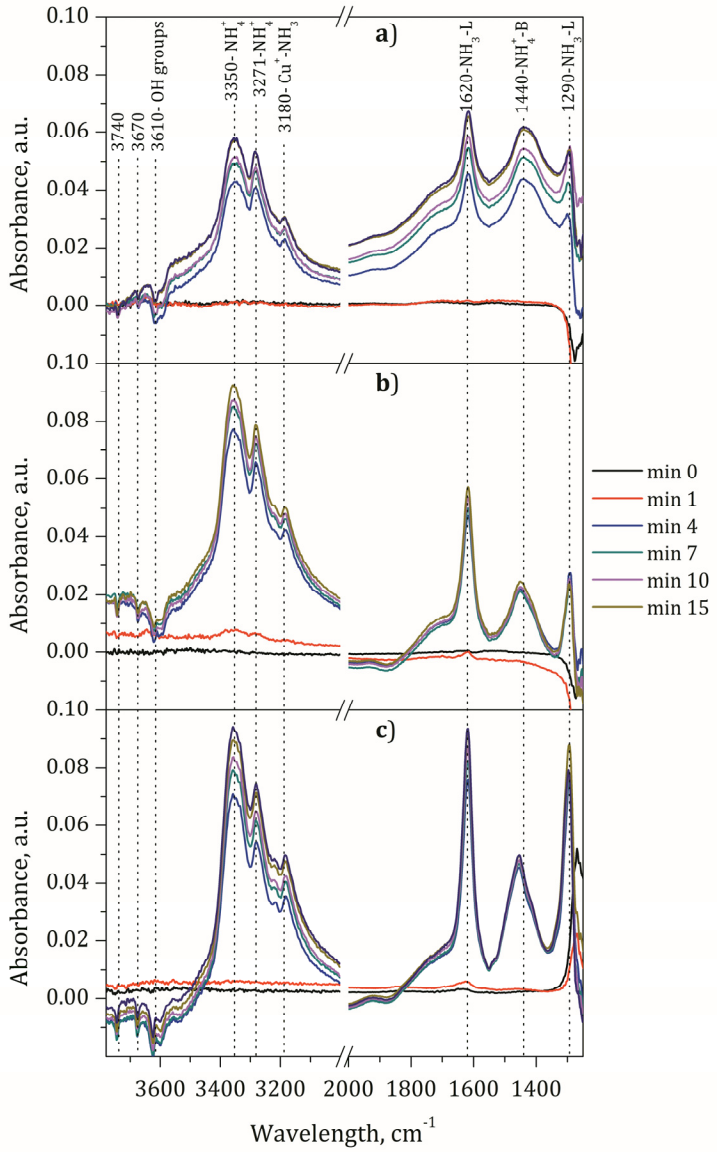

Figure 5.14. FTIR spectra during NH_3 adsorption in the presence of O_2 over Cu/SAPO-34 catalyst at 300(a), 200(b) and 100(c) °C with increasing time on stream to 30 minutes. Feed stream: 660 ppm of NH_3 and 6% of O_2 using N_2 as balance gas with a total flow rate of 500 ml min^{-1}.

5.2.1.4. NO and NH_3 co-adsorption in the presence and absence of oxygen

The NO and NH_3 co-adsorption was studied by FTIR in the presence and absence of oxygen. Figure 5.15 illustrates the FTIR spectra of Cu/SAPO-34 when the catalyst is contacted with a gas stream composed of 660 ppm of NH_3 and 660 ppm of NO using N_2 as balance gas with a total flow rate of 500 ml min^{-1} at 100, 200 and 300 °C.

As can be observed in Figure 5.15, almost all the bands observed during NO and NH_3 co-adsorption were assigned to NH_3 adsorbed species, indicating that NH_3 was preferentially adsorbed rather than NO, as De-La-Torre et al. [93] observed in their kinetic study. The absorption bands between 1610-1270 cm^{-1} were assigned to NH_3 adsorbed species on Brønsted and Lewis acid sites, as the growth of those bands was accompanied by the increase of bands located in the OH stretching region. At low temperature (100 °C), there are three absorption bands related to nitrates specie (1898, 1620 and 1600 cm^{-1}) that can only be observed for 1 minute of time on stream. The 1898 cm^{-1} band was assigned to Cu^{2+}-NO sites and the other two bands were assigned to nitrate species. The intensity of these bands is progressively reduced with increasing time and temperature, probably due to the activation of the slow NH_3-SCR reaction, which favors the reduction of NO by NH_3 in order to form N_2. Since Cu^{2+} is the active site, the adsorbed NH_3 species should migrate from the Brønsted acid sites to Lewis acid sites to participate in the SCR reaction [181].

Figure 5.16 illustrates the FTIR spectra of Cu/SAPO-34 catalyst when the catalyst is contacted with a gas stream composed of 660 ppm of NH_3, 660 ppm of NO and 6% O_2 using N_2 as balance gas with a total flow rate of 500 ml min^{-1} at 100, 200 and 300 °C.

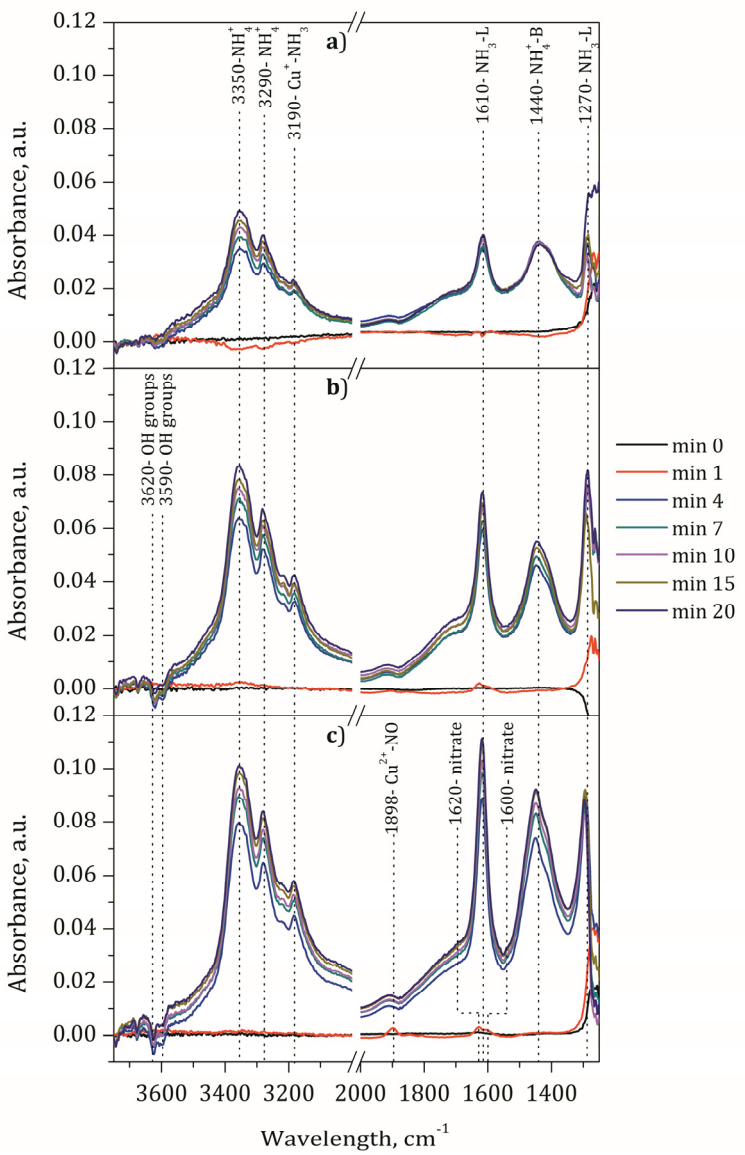

Figure 5.15. FTIR spectra during NH_3 and NO co-adsorption in the absence of O_2 over Cu/SAPO-34 catalyst at 300(a), 200(b) and 100(c) °C with increasing time on stream up to 30 minutes. Feed stream: 660 ppm of NO and 660 ppm of NH_3 using N_2 as balance gas with a total flow rate of 500 ml min^{-1}.

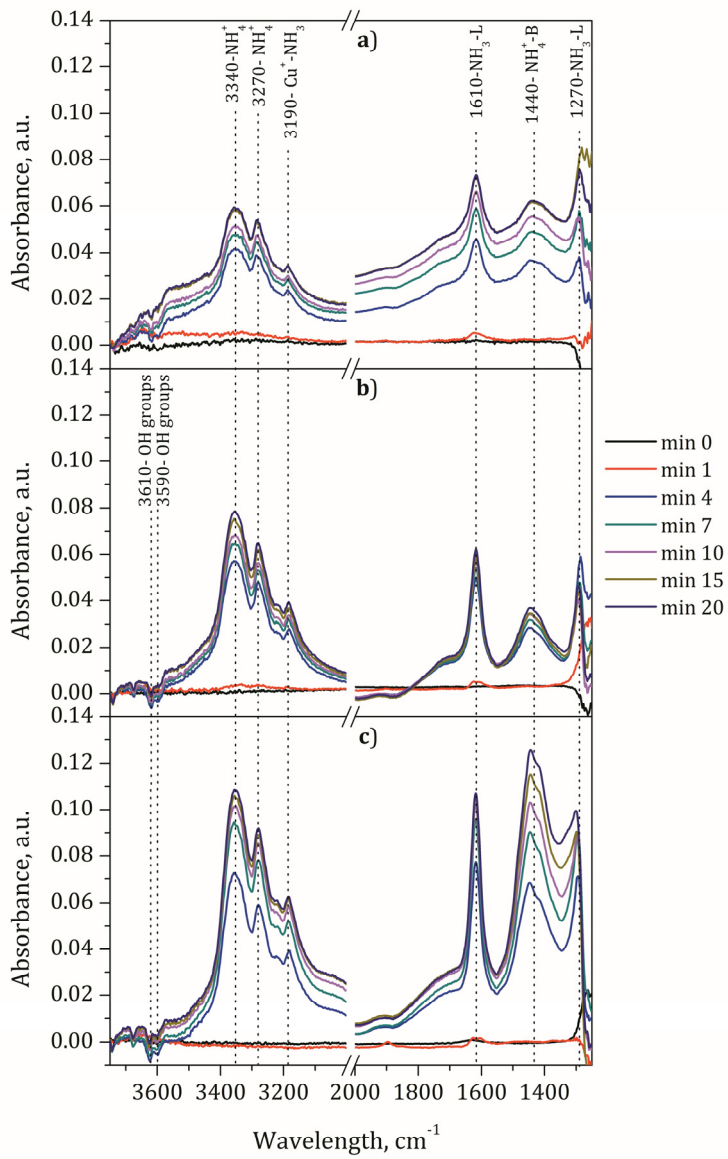

Figure 5.16. FTIR spectra during NH_3 and NO co-adsorption in the presence of O_2 over Cu/SAPO-34 catalyst at 300(a), 200(b) and 100(c) °C with increasing time on stream up to 30 minutes. Feed stream: 660 ppm of NO, 660 ppm of NH_3 and 6% of O_2 using N_2 as balance gas with a total flow rate of 500 ml min^{-1}.

After the co-adsorption of NO, NH_3 and O_2, only the features for adsorbed ammonia species were observed at all temperatures, indicating that the adsorption of ammonia is much stronger than NO on Cu/SAPO-34 catalyst [93].

Figure 5.16 shows the spectra of the catalyst at 100, 200 and 300 ºC during standard NH_3-SCR reaction conditions. As it has been previously observed, two bands assigned to NH_3 on Lewis (1610, 1270 cm^{-1}) acid sites were found. Also, two peaks around 1600 cm^{-1} can be observed for the first minute of time on stream. These bands are assigned to nitrate species and they disappeared for longer time on stream as can be observed in Figure 5.15. A large amount of NH_4^+ species adsorbed on Brønsted acid sites (bands at 3340, 3270 and 1440 cm^{-1}) were formed on the surface, and meanwhile two negative bands at 3610 and 3590 cm^{-1} were detected, suggesting the occupancy of Brønsted acid sites during the NH_3-SCR reaction. Additionally, the band at 3190 cm^{-1} related to the Cu^+-NH_3 species on the exchanged sites was found to be stable under the reaction conditions [230].

As the reaction temperature raised up to 280 °C, the bands attributed to NH_4^+ adsorbed on the Brønsted acid sites (1440 cm^{-1}) increased while Cu^+-NH_3 species decreased. Since NH_3 direct adsorption from gas phase on copper sites at this temperature is less favored thermodynamically, it can be deduced that NH_3 could gradually migrate from the NH_4^+ species firstly adsorbed on the Brønsted acid sites to the copper sites and then react with NO_x species to form N_2 [230].

As a result, it is suggested that the Brøsnted acid sites in Cu/SAPO-34 catalyst play a critical role in NH_3-SCR reactions, by supplying surface NH_3 species to the Cu sites for surface reactions with NO_x at high temperatures.

5.2.2. Identification of adsorbed species under transient gas stream composition

To continue the identification of adsorbed species during NH_3-SCR with Cu/SAPO-34 catalyst, a series of transient experiments have been carried out. The catalyst has been exposed to a concrete gas composition until saturation, and then, the gas composition is switched and the evolution of adsorbed species is analyzed. FTIR and reactor experiments have been carried out between 100 and 400 °C. In this section, the inlet NO and NH_3 concentrations for reactor experiments have been 1000 ppm. The total flow rate has been the same as in the previous experiments; 500 ml min^{-1} for FTIR and 2600 ml min^{-1} for the reactor.

5.2.2.1. Evolution of adsorbed species under transient gas stream swithching from NH_3 to NO in the presence and absence of oxygen

The evolution of adsorbed species during transient gas composition switching from NH_3 to NO in the presence and absence of oxygen was determined by FTIR. Besides, reactor experiments were also performed to follow the evolution of the concentration of reactants and products. Figure 5.17 illustrates the FTIR spectra of Cu/SAPO-34 when the catalyst is saturated under a gas stream containing 660 ppm NH_3 using N_2 (t=0) as balance gas with a total flow rate of 500 ml min^{-1}. Then, FTIR spectra are collected with increasing time on stream after the gas composition is switched to 660 ppm NO using N_2 as balance gas (during 30 min) with a total flow rate of 500 ml min^{-1}.

Figure 5.17 shows the evolution of the absorbance of adsorbed species during the gas composition switching from NH_3 to NO. Before admitting NO, the catalyst surface is populated by NH_3 adsorbed species on Lewis and Brønsted acid sites, as already explained in previous sections. At 100 °C, the admission of NO hardly affected the absorbance of NH_3 adsorbed species, revealing that the activity of the catalyst is almost negligible at such low

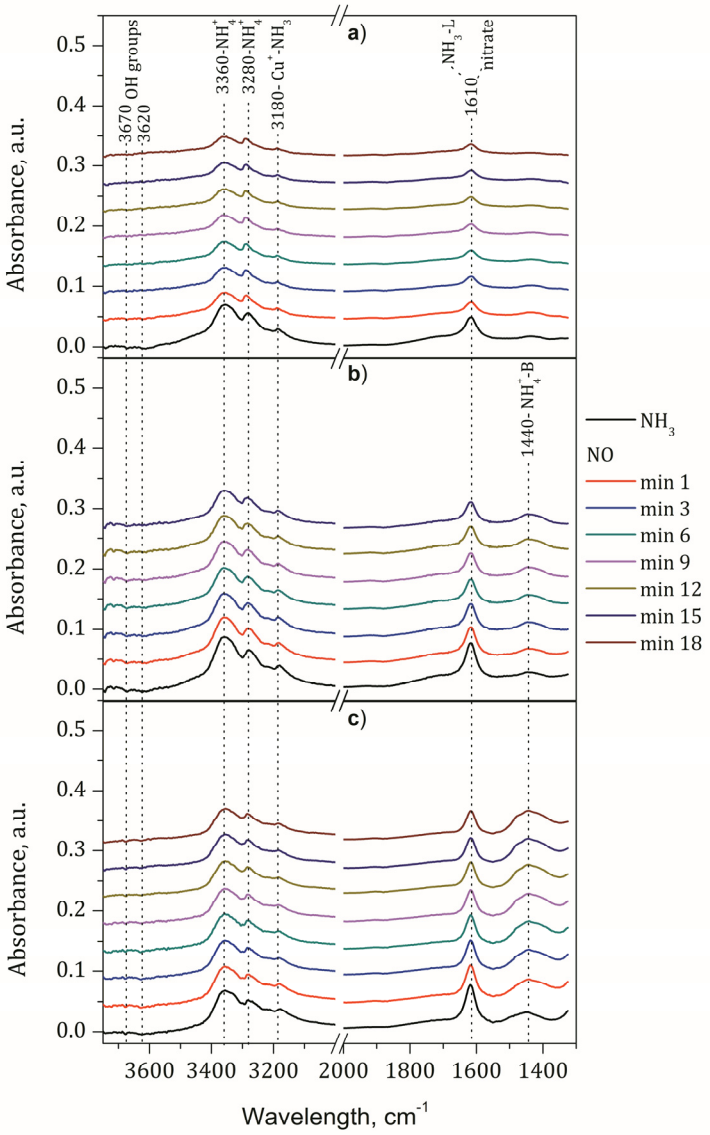

Figure 5.17. Evolution of adsorbed species with increasing time on stream once the catalyst has been saturated with NH_3 (t=0) and NO is admitted to the gas cell at 100 (c), 200 (b) and 300 °C (a). Feed stream: 1st) 660 ppm of NH_3 in 500 ml min^{-1} of N_2. 2nd) 660 ppm of NO in 500 ml min^{-1} of N_2.

temperature in the absence of oxygen. On the other hand, the signal diminution is notably higher at 200 and 300 °C, when the activity is enhanced. However, it is worth to note that adsorbed NH_3 species are not completely consumed even after 30 minutes of time on stream irrespective the reaction temperature.

Figure 5.18 shows the evolution of the concentration of NO, NH_3, N_2O and N_2 when the feed stream is switched from NH_3 to NO. The gas stream was composed of 1000 ppm NH_3 or 1000 ppm NO using Ar as balance gas with a total flow rate of 2600 ml min^{-1} at 150, 200, 300 and 400 °C. As can be observed in Figure 5.18 steady state NH_3 concentration is obtained before the feed stream switching, indicating that the catalyst is saturated with NH_3. The observed NH_3 concentration at the reactor outlet is close to the inlet value for low temperatures. Slightly lower NH_3 concentration is observed when increasing the reaction temperature due to NH_3 oxidation with adsorbed oxygen on the catalyst surface or due to the oxidation of NH_3 by Cu^{2+} ions that are reduced to Cu^{+}. The oxidation of some ppm of NH_3 can be corroborated by the increase of the concentration of N_2. When the feed stream composition is switched, the NO breakthrough is detected immediately after, revealing a poor reactivity of NO towards previously adsorbed NH_3 in the absence of oxygen. In line with the previous statement, very small quantities of N_2 and N_2O are detected. Only at the highest temperature (400 °C), the formation of N_2 and N_2O is slightly promoted. This results are in line with the adsorbed species observed by FTIR, where the signal due to NH_3 adsorbed species are slightly reduced but new bands attributed to other adsorbed species, such as nitrates, are absent.

Figure 5.19 illustrates the FTIR spectra of Cu/SAPO-34 when the catalyst is saturated under a gas stream containing 660 ppm NH_3 and 6% O_2 balanced to N_2 with a total flow rate of 500 ml min^{-1} (t=0). Then, FTIR spectra are collected with increasing time on stream after the gas stream composition is

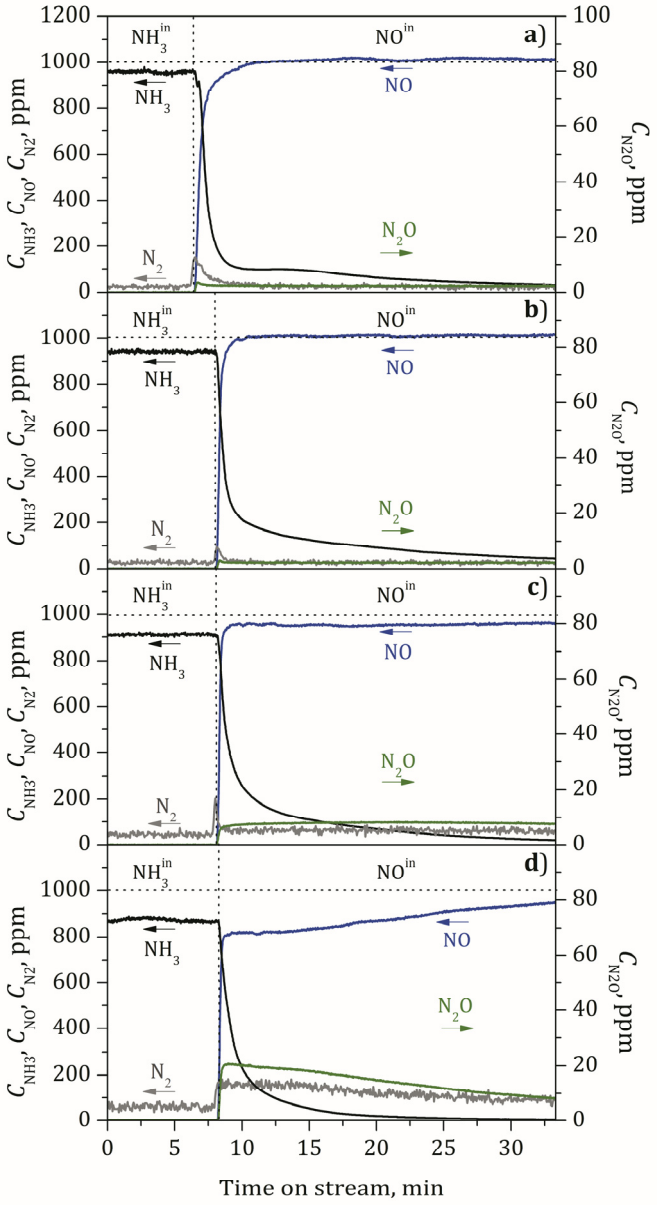

Figure 5.18. Transient experiments feeding NH_3 and then NO to the reactor at 150 °C (a), 200 °C (b), 300 °C (c) and 400 °C (d). Feed stream: 1000 ppm NO and 1000 ppm NH_3 using Ar as balance gas with a total flow rate of 2600 ml min^{-1}.

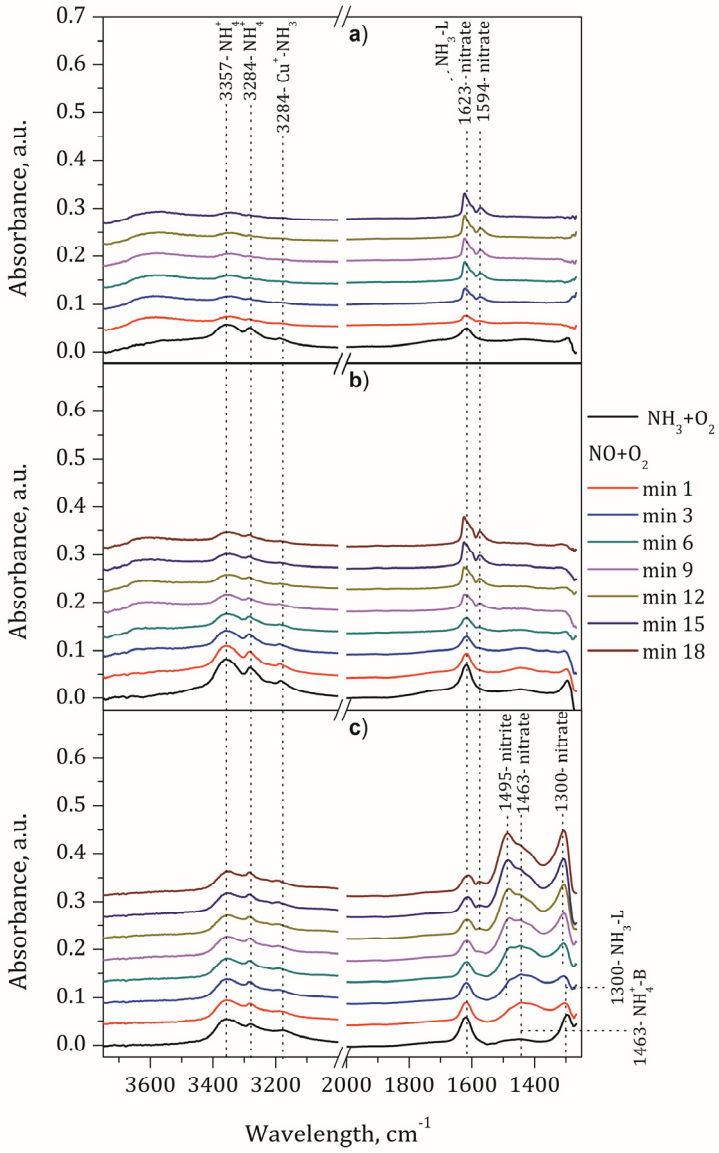

Figure 5.19. Evolution of adsorbed species with increasing time on stream once the catalyst has been saturated in presence of oxygen with NH_3 (t=0) and NO is admitted to the gas cell at 100(c), 200(b) and 300(a) °C. Feed stream: 1st) 660 ppm of NH_3 and 6% of O_2 in 500 ml min^{-1} of N_2. 2nd) 660 ppm of NO and 6% of O_2 in 500 ml min^{-1} of N_2.

switched to 660 ppm NO and 6% O_2 balanced to N_2 with the same total flow rate.

As observed in Figure 5.19, adsorbed NH_3 species populate the catalyst surface before the feed stream is switch to NO and O_2. At 100 °C, the signal intensity due to NH_3 adsorbed species is slightly reduced while increasing time on stream. Meanwhile, new bands appeared at 1495 due to surface nitrites and 1463 and 1300 cm^{-1} attributed to surface nitrates. Even though nitrites and nitrates are formed on the catalyst surface, NH_3 adsorbed species are still identified. This fact reveals the low reactivity of surface nitrates and nitrites with adsorbed NH_3 at low temperature (100 °C). Note that the absorption band of NH_3 adsorbed onto Lewis acid sites is overlapped with the absorption band of nitrates at 1623 cm^{-1}. However, the presence of adsorbed NH_3 species can be confirmed by the detection of NH_4^+ ions in the OH stretching region, which is not affected by the appearance of nitrates or nitrites. At 200 °C, the reactivity of surface nitrates and nitrites with adsorbed NH_3 is increased. Consequently, the signal of NH_3 adsorbed species in the OH stretching region becomes almost negligible after 18 minutes of time on stream. Meanwhile, nitrates located at 1623 and 1594 cm^{-1} are observable after 9 minutes of time on stream. Some other nitrates and nitrites species already detected at 200 °C are not detected at higher temperature due to their low thermal stability. At 300 °C, a similar behavior is observed. Now, the signal due to NH_3 adsorbed species becomes negligible after only 1 minute, and nitrates are evident after 3 minutes of time on stream, revealing a higher surface reactivity [226].

Reactor experiments with transient feed stream composition were also performed by first admitting 1000 ppm of NH_3 and 6% O_2 and then 1000 ppm of NO and 6% O_2. Figure 5.20 shows the evolution of the concentration of NO, NO_2, NH_3, N_2O and N_2 when the feed stream is switched from NH_3 to NO in the presence of oxygen. Before the gas composition switching, steady state NH_3 concentration is reached. As can be observed, the steady state concentration

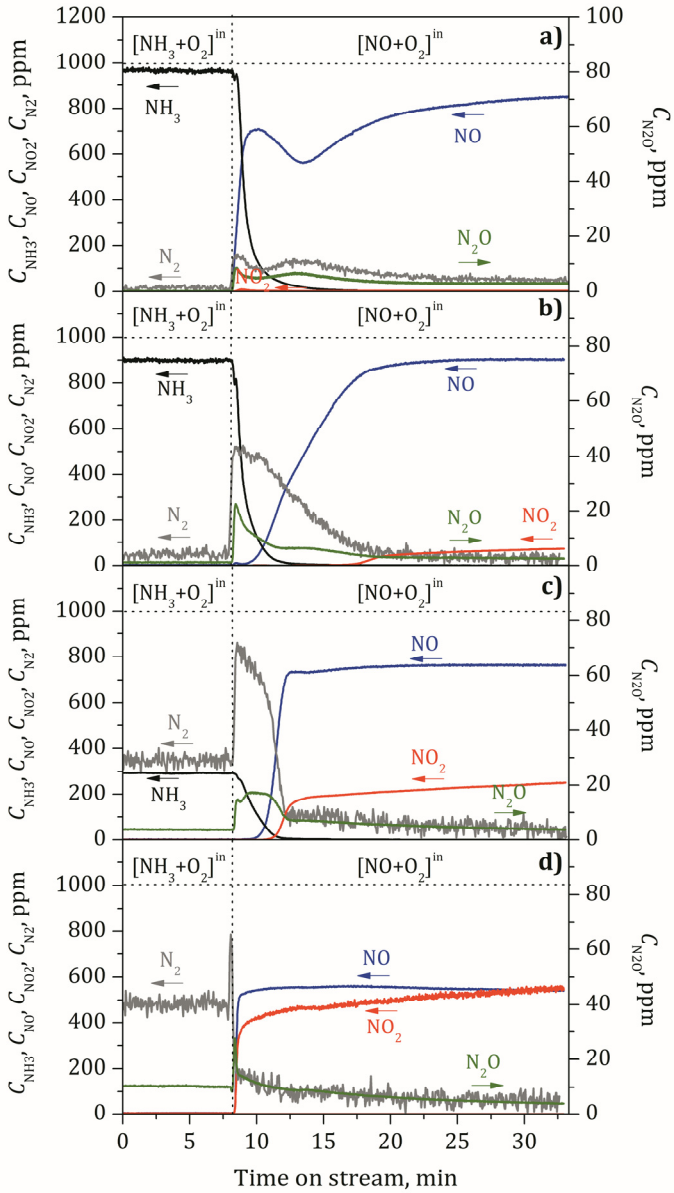

Figure 5.20. Transient experiments with NH_3+O_2 adsorption and then NO+O_2 adsorption at 150(a), 200(b), 300(c) and 400(d) °C. Feed stream: 1000 ppm NO, 1000 ppm NH_3 and 6% of O_2 using Ar as balance gas with a total flow rate of 2600 ml min^{-1}.

of NH_3 is temperature dependent. At low temperature, the outlet NH_3 concentration equals that at the inlet, i.e. 1000 ppm. With increasing the reaction temperature, a progressive decrease of the steady state NH_3 concentration is observed due to the oxidation of NH_3 by O_2 to form N_2. At 400 °C, total NH_3 oxidation is observed to form preferably N_2 and some N_2O. After the gas stream switching to NO and oxygen, the NO breakthrough was immediately detected and minor concentration of N_2 was observed at low temperature (150 °C). The picture changed notably at 200 °C. The NO breakthrough was delayed around 1 minute and N_2 formation was observed for 10 minutes. As already observed by FTIR, adsorbed NH_3 species react with surface nitrates in order to form nitrogen through the NH_3-SCR. At 300 °C, higher concentration of N_2 is detected but its formation is only extended for 5 minutes. In line with FTIR results, temperature promotes the reactivity between adsorbed NH_3 and nitrates. NO_2 is also observed due to the oxidation of NO by oxygen. Finally, at 400 °C, N_2 formation is not observed. The adsorption of NH_3 on the catalyst surface is not favored at such high temperature and there is a lack of reductant to reduce the adsorbed nitrates. Higher NO_2 concentration is observed due to the promotion of the NO oxidation reaction.

5.2.2.2. Evolution of adsorbed species during transient gas stream switching from NO to NH_3 in the presence and absence of oxygen

Figure 5.21 illustrates the FTIR spectra of Cu/SAPO-34 when the catalyst is saturated under a gas stream containing 660 ppm NO balanced to N_2 (t=0) with a total flow rate of 500 ml min^{-1}. Then, FTIR spectra are collected with increasing time on stream after the gas stream composition is switched to 660 ppm NH_3 balanced to N_2.

Nitrates located at 1617 cm^{-1} are only observed at low temperature (100 °C) before the gas stream switching to NH_3. After the switching, absorption bands attributed to NH_3 adsorbed species are clearly identified. Thus, NH_3

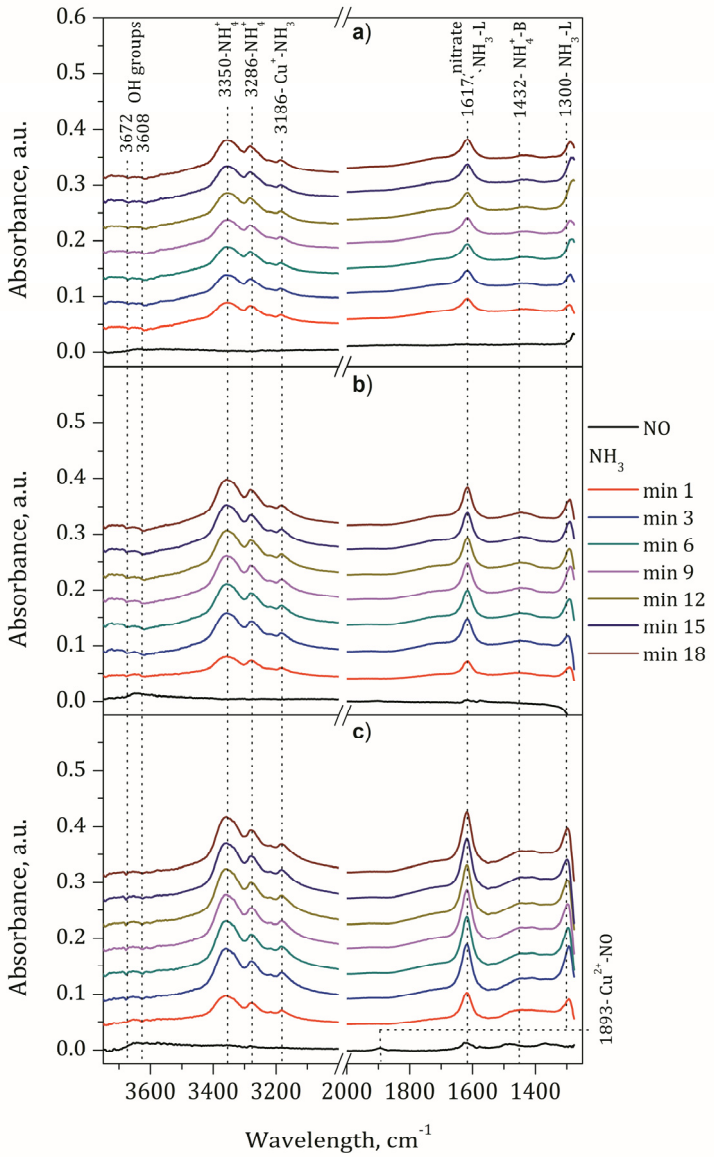

Figure 5.21. Evolution of adsorbed species with increasing time on stream once the catalyst has been saturated with NO (t=0) and NH_3 is admitted to the gas cell at 100(c), 200(b) and 300(a) °C. Feed stream: 1st) 660 ppm of NO in 500 ml min^{-1} of N_2. 2nd) 660 ppm of NH_3 in 500 ml min^{-1} of N_2.

adsorption is favored even though the catalyst has been previously exposed to NO. The absorbance of NH_3 adsorbed species decreases with temperature, as observed in previous sections.

Figure 5.22 shows the evolution of the concentration of NO, NH_3, N_2O and N_2 when the feed stream is switched from NO to NH_3 in the absence of oxygen. The feed stream was composed of 660 ppm NO or 660 ppm NH_3 using Ar as balance gas and with a total flow rate of 2600 ml min^{-1}. As can be observed, N_2 was not detected irrespective of the reaction temperature. Thus, there is not surface reactivity between adsorbed nitrate species and NH_3. The NH_3 breakthrough was delayed because of the storage of NH_3 on the acidic sites of the zeolite, as observed by FTIR. NH_3 was detected earlier in the reactor outlet as increasing the reaction temperature due to the lower NH_3 storage capacity.

Then, the evolution of adsorbed species during transient gas stream switching from NO to NH_3 in the presence of oxygen was studied (Figure 5.23). The catalyst was first pretreated with 660 ppm of NO and 6% O_2 for 30 minutes using N_2 as balance gas with a total flow rate of 500 ml min^{-1}. Afterwards, 660 ppm of NH_3 and 6% of O_2 balanced with N_2 was admitted to the gas cell. The presence of oxygen favors the stability of surface nitrate species, which are observable in all the temperatures studied, as opposite to that observed in the absence of O_2 (Figure 5.21). The signals attributed to surface nitrate species progressively tend to disappear after NH_3 is admitted. Note that nitrates located at 1573 cm^{-1} are not affected by the formation of adsorbed NH_3 species, revealing that after 3 minutes, nitrates are not present on the catalyst surface.

Figure 5.24 shows the evolution of the concentration of NO, NH_3, N_2O and N_2 when the feed stream is switched from NO to NH_3 in the presence of oxygen. Before the gas switching, steady state NO and NO_2 concentrations are reached. The concentration of NO_2 progressively increases with temperature due to the promotion of the NO oxidation. At 150 and 200 °C, N_2 was not detected after the gas switching. On the contrary, for higher temperatures N_2

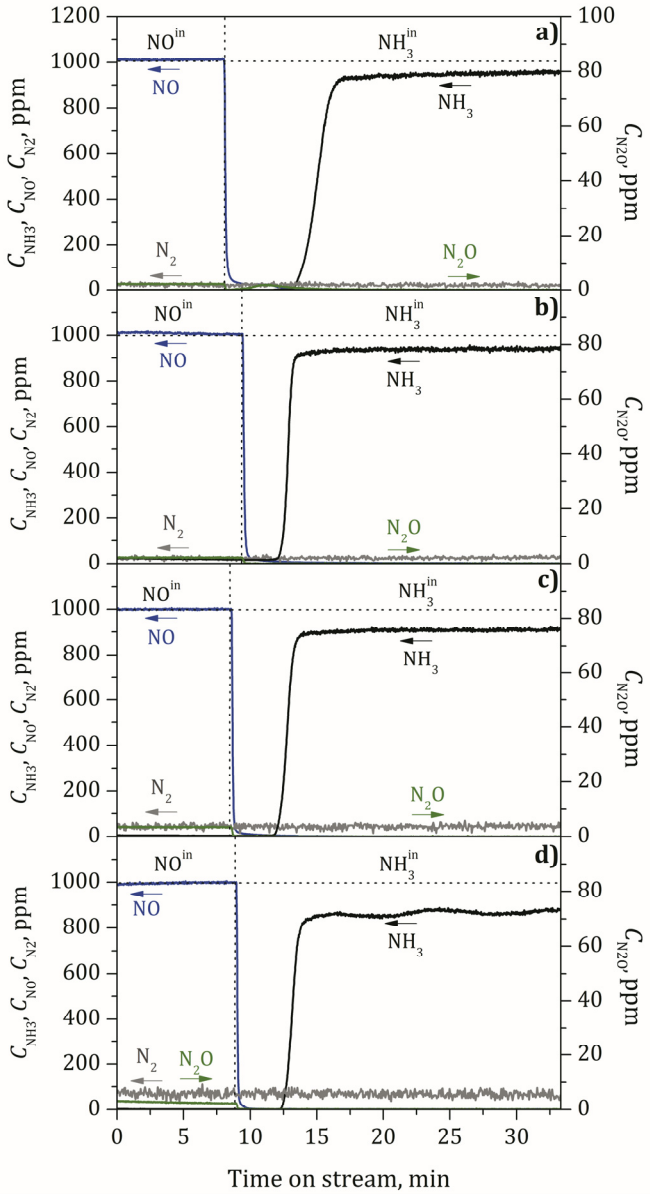

Figure 5.22. Transient experiments in the reactor with NH_3 adsorption on the catalyst saturated by NO at 150 (a), 200 (b), 300 (c) and 400 (d) °C. Feed stream: 1000 ppm NO and 1000 ppm NH_3 using Ar as balance gas with a total flow rate of 2600 ml min^{-1}. The amount of the catalyst is 0.8 g.

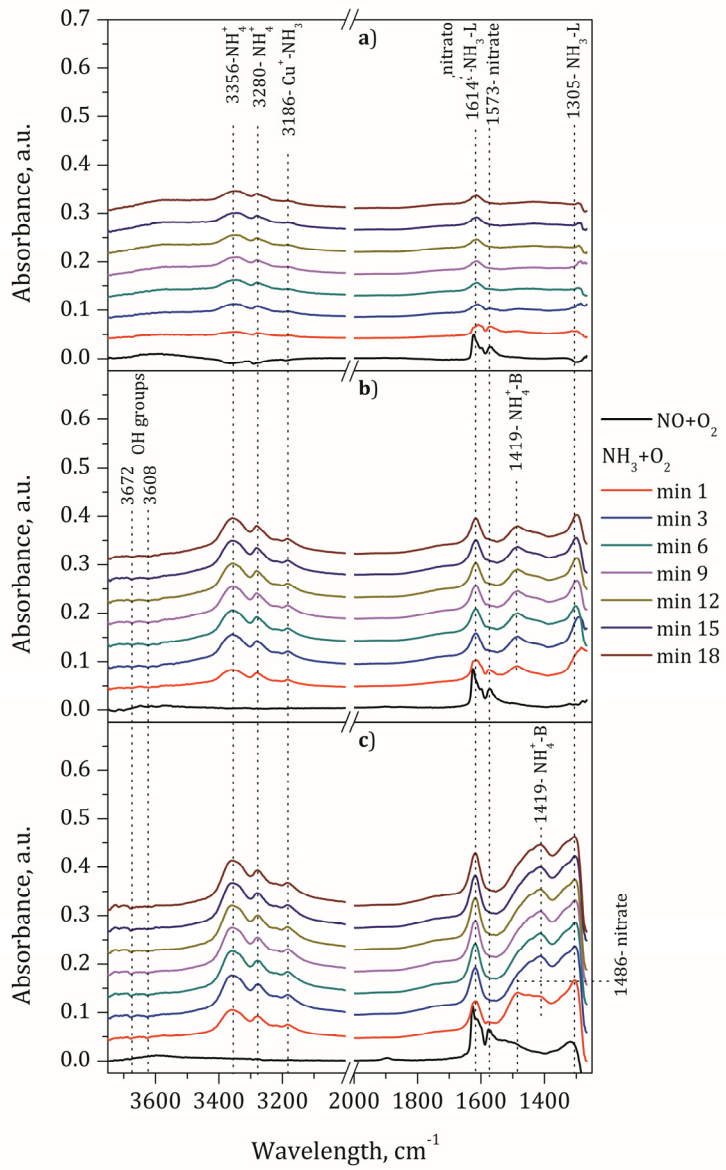

Figure 5.23. Evolution of adsorbed species with increasing time on stream once the catalyst has been saturated in presence of oxygen with NO (t=0) and NH_3 is admitted to the gas cell at 100 (a), 200 (b) and 300 (c) °C. Feed stream: 1st) 660 ppm of NO and 6% of O_2 in 500 ml min^{-1} of N_2. 2nd) 660 ppm of NH_3 and 6% of O_2 in 500 ml min^{-1} of N_2.

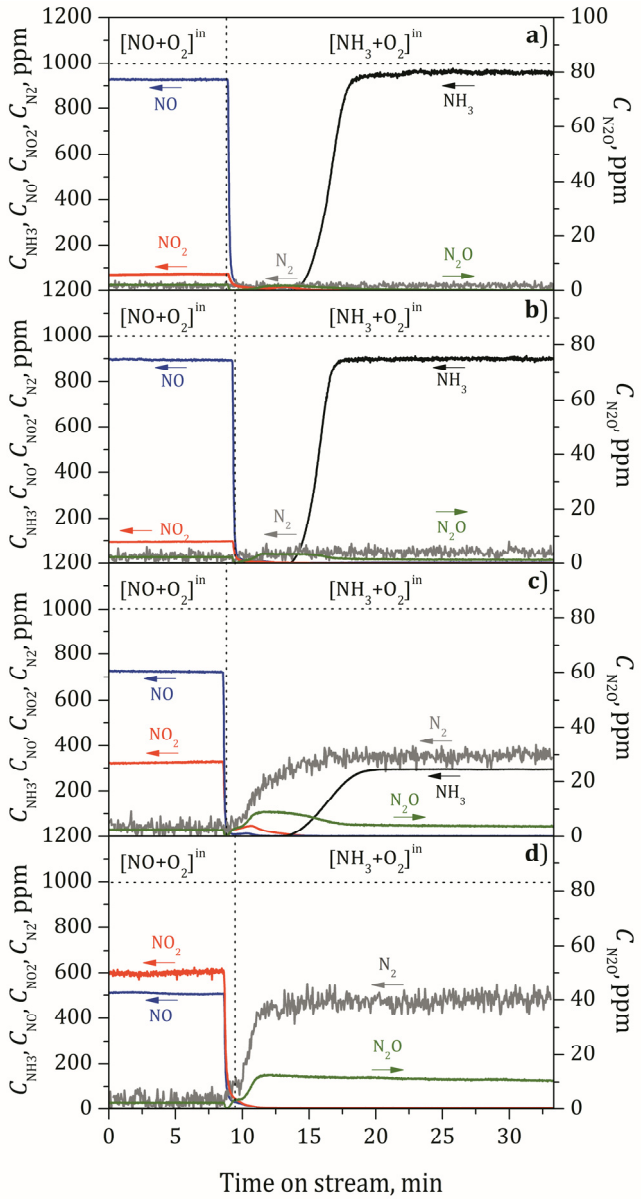

Figure 5.24. Transient experiments with NO and NH_3 in the presence of O_2 over Cu/SAPO-34 catalysts at 150 (a), 200 (b), 300 (c) and 400 (d) °C. Feed stream: 1000 ppm NO, 1000 ppm NH_3 and 6% of O_2 using Ar as balance gas with a total flow rate of 2600 ml min^{-1}. The amount of the catalyst is 0.8 g.

was detected as a product of the oxidation of NH_3 but its formation is not related to the NH_3-SCR reaction. Thus, it can be concluded that the NH_3-SCR reaction is not promoted when NH_3 is fed on pre-adsorbed nitrates, even in the presence of oxygen.

5.3. OVERALL VIEW AND CONCLUSIONS

The dominant NO_x ad-species at low temperature (200 °C) are bridging nitrites over Pt-Ba/Al_2O_3 catalyst. At higher temperature (300 °C), nitrates become the dominant NO_x ad-species and nitrites were only detected for short time on stream. The presence of ceria in Pt-Ba-Ce/Al_2O_3 catalyst enhances the stability of nitrites associated to the barium phase at low temperature. Ceria impedes the close contact between Pt and BaO and inhibits the oxidation of nitrites to nitrates.

Nitrites and nitrates are rapidly and totally decomposed when H_2 is admitted to the gas cell. Slightly slower reduction rate is observed at low temperature and especially for ceria containing catalysts, due to the absence of an intimate contact between Pt and Ba. CO is not as efficient as H_2 for the decomposition of stored nitrites and nitrates, as the presence of adsorbed NO_x ad-species is observable even after 30 min of time on stream at 200 °C. The decomposition of nitrites and nitrates is enhanced at higher temperatures. During the reduction step, additional signals attributed to adsorbed cyanate/isocyanate species over Ba or Al_2O_3, CO adsorption onto Pt and carbonates are detected. The ability of C_3H_6 to decompose adsorbed NO_x ad-species at low temperature is also limited. At higher temperature, decomposition of nitrites and nitrates is observed along with the evolution of signals attributed to carbonates, CO adsorbed onto Pt and adsorbed cyanate species. At 400 °C, the reductant C_3H_6 starts to be effective for NO_x decomposition and reduction, but NO_x removal from the catalyst surface is not complete.

Nitrites and nitrates are also detected over Cu/SAPO-34 catalyst when NO is admitted to the gas cell in the presence or absence of oxygen. The thermal stability of nitrates and nitrites is notably higher in the presence of oxygen. Specifically, nitrates are more stable than nitrites.

NH_3 is adsorbed onto Lewis and Brønsted acid sites of the Cu/SAPO-34 catalyst when NH_3 is admitted to the gas cell in the presence or absence of oxygen. The intensity of the absorption bands decreased when increasing the temperature indicating that the ammonia adsorption is restricted for high temperature. During NH_3 and NO co-adsorption in the presence or absence of oxygen, almost all the bands observed are assigned to NH_3 adsorbed species, indicating that NH_3 is preferentially adsorbed rather than NO. During this process, the NH_3 species adsorbed on the Brønsted acid sites decline slowly. Since the Cu^{2+} site is the active site, the adsorbed NH_3 species should migrate from the Brønsted acid sites to Lewis acid sites to participate in the SCR reaction.

During transient gas stream switching from NH_3 to NO in the absence of oxygen, the admission of NO hardly affected the absorbance of NH_3 adsorbed species at 100 °C. The signal diminution due to NH_3 adsorbed species is notably higher at 200 and 300 °C, when the NH_3-SCR activity is enhanced. Reactor experiments revealed that after the gas stream switching, the NO breakthrough was immediately after detected, suggesting a poor reactivity of NO towards previously adsorbed NH_3 in the absence of oxygen. Almost negligible quantities of N_2 are detected irrespective the reactor temperature.

During transient gas stream switching from NH_3 to NO in the presence of oxygen, the reactivity of adsorbed NH_3 with surface nitrates and nitrites is increased. Indeed, the NH_3-SCR reaction proceeds until NH_3 adsorbed species are completely consumed. Reactor experiments revealed that the NO breakthrough was delayed and N_2 formation was observed until complete depletion of adsorbed NH_3.

During transient gas stream switching in the opposite order, i.e. first admitting NO and then NH_3 in the absence of oxygen, absorption bands attributed to NH_3 adsorbed species are clearly identified. Thus, NH_3 adsorption is favored even though the catalyst has been previously exposed to NO. Reactor experiments revealed that N_2 was not detected irrespective of the reaction temperature when NH_3 was fed to the catalyst saturated with NO. Thus, there is not surface reactivity between adsorbed nitrate species and NH_3.

On the other hand, during transient gas stream switching from NO to NH_3 in the presence of oxygen, the stability of surface nitrate species is increased. Even though, the signals attributed to surface nitrate species progressively tend to disappear after NH_3 is admitted. Reactor experiments revealed that the NH_3 breakthrough was delayed because of the storage of NH_3 on the acidic sites of the zeolite. At low temperature, N_2 was not detected after the gas switching. On the contrary, for higher temperatures N_2 was detected as a product of the oxidation of NH_3 but its formation is not related to the NH_3-SCR reaction. Thus, it can be concluded that the NH_3-SCR reaction is not promoted when NH_3 is fed on pre-adsorbed nitrates, even in the presence of oxygen.

Chapter 6

INFLUENCE OF THE REDUCTANT NATURE ON DeNO$_x$ PERFORMANCE OF SINGLE NSR AND COMBINED NSR-SCR MONOLITHIC SYSTEMS

Chapter 6

INFLUENCE OF THE REDUCTANT NATURE ON DeNO$_x$ PERFORMANCE OF SINGLE NSR AND COMBINED NSR-SCR MONOLITHIC SYSTEMS

ABSTRACT

In this chapter it is reported the effects of feeding different type of reducing agents in the combined NO_x storage and reduction (NSR) and selective catalytic reduction (SCR) technologies (NSR-SCR). Pt-Ba/Al_2O_3 and Pt-Ba-Ce/Al_2O_3 monoliths are synthetized to be used as NSR catalysts, whereas Cu/BETA and Cu/SAPO-34 monoliths are synthesized to be used as SCR catalysts.

During the cycling fuel-lean and fuel-rich operation, CO_2 and H_2O are continuously added in the feed stream. Consequently, the extension of the reverse water gas shift (RWGS), water gas shift (WGS) and steam reforming (SR) reactions in the NSR catalyst is first analyzed when hydrogen, carbon monoxide or propylene are used as reductant, respectively.

Then, the NO_x conversion and product distribution at the outlet of the stand-alone NSR converter is analyzed as a function of the reaction temperature and reductant concentration. H_2 is the more efficient reductant at low temperature. The reducing capacity of CO is comparable to H_2 from 300 °C and onwards due to the promotion of the WGS. Higher temperature (400 °C) is needed for propylene to be as effective reductant as H_2 or CO due to the promotion of SR reaction. The NH_3 production at the outlet of the stand-alone NSR increases in the following order: C_3H_6<CO<H_2. Consequently, the benefit of the NSR-SCR configuration is more pronounced when using H_2 as reductant due to a higher availability of NH_3 to be used in the SCR catalyst. The formation of NH_3 only occurs at elevated temperature when using CO, propane or toluene as reductants. At high temperature, the ability of the SCR catalyst to store NH_3 is limited and thus, the benefit of the combined NSR-SCR configuration is not so noteworthy. The best results are achieved with the combined NSR-SCR configuration at 300 °C using H_2 as reductant with Pt-Ba-Ce/Al_2O_3 and Cu/SAPO-34 catalysts.

Capítulo 6

INFLUENCIA DE LA NATURALEZA DEL AGENTE REDUCTOR EN EL RENDIMIENTO DeNO$_x$ DEL SISTEMA SIMPLE NSR Y COMBINADO NSR-SCR

RESUMEN

En el presente capítulo se ha estudiado la influencia de distintos agentes reductores en la tecnología NSR y en la combinación de las tecnologías NSR-SCR. Los agentes reductores estudiados han sido H_2, CO, C_3H_6 y C_7H_8 y los catalizadores utilizados han sido Pt-Ba/Al_2O_3 y Pt-Ba-Ce/Al_2O_3 para la tecnología NSR y Cu/BETA y Cu/SAPO-34 para la tecnología SCR.

En los experimentos realizados se han introducido CO_2 y H_2O en todo momento para simular una alimentación real de un motor diésel. En primer lugar se ha estudiado en los catalizadores NSR la reacción inversa de desplazamiento de agua (RWGS) y la reacción de desplazamiento de agua (WGS) alimentando H_2 y CO, respectivamente. También, se ha estudiado la reacción de reformado con vapor (SR) alimentando C_3H_6.

Después, en función de la temperatura de reacción y de la concentración de los agentes reductores se ha analizado la conversión de NO_x y la distribución de los productos formados. A bajas temperaturas el agente reductor más eficiente es el H_2. La capacidad de reducción del CO es comparable al H_2 a 300 °C o a temperaturas superiores debido a la reacción de WGS. A temperaturas más altas (400 °C) la capacidad de reducción del propileno es comparable con la del H_2 y el C0. A la salida del catalizador NSR la cantidad de amoniaco formado sigue el orden: C_3H_6< CO<H_2. Por ello, cuando el H_2 es el agente reductor se obtienen mejores resultados en el sistema combinado NSR-SCR debido a que el amoniaco es utilizado en el catalizador SCR de forma más eficaz. Cuando el CO, C_3H_6 o el C_7H_8 son los agentes reductores, el amoniaco solo se forma a alta temperatura. Sin embargo, a alta temperatura la capacidad de almacenar el amoniaco en el catalizador SCR disminuye y los beneficios del sistema combinado decrecen. Los mejores resultados se han obtenido a 300 °C y con H_2 en el sistema combinado Pt-Ba-Ce/Al_2O_3 y Cu/SAPO-34.

6. INFLUENCE OF THE REDUCTANT NATURE ON DeNO$_x$ PERFORMANCE OF SINGLE NSR AND COMBINED NSR-SCR MONOLITHIC SYSTEMS

Regeneration of NSR catalyst or NSR-SCR system using different reductants, such as H_2, CO and hydrocarbons at different operating temperatures has been investigated. At low temperatures, there is a consensus that H_2 is better in comparison to CO and HC, possibly due to precious metal site poisoning or Ba site poisoning by residual isocyanates. At higher temperatures (T> 300 °C), H_2, CO and HC are to some extent comparable in their regeneration and reduction efficiencies due to at high temperatures there is H_2 production via Water Gas Shift (WGS) or Steam Reforming (SR) reactions with CO and HC as reducing agents [50]. For example, previous studies [232, 233] have shown that steam reforming of CH_4, C_3H_8 and C_7H_8 begins at approximately 325 to 350 °C over Pd and Pt/Rh based catalysts. Such data indicate that if H_2 is a necessary reductant, then NSR catalyst regeneration using such hydrocarbon species may be limited at temperatures below 350 °C, which is in the range that some authors reported equivalent performance between HCs and H_2 [50].

The objective of this chapter is to analyze the product distribution with different reducing agents (H_2, CO, C_3H_6 and C_7H_8) during the rich period, when the NO_x removal is carried out in a single system or combined with an SCR downstream the NSR in a double bed configuration [234]. Also, the influence of ceria loading on the NO_x storage and reduction performance of model Pt-Ba/Al_2O_3 catalyst is analyzed, because ceria can act as an oxygen storage compound [216]. Finally, the influence of different zeolites (BETA and H-SAPO-34) in the combined NSR-SCR system is analyzed with the different reducing agents.

6.1. NO_X STORAGE AND REDUCTION USING Pt-Ba/Al_2O_3 AND Pt-Ba-Ce/Al_2O_3 CATALYSTS WITH DIFFERENT REDUCING AGENTS

6.1.1. Regeneration of the trap with H_2 as reductant

6.1.1.1. Evaluation of the extension of the RWGS

The utilization of H_2 as reductant during the regeneration of the NO_x storage and reduction (NSR) catalyst in the presence of H_2O and CO_2 can activate the RWGS reaction, i.e. $H_2 + CO_2 \leftrightarrows CO + H_2O$. The occurrence of the RWGS reaction could have a notable impact on the NSR performance of the prepared catalysts, as hydrogen would be consumed in order to produce carbon monoxide, which is known to be a less efficient reductant than H_2 [52, 216, 220, 235], especially at low temperature. Consequently, specific experiments were performed under steady state feeding a gas stream composed of 5% H_2O, 5% CO_2 and 1% H_2 balanced to Ar with a total flow rate of 1800 ml min^{-1} in the temperature range of 200-500 °C, in order to evaluate the activity of the prepared samples in the RWGS.

Figure 6.1a shows the evolution of the H_2 conversion with temperature whereas Figure 6.1b shows the evolution of the concentration of H_2 and CO in ppm, both with the Pt-Ba/Al_2O_3 catalyst. Continuous lines are also depicted indicating the reactant conversion and the concentration of H_2 and CO at the equilibrium. As can be observed, the thermodynamics predicted a very low extension of the RWGS in the whole temperature range, with a slight tendency to increase with temperature, as usual for endothermic reactions (ΔH^0=41.16 kJ mol^{-1}). Pt-Ba/Al_2O_3 catalyst presented almost null H_2 conversion (<1%) for temperatures lower than 300 °C and only a slight increase was observed for higher temperatures, reaching a maximum H_2 conversion of 12.8% at 500 °C. This value is close to the equilibrium conversion predicted by thermodynamics at 500 °C (16.9%), which reveals that Pt-Ba/Al_2O_3 catalyst is rather active for the RWGS. As can be observed in Figure 6.1b, even at 500 °C,

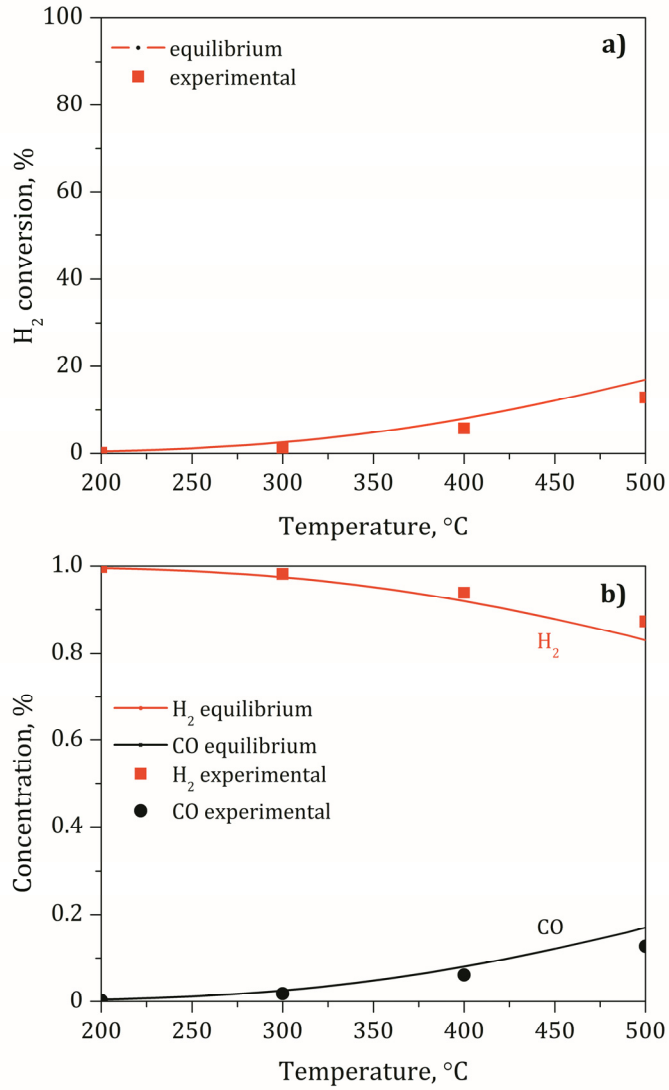

Figure 6.1. a) Evolution of the H_2 conversion with respect to temperature and b) Evolution of the concentration of H_2 and CO in Pt-Ba/Al_2O_3 catalyst. Feed stream: 1% H_2, 5% H_2O and 5% CO_2 with a total flow rate of 1800 ml min^{-1}.

when the extension of the RWGS is maximum, H_2 is the primary reductant with a concentration of 0.87%, whereas the concentration of CO remains as low as 0.13%, which equals the amount of reacted hydrogen, following the stoichiometry of the RWGS. Thus, the RWGS reaction is not thermodynamically favored and assures that hydrogen will be the main reductant even in the presence of CO_2 and H_2O in the feedstream, whatever the reaction temperature is.

Taking into account the composition of the feed stream, including H_2O, CO_2 and H_2, the CO_2 methanation reaction could also be expected, i.e. $CO_2 + 4H_2 \leftrightarrows CH_4 + 2H_2O$, or alternatively the CO methanation once the RWGS has taken place, i.e. $CO + 3H_2 \leftrightarrows CH_4 + H_2O$. Although CH_4 production is thermodynamically favored via CO_2 methanation at temperatures lower than 350 °C, the Pt-Ba/Al_2O_3 catalyst does not show enough activity at such low temperature. On the contrary, for temperatures higher than 350 °C, when the catalyst activity is enhanced, CH_4 formation is not thermodynamically favored. Although CH_4 formation was not experimentally determined during the experiment, the independent measurement of H_2 (by calibrated MS) and CO (FTIR) revealed that the concentration of both was complementary (see Figure 6.1b). This fact discards the formation of a significant quantity of CH_4, tough the formation of some ppm at low temperatures could not be totally ruled out [52, 236].

The activity of Pt-Ba-Ce/Al_2O_3 catalyst for the RWGS is illustrated in Figure 6.2. Similar conclusions can be arisen as for Pt-Ba/Al_2O_3 revealing that ceria does not play an important role in the RWGS reaction.

6.1.1.2. Temporal evolution of reactants and products and DeNO_x performance

Figure 6.3 shows the temporal evolution of the concentration of NO, NO_2, NO_x, N_2O, NH_3 and CO during two consecutive storage and reduction periods at 200, 300, 400 and 500 °C using Pt-Ba/Al_2O_3. The monolithic catalyst was exposed to 400 ppm NO and 8% O_2 during the lean period and 400 ppm NO

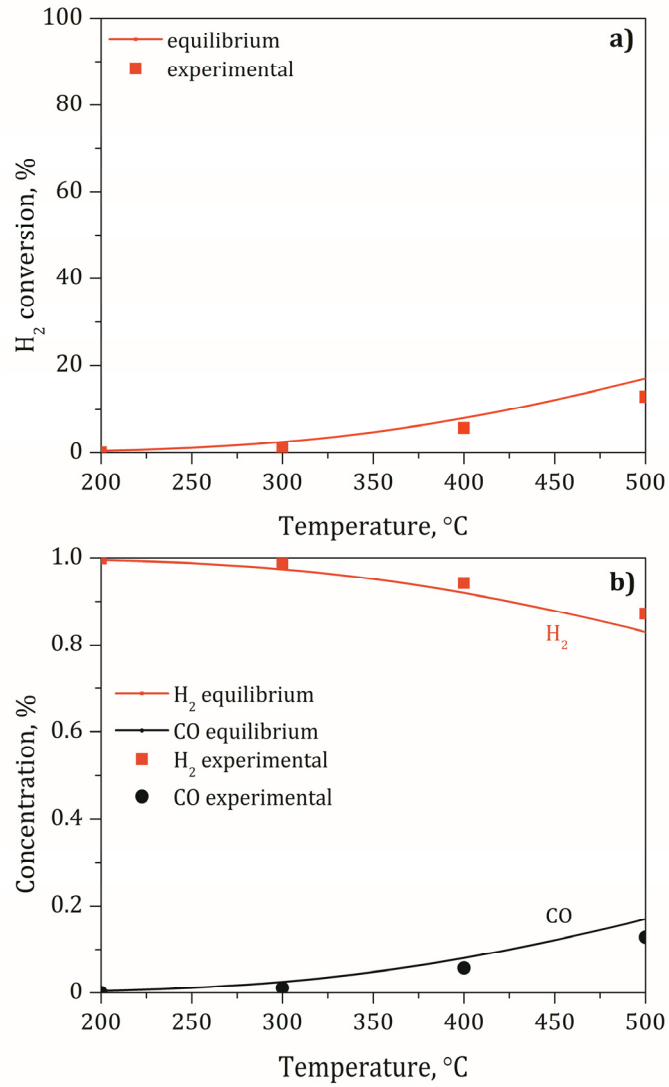

Figure 6.2. a) Evolution of the H_2 conversion with respect to temperature and b) Evolution of the concentration of H_2 and CO in Pt-Ba-Ce/Al_2O_3 catalyst. Feed stream: 1% H_2, 5% H_2O and 5% CO_2 with a total flow rate of 1800 ml min^{-1}.

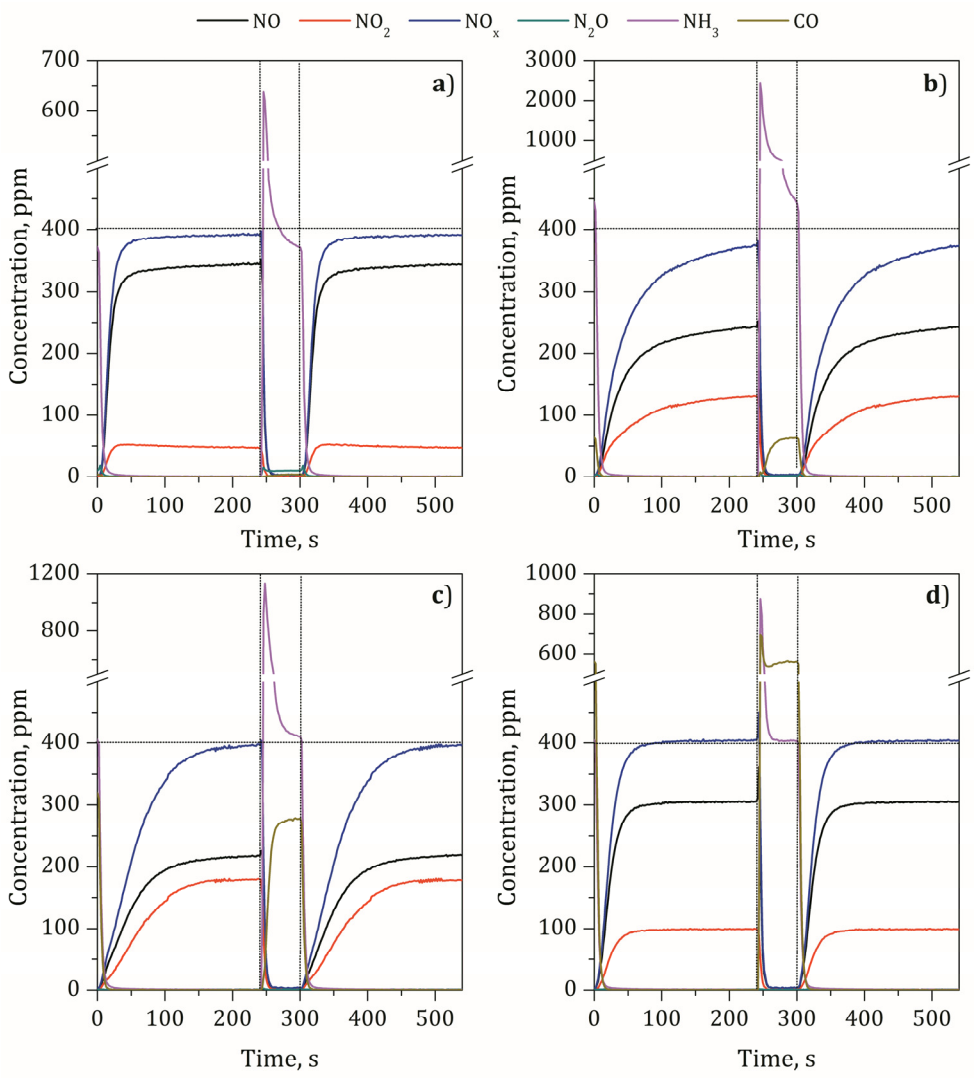

Figure 6.3. The evolution of the concentration of NO, NO_2, NO_x, N_2O, NH_3 and CO during two consecutive storage and reduction with H_2 at 200(a), 300(b), 400(c) and 500(d) °C using Pt-Ba/Al_2O_3 catalyst. Feed stream: Lean period: 400 ppm NO, 6% O_2, 5% H_2O and 5% CO_2 using Ar as balance gas with a total flow rate of 1800 ml min^{-1}. Rich period: 400 ppm NO, 0.5% H_2, 5% H_2O and 5% CO_2 using Ar as balance gas with a total flow rate of 1800 ml min^{-1}.

and 0.5% H_2 during the rich period. 5% H_2O and 5% CO_2 was continuously admitted to the reactor during lean and rich periods. The lean period was 240 s long, whereas the rich period was 60 s long.

During the lean period NO is partially oxidized to NO_2 assisted by platinum sites [237] and the NO_x is adsorbed into the barium sites mainly as nitrites and nitrates [24, 27]. NO_2 adsorption via disproportionation reaction ($BaCO_3 + 3NO_2 \rightarrow Ba(NO_3)_2 + NO + CO_2$) is favored with respect to NO [17] and consequently the oxidation of NO to NO_2 is considered as a primary step for NO_x adsorption. The oxidation capacity of the catalyst can be evaluated at the end of the lean period, when the catalyst is saturated with NO_x, dividing the NO_2 concentration by the NO concentration admitted to the reactor. At 200 °C, the oxidation capacity of the catalyst is low (12%) and thus results in a limited adsorption capacity. Note that the NO_x concentration is below the inlet value (400 ppm), i.e. the catalyst is storing NO_x, only for the first 50 s of the lean period, and afterwards the NO_x concentration rapidly equals the inlet value, meaning that the catalyst adsorption sites are saturated. It is worth to note that NO_x adsorption competes with the adsorption of H_2O and CO_2 in the basic storage sites in the form of $Ba(OH)_2$ and $BaCO_3$, respectively, and consequently, when those gases are present in the feed stream the NO_x adsorption capacity of the catalyst is significantly reduced [40, 41, 44].

Increasing the catalyst temperature up to 300 °C enhanced the oxidation capacity of the catalyst (30%) and improved the NO_x storage capacity, as illustrated by the lower NO_x concentration in the effluent gas for the whole lean period. Although the NO oxidation capacity of the catalyst was higher (44%) at 400 °C the NO_x outlet concentration was hardly affected because from 350 °C and onwards, the stability of the stored nitrates decreases, penalizing the storage capacity [17, 238]. At the highest temperature (500 °C) the NO oxidation capacity decreases to 25% due to thermodynamic restrictions and the stability of stored nitrates is further reduced, which

ultimately reduces the NO_x adsorption capacity of the catalyst and thus increases the NO_x concentration at the reactor outlet.

During the rich period, the hydrogen admitted to the reactor reacts with stored nitrates and nitrites to form a mixture of N_2, NH_3 and N_2O. At 200 °C, NH_3 is almost immediately detected after the beginning of the rich period reaching a concentration peak of 650 ppm, whereas the concentration of N_2O is almost negligible (<10 ppm). Meanwhile N_2 is also detected as a sharp peak (not shown in Figure 6.3 for clarity) just at the beginning of the rich period and afterwards its concentration is rapidly reduced almost to zero. Contrarily, NH_3 concentration approached a constant value around 350 ppm at the end of the rich period, which revealed that the NO admitted to the reactor reacts with H_2 to form preferably NH_3. Due to the low extension of the RWGS, CO concentration is negligible in the effluent gas during the rich period. N_2 and NH_3 formation is enhanced when the temperature is increased up to 300 °C due to the higher amount of stored NO_x in the previous lean period. However, a further temperature increase to 400 °C enhanced the formation of nitrogen at the expense of NH_3; note that the NH_3 peak is reduced from 2500 ppm at 300 °C to 1200 ppm at 400 °C. This observation is explained by the participation of NH_3 as an effective reducing agent for the reduction of NO_x located downstream, resulting in the consumption of NH_3 and the formation of additional nitrogen [33, 39, 41, 239]. A final temperature increase to 500 °C promotes the aforementioned reaction between NH_3 and NO_x and further reduces NH_3 slip in the effluent gas. As temperature is increased from 200 to 500 °C, CO formation is progressively promoted via the RWGS reaching a steady state concentration at the end of the rich period of 5, 60, 270 and 550 ppm at 200, 300, 400 and 500 °C, respectively. The excess of hydrogen during the rich period (detected by MS, not shown) along with its higher reducing efficiency suggest that the participation of CO as NO_x reducing agent will be limited, although cannot be completely ruled out.

The temporal evolution of reactants and products was qualitatively similar during lean/rich cycling experiments with ceria containing NSR catalyst (Figure 6.4). However, some differences are also observable. First, it can be observed that NO_x emission is lower for the catalyst containing ceria, due to its participation as NO_x trapping site along with Ba. Then, it is also observable that the NO_2 formation during the lean period is lower because of the lower exposed surface area of Pt. As already explained in Chapter 5, due to a strong metal support interaction ceria could encapsulate Pt.

Figure 6.5 shows the production of N_2O, NH_3 and N_2 along with the unconverted NO_x (empty column) during the whole NO_x storage and reduction operation in the temperature range of 200-500 °C and feeding different H_2 concentration during the rich period, i.e. 0.1, 0.5 and 1%, for Pt-Ba/Al_2O_3 (first column) and Pt-Ba-Ce/Al_2O_3 catalysts (second column).

In order to evaluate the catalytic parameters of the stand-alone NSR catalyst the following equations were used:

a) NO_x conversion (X_{NOx}, %) defined as the moles of converted NO_x with respect to the total moles of NO fed to the reactor, in percentage

$$X_{NO_x}(\%) = \frac{F_{NO}^{in}(t_L + t_R) - \int_0^{t_L+t_R} F_{NO_x} dt}{F_{NO}^{in}(t_L + t_R)} \times 100 \qquad (6.1)$$

where F_{NO}^{in} represents the NO molar flow (mol NO min^{-1}) in the gas stream admitted to the reactor, t_L and t_R is the duration of the lean and rich periods (s), respectively, and F_{NO_x} is the NO_x ($NO+NO_2$) molar flow (mol NO_x min^{-1}) evolution at the reactor exit during the whole operation.

b) N_2, NH_3 and N_2O yield (Y_{N_2}, Y_{NH_3}, Y_{N_2O}), defined as the moles of each product with respect to the total moles of NO fed to the reactor, expressed as percentage

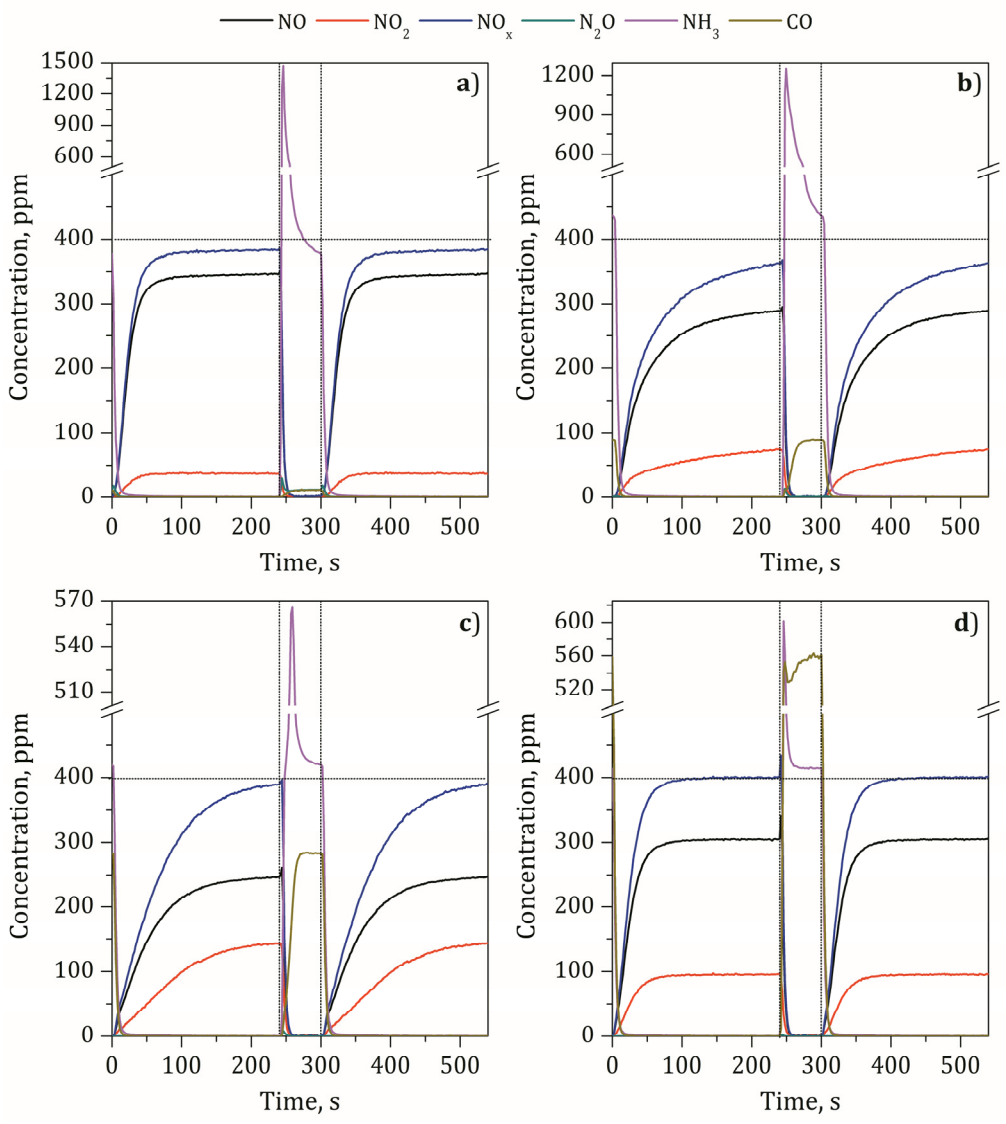

Figure 6.4. The evolution of the concentration of NO, NO_2, NO_x, N_2O, NH_3 and CO during one consecutive storage and reduction cycle with H_2 at 200, 300, 400 and 500 °C using Pt-Ba-Ce/Al_2O_3 catalyst. Feed stream: Lean period: 400 ppm NO, 6% O_2, 5% H_2O and 5% CO_2 using Ar as balance gas with a total flow rate of 1800 ml min^{-1}. Rich period: 400 ppm NO, 0.5% H_2, 5% H_2O and 5% CO_2 using Ar as balance gas with a total flow rate of 1800 ml min^{-1}.

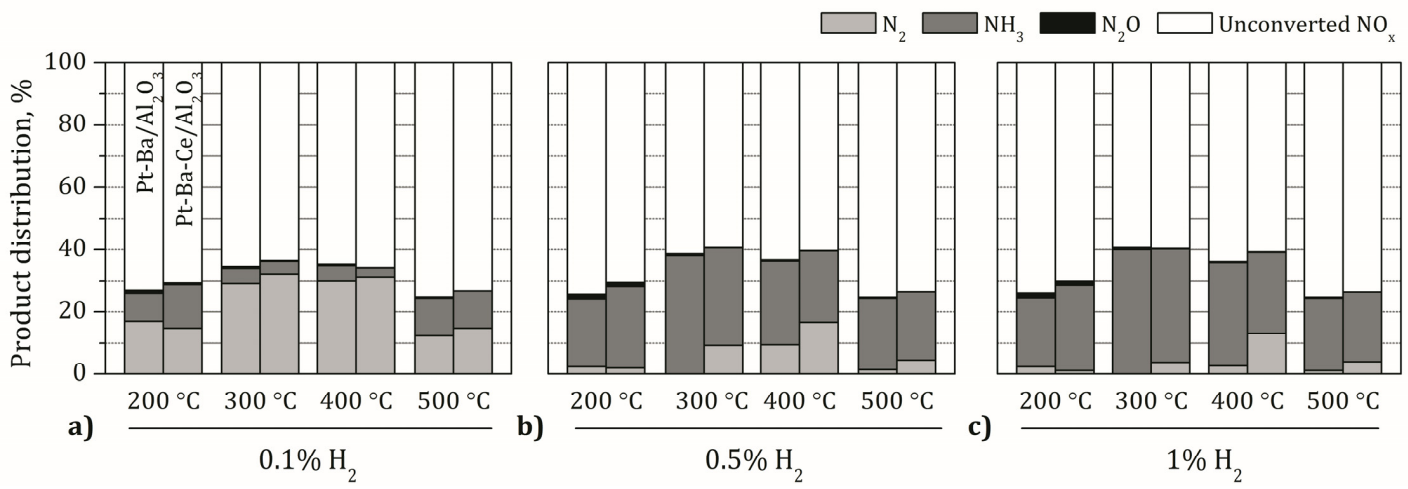

Figure 6.5. N_2, NH_3 and N_2O product distribution along with unconverted NO_x for 0.1% H_2 (a), 0.5% H_2 (b) and 1% H_2 (c) reducing agents in the temperature range of 200-500 °C using Pt-Ba/Al_2O_3 (1st column) and Pt-Ba-Ce/Al_2O_3 (2nd column) NSR catalysts. Feed stream: Lean period: 400 ppm NO, 8% O_2, 5% H_2O and 5% CO_2 using Ar as balance gas with a total flow rate of 1800 ml min^{-1}. Rich period: 400 ppm NO, 5% H_2O, 5% CO_2 and 0.1% H_2 (a); 0.5% H_2 (b); and 1% H_2 (c) using Ar as balance gas with a total flow rate of 1800 ml min^{-1}.

$$Y_{N_2}(\%) = \frac{\int_0^{t_L+t_R} F_{N_2} dt}{F_{NO}^{in}(t_L + t_R)} \times 100 \quad (6.2)$$

$$Y_{NH_3}(\%) = \frac{\int_0^{t_L+t_R} F_{NH_3} dt}{F_{NO}^{in}(t_L + t_R)} \times 100 \quad (6.3)$$

$$Y_{N_2O}(\%) = \frac{\int_0^{t_L+t_R} F_{N_2O} dt}{F_{NO}^{in}(t_L + t_R)} \times 100 \quad (6.4)$$

Irrespective of the H_2 concentration fed during the rich period, the NO_x conversion (addition of N_2O, NH_3 and N_2 productions) is maximum at 300 °C, due to an adequate balance between the oxidation capacity of the catalyst and thermal stability of the stored nitrates. Concerning product distribution, the admission of 0.1% H_2 during the rich period permits to drive the NO_x storage and reduction operation selectively to N_2. On the other hand, NH_3 production is promoted for higher H_2 concentration (0.5% and 1%) due to an excess of reductant with respect to the amount of NO_x to be reduced, or that is to say, a high local H_2/NO_x ratio [37, 49, 173, 240]. The addition of ceria to the model Pt-Ba/Al_2O_3 catalyst slightly enhanced the NO_x conversion due to the participation of cerium oxide as NO_x trapping site [173, 234, 241]. Besides, the ability of ceria to store oxygen, results in a promotion of nitrogen production ascribed to: i) the oxidation of NH_3 by stored oxygen to form N_2; and ii) the consumption of H_2 by the stored oxygen, which reduces the reductant excess and drives the selectivity towards N_2.

6.1.2. Regeneration of the trap with carbon monoxide as reductant

6.1.2.1. Evolution of the extension of the water gas shift during the regeneration period in the presence of carbon monoxide

The utilization of carbon monoxide as the reducing agent during the regeneration of NSR catalyst in the presence of CO_2 and H_2O can now activate

the Water Gas Shift (WGS) reaction, i.e. $CO + H_2O \leftrightarrows H_2 + CO_2$. The occurrence of the WGS reaction would now favor the regeneration of the trap, as CO would be consumed in order to form H_2, which is known to be a more efficient reductant [216]. Figure 6.6a shows the CO conversion in the studied temperature range and Figure 6.6b the evolution of the concentration of CO and H_2 in ppm, when feeding 1% CO, 5% H_2O and 5% CO_2 to Pt-Ba/Al_2O_3 catalyst. As can be observed by continuous lines, thermodynamics reveals that the WGS reaction is completely displaced to the side of products and thus total conversion of CO could be achieved at low temperatures (200 °C). However, the catalyst started to be active for the WGS only for temperatures higher than 300 °C due to kinetic limitations. After a fast activity increase, the catalyst reaches the equilibrium conversion around 450 °C. Thus, CO is consumed in order to form H_2 via WGS. In fact, hydrogen became the main reducing agent at 400 °C, with a concentration of 0.72% H_2, whereas unconverted CO was 0.28% (Figure 6.6b). Again, the formation of H_2 equals the amount of reacted CO and thus discards the presence of a significant amount of CH_4. The addition of ceria slightly promotes WGS (Figure 6.7). For example, the CO conversion results in 74.3% when ceria is included in the NSR formulation at 400 °C, whereas the CO conversion is 70.4% in the absence of ceria.

6.1.2.2. Temporal evolution of reactants and products and $DeNO_x$ performance

Figure 6.8 shows the temporal evolution of the concentration of NO, NO_2, NO_x, N_2O, NH_3 and CO during two consecutive storage and reduction periods at 200, 300, 400 and 500 °C using Pt-Ba/Al_2O_3. The feed stream was the same as that used in previous cycling experiments but using CO instead of H_2 as reducing agent. At low temperature (200 °C), CO is not able to participate as NO_x reducing agent, note that the NO_x concentration remains close to the inlet value (400 ppm) during the whole rich period, and the same is observed for CO concentration (5000 ppm). Therefore, the trap cannot be regenerated and the storage capacity in the subsequent lean period is also penalized. The

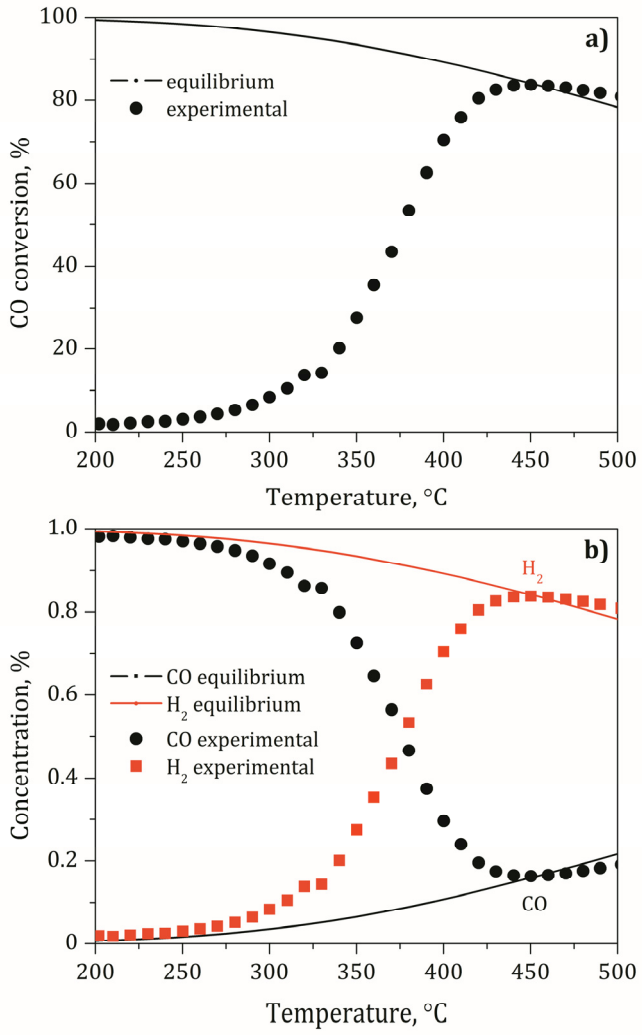

Figure 6.6. a) Evolution of the CO conversion with respect to temperature and b) Evolution of the concentration of CO and H_2 in Pt-Ba/Al_2O_3 catalyst. Feed stream: 1% CO, 5% H_2O, 5% CO_2 with a total flow rate of 1800 ml min^{-1}.

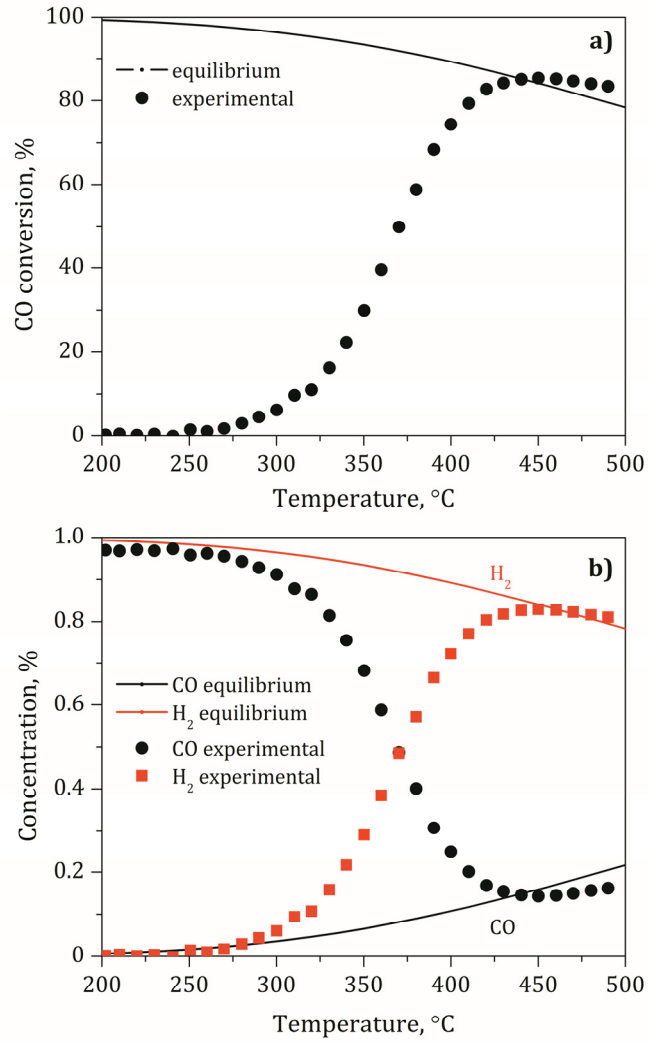

Figure 6.7. a) Evolution of the CO conversion with respect to temperature and b) Evolution of the concentration of CO and H_2 in Pt-Ba-Ce/Al_2O_3 catalyst. Feed stream: 1% CO, 5% H_2O, 5% CO_2 with a total flow rate of 1800 ml min^{-1}.

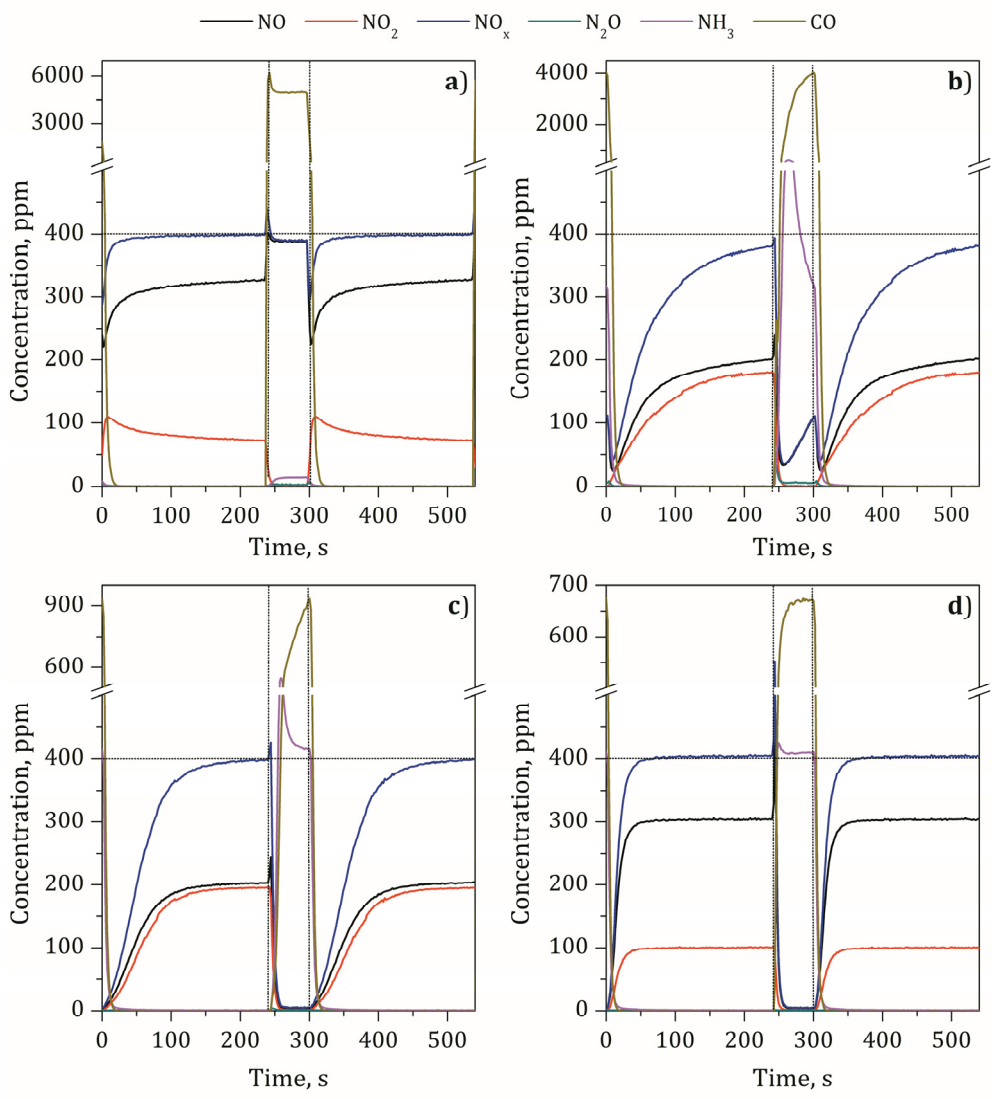

Figure 6.8. Evolution of the concentration of NO, NO_2, NO_x, N_2O, NH_3 and CO during one consecutive storage and reduction with CO at 200, 300, 400 and 500 °C using Pt-Ba/Al_2O_3 catalyst. Feed stream: Lean period: 400 ppm NO, 6% O_2, 5% H_2O and 5% CO_2 using Ar as balance gas with a total flow rate of 1800 ml min^{-1}. Rich period: 400 ppm NO, 0.5% CO, 5% H_2O and 5% CO_2 using Ar as balance gas with a total flow rate of 1800 ml min^{-1}.

picture changed significantly at 300 °C due to the higher reduction performance of the catalyst, as revealed by the complete NO_x conversion during the rich period. This fact could be attributed to the direct participation of CO as NO_x reducing agent ($Ba(NO_3)_2 + 5CO \rightarrow BaCO_3 + N_2 + 4CO_2$) to form N_2, or alternatively via formation of isocyanate species ($Ba(NO_3)_2 + 8CO \rightarrow Ba(NCO)_2 + 6CO_2$) which are further reduced to N_2 ($5Ba(NCO)_2 + Ba(NO_3)_2 \rightarrow 8N_2 + 8BaCO_3 + 2CO_2$) [216, 218, 220, 221]. Furthermore, the role of hydrogen in the promotion of the reduction performance cannot be ignored. Note that due to the activation of the WGS, the formation of around 1000 ppm of H_2 is expected (Figure 6.6) which will be surely involved in the NO_x reduction step. In fact, the detection of NH_3 in the effluent gas corroborates the participation of H_2 as reducing agent. NH_3 is not detected at the effluent gas when CO is used as the only reducing agent due to the formation of stable isocyanate species in the absence of CO_2 and H_2O in the feed [53, 216, 218]. Increasing the temperature to 400 °C further enhanced the NO_x reduction ability of the catalyst due to the promotion of the WGS, which increases the availability of H_2 and reduces the amount of CO in the effluent gas. The complete conversion of NO_x to NH_3 (400 ppm) once the trap has been regenerated, i.e. at the end of the rich period, reveals that hydrogen is in excess, also detected by MS. At 500 °C, the formation of H_2 via WGS is further enhanced as revealed by the lower CO concentration during the rich period.

The temporal evolution of reactants and products was qualitatively similar during lean/rich cycling experiments with ceria containing NSR catalyst (Figure 6.9). But it can be seen that in Pt-Ba-Ce/Al_2O_3 catalyst the NO_x storage capacity is higher than in the catalyst without ceria. However some differences are also observable. Again the NO oxidation and NO_2 formation is penalized for ceria containing catalyst due to SMSI between Pt and Ce. During the rich period higher concentration of NH_3 is detected for ceria containing catalyst at 200 °C due to the promotion of H_2 formation by the WGS reaction.

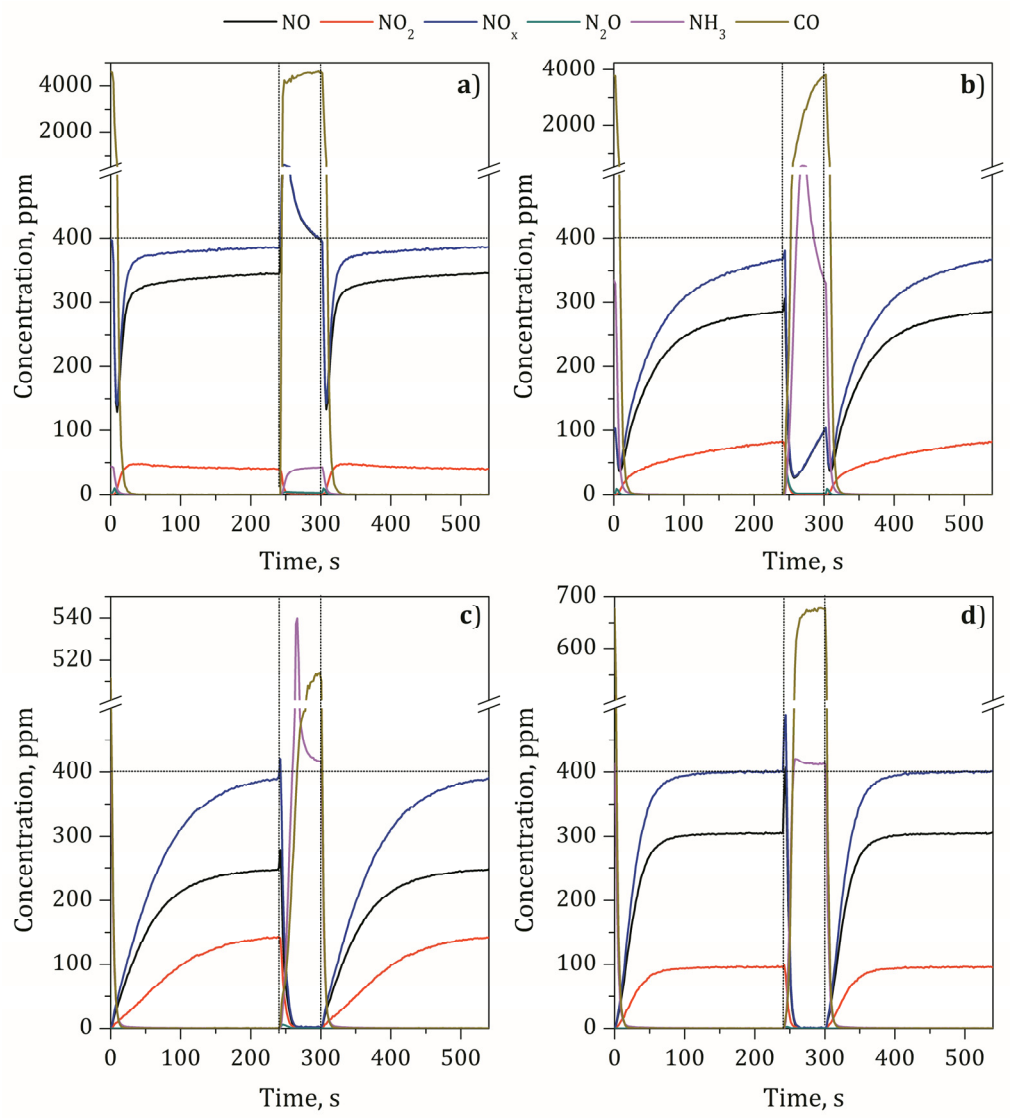

Figure 6.9. The evolution of the concentration of NO, NO_2, NO_x, N_2O, NH_3 and CO during one consecutive storage and reduction with CO at 200, 300, 400 and 500 °C using Pt-Ba-Ce/Al_2O_3 catalyst. Feed stream: Lean period: 400 ppm NO, 6% O_2, 5% H_2O and 5% CO_2 using Ar as balance gas with a total flow rate of 1800 ml min^{-1}. Rich period: 400 ppm NO, 0.5% CO, 5% H_2O and 5% CO_2 using Ar as balance gas with a total flow rate of 1800 ml min^{-1}.

Figure 6.10 shows the production of N_2O, NH_3 and N_2 along with the unconverted NO_x (empty column) during the whole NO_x storage and reduction operation in the temperature range of 200-500 °C and feeding different CO concentration during the rich period, i.e. 0.1, 0.5 and 1%, for Pt-Ba/Al_2O_3 (first column) and Pt-Ce-Ba/Al_2O_3 catalysts (second column). All these dates were calculated by Equations 6.1-6.4. As already observed during the cycling experiments, CO is not able to get involved in the reduction of NO_x at 200 °C, leading to a poor NSR performance irrespective of the reductant concentration. Furthermore, some previous works [49, 216, 235] also highlighted that CO could also be strongly bonded to Pt, thus, decreasing the rates of NO_x storage and reduction. At higher temperature, the reducing ability of the catalyst is enhanced mainly due to the H_2 produced via WGS. At 300 and 400 °C, N_2 is the only nitrogen-containing product when 0.1% CO is used, due to an adequate reductant dose, nor in defect nor in excess. For higher CO concentration, H_2 produced via WGS is in excess and promotes NH_3 formation.

It is no doubt that H_2 is a much more effective reductant than CO at low temperatures (200 °C). However, the reduction ability of both reductants is comparable from 300 °C and onwards. In fact, NO_x conversion results in 36.8% and 35.9% for H_2 and CO concentration of 0.5%, respectively, at 400 °C. Interestingly, product distribution moves from mostly NH_3 (27% NH_3/10% N_2) to a mixture of NH_3 and N_2 (20% NH_3/15% N_2) when using CO instead of H_2. It seems that the lower H_2 dose (produce via WGS) during the catalysts regeneration by CO inhibited at some extent the formation of NH_3.

The addition of ceria to the model Pt-Ba/Al_2O_3 catalyst produces different effects depending on the CO concentration admitted to the reactor. On one hand, the addition of Ce reduces the NO_x conversion for low CO concentration (0.1%), which can be due to the oxidation of CO to CO_2 by stored oxygen in ceria, producing a reductant defect. On the other hand, the admission of a

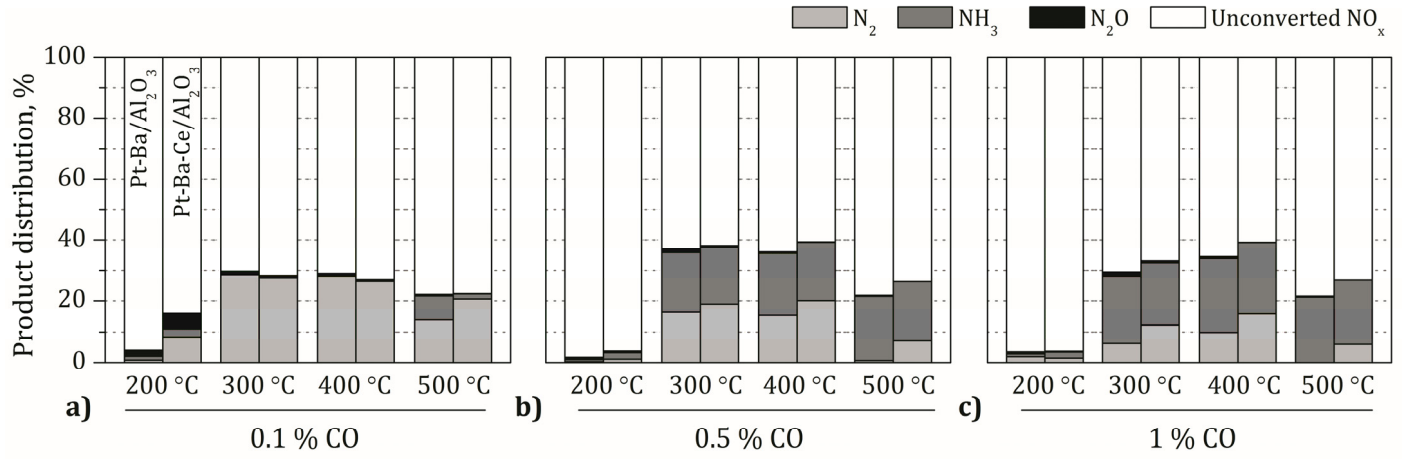

Figure 6.10. N_2, NH_3 and N_2O product distribution along with unconverted NO_x for 0.1% CO (a), 0.5% CO (b) and 1% CO (c) reducing agents in the temperature range of 200-500 °C using Pt-Ba/Al_2O_3 (1st column) and Pt-Ba-Ce/Al_2O_3 (2nd column) NSR catalysts. Feed stream: Lean period: 400 ppm NO, 8% O_2, 5% H_2O and 5% CO_2 using Ar as balance gas with a total flow rate of 1800 ml min^{-1}. Rich period: 400 ppm NO, 5% H_2O, 5% CO_2 and 0.1% CO (a); 0.5% CO (b); and 1% CO (c) using Ar as balance gas with a total flow rate of 1800 ml min^{-1}.

higher concentration of CO (0.5 and 1%) guarantees that the reductant dose is not in defect and the positive effect of the participation of ceria as NO_x storage compound is highlighted.

6.1.3. Regeneration of the trap with propylene as reductant

6.1.3.1. Evolution of the extension of the steam reforming during the regeneration period in the presence of propylene

The admission of C_3H_6 during the regeneration period in the presence of H_2O and CO_2, can activate the steam reforming of the hydrocarbon, i.e. $C_3H_6 + 3H_2O \leftrightarrows 3CO + 6H_2$. In order to evaluate the activity of the prepared catalysts towards the C_3H_6 steam reforming, specific experiments were carried out at steady state feeding 1111 ppm of C_3H_6, 5% H_2O and 5% CO_2 using Ar as balance gas with a total flow rate of 1800 ml min^{-1} in the temperature range of 200-500 °C. Figure 6.11a shows the conversion of C_3H_6 and Figure 6.11b the evolution of the concentration of C_3H_6, CO and H_2 in ppm. As can be observed by continuous lines, thermodynamics reveals that the steam reforming reaction is completely displaced to the side of products and thus total conversion of C_3H_6 could be achieved in the whole studied temperature range (200-500 °C). However, Pt-Ba/Al_2O_3 catalyst started to be active only for temperatures higher than 350 °C, and even at the highest temperature (500 °C), the conversion of C_3H_6 resulted only in 30%. As can be observed in Figure 6.11b, the formation of H_2 and CO due to C_3H_6 steam reforming did not follow the reaction stoichiometry, as H_2 formation was more than twice the amount of CO formed. Thus, once the C_3H_6 steam reforming is activated, WGS is also running, which consumes CO and produces additional H_2. At 500 °C the reductant mixture results in 0.35% H_2, 0.04% CO and 0.04% C_3H_6. As can be observed in Figure 6.12, the addition of ceria promotes the steam reforming of C_3H_6, increasing the C_3H_6 conversion from 9.8% for the model Pt-Ba/Al_2O_3 up to 16.3% for the ceria containing NSR at 450 °C.

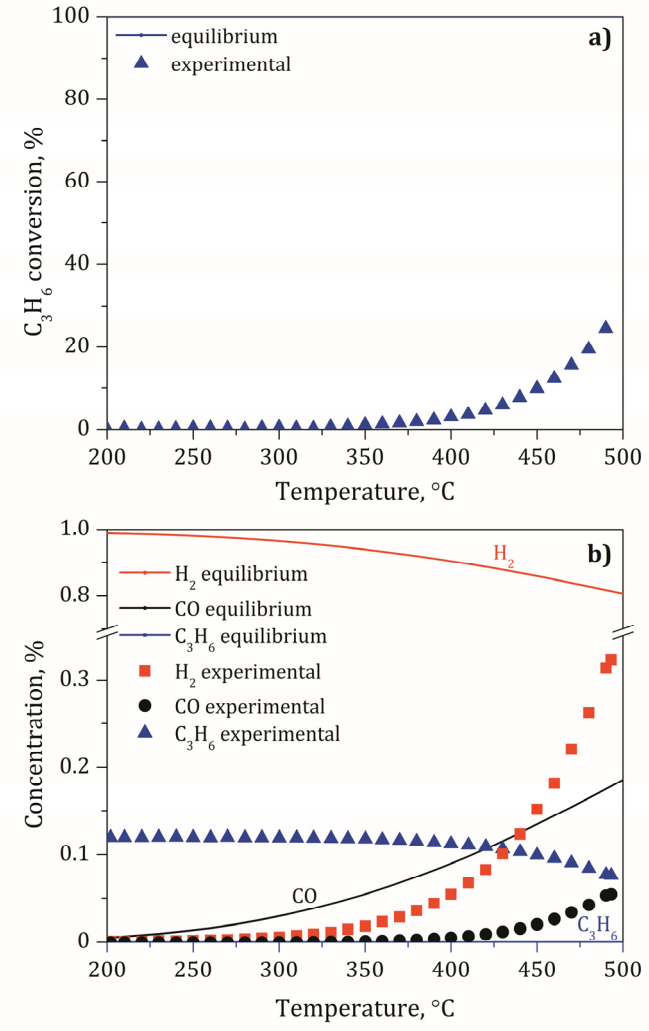

Figure 6.11. a) Evolution of the C_3H_6 conversion with respect to temperature and b) Evolution of the concentration of C_3H_6, CO and H_2 when feeding 1/9% C_3H_6, 5% H_2O and 5% CO_2 to Pt-Ba/Al_2O_3 catalyst in a total flow rate of 1800 ml min^{-1}.

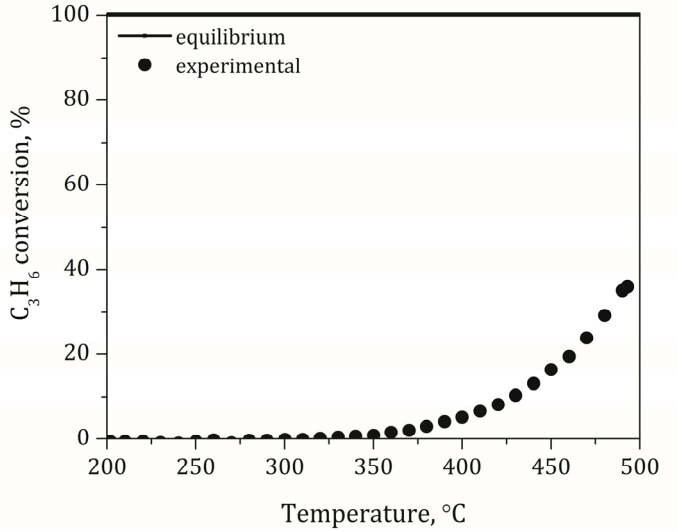

Figure 6.12. The evolution of the C_3H_6 conversion with respect to temperature in Pt-Ba-Ce/Al_2O_3 catalyst. Feed stream: 1/9% C_3H_6, 5% H_2O and 5% CO_2 using Ar as balance gas with a total flow rate of 1800 ml min^{-1}.

6.1.3.2. Temporal evolution of reactants and products and $DeNO_x$ performance

Figure 6.13 shows the temporal evolution of the concentration of NO, NO_2, NO_x, N_2O, NH_3, CO and C_3H_6 during two consecutive storage and reduction periods at 200, 300, 400 and 500 °C using Pt-Ba/Al_2O_3 catalyst and C_3H_6 as reductant. At low temperature (200 °C), C_3H_6 is not able to participate as NO_x reducing agent and results in a poor NSR performance, as was also observed using CO as reductant. At 300 °C, the NSR performance is enhanced due to the direct participation of C_3H_6 in NO_x reduction, as the presence of additional reductants is discarded due to the low activity of the catalyst in the steam reforming of C_3H_6 at such temperature (Figure 6.11). The presence of NH_3 and CO during the regeneration period at 400 °C, reveals that C_3H_6 steam reforming has taken place at some extent and the presence of additional reductants, mainly hydrogen, promotes the regeneration of the catalyst and

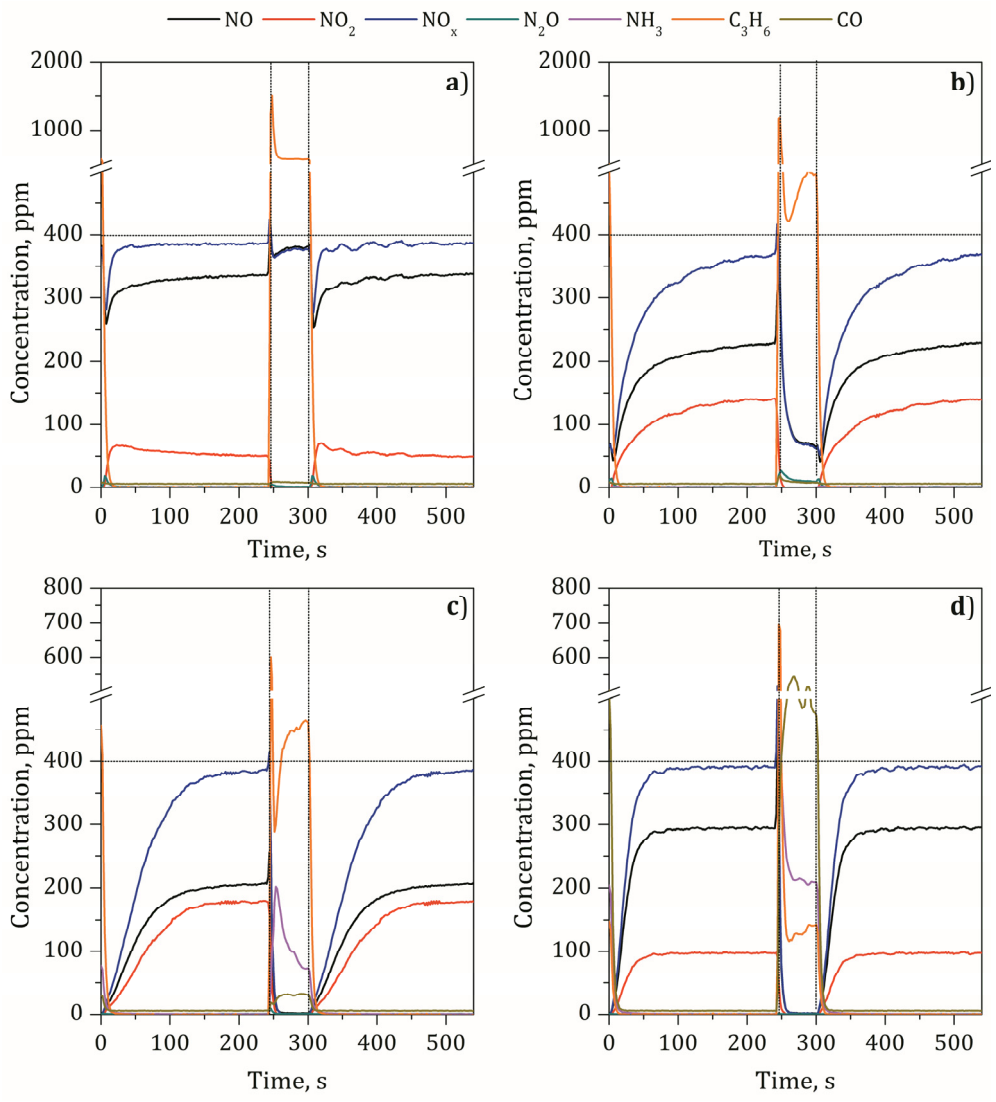

Figure 6.13. Evolution of the concentration of NO, NO_2, NO_x, N_2O, NH_3, CO and C_3H_6 during one consecutive storage and reduction with C_3H_6 at 200 (a), 300 (b), 400 (c) and 500 (d) °C using Pt-Ba/Al_2O_3 catalyst. Feed stream: Lean period: 400 ppm NO, 6% O_2, 5% H_2O and 5% CO_2 using Ar as balance gas with a total flow rate of 1800 ml min^{-1}. Rich period: 400 ppm NO, 0.5/9% C_3H_6, 5% H_2O and 5% CO_2 using Ar as balance gas with a total flow rate of 1800 ml min^{-1}.

lowers the NO_x concentration during the whole NSR operation. Higher concentrations of NH_3 and CO are detected at 500 °C, in line with the higher concentration of H_2 and CO expected due to the higher extension of the steam reforming.

The temporal evolution of reactants and products was qualitatively similar during lean/rich cycling experiments with ceria containing NSR catalyst (Figure 6.14). There are not relevant differences between Pt-Ba/Al_2O_3 and Pt-Ba-Ce/Al_2O_3 catalysts; the NO_x storage capacity is similar in both catalysts and in all temperatures. Also, in this case the NO_2 formation is lower as we have observed in Figure 6.4 and 6.9. The notable differences between these two catalysts are the outlet C_3H_6 concentration and ammonia production. In Pt-Ba-Ce/Al_2O_3 catalyst the outlet C_3H_6 concentration is lower and the ammonia production is higher than in catalyst without ceria, due to the ability of ceria to promote SR and WGS reactions and consequently the formation of H_2.

Figure 6.15 shows N_2O, NH_3 and N_2 product distribution along with unconverted NO_x (empty column) during the whole NO_x storage and reduction operation in the temperature range of 200-500 °C and feeding different C_3H_6 concentration during the rich period, i.e. 111, 550 and 1111 ppm, for Pt-Ba/Al_2O_3 (first column) and Pt-Ba-Ce/Al_2O_3 catalysts (second column). NO_x conversion increases with temperature up to 400 °C, irrespective the concentration of C_3H_6 admitted to the reactor. Concerning product distribution, N_2 is the main product along with minor amounts of N_2O at 200 and 300 °C, whereas significant amounts of NH_3 are produced for higher temperatures, although N_2 remains as the main product. The formation of NH_3 is detectable for temperatures higher than 400 °C due to the formation of H_2 during the steam reforming of C_3H_6.

Thus, C_3H_6 is not an effective reductant at low temperatures. However, as temperature is increased, the reducing ability of C_3H_6 increases progressively and at 400 °C obtains similar or even better results than H_2 or CO. In fact, the

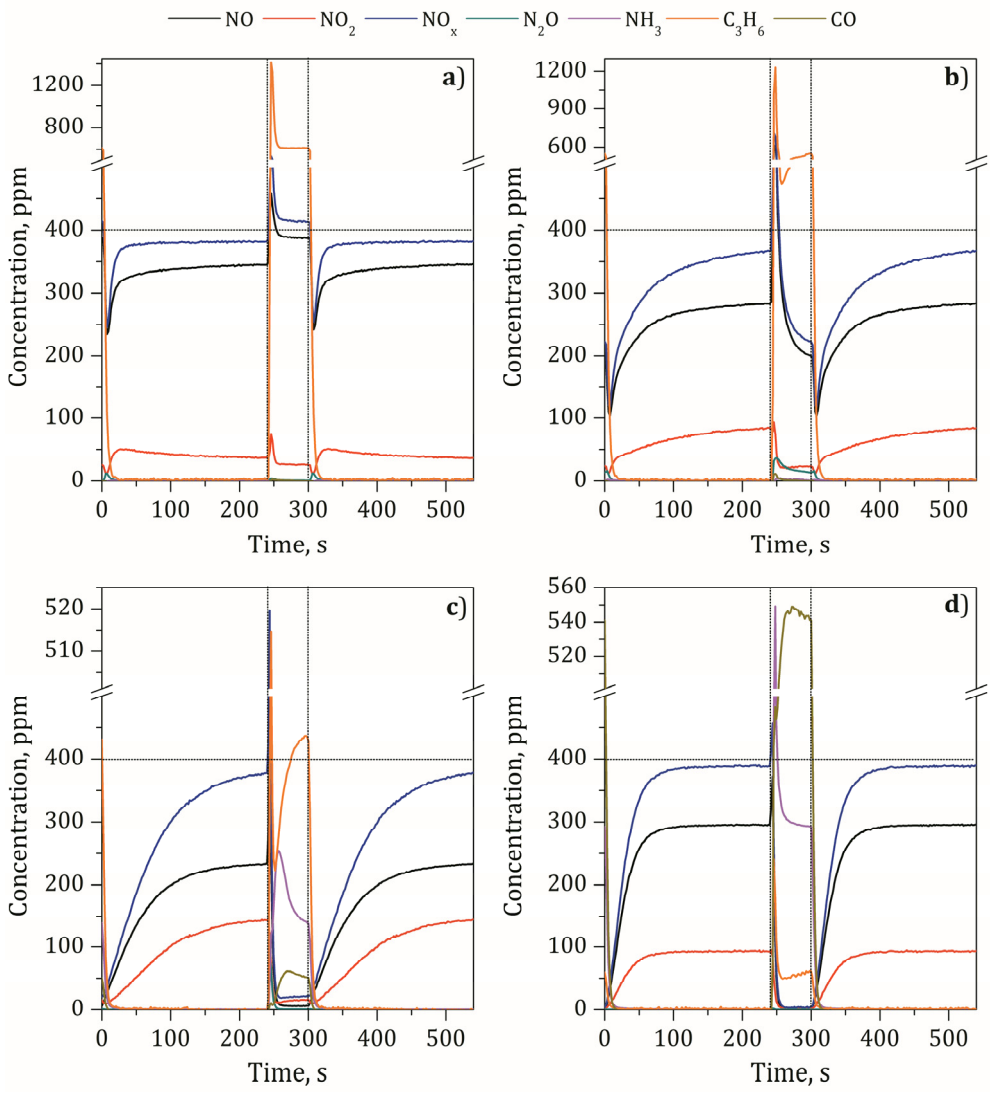

Figure 6.14. Evolution of the concentration of NO, NO_2, NO_x, N_2O, NH_3, CO and C_3H_6 during one consecutive storage and reduction with C_3H_6 at 200 (a), 300 (b), 400 (c) and 500 (d) °C using Pt-Ba-Ce/Al_2O_3 catalyst. Feed stream: Lean period: 400 ppm NO, 6% O_2, 5% H_2O and 5% CO_2 using Ar as balance gas with a total flow rate of 1800 ml min^{-1}. Rich period: 400 ppm NO, 0.5/9% C_3H_6, 5% H_2O and 5% CO_2 using Ar as balance gas with a total flow rate of 1800 ml min^{-1}.

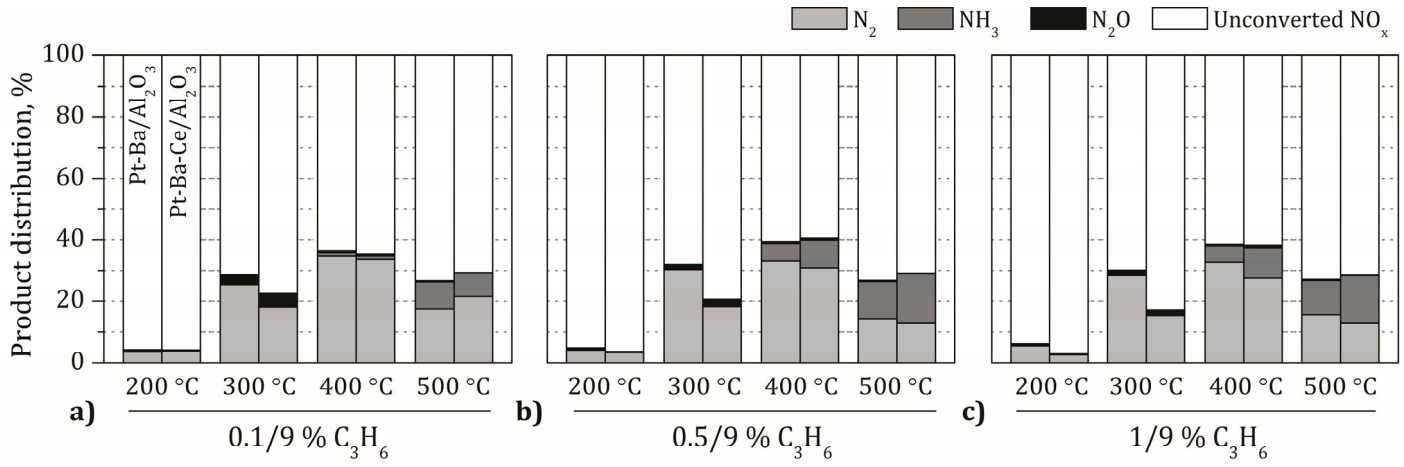

Figure 6.15. N_2, NH_3 and N_2O product distribution along with unconverted NO_x for 0.1/9% C_3H_6 (a), 0.5/9% C_3H_6 (b) and 1/9% C_3H_6 (c) reducing agents in the temperature range of 200-500 °C using Pt-Ba/Al_2O_3 (1st column) and Pt-Ba-Ce/Al_2O_3 (2nd column) NSR catalysts. Feed stream: Lean period: 400 ppm NO, 8% O_2, 5% H_2O and 5% CO_2 using Ar as balance gas with a total flow rate of 1800 ml min^{-1}. Rich period: 400 ppm NO, 5% H_2O, 5% CO_2 and 0.1/9% C_3H_6 (a), 0.5/9% C_3H_6 (b) and 1/9% C_3H_6 (c) using Ar as balance gas with a total flow rate of 1800 ml min^{-1}.

NO_x conversion results in 39.3% using C_3H_6, slightly higher than 36.8% and 35.9% using 0.5% of H_2 and CO, respectively. Furthermore, C_3H_6 is the best reductant to drive the selectivity towards N_2 at high temperature. N_2 production is 33.2%, 15.5% and 9.4% using C_3H_6, CO and H_2, respectively, at 400 °C.

The addition of ceria to the model Pt-Ba/Al_2O_3 catalyst penalized the NO_x conversion specifically at 300 °C. It is known that due to a strong metal support interaction (SMSI), ceria can partially cover or even encapsulate platinum reducing the exposed metallic surface area [173, 242]. Due to the aforementioned effect, the reducing capacity of the catalyst is limited and penalized the NO_x storage and reduction performance at 300 °C. On the contrary, the exposed platinum surface area is higher in the absence of ceria and enhances the NSR performance. For higher temperatures, the NO_x reducing rate is promoted and consequently the exposed platinum surface area is not a limiting step. Thus, the NSR performance of model or ceria containing catalyst at high temperature is similar or even slightly higher for ceria containing catalyst due to the participation of ceria as NO_x trapping site. Ceria containing catalyst promoted NH_3 formation in a higher extent than model Pt-Ba/Al_2O_3 because ceria promotes the steam reforming of C_3H_6 and consequently a higher amount of H_2 is produced.

6.2. DeNO$_x$ PERFORMANCE OF COUPLED NSR-SCR COMBINED SYSTEMS USING Cu/SAPO-34 AND Cu/BETA CATALYST AND DIFFERENT REDUCING AGENTS (H_2, CO, C_3H_6 OR C_7H_8)

Figure 6.16 shows the temporal evolution of the concentration of NO, NO_2, NO_x, N_2O, NH_3, CO and C_3H_6 during two consecutive storage and reduction periods at 300 °C using sequential NSR-SCR configuration with Pt-Ba-Ce/Al_2O_3 and Cu/SAPO-34 catalysts using H_2, CO and C_3H_6 as reductants. The key for improving the NO_x removal efficiency when using combined NSR-SCR configuration is to produce the adequate amount of NH_3 in the NSR to be

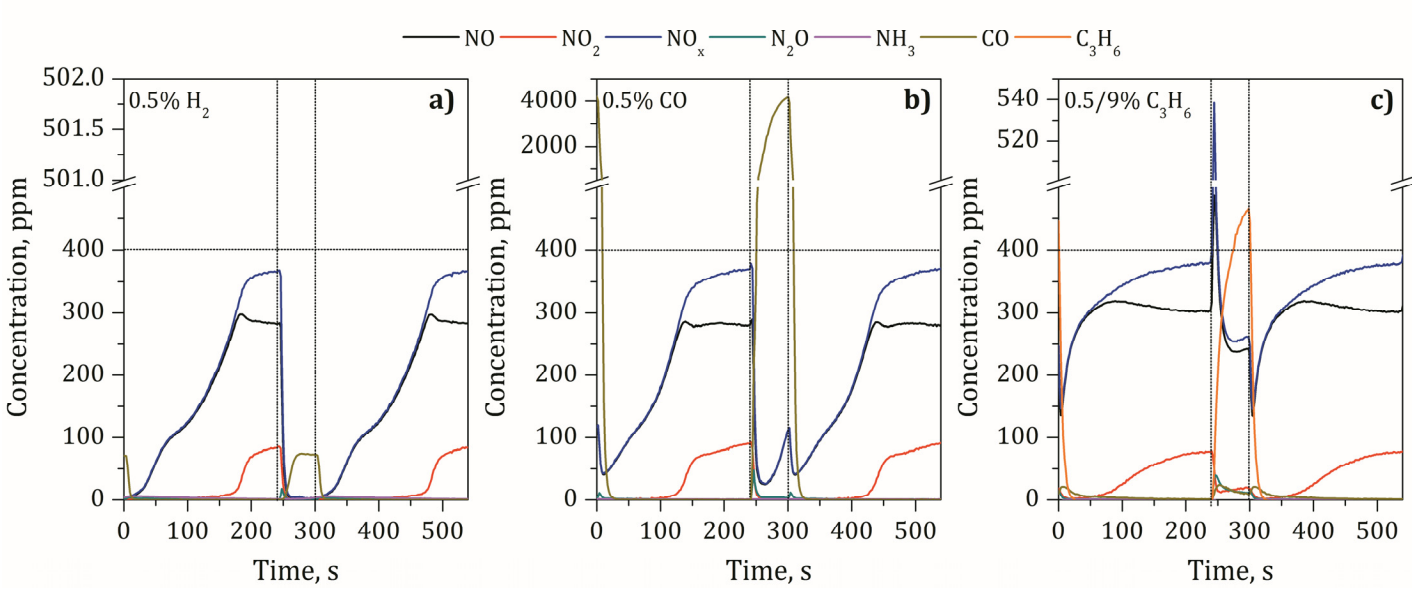

Figure 6.16. Evolution of the concentration of NO, NO_2, NO_x, N_2O, NH_3, CO and C_3H_6 during two consecutive storage and reduction period at 300 °C using sequential Pt-Ba-Ce/Al_2O_3 and Cu/SAPO-34 configuration and using H_2 (a), CO (b) and C_3H_6 (c) as reductants. Feed stream: lean period: 400 ppm NO, 8% O_2, 5% CO_2 and 5% H_2O using as balance gas Ar with a total flow rate of 1800 ml min^{-1}. Rich period: a) 400 ppm NO, 0.5% H_2, 5% CO_2 and 5% H_2O; b) 400 ppm NO, 0.5% CO, 5% CO_2 and 5% H_2O; c) 400 ppm NO, 0.5/9% C_3H_6, 5% CO_2 and 5% H_2O using Ar as balance gas with a total flow rate of 1800 ml min^{-1}.

stored in the SCR [152, 175, 178, 243, 244], which then reacts with NO or NO_2 that slips the NSR. As can be observed in Figure 6.16a, all the NH_3 produced in the NSR during the rich period (Figure 6.5b) is efficiently adsorbed on the SCR catalyst when H_2 is used as reductant; note that only a few ppm of NH_3 (<20 ppm) is detected at the effluent gas of the combined NSR-SCR reactor configuration. Then, the adsorbed NH_3 in the SCR reacts with a mixture of NO and NO_2 produced at the exit of the NSR, activating the fast NH_3-SCR ($NO + NO_2 + 2NH_3 \rightarrow 2N_2 + 3H_2O$) reaction. As a consequence, the concentration of NO and NO_2 is significantly reduced during the lean period. In fact, NO_2 is totally converted and only after 150 s is detected at the exit of the combined NSR-SCR reactor configuration. During the rich period, CO is also detected due to the occurrence of the RWGS in the NSR. The CO formed in the NSR passes through the SCR without being significantly adsorbed (as deduced by comparing the CO profile of Figure 6.4b for the stand-alone NSR) and thus its participation as NO_x reductant in the SCR is considered negligible.

The arrangement of SCR catalyst downstream the NSR produces also a beneficial effect when feeding CO as reductant (Figure 6.16b). At 300 °C, the H_2 produced due to the WGS participates as NO_x reducing agent in the NSR and produces NH_3, as already observed in Figure 6.8b. Ammonia is efficiently adsorbed in the SCR and participates in the reduction of additional NO_x. Note that the amount of NH_3 formed during the NSR regeneration with CO is lower than that formed with H_2. Consequently, the beneficial effect of the NSR-SCR arrangement using CO as reductant is not as remarkable as using H_2.

In line with the previous statement, due to the fact that NH_3 is not formed when C_3H_6 is used as NSR reducing agent at 300 °C (Figure 6.13b), the NSR-SCR combined system does not significantly modify the reactants and products profiles with respect to the stand-alone NSR.

Figure 6.17 shows N_2, NH_3 and N_2O product distribution along with unconverted NO_x for different reducing agents and different concentrations of reductants in the temperature range of 200-500 °C using Pt-Ba-Ce/Al_2O_3 as

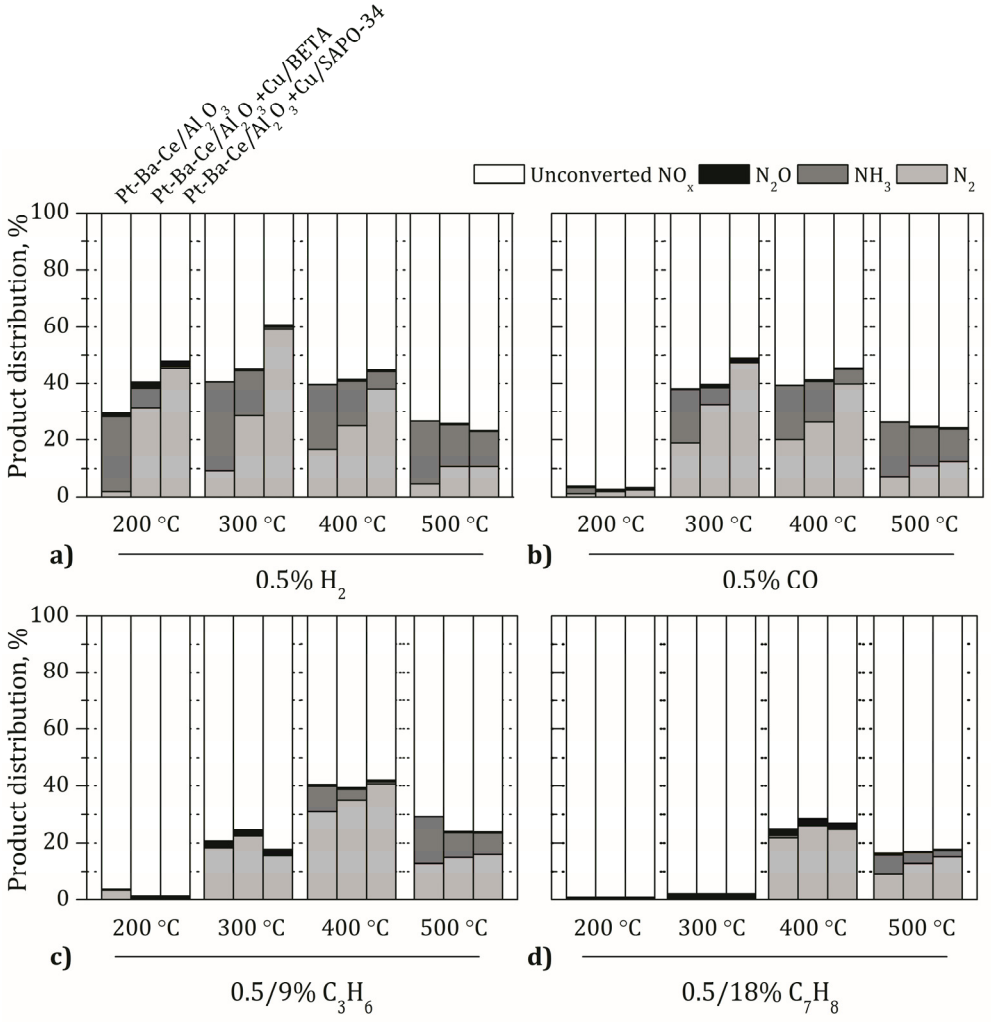

Figure 6.17. N_2, NH_3 and N_2O product distribution along with unconverted NO_x for 0.5% H_2 (a), 0.5% CO (b), 0.5/9% C_3H_6 (c) and 0.5/18% C_7H_8 (d) reducing agents in the temperature range of 200-500 °C using Pt-Ba-Ce/Al_2O_3 as stand-alone NSR (1st column) and Cu/BETA (2nd column) and Cu/SAPO-34 (3th column) as SCR catalysts for the combined NSR-SCR configuration. Feed stream: Lean period: 400 ppm NO, 8% O_2, 5% H_2O and 5% CO_2 using Ar as balance gas with a total flow rate of 1800 ml min^{-1}. Rich period: 400 ppm NO, 5% H_2O, 5% CO_2 and a) 0.5% H_2; b) 0.5% CO; c) 0.5/9% C_3H_6; d) 0.5/18% C_7H_8 using Ar as balance gas with a total flow rate of 1800 ml min^{-1}.

stand-alone NSR (1st column) and Cu/BETA and Cu/SAPO-34 as SCR catalysts for the combined NSR-SCR configuration (2nd and 3th column, respectively).

Figure 6.17a shows the catalytic performance using 0.5% H_2 as reductant. As can be observed, NH_3 production is reduced when using the NSR-SCR reactor configuration with respect to the stand-alone NSR, irrespective of the catalyst temperature. As already observed, this fact is ascribed to the adsorption of NH_3 in the acidic sites of the zeolite, which then reacts with NO or NO_2 that slips the NSR in order to produce N_2 via SCR reaction. Thus, N_2 production is increased from 2% with the stand-alone NSR up to 31% and 45% with the combined NSR-SCR configuration using Cu/BETA and Cu/SAPO-34, respectively, at 200 °C. Cu/SAPO-34 catalyst improves in a higher extent the production of N_2 due to the higher NH_3-SCR activity and NH_3 adsorption capacity [75, 164, 178]. In fact, almost no NH_3 (<1%) is detected at the outlet of the NSR-SCR reactor configuration when using Cu/SAPO-34, which means that all the NH_3 produced in the NSR (26%) is efficiently adsorbed. On the other hand, 7% of NH_3 leaves the reactor when using Cu/BETA due to the lower NH_3 adsorption capacity of BETA zeolite.

The N_2 production of the NSR-SCR configuration is increased up to 59% when increasing the temperature to 300 °C using Cu/SAPO-34 as SCR catalyst. This result is ascribed to the improvement of the NO_x storage and reduction performance of the stand-alone NSR catalyst, which results in a higher NO_x conversion (41%) and higher N_2 (9%) and NH_3 (31%) production with respect to 200 °C. On the contrary, the N_2 production of the NSR-SCR configuration slightly decreases from 31% (200 °C) to 28% (300 °C) when using Cu/BETA catalyst. This penalization in N_2 production is due to the lower ability of BETA zeolite to store NH_3 with increasing temperature, i.e. from a total NH_3 production of 31% at the outlet of the NSR, 16% leaves the reactor unreacted with Cu/BETA while only 0.7% with Cu/SAPO-34.

The beneficial effect of the combined NSR-SCR configuration with respect to the stand-alone NSR is not so noteworthy at elevated temperatures, i.e. 400

and 500 °C, because NH_3 production progressively decreases to 23% (400 °C) and 22% (500 °C) at the outlet of the NSR and thus there is a lack of NH_3 supply to activate the NH_3-SCR. Furthermore, the ability to store NH_3 is penalized for Cu/BETA and Cu/SAPO-34, which further highlights the lack of reductant and increases the NH_3 slip to 15% and 12% at 500 °C, respectively.

Unexpectedly, the NO_x conversion was lower for the combined NSR-SCR reactor configuration than the stand-alone NSR at elevated temperature (500 °C). At such high temperature, the NH_3 formed in the NSR could be oxidized to N_2 or even NO by copper species present in the SCR catalyst, thus penalizing the NO_x conversion in the case of NO formation. The NH_3 oxidation capacity has been reported to be higher for Cu/SAPO-34 or Cu/SSZ-13 than Cu/BEA [178], which is in line with the results reported in Figure 6.17a.

Figure 6.17b shows the catalytic performance of the stand-alone NSR and combined NSR-SCR configuration using CO as reductant at different temperature. The main difference with respect to H_2 (Figure 6.17a) is that CO is not able to participate as NO_x reducing agent at low temperature (200 °C) and thus the NO_x removal performance is very restricted, with NO_x conversion below 4% irrespective of the catalytic configuration, i.e. NSR or NSR-SCR. At 300 °C, the reducing ability of CO increases mainly due to the production of H_2 via the RWGS reaction, which promotes NH_3 formation in the NSR (19%), although in a lower extent than using H_2 as reductant (31%). Maximum N_2 production of 32% and 47% is obtained at 300 °C with the combined NSR-SCR using Cu/BETA and Cu/SAPO-34 as SCR catalyst, respectively. For higher temperatures NO_x conversion decreases progressively with temperature and product distribution moves towards NH_3, increasing the ammonia slip.

Figure 6.17c shows the catalytic performance of the stand-alone NSR and combined NSR-SCR configuration using C_3H_6 as reductant at different temperature. Similarly to CO, C_3H_6 is not able to get involved in NO_x reduction in the NSR and thus NO_x conversion is below 4% irrespective of the catalytic configuration, i.e. NSR or NSR-SCR. The NO_x reduction ability of C_3H_6 in the

NSR increases at 300 °C, with the corresponding increase in the NO_x conversion (20 %), mainly producing N_2 (18 %) along with a minor amount of N_2O (2%). The absence of NH_3 as NO_x reduction byproduct in the NSR reduces the applicability of the combined NSR-SCR configuration. Indeed, the addition of Cu/SAPO-34 catalysts downstream the NSR does not produce any beneficial result. Interestingly, the addition of Cu/BETA as SCR catalyst results in a slight promotion of N_2 production (22%). In the absence of NH_3, the enhancement of N_2 production could be explained by the ability of BEA zeolite to store C_3H_6 and/or NO/NO_2 and then activate the HC-SCR. It has been reported [245, 246] that the pore size, Si/Al ratio, presence or absence of cavities in the framework and the type of exchanged metal are parameters affecting HC-SCR with zeolites. Specifically, Brønsted and Lewis acid sites of the zeolites have an important role in the reaction [247, 248]. Szanyi and Paffet [249] proposed that acid sites would nucleate NO by the formation of N_xO_y species leading to surface nitrates, which would react with C_3H_6 to form N_2 and CO_2 and H_2O following the overall HC-SCR reaction: $C_3H_6 + 9/2NO_2 \rightarrow 3CO_2 + 3H_2O + 9/4N_2$ [250]. Alternatively, Gorce et al. [251] proposed that organic nitro intermediates formed by the reaction of C_3H_6 and ad-NO_x species decompose to NO and oxygenates (C_xH_yO, such as acrolein), which further react with NO_2 or ($NO+O_2$) to proceed the HC-SCR pathway ($C_xH_yO + NO + O_2 \rightarrow CO_2 + N_2 + H_2O$). Thus, it seems that physico-chemical properties of BETA zeolite are more suitable than those of H-SAPO-34 to activate HC-SCR at 300 °C. Unlike H_2 and CO, the highest N_2 production (41%) was obtained at 400 °C for the combined NSR-SCR configuration with Cu/SAPO-34 as SCR catalyst and using C_3H_6 as reductant. The activation of C_3H_6 steam reforming at 400 °C produces H_2 that enables a deep regeneration of the NSR and NH_3 formation. Although steam reforming is further enhanced at 500 °C, and consequently NH_3 formation, the NO_x conversion over NSR-SCR is reduced due to the lower stability of the stored nitrates in the NSR and the low ability to store NH_3 of the Cu exchanged zeolite based catalysts.

Similar conclusions can be extracted from Figure 6.17d when using C_7H_8 as reductant. At low temperature (200 and 300 °C) there is not NO_x reduction due to C_7H_8 is not efficient at these temperatures. Maximum N_2 production (26%) is obtained at 400 °C with Cu/BETA as SCR catalyst. Note that the production of N_2 is not significant up to 400 °C due to the low ability of C_7H_8 to reduce NO_x in the NSR and the low steam reforming activity, which finally impedes the formation of H_2 and a deep regeneration of the NSR.

6.3. OVERALL VIEW AND CONCLUSIONS

Model Pt-Ba/Al_2O_3 and Pt-Ba-Ce/Al_2O_3 NSR catalysts and Cu/BETA and Cu/SAPO-34 SCR catalysts have been prepared and deposited on cordierite monoliths. NO_x removal conversion and product distribution, with focusing principal attention on NH_3 generation, have been evaluated for the stand-alone NSR monoliths. The production of ammonia has been linked to the global NO_x-to-N_2 conversion achieved when the different NSR-SCR two-monoliths combinations are tested under the lean-rich cycled operation, including CO_2 and water in the feed stream.

The use of H_2, CO, C_3H_6 and C_7H_8 as reductant during the rich period influences the generation of ammonia at the exit of the NSR catalyst, also depending on the temperature. The reverse water gas shift (RWGS) reaction in the presence of CO_2, and steam reforming (SR) reaction in the presence of hydrocarbons, occur at low extent up to 350 °C and only moderate conversions were observed even at 500 °C. The presence of Ce in the NSR catalyst did not affect the RWGS reaction conversion and only increased slightly the SR reactions conversion at higher temperature.

Hydrogen resulted in a more efficient reductant for the regeneration of the NSR than CO and hydrocarbons. The NO_x storage capacity of the NSR catalyst is enhanced with temperature, although the stability of the stored NO_x decreases, which forms a maximum storage capacity at intermediate

temperature of 300-350 °C. During the rich period, the reductant admitted reacts with stored NO_x to form a mixture of N_2, NH_3 and N_2O. When H_2 is the reductant, the NO admitted to the reactor reacts with H_2 to form preferably NH_3, which also participates as effective reductant for NO_x located downstream to form additional nitrogen. The amount of H_2 injected by choosing the used concentration needs to be balanced as to convert selectively NO_x-to-N_2 and eliminate either NO_x slip or NH_3 slip out of the reactor. CO is not effective in the reduction of NO_x at low temperature, which is enhanced at 300 °C and onwards because of H_2 production via WGS reaction. In fact, the efficiency of CO and H_2 as reductants resulted comparable from 300 °C and onwards. This inhibits in some extent the generation of NH_3. C_3H_6 resulted the less effective reductant, which only is comparable to H_2 and CO at temperature as high as 400 °C. At that temperature, the formation of NH_3 is detectable due to H_2 generation by steam reforming.

The NSR-SCR arrangement produces a beneficial effect, achieving good NO_x control performance at lower temperature. The formation of ammonia at the exit of the NSR catalyst, which is stored in the SCR catalyst and then used to reduce NO_x slipping from the NSR catalyst, should be controlled by adjusting the reductant concentration during the rich period. Thus, NO_x that breaks out the NSR is further reduced in the SCR catalyst, and NH_3 slip is markedly reduced and consequently, NH_3 emissions in the exhaust gases are very limited. As enough ammonia is generated at lower temperature with relative low H_2 concentration, the beneficial effects of the NSR-SCR configuration are more pronounced when using hydrogen as reductant, achieving better NO_x removal than the stand-alone NSR catalyst at 200 and 300 °C. As the formation of NH_3 does not occur with CO and C_3H_6 until higher temperatures, together with the lower reduction efficiency of these reductants, the beneficial effect of the NSR-SCR configuration is not appreciated until a temperature of 300 and 400 °C in the case of CO and C_3H_6, respectively. When using C_7H_8, the $DeNO_x$ behavior even of the stand-alone NSR is poor.

Concerning the composition of the NSR catalyst, the incorporation of Ce to the Pt-Ba/Al_2O_3 catalyst seems to slightly affect the behavior of the stand-alone NSR catalyst not the coupled NSR-SCR configuration. For application in the NSR-SCR configuration, an improvement of activity and selectivity can be observed with the Cu/SAPO-34 than with Cu/BETA, which is particularly enhanced when H_2 is used as reductant, less with CO and no influence when the reductants are hydrocarbons (C_3H_6 and C_7H_8).

Chapter 7

SUMMARY, CONCLUSIONS AND FUTURE PROPOSALS

7. SUMMARY, CONCLUSIONS AND FUTURE PROPOSALS

7.1. SUMMARY

The elimination of environmental pollutant from vehicle emissions is a permanent challenge, which requires large amount of research and development. This includes NO_x, CO and hydrocarbon removal and there is also an increasing concern over vehicle CO_2 emissions due to its contribution to the greenhouse effect. The use of lean-burn gasoline or diesel engines has been encouraged during last decades as a way to reduce CO_2 emissions and increase fuel economy. However, these engines run at high air/fuel ratios, which makes NO_x reduction challenging in such an oxidant environment. Two main approaches towards NO_x reduction have been mainly investigated as alternative technologies: the NO_x storage and reduction (NSR) and the NO_x selective catalytic reduction (SCR).

Model NSR catalysts consist of an alkali or alkali-earth oxide (e.g. BaO) and noble metal (usually Pt) on alumina. In NSR technology, the catalyst works under cyclic fuel lean and fuel rich conditions. During the lean period the NO_x are stored on the catalyst and during the rich period the stored NO_x are reduced to N_2 and other by-products. One of the main drawbacks of the NSR technology is the emission of ammonia during the rich period.

SCR catalysts consist of non-noble metals (Cu, Fe) over zeolites as H-SZM-5, BETA, SAPO-34 and SSZ-13. The SCR technology runs under continuous lean mode and ammonia is used as the external reducing agent to complete the catalytic reduction selectively to N_2.

The coupling of NSR and SCR in a single device has been proposed aiming to overtake individual limitations of the stand-alone NSR and stand-alone SCR devices. In this concept, the management of NH_3 formation at the outlet of NSR catalyst is converted into an advantage. NH_3 is trapped or stored on acidic sites of the metal-exchanged zeolite (SCR catalyst, placed downstream of the

NSR catalyst) during the rich period, and then is utilized to reduce NO_x that slips from the NSR during the subsequent lean period.

In this thesis, NSR and SCR technologies are studied under different architectures: as stand-alone and combined as two monoliths in series or in a dual-layer single monolith. NSR catalysts have been prepared under our own protocol already optimized in a previous thesis. Cu/BETA catalysts are prepared starting from protonic or ammonic BEA zeolite following liquid ion exchange with copper. Alternatively, an intermediate ion exchange with Na ions is performed before copper ion exchange. Cu/BETA catalysts are extensively characterized by different characterization techniques in order to identify copper oxidation state and copper species. NSR and SCR monoliths are prepared with different washcoat loadings and the optimal thickness of the layers is determined for improving $DeNO_x$ performance.

As more advanced formulations, Cu/SAPO-34 catalysts are prepared by solid state ion exchange (SSIE) and liquid ion exchange (LIE). The SSIE preparation method is carried out calcining a physical mixture of H-SAPO-34 zeolite and CuO nanoparticles at elevated temperatures (500-800 °C). The LIE preparation method is carried out exchanging the Na/SAPO-34 with $Cu(COOCH_3)_2$ aqueous solution and final calcination step at 500 °C. These catalysts are characterized focusing on Cu species identification, and then the activity performance for NO removal by selective catalytic reduction with NH_3 (NH_3-SCR) is evaluated and some kinetic parameters are determined.

The influence of the nature and composition of reductant on the reaction mechanisms is analyzed by infrared spectroscopy. DRIFT is used for Pt-Ba/Al_2O_3 and Pt-Ba-Ce/Al_2O_3 catalysts by adsorbing NO and O_2 during the lean period and NO and reductant (H_2 or CO or C_3H_6) during the rich period, but in the absence of H_2O and CO_2 to simplify the reaction network. On the other hand, Cu/SAPO-34 catalyst species are analyzed by FTIR when NO, O_2, NO_2, NH_3 in N_2 are adsorbed at different temperatures until the catalyst saturation.

Similar experiments are carried out at the bench reactor to verify the NH_3-SCR mechanisms from a global point of view.

Finally, the effects of feeding different type of reducing agents (H_2, CO, C_3H_6, C_7H_8) on $DeNO_x$ efficiency of the different architectures: single NSR (Pt-Ba/Al_2O_3 and Pt-Ba-Ce/Al_2O_3 monoliths), single SCR (Cu/BETA and Cu/SAPO-34 monoliths) and combined NSR-SCR, is analyzed. In these experiments CO_2 and H_2O are continuously added during the cycling fuel-lean and fuel-rich operation, so as to mimic the real composition of the diesel engine exhaust.

The extension of the reverse water gas shift (RWGS), water gas shift (WGS) and steam reforming (SR) reactions in the NSR catalyst have also been studied. $DeNO_x$ conversion and product distribution have been compared for all architectures as a function of the reaction temperature and concentration of each reductant.

7.2. CONCLUSIONS

The analysis of results shown in this thesis and other related work in literature allowed us setting important conclusions which have been drawn at the end of every chapter. Here, we are summarizing those conclusions with major relevance in a simpler and more comprehensive way.

a) On Cu/BETA catalysts

The liquid ion exchange preparation methodology affects notably the formation of copper species in Cu/BETA catalysts. H/Cu and NH_4/Cu catalysts only present Cu^{2+} ions and the other two catalysts prepared with intermediate ion exchange with sodium (NH_4/Na/Cu and H/Na/Cu) present Cu^{2+} ions and Cu^{+} ions. FTIR and H_2-TPR experiments revealed three different locations of copper ions in the framework of each catalyst. NH_4/Na/Cu catalysts present the highest NH_3-SCR activity due to the coexistence of Cu^{2+} and Cu^{+} ions located at a more accessible location than in the other three catalysts.

Three NSR/SCR dual layer catalysts and one NSR-SCR system in serie have been synthesized. Increasing the loading of SCR layer of the dual layer catalyst, the storage capacity of ammonia increases but also the diffusion resistance due to wider thickness of the layer. However, if single NSR catalyst, a dual-layer catalyst and a combined NSR-SCR system in series are compared the latter achieves significantly higher $DeNO_x$ efficiency.

b) On preparation microporous chabazite zeolites

A series of Cu/SAPO-34 catalysts have been synthesized by solid state ion exchange with six different ion exchange temperatures. The copper dispersion and the amount of copper ions increase with ion exchange temperature. However, when the ion exchange temperature is very high (≥700 °C) the framework of the zeolite can suffer damage and consequently the surface area and acidity decrease and the formation of copper aluminate is favored. The activation energy of all the catalysts resulted in similar values (around 40 kJ mol^{-1}), except for the catalyst prepared at 500 °C, due to the apparent absence of copper ions in this catalyst. The catalyst prepared at 700 °C presents the highest reaction rate per mol of copper, due to the highest Cu^{2+}/Cu ratio.

In Cu/SAPO-34 catalysts prepared by liquid ion exchange and solid state ion exchange with different copper loading, the highest reaction rate per mol of copper is achieved with low copper loading catalysts due to the higher $(Cu^{2+} + Cu^{+})/Cu$ ratio. *TOF* values of the catalysts prepared by SSIE are higher than those prepared by LIE, because the former preparation methodology incorporates copper ions more randomly, at more accessible locations, than catalyst prepared by LIE.

c) On a catalyst surface species by infrared spectroscopy

In Pt-Ba-(Ce)/Al_2O_3 catalysts the DRIFT experiments carried out showed that the dominant NO_x ad-species are nitrites and nitrates at 200 °C and 300 °C, respectively. When H_2 is admitted to the gas cell, nitrites and nitrates are rapidly decomposed. The reduction of these species is lower in the

Pt-Ba-Ce/Al_2O_3 catalyst due to the less intimate contact between Pt and Ba in the catalyst surface. CO and C_3H_6 reductants are not as efficient as H_2 for the decomposition of stored nitrites and nitrates. However, the reduction capacity of CO and C_3H_6 reductants increases with temperature. With these two reductants cyanate/isocyanante species over Ba and Al and CO adsorption onto Pt and carbonates are detected.

With Cu/SAPO-34 catalyst, when NO is fed in the presence or absence of oxygen nitrites and nitrates are detected by FTIR, and the stability of these species is promoted in the presence of oxygen. Ammonia is adsorbed onto Lewis and Brønsted acid sites and the intensity of the adsorption bands decrease when increasing the temperature disregarded of the presence or absence of oxygen. When NH_3 and NO are jointly fed, the ammonia species adsorbed on the Brønsted acid sites decline slowly as ammonia migrates to Lewis acid sites to participate in the SCR reaction.

During transient experiments with Cu/SAPO-34 catalyst first saturated with NH_3, a low SCR activity is registered when NO is fed to the catalyst in the absence of oxygen. The activity is promoted in the presence of oxygen. When NH_3 is fed to the catalyst first saturated with NO, the nitrates species decrease and the NH_3 species can be clearly identified. Under these conditions, the NH_3-SCR is not promoted, even in the presence of oxygen.

d) On the chemical nature of reductants

Prepared Pt-Ba-(Ce)/Al_2O_3 catalysts have been analyzed in the reactor with different reductants injection during the rich period. During the NSR reaction, it could be observed that H_2 is a more efficient reductant than CO and HCs. When H_2 is the reductant, the stored NO_x reacts with H_2 to form preferably NH_3 and then this ammonia is diffused along the catalyst to reduce the stored NO_x. At low temperature CO is not an effective reductant but at higher temperature the NSR efficiency is enhanced because of H_2 production via WGS reaction. C_3H_6 is the less effective reductant and above 400 °C H_2 generation can be detected by SR.

NSR-SCR combined system enhances significantly $DeNO_x$ efficiency (66%) with respect to stand-alone NSR when H_2 is the reductant, at so low temperature as 200 °C. Selectivity to N_2 in the configuration is 95%. When CO and C_3H_6 are the reductants, the beneficial effect of the NSR-SCR configuration is not appreciated until 300 and 400 °C, respectively. Comparing the Cu/zeolite SCR catalyst, Cu/SAPO-34 achieves optimal $DeNO_x$ efficiency with extraordinary resistance to hydrothermal deactivation.

7.3. FUTURE PROPOSALS

To finalize the thesis, new ideas appear that would complement the obtained results or suggest other aspects we would like to address. Below are the new ideas:

- In typical lean or diesel fuel there is sulfur and this sulfur is present almost in the form of SO_2. Sulfur is a poison for NSR and SCR catalysts. The Pt/alkali or alkaline-earth/Al_2O_3 is an excellent sulfur trap and Cu/zeolite catalysts are deactivated. For these reasons, the work to carry out is to research about new NSR catalyst formulation resistant to sulfur poisoning. Analyze the influence of the amount and type of S on the catalysts.
- The use of NH_3 causes high costs due to the necessary safety technology during transport and storage, damages by corrosion as well as the costs for the reducing agent itself. However, hydrocarbons and oxygenates are ingredients of off-gases. For these reason, the objective is to analyze the influence of hydrocarbons in Cu/zeolite catalysts with different zeolites as SAPO-34, SSZ-13 and BETA.
- Analyze the HC poisoning effect in NSR-SCR combined system. In order to analyze the poisoning, experiments with different length of rich period should be designed. Moreover, to quantify the hydrocarbons formed on the surface, the SCR catalyst will be run separately in temperature

programmed oxidation (TPO) experiments, where the stored hydrocarbons will be oxidized to form CO and CO_2.

- The model Pt-Ba/Al_2O_3 catalyst has been quite successful in NO_x emission control, but the presence of precious metal (PGM) makes the catalyst highly expensive. For this reason, new cheaper catalysts with much lower or even absence of PGM in their formulation should be developed. As an example, perovskite oxide-based materials or hydrotalcites could be plausible alternative to the current NSR model catalyst.

Capítulo 8

NOMENCLATURA

8. NOMENCLATURA

Acrónimos

BET	Brunauer, Emmett y Teller
EPA	Environmental Protection Agency
ExACT	Exhaust Aftertreatment Components Toolbox
IUPAC	International Union of Pure and Applied Chemistry
NEDC	New European Driving Cycle
PDF	Powder Diffraction File

Abreviaturas

ASC	Ammonia Slip Catalyst (Catalizador para amoniaco residual)
CE	Comisión Europea
CEM	Controlled Evaporation Mixing (Controlador de evaporación)
COP	Conformity of Production (Conformidad de producción)
DEF	Diesel Exhaust Fluid/AdBlue, aditivo compuesto de urea, inyectable en los gases de escape de motores diesel
DI	Direct injection (Inyección directa)
DOC	Diesel Oxidation Catalyst (Catalizador de oxidación diésel)
DPF	Diesel Particulate Filter (Filtro de partículas)
DRIFT	Diffuse Reflectance Infrared Fourier Transform Spectroscopy (Espectroscopía infrarroja por reflectancia difusa)
EEUU	Estados Unidos

EPR	Electronic Paramagnetic Resonance (Resonancia electrónica paramagnética)
FTIR	Fourier Transform Infrared Spectroscopy (Espectroscopía de infrarrojo con tranformada de Fourier)
HCs	Hydrocarbons (Hidrocarburos)
H_2-TPR	Temperature Programmed Reduction (Reducción a temperatura programada con H_2)
IDI	Indirect diesel injection (Inyección indirecta)
IR	Infrared Spectroscopy (Espectroscopía infrarroja)
LIE	Liquid Ion Exchange (Intercambio iónico en fase líquida)
LNT	Lean NO_x trap (Trampa para NO_x en mezcla pobre)
MFC	Mass Flow Controller (Controlador de flujo másico)
MS	Mass Spectroscopy (Espectroscopía de masas)
NH_3-TPD	Ammonia Temperature Programmed Desorption (Desorción de amoniaco a temperatura programada)
NO_x	Óxidos de nitrógeno (NO + NO_2)
NSR	NO_x Storage and Reduction (Almacenamiento y reducción de NO_x)
OSC	Oxygen Storage Capacity (Capacidad de almacenamiento de oxígeno)
PM	Particulate matter (Materia particulada)
PMP	Particle Measurement Programme (Programa de medición de partículas)
PN	Particles number (Número de partículas)
QMS	Quadrupole Mass Spectrometry (Cuadrupolo para espectrometría de masas)

RWGS	Reverse Water Gas Shift ($CO_2 + H_2 \rightleftarrows CO + H_2O$)
SEM-EDX	Scanning Electronic Microcopy-Energy Dispersed X-Ray Spectroscopy (Microscopía electrónica de barrido-espectroscopia de rayos X de energía dispersa)
SCR	Selective Catalytic Reduction (Reducción catalítica selectiva)
SGIker	Servicios Generales de Investigación de la Universidad del País Vasco, UPV/EHU
SMSI	Strong Metal Support Interaction (Interacción fuerte del metal con el soporte)
SSIE	Solid State Ion Exchange (Intercambio iónico en estado sólido)
STEM	Scanning Transmission Electron Microscopy (Microscopía electronica de transmisión y barrido)
SR	Steam Reforming (Reformado con vapor)
TCD	Thermal Conductivity Detector (Detector de conductividad térmica)
TEM	Transmission Electronic Microscopy (Microscopia electrónica de transmisión)
TPR	Temperature Programmed Reduction (Reducción a temperature programada)
TQSA	Tecnologías Químicas para la Sostenibilidad Ambiental
TWC	Three Way Catalyst (Catalizador de tres vías)
UV-vis	Ultraviolet-visible (Ultravioleta-visible)
WDXRF	Wavelength Dispersive X-ray Fluorescence (Espectrometría de fluorescencia de rayos X por dispersión de longitud de onda)
WGS	Water Gas Shift ($CO + H_2O \rightleftarrows CO_2 + H_2$)

XRD X-Ray Difraction (Difracción de rayos X)

Variables y constantes físicas

A/C Relación aire/combustible

A_i Factor preexponencial para la reacción i, unidades de k_i

A_m Área de sección transversal de una molécula, nm^2

C Parámetro asociado con las entalpías de adsorción y desorción del adsorbato

C_{NO}^{in} Concentración del NO a la entrada del reactor, ppm

C_{NO}^{out} Concentración del NO a la salida del reactor, ppm

C_{NH_3} Concentración del NH_3, ppm

C_{O_2} Concentración del O_2, ppm

c Velocidad de la luz, m s^{-1}

e Espesor de la capa adsorbida, nm

E_a Energía de activación, kJ mol^{-1}

E_K Energía cinética de un fotoelectrón, J

D_{ext} Diametro exterior, cm

D_{in} Diametro interior, cm

F_{NO} Caudal molar de NO en el reactor, mol min^{-1}

F_{N_2} Caudal molar de N_2 en el reactor, mol min^{-1}

F_{NH_3} Caudal molar de NH_3 en el reactor, mol min^{-1}

F_{N_2O} Caudal molar de N_2O en el reactor, mol min^{-1}

F_{NO}^{in}	Caudal molar de NO a la entrada del reactor, mol min^{-1}
$F_{NO_x}^{out}$	Caudal molar de NO a la salida del reactor, mol min^{-1}
$F_{N_2}^{out}$	Caudal molar de N_2 a la salida del reactor, mol min^{-1}
$F_{NH_3}^{out}$	Caudal molar de NH_3 a la salida del reactor, mol min^{-1}
$F_{NO_2}^{out}$	Caudal molar de NO_2 a la salida del reactor, mol min^{-1}
$F_{N_2O}^{out}$	Caudal molar de N_2O a la salida del reactor, mol min^{-1}
g	Factor de Landé
$GHSV$	Gas Hour Space Velocity (velocidad espacial), h^{-1}
h	Constante de Planck, $6{,}62 \times 10^{-34}$, J s
k_i	Constante cinética de reacción i, unidades en Tabla 1.5
L	Longitud, m
m	masa, g
M_i	Peso molecular de i, kg mol^{-1}
N_A	Número de Avogadro, $6{,}023 \times 10^{23}$, mol^{-1}
$N_{Cu,ions}$	moles de iones de cobre, mol Cu_{ions}
NSC	NO_x Storage Capacity (Capacidad de almacenamiento de NO_x), Ecuación (3.7), %
P	Presión, Pa
P_0	Presión de saturación, Pa
Q	Caudal de entrada, ml min^{-1}
R	Constante universal de los gases ideales, 8.314 J mol^{-1} K^{-1}
r_i	Velocidad de reacción, mol g^{-1} h^{-1}

r'_{NO}	Velocidad de reacción por moles de cobre, mol NO mol Cu^{-1} h^{-1}
r_p	Radio de poro, nm
S_{BET}	Área superficial BET, m^2 g^{-1}
S_{N_2}	Selectividad de NO hacia N_2, Ecuaciones (3.5) y (3.13), %
S_{N_2O}	Selectividad de NO hacia N_2O, Ecuaciones (3.4) y (3.10), %
S_{NO_2}	Selectividad de NO hacia NO_2, Ecuación (3.3), %
S_{NO}	Selectividad de NO, Ecuación (3.6), %
S_{NH_3}	Selectividad de NO hacia NH_3, Ecuación (3.9), %
T	Temperatura, °C
TOF	Turnover frequency, Ecuación (4.6), h^{-1}
t_L	Duración del periodo pobre (lean), s
t_R	Duración del periodo rico (rich), s
V_{ads}	Volumen de gas adsorbido, cm^3 g^{-1}
V_m	Volumen de gas adsorbido en la monocapa, , cm^3 g^{-1}
V_{mol}	Volumen molar del gas, cm^3 mol^{-1}
V_p	Volumen total de poros, cm^3 g^{-1}
W	Masa de catalizador, g
X_{NH_3}	Conversión de NH_3, Ecuación (3.2), %
X_{NO}	Conversión de NO, Ecuación (3.1), %
X_{NO_x}	Conversión de NO_x (NO + NO_2), Ecuación (6.1), %

X_R	Conversión de reducción de NO_x ($NO + NO_2$) durante el periodo rico, Ecuación (3.8), %
Y_{N_2}	Producción de N_2 en el sistema, Ecuación (6.2), %
Y_{NH_3}	Producción de NH_3 en el sistema, Ecuación (6.3), %
Y_{N_2O}	Producción de N_2O en el sistema, Ecuación (6.4), %

Símbolos griegos

ΔH_i	Variación de entalpía en la reacción i, kJ mol^{-1}
Δm_s	Variación en el estado de spin
θ	Ángulo de incidencia de radiación X
λ	Longitud de onda, nm
μ_B	Magnetón de Bohr
υ	Ángulo de contacto de la fase condensada y las paredes del sólido
Ψ	Tensión superficial del adsorbato, N m^{-1}

Capítulo 9

BIBLIOGRAFÍA

9. BIBLIOGRAFÍA

[1] N. Hooftman, M. Messagie, J.V. Mierlo, T. Coosemans, "A review of the European passenger car regulations-Real driving emissions vs. local air quality", Renew. Sustain. Energy Rev. 86 (2018) 1–21.

[2] I. Meyer, M. Leimbach, C.C. Jaeger, "International passenger transport and climate change: A sector analysis in car demand and associated CO_2 emissions from 2000 to 2050", Energy Policy 35 (2007) 6332–6345.

[3] M.V. Twigg, "Catalytic control of emissions from cars", Catal. Today 163 (2011) 33–41.

[4] A. Russell, W.S. Epling, "Diesel Oxidation Catalysts", Catal. Rev. Sci. Eng. 53 (2011) 337-423.

[5] R.M. Heck, R.J. Farrauto, "Automobile exhaust catalysts", Appl. Catal. A: Gen. 221 (2001) 443–457.

[6] D. Fino, S. Bensaid, M. Piumetti, N. Russo, "A review on the catalytic combustion of soot in Diesel particulate filters for automotive applications: From powder catalysts to structured reactors", Appl. Catal. A: Gen. 509 (2016) 75–96.

[7] B. Guan, R. Zhan, H. Lin, Z. Huang, "Review of the state-of-the-art of exhaust particulate filter technology in internal combustion engines", J. Environ. Manage. 154 (2015) 225-258.

[8] M.V. Twigg, "Progress and future challenges in controlling automotive exhaust gas emissions", Appl. Catal. B: Environ. 70 (2007) 2–15.

[9] J.R. González-Velasco, B. Pereda-Ayo, U. De-La-Torre, M. Urrutxua, R. Lopez-Fonseca, "Coupled NSR-SCR systems for NO_x Removal in Light-Duty Vehicles", ChemCatChem 10 (2018) 2928-2940.

[10] P. Granger, V.I. Parvulescu, "Catalytic NO_x Abatement Systems for Mobile Sources: From Three-Way to Lean Burn after Treatment Technologies", Chem. Rev. 111 (2011) 3155-3207.

[11] R.M. Heck, R.K. Farrauto, S.T. Gulati, "Catalytic Air Pollution Control; Commercial Technologies", John Wiley & Sons, Inc., Hoboken, New Jersey, 2009.

[12] I. Nova, E. Tronconi (eds.), "Urea-SCR Technology for DeNO$_x$ After Treatment of Diesel Exhausts", Springer, New York, 2014.

[13] N. Miyoshi, S. Matsumoto, K. Katoh, T. Tanaka, J. Jarada, N. Takahashi, K. Yokota, M. Sugiura, K. Kasahara, "Development of New Concept Three-Way Catalyst for Automotive Lean-Burn Engines", SAE Technical Paper 950809, 1995.

[14] N. Takahashi, H. Shinjoh, T. Iijima, T. Suzuki, K. Yamazaki, K. Yokota, H. Suzuki, N. Miyoshi, S. Matsumoto, T. Tanizawa, T. Tanaka, S. Tateishi, K. Kasahara, "The new concept 3-way catalyst for automotive lean-burn engine: NO$_x$ storage and reduction catalyst", Catal. Today 27 (1996) 63-69.

[15] Y. Li, S. Roth, J. Dettling, T. Beutel, "Effects of lean/rich timing and nature of reductant the performance of a NO$_x$ trap catalyst", Top. Catal. 16/17 (2001) 139-144.

[16] W.S. Epling, A. Yezerets, N.W. Currier, "The effect of exothermic reactions during regeneration on the NO$_x$ trapping efficiency of a NO$_x$ storage/reduction catalyst", Catal. Lett. 110 (2006) 143-148.

[17] W.S. Epling, L.E. Campbell, A. Yezerets, N.W. Currier, J.E. Parks II, "Overview of the Fundamental Reactions and Degradation Mechanisms of NO$_x$ Storage/ Reduction Catalysts", Catal. Rev. Sci. Eng. 46 (2004) 163-245.

[18] B. Pereda-Ayo, R. López-Fonseca, J.R. González-Velasco, "Influence of the preparation procedure of NSR monolithic catalysts on the Pt-Ba dispersion and distribution", Appl. Catal. A: Gen. 363 (2009) 73-80.

[19] S. Roy, A. Baiker, "NO$_x$ Storage-Reduction Catalysis: From Mechanism and Materials Properties to Storage-Reduction Performance", Chem. Rev. 109 (2009) 4054-4091.

[20] H. Abdulhamid, E. Fridell, M. Skoglundh, "The reduction phase in NO_x storage catalysis: Effect of type of precious metal and reducing agent", Appl. Catal. B: Environ. 62 (2006) 319-328.

[21] B. Pereda-Ayo, D. Divakar, R. López-Fonseca, J.R. González-Velasco, "Influence of platinum and barium precursors on the NSR behavior of Pt–Ba/Al_2O_3 monoliths for lean-burn engines", Catal. Today 147S (2009) S244-S249.

[22] T.A. Nijhuis, A.E W. Beers, T. Vergunst, I. Hoek, F. Kapteijn, J.A. Moulijn, "Preparation of monolithic catalysts", Catal. Rev. Sci. Eng. 43 (2001) 345-380.

[23] L. Lietti, L. Castoldi (eds.), "NO_x Trap Catalysts and Technologies", Royal Society of Chemistry, London, 2018.

[24] E. Fridell, M. Skoglundh, B. Westerberg, S. Johansson, G. Smedler, "NO_x Storage in Barium-Containing Catalysts", J. Catal. 183 (1999) 196-209.

[25] B. Westerberg, E. Fridell, "A transient FTIR study of species formed during NO_x storage in the Pt/BaO/Al_2O_3 system", J. Mol. Catal. A: Chem. 165 (2001) 249–263.

[26] P. Broqvist, H. Grönbeck, E. Fridell, I. Panas, "NO_x storage on BaO: theory and experiment", Catal. Today 96 (2004) 71-78.

[27] L. Lietti, P. Forzatti, I. Nova, E. Tronconi, "NO_x Storage Reduction over Pt-Ba/γ-Al_2O_3 Catalyst", J. Catal. 204 (2001) 175–191.

[28] F. Prinetto, G. Ghiotti, I. Nova, L. Lietti, E. Tronconi, P. Forzatti, "FT-IR and TPD Investigation of the NO_x Storage Properties of BaO/Al_2O_3 and Pt-BaO/Al_2O_3 Catalysts", J. Phys. Chem. B 105 (2001) 12732-12745.

[29] I. Nova, L. Castoldi, L. Lietti, E. Tronconi, P. Forzatti, "On the dynamic behavior of "NO_x-storage/reduction" Pt–Ba/Al_2O_3 catalyst", Catal. Today 75 (2002) 431–437.

[30] I. Nova, L. Castoldi, L. Lietti, E. Tronconi, P. Forzatti, F. Prinetto, G. Ghiotti, "NO_x adsorption study over Pt-Ba/alumina catalysts: FT-IR and pulse experiments", J. Catal. 222 (2004) 377–388.

[31] I. Nova, L. Castoldi, F. Prinetto, V.D. Santo, L. Lietti, E. Tronconi, P. Forzatti, G. Ghiotti, R. Psaro, S. Recchia, "NO_x adsorption study over Pt-Ba/alumina catalysts: FT-IR and reactivity study", Top. Catal. 30/31 (2004) 181-186.

[32] P. Forzatti, L. Castoldi, I. Nova, L. Lietti, E. Tronconi, "NO_x removal catalysis under lean conditions", Catal. Today 117 (2006) 316-320.

[33] L. Cumaranatunge, S.S. Mulla, A. Yezerets, N.W. Currier, W.N. Delgass, F.H. Ribeiro, "Ammonia is a hydrogen carrier in the regeneration of $Pt/BaO/Al_2O_3$ NO_x traps with H_2", J. Catal. 246 (2007) 29–34.

[34] V. Medhekar, V. Balakotaiah, M.P. Harold, "TAP study of NO_x storage and reduction on Pt/Al_2O_3 and $Pt/Ba/Al_2O_3$", Catal. Today 121 (2007) 226–236.

[35] Z. Liu, J.A. Anderson, "Influence of reductant on the thermal stability of stored NO_x in $Pt/Ba/Al_2O_3$ NO_x storage and reduction traps", J. Catal. 224 (2004) 18–27.

[36] I. Nova, L. Lietti, P. Forzatti, "Mechanistic aspects of the reduction of stored NO_x over $Pt\text{-}Ba/Al_2O_3$ lean NO_x trap systems", Catal. Today 136 (2008) 128–135.

[37] B. Pereda-Ayo, D. Duraiswami, J.J. Delgado, R. López-Fonseca, J.J. Calvino, S. Bernal, J.R. González-Velasco, "Tuning operational conditions for efficient NO_x storage and reduction over a $Pt–Ba/Al_2O_3$ monolith catalyst", Appl. Catal. B: Environ. 96 (2010) 329–337.

[38] B. Pereda-Ayo, D. Duraiswami, J.A. González-Marcos, J.R. González-Velasco, "Performance of NO_x storage-reduction catalyst in the temperature–reductant concentration domain by response surface methodology", Chem. Eng. J. 169 (2011) 58–67.

[39] B. Pereda-Ayo, J.R. González-Velasco, R. Burch, C. Hardacre, S. Chansai, "Regeneration mechanism of a Lean NO_x Trap (LNT) catalyst in the presence of NO investigated using isotope labelling techniques", J. Catal. 285 (2012) 177-186.

[40] W.S. Epling, G.C. Campbell, J.E. Parks, "The effects of CO_2 and H_2O on the NO_x destruction performance of a model NO_x storage/reduction catalyst", Catal. Lett. 90 (2003) 45-56.

[41] A. Lindholm, N.W. Currier, E. Fridell, A. Yezerets, L. Olsson, "NO_x storage and reduction over Pt based catalysts with hydrogen as the reducing agent Influence of H_2O and CO_2", Appl. Catal. B: Environ. 75 (2007) 78-87.

[42] A. Amberntsson, H. Persson, P. Engström, B. Kasemo, "NO_x release from a noble metal/BaO catalyst: dependence on gas composition", Appl. Catal. B: Environ. 31 (2001) 27-38.

[43] W.S. Epling, J.E. Parks, G.C. Campbell, A. Yezerets, N.W. Currier, L.E. Campbell, "Further evidence of multiple NO_x sorption sites on NO_x storage/reduction catalysts", Catal. Today 96 (2004) 21-30.

[44] T.J. Toops, D.B. Smith, W.S. Epling, J.E. Parks, W.P. Partridge, "Quantified NO_x adsorption on Pt/K/gamma-Al_2O_3 and the effects of CO_2 and H_2O", Appl. Catal. B: Environ. 58 (2005) 255-264.

[45] L. Olsson, M. Abul-Milh, H. Karlsson, E. Jobson, P. Thormählen, A. Hinz, "The effect of a changing lean gas composition on the ability of NO_2 formation and NO_x reduction over supported Pt catalysts", Top. Catal. 30/31 (2004) 85-90.

[46] J. Theis, H.W. Jen, R. McCabe, M. Sharma, V. Balakotaiah, M.P. Harold, "Reductive Elimination as a Mechanism for Purging a Lean NO_x Trap", SAE Technical Paper 2006-01-1067, 2006.

[47] X.P. Auvray, L. Olsson, "Effect of Enhanced Support Acidity on the Sulfate Storage and the Activity of Pt/γ-Al_2O_3 for NO Oxidation and Propylene Oxidation", Catal. Lett. 144 (2014) 22-31.

[48] Y. Ren, M.P. Harold, "NO_x Storage and Reduction with H_2 on Pt/Rh/BaO/CeO_2: Effects of Rh and CeO_2 in the Absence and Presence of CO_2 and H_2O" ACS Catal. 1 (2011) 969-988.

[49] N. L. Phuc, X. Courtois, F. Can, S. Berland, S. Royer, P. Marecot, D. Duprez, "A study of the ammonia selectivity on $Pt/BaO/Al_2O_3$ model catalyst during the NO_x storage and reduction process", Catal. Today 176 (2011) 424-428.

[50] B. Pereda-Ayo, D. Duraiswami, J.R. González-Velasco, "Control of NO_x storage and reduction in NSR bed for designing combined NSR–SCR systems", Catal. Today 172 (2011) 66-72.

[51] M. AL-Harbi, D. Radtke, W.S. Epling, "Regeneration of a model NO_x storage/reduction catalyst using hydrocarbons as the reductant", Appl. Catal. B: Environ. 96 (2010) 524-532.

[52] L. Masdrag, X. Courtois, F. Can, D. Duprez, "Effect of reducing agent (C_3H_6, CO, H_2) on the NO_x conversion and selectivity during representative lean/rich cycles over monometallic platinum-based NSR catalysts. Influence of the support formulation", Appl. Catal. B: Environ. 146 (2014) 12-23.

[53] H. Abdulhamid, E. Fridell, M. Skoglundh, "Influence of the type of reducing agent (H_2, CO, C_3H_6 and C_3H_8) on the reduction of stored NO_x in a $Pt/BaO/Al_2O_3$ model catalyst", T. Catal. 30/31 (2004) 161-168.

[54] R.J. Farrauto, C.H. Bartholomew, "Fundamentals of Industrial Catalytic Processes", Blackie Academic & Professional, London, 1997.

[55] C.N. Satterfield, "Heterogeneous Catalysis in Industrial Practice", Krieger Publishing Company, Florida, 1996.

[56] X. Wang, R.J. Gorte, J.P. Wagner, "Deactivation Mechanisms for Pd/Ceria during the Water–Gas-Shift Reaction", J. Catal. 212 (2002) 225-230.

[57] T. Utaka, T. Okanishi, T. Takeguchi, R. Kikuchi, K. Eguchi, "Water gas shift reaction of reformed fuel over supported Ru catalysts", Appl. Catal. A: Gen. 245 (2003) 343-351.

[58] J. Kaspar, P. Fornasiero, N. Hickey, "Automotive catalytic converters: current status and some perspectives", Catal. Today 77 (2003) 419-449.

[59] J.A. Botas, M.A. Gutiérrez-Ortiz, M.P. Gonzalez-Marcos, J.A. Gonzalez-Marcos, J.R. Gonzalez-Velasco, "Kinetic considerations of three-way catalysis in automobile exhaust converters", Appl. Catal. B: Environ. 32 (2001) 243-256.

[60] J. Li, J. Theis, W. Chun, C. Goralski, R. Kudla, J. Ura, W. Watkins, M. Chattha, R. Hurley, "Sulfur poisoning and desulfation of the lean NO_x trap", SAE Technical Paper Series 2001-01-2503, 2001.

[61] L. Limousy, H. Mahzoul, J.F. Brilhac, P. Gilot, F. Garin, G. Maire, "SO_2 sorption on fresh and aged SO_x traps", Appl. Catal. B: Environ. 42 (2003) 237-249.

[62] S. Salasc, M. Skoglundh, E. Fridell, "A comparison between Pt and Pd in NO_x storage catalysts", Appl. Catal. B: Environ. 36 (2002) 145–160.

[63] L.F. Liotta, A. Macaluso, G.E. Arena, M. Livi, G. Centi, G. Deganello, "A study of the behaviour of Pt supported on CeO_2–ZrO_2/Al_2O_3–BaO as NO_x storage–reduction catalyst for the treatment of lean burn engine emissions", Catal. Today 75 (2002) 439-449.

[64] L. Olsson, E. Fridell, M. Skoglundh, B. Andersson, "Mean field modelling of NO_x storage on Pt/BaO/Al_2O_3", Catal. Today 73 (2002) 263–270.

[65] G.E. Arena, A. Bianchini, G. Centi, F. Vazzana, "Transient surface processes of storage and conversion of NO_x species on Pt–Me/Al_2O_3 catalysts (Me=Ba, Ce, Cu)", Top. Catal. 16/17 (2001) 157-164.

[66] T.V. Jonhson, "Review of selective catalytic reduction (SCR) and related technologies for mobile applications", Cap. 1 en Urea-SCR technology for DeNO_x after treatment of diesel exhausts, E. Tronconi, I. Nova (editores), Springer, Nueva York, 2014.

[67] A. Walker, "Future challenges and incoming solutions in the global catalyst based emission control area", SAE Heavy-Duty Diesel Emission Control Symposium, Septiembre 2014, Gothenburg, Suecia.

[68] A. Walker, "Current and future trends in catalyst-based emission control system design'', SAE Heavy-Duty Diesel Emission Control Symposium, Septiembre 2012, Gothenburg, Suecia.

[69] C. Narula, X. Yang, P. Bonnesen, E. Hagaman, "High performance NH_3 SCR zeolite catalysts for treatment of NO_x in emissions from off-road diesel engine", SAE Technical Paper 2011-01-1330, 2011.

[70] X. Yang, C. Narula, "Simple approach to tuning catalytic activity of MFI zeolites for low temperature SCR of NO_x", US Department of Energy directions in engine efficiency and Emissions Research (DEER) conference, Septiembre 2010, Detroit, EEUU.

[71] A. Heibel, "Advances in substrate technology", SAE Heavy-Duty Diesel Emissions Control Symposium, Septiembre 2010, Gothenburg, Suecia.

[72] G.J. Bartley, C.J. Chadwell, T.W. Kostek, R. Zhan, "SCR deactivation kinetics for model-based control and accelerated aging applications", SAE Technical Paper 2012-01-1077, 2012.

[73] K. Kamasamudram, C. Henry, N. Currier, A. Yezerets, "N_2O formation and mitigation in diesel aftertreatment systems", SAE Int. J. Engines 5 2012-01-1085, 2012.

[74] D.W. Fickel, E. D'Addio, J.A. Lauterbach, R.F. Lobo, "The ammonia selective catalytic reduction activity of copper-exchanged small-pore zeolites", Appl. Catal. B: Environ. 102 (2011) 441-448.

[75] J.H. Kwak, R.G. Tonkyn, D.H. Kim, J. Szanyi, C.H.F. Peden, "Excellent activity and selectivity of Cu-SSZ-13 in the selective catalytic reduction of NO_x with NH_3", J. Catal. 275 (2010) 187-190.

[76] S.T. Korhonen, D.W. Fickel, R.F. Lobo, B.M. Weckhuysen, A.M. Beale, "Isolated Cu^{2+} ions: active sites for selective catalytic reduction of NO", Chem. Commun. 47 (2011) 800-802.

[77] D.W. Fickel, R.F. Lobo, "Copper coordination in Cu-SSZ-13 and Cu-SSZ-16 Investigated by Variable-Temperature XRD", J. Phys. Chem. C 114 (2010) 1633-1640.

[78] J.H. Kwak, H.Y. Zhu, J.H. Lee, C.H.F. Peden, J. Szanyi, "Two different cationic positions in Cu-SSZ-13?", Chem. Commun. 48 (2012) 4758-4760.

[79] F. Gao, E.D. Walter, E.M. Karp, J. Luo, R.G. Tonkyn, J.H. Kwak, J. Szanyi, C.H.F. Peden, "Structure-activity relationships in NH_3-SCR over Cu-SSZ-13 as probed by reaction kinetics and EPR studies", J. Catal. 300 (2013) 20-29.

[80] L. Wang, W. Li, G. Qi, D. Weng, "Location and nature of Cu species in Cu/SAPO-34 for selective catalytic reduction of NO with NH_3", J. Catal. 289 (2012) 21-29.

[81] S.A. Bates, A.A. Verma, C. Paolucci, A.A. Parekh, T. Anggara, A. Yezerets, W.F. Schneider, J.T. Miller, W.N. Delgass, F.H. Ribeiro, "Identification of the active Cu site in standard selective catalytic reduction with ammonia on Cu-SSZ-13", J. Catal. 312 (2014) 87-97.

[82] T. Ishihara, M. Kagawa F. Hadama, Y. Takita, "Copper Ion-Exchanged SAPO-34 as a Thermostable Catalyst for Selective Reduction of NO with C_3H_6", J. Catal. 169 (1997) 93–102.

[83] T. Ishihara, M. Kagawa, Y. Mizuhara, Y. Takita, "Selective Reduction of Nitrogen Monoxide with Propene over Cu-Silico-aluminophosphate (SAPO) under Oxidizing Atmosphere", Chem. Lett. (1992) 2119–2122.

[84] D.B. Akolekar, S.K. Bhargava, K. Foger, "FTIR investigations of the adsorption and disproportionation of NO on Cu-exchanged silicoaluminophophate of type 34", J. Chem. Soc., Faraday Trans. 94 (1998) 155–160.

[85] A. Frache, B.I. Palella, M. Cadoni, R. Pirone, H.O. Pastore, L. Marchese, "CuAPSO-34 catalysts for N_2O decomposition in the presence of H_2O. A study of zeolitic structure stability in comparison to Cu-SAPO-34 and Cu-ZSM-5", Top. Catal. 22 (2003) 53–57.

[86] A. Frache, B. Palella, M. Cadoni, R. Pirone, P. Ciambelli, H.O. Pastore, L. Marchese, "Catalytic $DeNO_x$ activity of cobalt and copper ions in microporous MeALPO-34 and MeAPSO-34", Catal. Today 75 (2002) 359–365.

[87] S.I. Zones, L.T. Yuen, S.J. Miller, "Small crystallite zeolite CHA.", U.S. Patent US 6,709,644, 2004.

[88] H.Y. Chen, Q. Sun, B. Wen, Y.H. Yeom, E. Weitz, W.M.H. Sachtler, "Reduction over zeolite-based catalysts of nitrogen oxides in emissions containing excess oxygen Unraveling the reaction mechanism", Catal. Today 96 (2004) 1–10.

[89] I. Bull, W.M. Xue, P. Burk, "Copper CHA zeolite catalysts", U.S. Patent US 7,601,662, 2009.

[90] P.J. Andersen, J.E. Bailie, J.L. Casci, "Transition metal/zeolite SCR catalysts", Patent Application WO 2008/132452, 2008.

[91] J.H. Kwak, D. Tran, S.D. Burton, J. Szanyi, J.H. Lee, C.H.F. Peden, "Effects of hydrothermal aging on NH_3-SCR reaction over Cu/zeolites", J. Catal. 287 (2012) 203–209.

[92] M. Colombo, I. Nova, E. Tronconi, "A comparative study of the NH_3-SCR reactions over a Cu-zeolite and a Fe-zeolite catalyst", Catal. Today 151 (2010) 223-230.

[93] U. De-La Torre, B. Pereda-Ayo, M.A. Gutiérrez-Ortiz, J.A. González-Marcos, J.R. González-Velasco, "Steady-state NH_3-SCR global model and kinetic parameter estimation for NO_x removal in diesel engine exhaust aftertreatment with Cu/chabazite", Catal. Today 296 (2017) 95-104.

[94] T. Komatsu, M. Nunokawa, I.S. Moon, T. Takahara, S.Namba, T. Yasima, "Kinetic Studies of Reduction of Nitric Oxide with Ammonia on Cu^{2+}-Exchanged Zeolites", J. Catal. 148 (1994) 427-437.

[95] Y.H. Yeom, J. Henao, M.J. Li, W.M.H. Sachtler, E. Weitz, "The role of NO in the mechanism of NO_x reduction with ammonia over a BaNa–Y catalyst", J. Catal. 231 (2005) 181-193.

[96] A. Grossale, I. Nova, E. Tronconi, D. Chatterjee, M. Weibel, "The chemistry of the NO/NO_2–NH_3 "fast" SCR reaction over Fe/ZSM5 investigated by transient reaction analysis", J. Catal. 256 (2008) 312-322.

[97] M. Koebel, M. Elsener, G. Madia, "Reaction pathways in the Selective Catalytic Reduction Process with NO and NO_2 at Low Temperatures", Ind. Eng. Chem. Res. 40 (2001) 52-59.

[98] G. Madia, M. Koebel, M. Elsener, A. Wokaun, "Side reactions in the Selective Catalytic Reduction of NO_x with Various NO_2 Fractions", Ind. Eng. Chem. Res. 41 (2002) 4008-4015.

[99] I. Nova, C. Ciardelli, E. Tronconi, D. Chatterjee, B. Bandl-Konrad, "NH_3-SCR of NO over a V-based catalyst: Low-T Redox Kinetics with NH_3 inhibition", AIChE J. 52 (2006) 3222-3233.

[100] Y.H. Yeom, B. Wen, W.M.H. Sachtler, E. Weitz, "NO_x Reduction from Diesel Emissions over a Non transition Metal Zeolite Catalyst: A Mechanistic Study Using FTIR Spectroscopy", J. Phys. Chem. B. 108 (2004) 5386-5404.

[101] Y. Yeom, M. Li, A. Savara, W. Sachtler, E. Weitz, "An overview of the mechanisms of NO_x reduction with oxygenates over zeolite and γ-Al_2O_3 catalysts", Catal. Today 136 (2008) 55-63.

[102] M. Devadas, O. Krocher, M. Elsener, A. Wokaun, N. Söger, M. Pfeifer, Y. Demel, L. Mussmann, "Influence of NO_2 on the selective catalytic reduction of NO with ammonia over Fe-ZSM5", Appl. Catal. B: Environ. 67 (2006) 187-196.

[103] E.V. Kondratenko, V.A. Kondratenko, M. Santiago, J. Pérez-Ramírez, "Mechanistic origin of the different activity of Rh-ZSM-5 and Fe-ZSM-5 in N_2O decomposition", J. Catal. 256 (2008) 248-258.

[104] K. Rahkamaa-Tolonen, T. Maunula, M. Lomma, M. Huuhtanen, R.L. Keiski, "The effect of NO_2 on the activity of fresh and aged zeolite catalysts in the NH_3-SCR reaction", Catal. Today 100 (2005) 217-222.

[105] F. Can, X. Courtois, S. Roger, G. Blanchard, S. Rousseau, D. Duprez, "An overview of the production and use of ammonia in NSR + SCR coupled system for NO_x reduction from lean exhaust gas", Catal. Today 197 (2012) 144-154.

[106] P.S. Metkar, M.P. Harold, V. Balakotaiah, "Experimental and kinetic modeling study of NH_3-SCR of NO_x on Fe-ZSM-5, Cu-chabazite and combined Fe- and Cu-zeolite monolithic catalysts", Chem. Eng. Sci. 87 (2013) 51-66.

[107] L. Olsson, H. Sjövall, R.J. Blint, "A kinetic model for ammonia selective catalytic reduction over Cu-ZSM-5", Appl. Catal. B: Environ. 81 (2008) 203- 217.

[108] G. Busca, L. Lietti, G. Ramis and F. Berti, "Chemical and mechanistic aspects of the selective catalytic reduction of NO_x by ammonia over oxide catalysts: A review", Appl. Catal. B: Environ. 18 (1998) 1-36.

[109] S. Brandenberger, O. Kröcher, A. Tissler, R. Althoff, "The State of the Art in Selective Catalytic Reduction of NO_x by Ammonia Using Metal-Exchanged Zeolite Catalysts", Catal. Rev. 50 (2008) 492-531.

[110] M. Koebel, M. Elsener, M. Kleemann, "Urea-SCR: a promising technique to reduce NO_x emissions from automotive diesel engines", Catal. Today 59 (2000) 335-345.

[111] Y. Liu, M.P. Harold, D. Luss, "Coupled NO_x storage and reduction and selective catalytic reduction using dual-layer monolithic catalysts", Appl. Catal. B: Environ. 121-122 (2012) 239-251.

[112] J. Guenther, B. Konrad, B. Krutzsch, A. Nolte, D. Voigtlaender, M. Weibel, M. Weirich, G. Wenninger, "Exhaust gas purification process and apparatus with internal generation of ammonia for reducing nitrogen oxide", U. S. Patent 6338224 B1, 2002.

[113] H.S. Gandhi, J.V. Cavataio, R.H. Hammerle, Y. Cheng, "Catalyst system for NO_x and NH_3 emission", U. S. Patent 76565 A1, 2004.

[114] K. Sakurai, "Exhaust purifying system for internal combustion engine", U. S. Patent 138783 A1, 2011.

[115] L. Xu, R.W. McCabe, "LNT + in situ SCR catalyst system for diesel emissions control", Catal. Today 184 (2012) 83-94.

[116] T. Nakatsuji, M. Matsubara, J. Rouistenmäki, N. Sato, H. Ohno, "A NO_x reduction system using ammonia-storage selective catalytic reduction in rich/lean excursions", Appl. Catal. B: Environ. 77 (2007) 190-201.

[117] Y. Liu, Y. Zheng, M.P. Harold, D. Luss, "Lean NO_x reduction on LNT-SCR dual-layer catalysts by H_2 and CO", Appl. Catal. B: Environ. 132–133 (2013) 293-303.

[118] U. De-La-Torre, M. Urrutxua, B. Pereda-Ayo, J.R. González-Velasco, "On the Cu species in Cu/beta catalysts related to DeNO$_x$ performance of coupled NSR-SCR technology using sequential monoliths and dual-layer monolithic catalysts", Catal. Today 273 (2016) 72-82.

[119] Y. Zheng, Y. Liu, M.P. Harold, D. Luss, "LNT–SCR dual-layer catalysts optimized for lean NO$_x$ reduction by H_2 and CO", Appl. Catal. B: Environ. 148-149 (2014) 311-321.

[120] S. Andonova, V. Marchionni, M. Borelli, R. Nedyalkova, L. Lietti, L. Olsson, "Mechanistic investigation of the promoting role of Rh on the NSR performance of NO$_x$ storage BaO-based catalysts", Appl. Catal. B: Environ. 132-133 (2013) 266-281.

[121] S. Andonova, V. Marchionni, L. Lietti, L. Olsson, "Micro-calorimetric studies of NO_2 adsorption on Pt/BaO-supported on ɣ–Al_2O_3 NO$_x$ storage and reduction (NSR) catalysts-Impact of CO_2", Mol. Catal. 436 (2017) 43-52.

[122] F. Pinna, "Supported metal catalysts preparation", Catal Today 41 (1998) 129-137.

[123] B. Pereda-Ayo, U. De La Torre, M. Romero-Sáez, A. Aranzabal, J.A. González-Marcos, J.R. González-Velasco, "Influence of the washcoat characteristics on NH_3-SCR behavior of Cu-zeolite monoliths", Catal. Today 216 (2013) 82-89.

[124] A.K.S. Clemens, A. Shishkin, P.-A. Carlsson, M. Skoglundh, F.J. Martinez-Casado, Z. Matej, O. Balmes, H. Härelind, "Reaction-driven Ion Exchange of Copper into Zeolite SSZ-13" ACS Catal. 5 (2015) 6209-6218.

[125] S. Shwan, M. Skoglundh, L.F. Lundegaard, R.R. Tiruvalam, T.V.W. Janssens, A. Carlsson, P.N.R. Vennestrøm, "Solid-State Ion-Exchange of Copper into Zeolites Facilitated by Ammonia at Low Temperature", ACS Catal. 5 (2015) 16-19.

[126] F. Gao, E.D. Walter, N.M. Washton, J. Szanyi, C.H.F. Peden, "Synthesis And evaluation of Cu/SAPO-34 catalysts for NH_3-SCR 2: Solid-state ion exchange and one-pot synthesis", Appl. Catal. B: Environ. 162 (2015) 501-514.

[127] R. Thomas, "Beginner's guide to ICP-MS. Part VI: The mass analyzer", Spectroscopy 16 (2001) 44-48.

[128] S. Brunauer, P.H. Emmett, E. Teller, "Adsorption of Gases in Multimolecular Layers", J. Am. Chem. Soc. 60 (1938) 309-319.

[129] K.S.W. Sing, "Empirical method for analysis of adsorption isotherms", Chem. Ind. 44 (1968) 1520-1521.

[130] J. Rouquerol, D. Avnir, D.H. Everett, C. Fairbridge, M. Haynes, N. Pernicone, J.D.F. Ramsay, K.S.W. Sing, K.K. Unger, "Guidelines for the Characterization of Porous Solids", Stud. Surf. Sci. Catal. 87 (1994) 1-9.

[131] S. Petr, "Adsorption isotherms of microporous-mesoporous solids revisited", Appl. Catal. A: Gen. 129 (1995) 157-165.

[132] K. Katsumi, "Determination of pore size and pore size distribution: 1. Adsorbents and catalysts", J. Membrane Sci. 96 (1994) 59-89.

[133] K.S.W. Sing, D.H. Everett, R.A.W. Haul, L. Moscou, R.A. Pierotti, J. Rouquerol, T. Siemieniewska, "Reporting physisorption data for gas solid systems with special reference to the determination of surface-area and porosity (Recommendations 1984)", Pure and Appl. Chem. 57 (1985) 603-619.

[134] E.P. Barrett, L.G. Joyner, P.P. Halenda, "The determination of pore volume and area distributions in porous substances. 1. Computations from nitrogen isotherms", J. Am. Chem. Soc. 73 (1951) 373-380.

[135] J.A. Helsen, A. Kuczumow, "Wavelength-dispersive X-ray fluorescence", en R.E. Van Grieken, A.A. Markowicz (Eds.), Handbook of X-Ray Spectromotry, CRC Press, Nueva York (2002) 95-198.

[136] B. Beckhoff, B. Kanngießer, N. Langhoff, R. Wedell, H. Wolff (Eds.), "Handbook of pratical X-ray fluorescence analysis", Springer, Berlín, 2006.

[137] H.P. Klug, L.E. Alexander, "X-Ray diffraction procedures for polycrystalline and amorphous materials", John Wiley, Nueva York, 1977.

[138] R. Ferret Poza, "Síntesis de cordierita por reacción en estado sólido y optimación del proceso de extrusión en estructuras monolíticas", Tesis Doctoral, Universidad del País Vasco/EHU, Bilbao, 2000.

[139] A. Aranzabal, D. Iturbe, M. Romero-Sáez, M.P. González-Marcos, J.R. González-Velasco, J.A González-Marcos, "Optimization of process parameters on the extrusion of honeycomb shaped monolith of H-ZSM-5 zeolite", Chem. Eng. J. 162 (2010) 415-423.

[140] P. Gallezot, "X-Ray techniques in catalysis, Catalysis, science and technology", 221-273, J.R. Anderson, M. Boudart (editores), Springer-Verlag, Berlin, 1984.

[141] K. Nakamoto, "Infrared and Raman Spectra of Inorganic and Coordination Compounds. Part B: Applications in Coordination, Organometallic, and Bioinorganic Chemistry", John Widely & Sons, New Jersey, 2009".

[142] L.Z. Gao, C. T. Au, "CO_2 Hydrogenation to Methanol on a $YBa_2Cu_3O_7$ Catalyst", J. Catal. 189 (2000) 1-15.

[143] G. Busca, E. Finocchio, V. Lorenzelli, G. Ramis, M. Baldi, "IR studies on the activation of C-H hydrocarbon bonds on oxidation catalysts", Catal. Today 49 (1999) 453-465.

[144] O. Alexeev, D.W. Kim, G.W. Graham, M. Shelef, B.C. Gates, "Temperature-Programmed Desorption of Hydrogen from Platinum Particles on γ-Al_2O_3: Evidence of Platinum-Catalyzed Dehydroxylation of γ-Al_2O_3", J. Catal. 185 (1999) 170-181.

[145] L. Lietti, I. Nova, G. Ramis, L. Dall'Acqua, G. Busca, E. Giamello, P. Forzatti, F. Bregani, "Characterization and Reactivity of V_2O_5-MoO_3/TiO_2 De-NO_x SCR Catalysts", J. Catal. 187 (1999) 419-435.

[146] G. Busca, "The use of vibrational spectroscopies in studies of heterogeneous catalysis by metal oxides: an introduction", Catal. Today 27 (1996) 323-352.

[147] M. Weyland, "Electron tomography of catalysts", Top. Catal. 21 (2002) 175-183.

[148] S. Bernal, J.J. Calvino, M.A. Cauqui, J.M. Gatica, C. López Cartes, J.A. Pérez Omil, J.M. Pintado, "Some contributions of electron microscopy to the characterization of the strong metal-support interaction effect", Catal. Today 77 (2003) 385-406.

[149] R.G. Sajfutdinov, L.I. Larina, T.I. Vakulskaya, M. G. Voronkov, "Electron paramagnetic resonance in biochemistry and medicine", Springer, New York, 2001.

[150] M. Faraldos, C. Goberna, "Técnicas de Análisis y Caracterización de Materiales", Consejo Superior de Investigaciones Científicas, Madrid 2002.

[151] D.A. Skoog, F.J. Holler, T.A. Nieman, "Principios de Análisis Instrumental", McGraw Hill, 2000.

[152] E.C. Corbos, M. Haneda, X. Courtois, P. Marecot, D. Duprez, H. Hamada, "NO_x abatement for lean-burn engines under lean–rich atmosphere over mixed NSR-SCR catalysts: Influences of the addition of a SCR catalyst and of the operational conditions" Appl. Catal. A: Gen. 365 (2009) 187-193.

[153] C.D. DiGiulio, J.A. Pihl, J.S. Choi, J.E. Parks II, M.J. Lance, T.J. Toops, M.D. Amiridis, "NH_3 formation over a lean NO_x trap (LNT) system: Effects of lean/rich cycle timing and temperature" Appl. Catal. B: Environ. 147 (2014) 698-710.

[154] M. Iwamoto, H. Furukawa, Y. Mine, F. Uemura, S.I. Mikuriya, S. Kagawa, "Copper(ii) Ion-exchanged ZSM-5 Zeolites as Highly Active Catalysts for Direct and Continuous Decomposition of Nitrogen Monoxide" J. Chem. Soc. Chem. Commun. (1986) 1272-1273.

[155] H.S. Gandhi, J.V. Cavataio, R.H. Hammerle, Y. Cheng, "Catalyst system for the reduction of NO_x and NH_3 emissions", U.S. Patent US 7,332,135 B2, 2008.

[156] O. Mihai, C.R. Widyastuti, S. Andonova, K. Kamasamudram, J. Li, S.Y. Joshi, N.W. Currier, A. Yezerets, L. Olsson, "The effect of Cu-loading on different reactions involved in NH_3-SCR over Cu-BEA catalysts", J. Catal. 311 (2014) 170-181.

[157] F. Giordanino, P.N.R. Vennestrøm, L.F. Lundegaard, F.N. Stappen, S. Mossin, P. Beato, S. Bordiga, C. Lamberti, "Characterization of Cu-exchanged SSZ-13: a comparative FTIR, UV-Vis, and EPR study with Cu-ZSM-5 and Cu-β with similar Si/Al and Cu/Al ratios", Dalton Trans. 42 (2013) 12741-12761.

[158] A. Corma, V. Fornés, E. Palomares, "Selective catalytic reduction of NO_x on Cu-beta zeolites", Appl. Catal. B: Environ. 11 (1997) 233-242.

[159] K.I. Hadjiivanov, "Identification of Neutral and Charged N_xO_y Surface Species by IR Spectroscopy", Catal. Rev. Sci. Eng. 42 (2000) 71-144.

[160] M. Iwasaki, H. Shinjoh, "NO evolution reaction with NO_2 adsorption over Fe/ZSM-5: In situ FT-IR observation and relationships with Fe sites", J. Catal. 273 (2010) 29-38.

[161] C. Lamberti, S. Bordiga, M. Salvalaggio, G. Spoto, A. Zecchina, F. Geobaldo, G. Vlaic, M. Bellatreccia, "XAFS, IR, and UV-Vis Study of the Cu^I Environment in Cu^I-ZSM-5", J. Phys. Chem. B 101 (1997) 344-360.

[162] H. Yahiro, Y. Ohmori, M. Shiotani, "Magnetic interaction between copper (II) ion and paramagnetic NO and O_2 molecules in Y-type zeolite at low temperature: An EPR study", Microporous Mesoporous Mater. 83 (2005)165-171.

[163] P. Decyk, "States of transition metal ions in modified mesoporous MCM-41 and in microporous ZSM-5 studied by ESR spectroscopy", Catal. Today 114 (2006) 142-153.

[164] J. Xue, X. Wang, G. Qi, J. Wang, M. Shen, W. Li, "Characterization of copper species over Cu/SAPO-34 in selective catalytic reduction of NO_x with ammonia: Relationships between active Cu sites and de-NO_x performance at low temperature", J. Catal. 297 (2013) 56-64.

[165] R. Martínez-Franco, M. Moliner, P. Concepcion, J.R. Thogersen, A. Corma, "Synthesis, characterization and reactivity of high hydrothermally stable Cu-SAPO-34 materials prepared by ''one-pot'' processes", J. Catal. 314 (2014) 73-82.

[166] J. Wang, T. Yu, X. Wang, G. Qi, J. Xue, M. Shen, W. Li, "The influence of silicon on the catalytic properties of Cu/SAPO-34 for NO_x reduction by ammonia-SCR", Appl. Catal. B: Environ.127 (2012) 137-147.

[167] D. Wang, L. Zhang, J. Li, K. Kamasamudram, W.S. Epling, "NH_3-SCR over Cu/SAPO-34 – Zeolite acidity and Cu structure changes as a function of Cu loading", Catal. Today 231(2014) 64-74.

[168] B. Pereda-Ayo, U. De La Torre, M.J. Illán-Gómez, A. Bueno-López, J.R. González-Velasco, "Role of the different copper species on the activity of Cu/zeolite catalysts for SCR of NO_x with NH_3", Appl. Catal. B: Environ. 147 (2014) 420-428.

[169] J. Zhou, Q.-H. Xia, S. Shen, S. Kawi, K. Hidajat, "Catalytic oxidation of pyridine on the supported copper catalysts in the presence of excess oxygen", J. Catal. 225 (2004) 128-137.

[170] T. Nanba, S. Masukawa, A. Ogata, J. Uchisawa, A. Obuchi, "Active sites of Cu-ZSM-5 for the decomposition of acrylonitrile", Appl. Catal. B: Environ. 61 (2005) 288-296.

[171] A. Sultana, T. Nanba, M. Haneda, M. Sasaki, H. Hamada, "Influence of cocations on the formation of Cu^+ species in Cu/ZSM-5 and its effect on selective catalytic reduction of NO_x with NH_3", Appl. Catal. B: Environ. 101 (2010) 61-67.

[172] C. Torre-Abreu, M.F. Ribeiro, C. Henriques, G. Delahay, "NO TPD and H_2-TPR studies for characterization of CuMOR catalysts The role of Si/Al ratio, copper content and cocation", Appl. Catal. B: Environ. 14 (1997) 261-272.

[173] B. Pereda-Ayo, U. De La Torre, M.P. González-Marcos, J.R. González-Velasco, "Influence of ceria loading on the NO_x storage and reduction performance of model Pt–Ba/Al_2O_3 NSR catalyst", Catal. Today 241 (2015) 133-142.

[174] S.S. Mulla, S.S. Chaugule, A. Yezerets, N.W. Currier, W.N. Delgass, F.H. Ribeiro, "Regeneration mechanism of Pt/BaO/Al_2O_3 lean NO_x trap catalyst with H_2", Catal. Today 136 (2008) 136-145.

[175] U. De La Torre, B. Pereda-Ayo, J.R. González-Velasco, "Cu-zeolite NH_3-SCR catalysts for NO_x removal in the combined NSR–SCR technology", Chem. Eng. J. 207–208 (2012) 10-17.

[176] E.C. Corbos, M. Haneda, X. Courtois, P. Marecot, D. Duprez, H. Hamada, "Cooperative effect of Pt–Rh/Ba/Al and CuZSM-5 catalysts for NO_x reduction during periodic lean-rich atmosphere", Catal. Commun. 10 (2008) 137-141.

[177] A. Aranzabal, J.A. González-Marcos, M. Romero-Sáez, J.R. González-Velasco, M. Guillemot, P. Magnoux, "Stability of protonic zeolites in the catalytic oxidation of chlorinated VOCs (1,2-dichloroethane)", Appl. Catal. B: Environ. 88 (2009) 533-541.

[178] U. De-La-Torre, B. Pereda-Ayo, M. Moliner, J.R. González-Velasco, A. Corma, "Cu-zeolite catalysts for NO_x removal by selective catalytic reduction with NH_3 and coupled to NO storage/reduction monolith in diesel engine exhaust aftertreatment systems", Appl. Catal. B: Environ. 187 (2016) 419-427.

[179] M. Moliner, C. Franch, E. Palomares, M. Grill, A. Corma, "Cu–SSZ-39, an active and hydrothermally stable catalyst for the selective catalytic reduction of NO_x", Chem. Commun. 48 (2012) 8264-8266.

[180] J. Ma, Z. Si, D. Weng, X. Wu, Y. Ma, "Potassium poisoning on Cu/SAPO-34 catalyst for selective catalytic reduction of NO_x with ammonia", Chem. Eng. J. 267 (2015) 191-200.

[181] T. Yu, T. Hao, D. Fan, J. Wang, M. Shen, W. Li, "Recent NH_3-SCR Mechanism Research over Cu/SAPO-34 Catalyst", J. Phys. Chem. C 118 (2014) 6565-6575.

[182] L. Wang, J.R. Gaudet, W. Li, D. Weng, "Migration of Cu species in Cu/SAPO-34 during hydrothermal aging", J. Catal. 306 (2013) 68-77.

[183] F. Gao, E.D. Walter, M. Kollar, Y. Wang, J. Szanyi, C.H.F. Peden, "Understanding ammonia selective catalytic reduction kinetics over Cu/SSZ-13 from motion of the Cu ions", J. Catal. 319 (2014) 1-14.

[184] A.M. Beale, F. Gao, I. Lezcano-Gonzalez, C.H.F. Peden, J. Szanyi, "Recent advances in automotive catalysis for NO_x emission control by small-pore microporous materials" Chem. Soc. Rev. 44 (2015) 7371-7405.

[185] T. Yu, J. Wang, M. Shen, W. Li, "NH_3-SCR over Cu/SAPO-34 catalysts with various acid contents and low Cu loading", Catal. Sci. Technol. 3 (2013) 3234-3241.

[186] A.V. Kucherov, C.P. Hubbard, T.N. Kucherova, M. Shelef, "Stabilization of the ethane oxidation catalytic activity of Cu-ZSM-5" Appl. Catal. B: Environ. 7 (1996) 285-298.

[187] S. Dzwigaj, L. Stievano, F.E. Wagner, M. Che, "Effect of preparation and metal content on the introduction of Fe in BEA zeolite, studied by DR UV–vis, EPR and Mössbauer spectroscopy", J. Phys. Chem. Solids 68 (2007) 1885-1891.

[188] E.A. Zhilinskaya, G. Delahay, M. Mauvezin, B. Coq, A. Aboukaïs, "EPR Investigation of Fe-Exchanged Beta-Zeolites", Langmuir 19 (2003) 3596-3602.

[189] C. Torre-Abreu, M.F. Ribeiro, C. Henriques, G. Delahay, "Characterisation of CuMFI catalysts by temperature programmed desorption of NO and temperature programmed reduction. Effect of the zeolite Si/Al ratio and copper loading", Appl. Catal. B: Environ. 12 (1997) 249-262.

[190] M. Richter, M.J.G. Fait, R. Eckelt, E. Schreier, M. Schneider, M.-M. Pohl, R. Fricke, "Oxidative gas phase carbonylation of methanol to dimethyl carbonate over chloride-free Cu-impregnated zeolite Y catalysts at elevated pressure", Appl. Catal. B: Environ 73 (2007) 269-281.

[191] T. Zhang, F. Qiu, H. Chang, X. Li, J. Li, "Identification of active sites and reaction mechanism on low-temperature SCR activity over Cu-SSZ-13 catalysts prepared by different methods", Catal. Sci. Technol. 6 (2016) 6294-6304.

[192] U. Deka, I. Lezcano-Gonzalez, S.J. Warrender, A.L. Picone, P.A. Wright, B.M. Weckhuysen, A.M. Beale, "Changing active sites in Cu–CHA catalysts: deNO_x selectivity as a function of the preparation method", Microporous Mesoporous Mater. 166 (2013) 144-152.

[193] R. Martínez-Franco, M. Moliner, C. Franch, A. Kustov, A. Corma, "Rational direct synthesis methodology of very active and hydrothermally stable Cu-SAPO-34 molecular sieves for the SCR of NO_x", Appl. Catal. B: Environ. 127 (2012) 273-280.

[194] M. Cortés-Reyes, E. Finocchio, C. Herrera, M.A. Larrubia, L.J. Alemany, G. Busca, "A study of Cu-SAPO-34 catalysts for SCR of NO_x by ammonia", Microporous Mesoporous Mater. 241 (2017) 258-265.

[195] T.T.H. Dang, H.L. Zubowa, U. Bentrup, M. Richter, A. Martin, "Microwave-assisted synthesis and characterization of Cu-containing $AlPO_4$-5 and SAPO-5", Microporous Mesoporous Mater. 123 (2009) 209-220.

[196] A.N. Pestryakov, V.P. Petranovskii, A. Kryazhov, O. Ozhereliev, N. Pfänder, A. Knop-Gericke, "Study of copper nanoparticles formation on supports of different nature by UV–Vis diffuse reflectance spectroscopy", Chem. Phys. Lett. 385 (2004) 173-176.

[197] J. Kecht, Z. Tahri, V. De Waele, M. Mostafavi, S. Mintova, T. Bein, "Colloidal Zeolites as Host Matrix for Copper Nanoclusters", Chem. Mater. 18 (2006) 3373-3380.

[198] Y. Cao, S. Zou, L. Lan, Z. Yang, H. Xu, T. Lin, M. Gong, Y. Chen, "Promotional effect of Ce on Cu-SAPO-34 monolith catalyst for selective catalytic reduction of NO_x with ammonia", J. Mol. Catal. A: Chem. 398 (2015) 304-311.

[199] I. Lezcano-Gonzalez, U. Deka, B. Arstad, A. Van Yperen-De Deyne, K. Hemelsoet, M. Waroquier, V. V. Speybroeck, B.M. Weckhuysen, A.M. Beale, "Determining the storage, availability and reactivity of NH_3 within Cu-Chabazite-based Ammonia Selective Catalytic Reduction systems", Phys. Chem. Chem. Phys. 16 (2014) 1639-1650.

[200] J. Li, H. Chang, L. Ma, J. Hao, R.T. Yang, "Low-temperature selective catalytic reduction of NO_x with NH_3 over metal oxide and zeolite catalysts-A review", Catal. Today 175 (2011) 147-156.

[201] C. Ciardelli, I. Nova, E. Tronconi, D. Chatterjee, B. Bandl-Konrad, M. Weibel, B. Krutzsch, "Reactivity of NO/NO_2–NH_3 SCR system for diesel exhaust aftertreatment: Identification of the reaction network as a function of temperature and NO_2 feed content", Appl. Catal. B: Environ. 70 (2007) 80-90.

[202] M. Colombo, I. Nova, E. Tronconi, "Detailed kinetic modeling of the NH_3–NO/NO_2 SCR reactions over a commercial Cu-zeolite catalyst for Diesel exhausts after treatment", Catal. Today 197 (2012) 243-255.

[203] X. Hu, M. Yang, D. Fan, G. Qi, J. Wang, J. Wang, T. Yu, W. Li, M. Shen, "The role of pore diffusion in determining NH_3 SCR active sites over Cu/SAPO-34 catalysts", J. Catal. 341 (2016) 55-61.

[204] J. Wang, D. Fan, T. Yu, J. Wang, T. Hao, X. Hu, M. Shen, W. Li, "Improvement of low-temperature hydrothermal stability of Cu/SAPO-34 catalysts by Cu^{2+} species", J. Catal. 322 (2015) 84-90.

[205] T. Yu, D. Fan, T. Hao, J. Wang, M. Shen, W. Li, "The effect of various templates on the NH_3-SCR activities over Cu/SAPO-34 catalysts", Chem. Eng. J. 243 (2014) 159-168.

[206] F. Gao, Y. Wang, N.M. Washton, M. Kollar, J. Szanyi, C.H.F. Peden, "Effects of Alkali and Alkaline Earth Cocations on the Activity and Hydrothermal Stability of Cu/SSZ-13 NH_3–SCR Catalysts", ACS Catal. 5 (2015) 6780-6791.

[207] X. Dong, J. Wang, H. Zhao, Y. Li, "The promotion effect of CeO_x on Cu-SAPO-34 catalyst for selective catalytic reduction of NO_x with ammonia", Catal. Today 258 (2015) 28-34.

[208] R. Kefirov, A. Penkova, K. Hadjiivanov, S. Dzwigaj, M. Che, "Stabilization of Cu^+ ions in BEA zeolite: Study by FTIR spectroscopy of adsorbed CO and TPR", Microporous Mesoporous Mater. 116 (2008) 180-187.

[209] J. Ryczkowski, "IR spectroscopy in catalysis", Catal. Today 68 (2001) 263-381.

[210] F.E. López-Suárez, M.J. Illán-Gómez, A. Bueno-López, J.A. Anderson, "NO_x storage and reduction on a $SrTiCuO_3$ perovskite catalyst studied by operand DRIFTS", Appl. Catal. B: Environ. 104 (2011) 261-267.

[211] J.A. Anderson, Z. Liu, M. Fernández García, "Use of in situ FT-IR and XAS/XRD to study SO_2 poisoning over model $Pt/Ba/Al_2O_3$ NO_x storage and reduction (NSR) catalysts", Catal. Today 113 (2006) 25-33.

[212] A.J. McCue, G.A. Mutch, A.I. McNab, S. Campbell, J.A. Anderson, "Quantitative determination of surface species and adsorption sites using Infrared spectroscopy", Catal. Today 259 (2015) 19-26.

[213] I. Malpartida, M.O. Guerrero-Pérez, M.C. Herrera, M.A. Larrubia, L.J. Alemany, "MS-FTIR reduction stage study of NSR catalysts", Catal. Today 126 (2007) 162-168.

[214] L. Castoldi, I. Nova, L. Lietti, P. Forzatti, "Study of the effect of Ba loading for catalytic activity of $Pt\text{-}Ba/Al_2O_3$ model catalysts", Catal. Today 96 (2004) 43-52.

[215] C.M.L. Scholz, B.H.W. Maes, M.H.J.M. de Croon, J.C. Schouten, "Influence of reducing agent (CO, H_2 and C_2H_4) and of H_2O on NO_x reduction on a $Pt\text{-}Ba/\gamma\text{-}Al_2O_3$ catalyst", Appl. Catal. A: Gen. 332 (2007) 1-7.

[216] X. Wang, Y. Yu, H. He, "Effects of temperature and reductant type on the process of NO_x storage reduction over $Pt/Ba/CeO_2$ catalysts", Appl. Catal. B: Environ. 104 (2011) 151-160.

[217] J. Wang, X. Wang, J. Zhu, J. Wang, M. Shen, "Elucidating N_2O Formation during the Cyclic NO_x Storage and Reduction Process Using CO as a Reductant", Environ. Sci. Technol. 49 (2015) 7965-7973.

[218] C.D. DiGiulio, V.G. Komvokis, M.D. Amiridis, "In situ FTIR investigation of the role of surface isocyanates in the reduction of NO_x by CO and C_3H_6 over model $Pt/BaO/Al_2O_3$ and $Rh/BaO/Al_2O_3$ NO_x storage and reduction (NSR) catalysts", Catal. Today 184 (2012) 8-19.

[219] H. Abdulhamid, J. Dawody, E. Fridell, M. Skoglundh, "A combined transient in situ FTIR and flow reactor study of NO_x storage and reduction over $M/BaCO_3/Al_2O_3$ (M=Pt, Pd or Rh) catalysts", J. Catal. 244 (2006) 169-182.

[220] T. Szailer, J.H. Kwak, D.H. Kim, J.C. Hanson, C.H.F. Peden, J. Szanyi, "Reduction of stored NO_x on Pt/Al_2O_3 and $Pt/BaO/Al_2O_3$ catalysts with H_2 and CO", J. Catal. 239 (2006) 51-64.

[221] I. Nova, L. Lietti, P. Forzatti, F. Prinetto, G. Ghiotti, "Experimental investigation of the reduction of NO_x species by CO and H_2 over Pt–Ba/Al_2O_3 lean NO_x trap systems", Catal. Today 151 (2010) 330-337.

[222] N. Macleod, R.M. Lambert, "An in situ DRIFTS study of efficient lean NO_x reduction with H_2+CO over Pd/Al_2O_3: the key role of transient NCO formation in the subsequent generation of ammonia", Appl. Catal. B: Environ. 46 (2003) 483-495.

[223] S. Suárez, S.M. Jung, P. Avila, P. Grange, J. Blanco, "Influence of NH_3 and NO oxidation on the SCR reaction mechanism on copper/nickel and vanadium oxide catalysts supported on alumina and titania", Catal. Today 75 (2002) 331–338.

[224] D. Wang, L. Zhang, K. Kamasamudram, W.S. Epling, "In Situ- DRIFTS Study of Selective Catalytic Reduction of NO_x by NH_3 over Cu-Exchanged SAPO-34", ACS Catal. 3 (2013) 871–881.

[225] A. Grossale, I. Nova, E. Tronconi, "Role of Nitrate Species in the ''NO_2-SCR'' Mechanism over a Commercial Fe-zeolite Catalyst for SCR Mobile Applications", Catal. Lett. 130 (2009) 525–531.

[226] M. Cheng, B. Jiang, S. Yao, J. Han, S. Zhao, X. Tang, J. Zhang, T. Wang, "Mechanism of NH_3 Selective Catalytic Reduction Reaction for NO_x Removal from Diesel Engine Exhaust and Hydrothermal Stability of Cu-Mn/Zeolite Catalysts", J. Phys. Chem. C 122 (2018) 455-464.

[227] M.P. Ruggeri, I. Nova, E. Tronconi, J.A. Pihl, T.J. Toops, W.P. Patridge, "In-situ DRIFTS measurements for the mechanistic study of NO oxidation over a commercial Cu-CHA catalyst", Appl. Catal. B: Environ. 166-167 (2015) 181-192.

[228] L. Ma, Y. Cheng, G. Cavataio, R.W. McCabe, L. Fu, J. Li, "In situ DRIFTS and temperature-programmed technology study on NH_3-SCR of NO_x over Cu-SSZ-13 and Cu-SAPO-34 catalysts", Appl. Catal. B: Environ. 156-157 (2014) 428-437.

[229] C. Yu, B. Huang, L. Dong, F. Chen, X. Liu, "In situ FT-IR study of highly dispersed MnO_x/SAPO-34 catalyst for low-temperature selective catalytic reduction of NO_x by NH_3", Catal. Today 281 (2017) 610-620.

[230] L. Wang, W. Li, S.J. Schmieg, D. Weng, "Role of Brønsted acidity in NH_3 selective catalytic reduction reaction on Cu/SAPO-34 catalysts", J. Catal. 324 (2015) 98-106.

[231] X. Liu, X. Wu, D. Weng, Z. Si, R. Ran, "Evolution of copper species on Cu/SAPO-34 SCR catalysts upon hydrothermal aging", Catal. Today 281 (2017) 596-604.

[232] J. Barbier, D. Duprez, "Hydrogen formation in propane oxidation on Pt-Rh/CeO_2/Al_2O_3 catalysts", Appl. Catal. A: Gen. 85 (1992) 89-100.

[233] F. Arosio, S. Colussi, A. Trovarelli, G. Groppi, "Effect of alternate CH_4-reducing/lean combustion treatments on the reactivity of fresh and S-poisoned Pd/CeO_2/Al_2O_3 catalysts", Appl. Catal. B: Environ. 80 (2008) 335-342.

[234] L. Zhang, J. Pierce, V.L. Leung, D. Wang, W.S. Epling, "Characterization of Ceria's Interaction with NO_x and NH_3", J. Phys. Chem. C 117 (2013) 8282-8289.

[235] M. Al-Harbi, W.S. Epling, "The effects of regeneration-phase CO and/or H_2 amount on the performance of a NO_x storage/reduction catalyst", Appl. Catal. B: Environ. 89 (2009) 315-325.

[236] L. Masdrag, X. Courtois, F. Can, S. Royer, E. Rohart, G. Blanchard, P. Marecot, D. Duprez, "Understanding the role of C_3H_6, CO and H_2 on efficiency and selectivity of NO_x storage reduction (NSR) process", Catal. Today 189 (2012) 70-76.

[237] L. Olsson, B. Westerberg, H. Persson, E. Fridell, M. Skoglundh, B. Andersson, "A Kinetic Study of Oxygen Adsorption/Desorption and NO Oxidation over Pt/Al_2O_3 Catalysts", J. Phys. Chem. B 103 (1999) 10433-10439.

[238] W.S. Epling, A. Yezerets, N.W. Currier, "The effects of regeneration conditions on NO_x and NH_3 release from NO_x storage/reduction catalysts", Appl. Catal. B: Environ. 74 (2007) 117-129.

[239] I. Nova, L. Lietti, P. Forzatti, "Regeneration mechanism of a Lean NO_x Trap (LNT) catalyst in the presence of NO investigated using isotope labelling techniques", Catal. Today 136 (2008) 128-135.

[240] R.D. Clayton, M.P. Harold, V. Balakotaiah, "Performance Features of Pt/BaO Lean NO_x Trap with Hydrogen as Reductant", AIChE J. 55 (2009) 687-700.

[241] Y. Ji, T.J. Toops, M. Crocker, "Effect of Ceria on the Storage and Regeneration Behavior of a Model Lean NO_x Trap Catalyst", Catal. Lett. 119 (2007) 257-264.

[242] C.M.Y. Yeung, K.M.K. Yu, Q.J. Fu, D. Thompsett, M.I. Petch, S.C. Tsang, "Engineering Pt in Ceria for a Maximum Metal-Support Interaction in Catalysis", J. Am. Chem. Soc. 127 (2005) 18010-18011.

[243] A. Lindholm, H. Sjövall, L. Olsson, "Reduction of NO_x over a combined NSR and SCR system", Appl. Catal. B: Environ. 98 (2010) 112-121.

[244] P. Forzatti, L. Lietti, "The reduction of NO_x stored on LNT and combined LNT–SCR systems", Catal. Today 155 (2010) 131-139.

[245] R. Mrad, A. Aissat, R. Cousin, D. Courcot, S. Siffert, "Catalysts for NO_x selective catalytic reduction by hydrocarbons (HC-SCR)", Appl. Catal. A: Gen. 504 (2015) 542-548.

[246] A.E. Palomares, C. Franch, A. Corma, "Determining the characteristics of a Co-zeolite to be active for the selective catalytic reduction of NO_x with hydrocarbons", Catal. Today 176 (2011) 239-241.

[247] G. Centi, S. Perathoner, L. Dall'Olio, "High activity of copper-boralite in the reduction of nitric oxide with propane / oxygen", Appl. Catal. B: Environ. 4 (1994) L275-L281.

[248] K. Shimizu, M. Hashimoto, J. Shibata, T. Hattori, A. Satsuma, "Effect of modified-alumina supports on propane–hydrogen-SCR over Ag/alumina", Catal. Today 126 (2007) 266-271 .

[249] J. Szanyi, M.T. Paffett, "The Adsorption of NO and Reaction of NO with O_2 on H-, NaH-, CuH-, and Cu-ZSM-5: An in Situ FTIR Investigation", J. Catal. 164 (1996) 232-245.

[250] Y. Zheng, M.P. Harold, D. Luss, "Effects of CO, H_2 and C_3H_6 on Cu-SSZ-13 catalyzed NH_3-SCR", Catal. Today 264 (2016) 44-54.

[251] O. Gorce, F. Baudin, C. Thomas, P. Da Costa, G. Djéga-Mariadassou, "On the role of organic nitrogen-containing species as intermediates in the hydrocarbon-assisted SCR of NO_x", Appl. Catal. B: Environ. 54 (2004) 69-84.

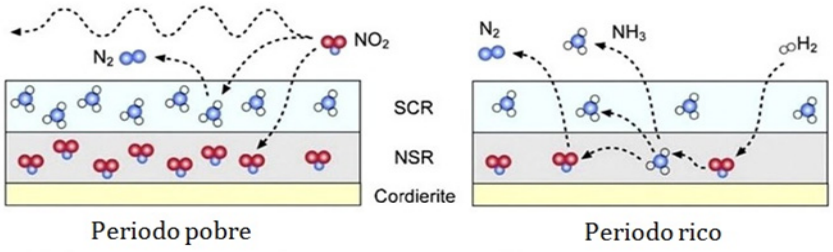

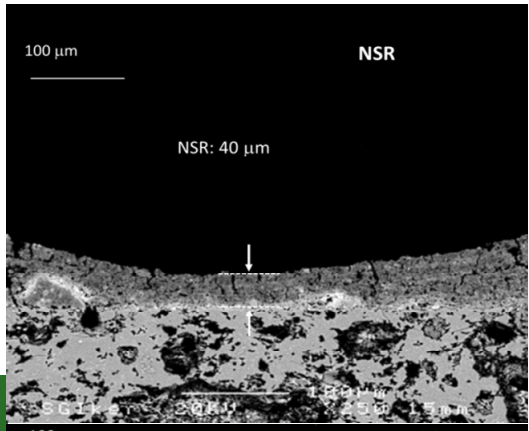

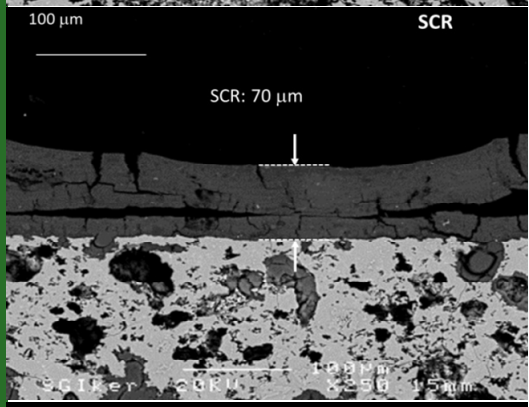

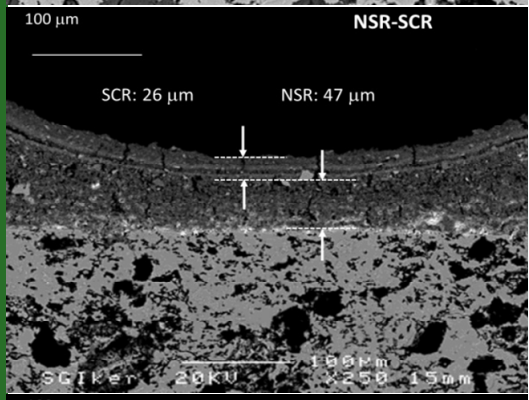

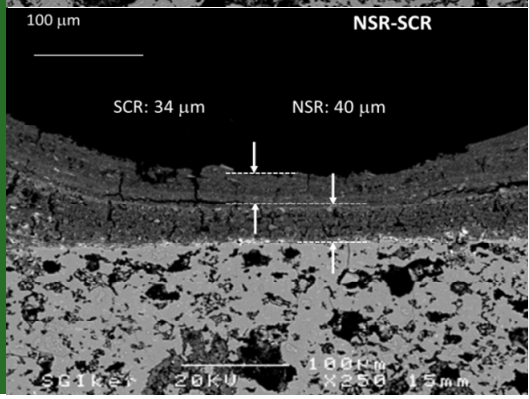

The elimination of environmental pollutant from vehicle emissions is a permanent challenge. Diesel engines run at high air/fuel ratios, which makes NO_x reduction challenging in such an oxidant environment. The coupling of NSR and SCR in a single device converts the management of NH_3 formation in the NSR catalyst into an advantage; NH_3 is trapped on acidic sites of the SCR catalyst during a period, and then is utilized to reduce NO_x that slips from the NSR catalyst. Different catalyst formulations are synthesized, characterized and tested under conditions simulating real application in the automobile. The effects of feeding different type of reducing agents (H_2, CO, C_3H_6, C_7H_8) on $DeNO_x$ efficiency of the different architectures —single NSR (Pt-Ba-(Ce)/Al_2O_3 monolith), single SCR (Cu/BETA and Cu/SAPO-34 monoliths) and combined NSR-SCR in series or dual layer— are analyzed.

La eliminación de contaminantes de las emisiones de automóviles es un reto permanente. Los motores diésel operan con elevada relación aire/combustible, lo que dificulta la reducción de los NO_x en un entorno altamente oxidante. El acoplamiento de NSR y SCR permite utilizar el NH_3 generado en el catalizador NSR para mejorar la eliminación de NO_x; el NH_3 se almacena en los centros ácidos del catalizador SCR durante un tiempo, que consecutivamente se liberan para reducir los NO_x no convertidos en el catalizador NSR. Se han sintetizado, caracterizado y probado distintas formulaciones en condiciones que simulan la aplicación real en el automóvil. Se ha estudiado la influencia de utilizar distintos compuestos reductores (H_2, CO, C_3H_6, C_7H_8) en la eficiencia $DeNO_x$ de las distintas arquitecturas: monolito NSR sólo (Pt-Ba-(Ce)/Al_2O_3), monolito SCR (Cu/BETA y Cu/SAPO-34) y combinaciones de NSR y SCR en serie y dispuestos en doble capa.

ZTF-FCT
Zientzia eta Teknologia Fakultatea
Facultad de Ciencia y Tecnología

Ingeniaritza Kimikoa Saila
Departamento de Ingeniería Química